ACTIVE AND REACTIVE ULTRAFILTRATION MEMBRANES FOR WATER TREATMENT

ACTIVE AND REACTIVE ULTRAFILTRATION MEMBRANES FOR WATER TREATMENT

By NAN ZHANG, B.Eng., M. Eng.

A Thesis Submitted to the School of Graduate Studies in Partial Fulfilment of the Requirements for the Degree Doctor of Philosophy

DOCTOR OF PHILOSOPHY (2022)

Chemical Engineering, McMaster University

1280 Main St W, Hamilton, Ontario L8S 4L7

TITLE: Active and Reactive Ultrafiltration Membranes for Water Treatment

AUTHOR: Nan Zhang

B.Eng. (Tianjin University, China)

M.Eng. (Tianjin University, China)

SUPERVISOR: Dr. Charles-François de Lannoy

NUMBER OF PAGES: xxvi, 225

Lay abstract

Climate change, industrial and agricultural activities, and population growth exacerbate global water stress. A variety of advanced technologies have been studied to alleviate water scarcity and water pollution. Membrane technology owing to its low footprints and ease of operation, has drawn intensive attention for water purification and wastewater treatment. Further, integrating membrane technology, electrochemistry and catalysis can improve separation and selectivity of the filtration process. This work aims to fabricate high-performance active and reactive ultrafiltration membranes involving electrically conductive membranes, catalytic membranes and electrocatalytic membranes. Their use in water treatment inspires the development of advanced functionalized membranes and further accelerates the transition to industrial applications.

Abstract

Water pollution is of great concern worldwide as a result of increasing global industrialization, booming populations and human activity-induced pollution. Such water stress has increased the demand for developing water treatment technologies. The environmental-friendly membrane technology is attractive due to its simple modularity and ease of operation. This thesis focuses on the development and application of active and reactive ultrafiltration membranes based on the following five sub-research projects.

First, the occurrence of membrane fouling increases energy consumption and decreases membrane permeability for long-lasting membrane operation. Monitoring of membrane fouling evolution enables the adoption of appropriate cleaning strategies. This project investigates the use of electrical impedance spectroscopy (EIS) to measure the earliest fouling development on the surface of electrically conductive membranes (ECMs). The impact of latex foulants on impedance signals was investigated. Results confirmed the ability of *ex-situ* EIS to monitor fouling evolution, especially the quick response to the onset of fouling.

Further, fouling sensing by *in-situ* EIS on ECMs was explored in a two-electrode membrane filtration system where sticky biofouling was used to challenge the filtration process. The normalized diffusion-related impedance (R_d), an EIS-derived parameter, demonstrated that EIS detection was more sensitive to changes compared to the decline of permeate flux during the early stage of biofouling. With early detection of fouling evolution, applying an intermittent cathodic potential delayed biofilm growth. Hence

ECMs were demonstrated to play a dual function: EIS-enabled detection of biofouling evolution and surface biofouling mitigation.

A catalytic membrane microreactor (CMMR) combines catalysis and membranes for continuous water decontamination. In the next phase of research, a novel Pd-immobilized membrane was fabricated *via* batch impregnation. Its catalytic activity was evaluated by toxic 4-nitrophenol (4-NP) transformation with the assistance of sodium borohydride in a flow-through CMMR system. Further, Pd-immobilized membranes were used for mixed wastewater treatment, showing >99% of small molecular 4-NP conversion and >90% of macromolecular polyethylene oxide (PEO) rejection. Hence CMMRs demonstrate a great potential to be applied in the high-performance purification of mixed wastewater.

Following this preliminary noble metal immobilized CMMR, inexpensive Ni-Cu bimetallic CMMRs were prepared *via* either sequential impregnation or co-impregnation. Synergistic effects of electronic and geometric configurations of bimetals were hypothesized to account for the high catalytic conversion. Investigating the influence of operating conditions on catalytic activity indicated that 4-NP conversion followed the Langmuir-Hinshelwood (L-H) mechanism. The stability of Ni-Cu bimetallic CMMRs was attributed to both the polydopamine-assisted fabrication and the tortuous membrane pore structure.

Finally, electrocatalytic degradation is a reagent-free process compared to chemical catalysis by adding excess reducing agents. Electrocatalytic reductive degradation is controllable for detoxifying chlorophenols, while oxidative dechlorination likely causes

hazardous byproducts. A noble metal-free nickel phosphorous (Ni-P) membrane was fabricated for electrochemical reductive dechlorination of 2-chlorophenol (2-CP). Dechlorination was achieved by the catalytic production of atomic H* by water splitting, the stabilization of atomic H* *via* Ni-H* bonds and the adsorption of chlorinated compounds *via* Ni-Cl bonds. We observed 2-CP dechlorination of 42.7%, the reaction rate constant of 1.612 min^{-1} and Faradaic efficiency of 24.5% when an optimized cathodic potential of -2.50 V was applied to the Ni-P membrane.

Acknowledgements

First of all, I want to thank my supervisor Prof. Charles-François de Lannoy, for all the support during my Ph.D. period. His passion for delivering knowledge and curiosity for cross-disciplinary research are impressive. I was motivated to express opinions publicly and strive for excellence in personal growth and career development.

I would like to thank my supervisory committee, Prof. Raja Ghosh, Prof. Ravi Selvaganapathy, and Prof. Jamal Deen, for their constructive criticisms of my research. As a result, I was enlightened to have an in-depth understanding of experimental phenomena and develop a critical thinking ability.

I would like to thank the students from Prof. Robert Pelton Lab, Prof. Todd Hoare Lab, Prof. David Latulippe Lab, Prof. Zeinab Hosseinidoust Lab and Prof. Ayse Turak Lab for equipment training and usage. Many thanks to Michelle Whalen and Linda Ellis for handling the administrative work, and to Michael Clarke, Paul Gatt, Doug Keller, Tim Stephens and the staff at Canadian Center for Electron Microscopy (CCEM), and McMaster Analytical X-Ray Diffraction Facility (MAX), Biointerfaces Institutes (BI) and McMaster Regional Centre for Mass Spectrometry (MRCMS) for their technical supports.

I am grateful that colleagues in de Lannoy lab and my dear friends accompanied me to get through this journey filled with happiness and frustration. Special thanks to Yichen Wu, Mohamed Elganzoury, Hye-Jin Lee, Mohamad Amin Halali, Cassandra Chidiac, Scott Laengert, Alexander Sutherland, Colin Gibson, Daniel Osorio, Melissa Larocque,

Maria Ximena Ruiz-Caldas, Hannah Grewal, Erik Fréchette and Gavin Yuen, Lei Tian, Fengyan Wang, Yuanhua (Zela) Li, Ruonan Li, Liting Shi, Xiaotian Ju, Xueying (Sarah), Gaoyin He, Xiao Wu, Dongyang Li, Jinlei Li, Hongfeng Zhang, Lu Zhu, Dong Yang, Naveen Kumar Vasudevan, Zhicheng Pan, and Kaiyang Li.

I want to dedicate all the achievements to my dear parents and my sister, who make me believe that I deserve unconditional backup. Be proud to be the first person pursuing a Ph.D. in my family.

Lastly, I would like to thank myself for being brave to study at McMaster, which I never imagined ten years ago. I am fortunate to obtain courage and resilience from my favorite music and sports. I believe that every decision and action I made in the past determines who I am, so I hope I will still have the courage to pursue the self-value and experience the adventures in the next ten years.

Table of Contents

List of Figures and Tables

Chapter 1

Chapter 2

Chapter 3

Chapter 4

Chapter 5

Chapter 6

Chapter 2 Supplementary Information

Chapter 3 Supplementary Information

Chapter 4 Supplementary Information

Chapter 5 Supplementary Information

Chapter 6 Supplementary Information

Chapter 1

Chapter 2

Chapter 4

Chapter 2 Supplementary Information

Chapter 3 Supplementary Information

Chapter 5 Supplementary Information

Chapter 6 Supplementary Information

List of Abbreviations and Symbols

AC	Activated Carbon
AFM	Atomic Force Microscopy
ALD	Atomic Layer Deposition
AOP	Advanced Oxidation Process
BET	Brunauer -Emmett-Teller
BSA	Bovine Serum Albumin
BPA	Bisphenol A
CA	Cellulose Acetate
CDI	Capacitive Deionization
CE	Counter Electrode
CMMR	Catalytic Membrane Microreactors
CCEM	Canadian Centre For Electron Microscopy
CIP	Clean-In-Place
CLSM	Confocal Laser Scanning Microscopy
CNS	Carbon Nanostructure
CNT	Carbon Nanotube
COD	Chemical Oxygen Demand
CPE	Constant Phase Element
CR	Congo Red
CV	Cyclic Voltammetry
DBP	Disinfection Byproduct

DCMD	Direct Contact Membrane Distillation
DFT	Density Function Theory
DI	Deionized
DMF	Dimethylformamide
DP	Diffusion Polarization
EC	Electrochemical Coagulation
ECM	Electrically Conductive Membrane
EDL	Electrical Double Layer
EDS	Energy Dispersive X-Ray Spectroscopy
EIS	Electrically Impedance Spectroscopy
EPS	Extracellular Polymeric Substances
EU	European Union
FRA	Frequency Response Analysis
FO	Forward Osmosis
f-SW/DWCNT	Single-Walled/Double-Walled Carbon Nanotubes
FTIR	Fourier Transform – Infrared Spectroscopy
GC-MS	Gas Chromatography – Mass Spectrometry
GO	Graphene Oxide
GWF	Global Water Futures
ICP-OES	Inductively Coupled Plasma-Optical Emission Spectroscopy
LBL	Layer-By-Layer Assembly
MB	Methylene Blue

MBR	Membrane Bioreactor
MF	Microfiltration
MI	Membrane Distillation
MO	Methyl Orange
MOF	Metal Organic Framework
MW	Molecular Weight
MWCO	Molecular Weight Cut-Off
NF	Nanofiltration
NOM	Natural Organic Matters
NP	Nanoparticle
nZVI	Nano Zerovalent Iron
OCP	Open Circuit Potential
OD	Optical Density
PA	Polyamide
PBS	Phosphate-Buffered Saline
PC	Principal Component
PC	Polycarbonate
PCA	Principal Component Analysis
PDA	Polydopamine
PEO	Polyethylene Oxide
PEG	Polyethylene Glycol
PES	Polyethersulfone

PNP	*P*-Nitrophenol
PPCP	Pharmaceutical And Personal Care Product
PSF	Polysulfone
PVDF	Polyvinylidene Difluoride
PZC	Point Of Zero Charge
PVA	Poly Vinyl Alcohol
RCS	Active Chlorine Species
RE	Reference Electrode
rGO	Reduced Graphene Oxide
RMSE	Root-Mean-Square-Error
RO	Reverse Osmosis
ROS	Reactive Oxygen Species
SAED	Selected Area Electron Diffraction
SDS	Sodium Dodecyl Sulfate
SEM	Scanning Electron Microscopy
SIP	Sequential Impregnation
SMSI	Strong Metal-Support Interaction
TC	Tetracycline
TEM	Transmission Electron Microscopy
TFC	Thin Film Composite
TFN	Thin Film Nanocomposite
TMP	Transmembrane Pressure

TN	Total Nitrogen
TOC	Total Organic Carbon
UF	Ultrafiltration
US EPA	United States Environmental Protection Agency
USGS	United States Geological Survey
XPS	X-Ray Photoelectron Spectroscopy
XRD	X-Ray Powder Diffraction
WE	Working Electrode
WWTP	Wastewater Treatment Plant
4-AP	4-Aminophenol
4-NP	4-Nitrophenol

Declaration of Academic Achievement

This Ph.D. dissertation is organized in a "sandwich style" based on published, submitted and prepared for submission articles described as follows.

Chapter 2: **N. Zhang**, M.A. Halali, C.-F. de Lannoy, Detection of fouling on electrically conductive membranes by electrical impedance spectroscopy, Separation & Purification Technology, 2020.

https://doi.org/10.1016/j.seppur.2020.116823

Chapter 3: **N. Zhang**, H. Lee, Y. Wu, M. A. Ganzoury, C.-F. de Lannoy, Integrating biofouling sensing with fouling mitigation in a two-electrode electrically conductive membrane filtration system, Separation & Purification Technology, 2022.

https://doi.org/10.1016/j.seppur.2022.120679

Chapter 4: **N. Zhang**, Y. Wu, G. Yuen, C.-F. de Lannoy, Ultrafiltration Pd-immobilized catalytic membrane microreactors continuously reduce nitrophenol: A study of catalytic activity and simultaneous separation, In preparation

Chapter 5: **N. Zhang**, Y. Wu, C.-F. de Lannoy, Stable Ni-Cu Bimetallic catalytic membranes for continuous nitrophenol conversion, Applied Catalysis B: Environmental, In preparation

Chapter 6: **N. Zhang**, Y. Wu, M. A. Ganzoury, C.-F. de Lannoy, Electrochemical reductive dechlorination of 2-chlorophenol in a Ni-P ultrafiltration membrane reactor, ACS Applied Materials & Interfaces, In preparation.

Nan Zhang developed the methodology, conducted the investigation and formal analyses, and wrote the original manuscripts under the direct supervision of Dr. Charles-François de Lannoy, who was also responsible for funding acquisition, project planning and paper reviewing. Dr. Yichen Wu, Mohamed A. Ganzoury, Dr. Hye-jin Lee, and Dr. Mohamad Amin Halali, and Gavin Yuen, helped with some experiments and data analyses. All the co-authors have critically reviewed the manuscripts and provided valuable insights for improvements.

Chapter 1

Introduction

1.1 Pollutants in water sources

The demand for fresh water is increasing annually throughout the world with the development of industrialization and globalization. However, water scarcity is exacerbated due to climate change-induced severe conditions, such as flooding, droughts and potentially water and soil loss. Moreover, water pollution from industrial, municipal and agricultural activities accelerates water scarcity of potable drinking water and even induces water-related diseases after exposure to a diversity of pollutants. These pollutants are mainly categorized as heavy metals, organic matters, and disease-causing microorganisms.

1.1.1 Heavy metals

Heavy metals are of great concern in industrial and municipal wastewater, originating from electronics production, chemical manufacturing, steel manufacturing, fossil fuel combustion and household plumbing system. Heavy metals, i.e., arsenic (As), cadmium (Cd), chromium (Cr), copper (Cu), lead (Pd) and mercury (Hg), have been reported to cause damage on the skin, the circulatory system, organs (kidney/liver) and the nervous system of human beings [1].

1.1.2 Organic pollutants

Organic pollutants from industrial wastewater are often chemically and biologically stable and recalcitrant in water, which can cause severe environmental issues and pose threats to human health, i.e., cancer, fertility, organ damage, and nervous and immunity systems damage. The organic pollutants include pharmaceuticals and personal care

products (PPCPs), pesticides, chemical precursors for manufacturing and organic dyes [2, 3].

Pharmaceuticals and personal care products (PPCPs) including soaps, detergents, lotions, fragrances and sunscreen creams accumulate in water bodies. These synthetic organic molecules have long-lasting impacts on human beings and wildlife as they are not easily degraded in natural ecosystems [4]. Among the pharmaceutical drugs, ibuprofen (anti-inflammatory) and tetracycline (TC) are regarded as the typical antibiotics in wastewater treatment plant effluents, which have the potential to increase pathogen resistance even at a trace level [5-7].

Large quantities of pesticides are utilized in agricultural activity to increase the production of crops and vegetables in the post-industrial period. However, the leaching of pesticides and their residuals causes groundwater pollution, and the gradual accumulation through food chains would ultimately pose a hazardous effect on humans. The popular pesticides include herbicides (i.e., atrazine), insecticides (i.e., clothianidin) and fungicides (i.e., tricyclazole) [8].

A variety of organic precursors and intermediates are consumed to manufacture high-value chemical products in painting, paper making, adhesives and plastic industries [9], during which the unreacted reactants and the byproducts require to be remediated before discharging into the surface water. For example, bisphenol A (BPA), phenol and its derivatives (p-substituted phenols, p-methoxyphenol, p-nitrophenol, p-benzoquinone), oxalic acid (OA), formaldehyde, methanol (MeOH) and ethanol (EtOH) are commonly

used organic precursors for manufacturing processes [10-12]. Additionally, aromatic pollutants - organic dyes - from the textile industry have raised increasing attention in the past decades due to the release of enormous quantities of contaminated effluents into ecosystems with potential hazards for aquatic life. For example, millions of tons of reactive pigments (i.e., methyl orange, methylene blue, Rhodamine B, Congo red, acid orange, and nitrophenol) in dyeing and finishing processes are consumed annually, and the unfixed dyes account for 10-30% of the total pigments, with an average concentration of 2000 ppm [13-15]. Such high dye concentrations have a strong color in discharged effluents which partially blocks and filters light necessary for aquatic plants, while also affecting dissolved oxygen concentrations, ultimately deteriorating the water quality. Human exposure to dye-contaminated water also causes skin irritation and even induces cancers [16]. According to North America and European Union (EU) regulations, the dye concentration is confined to ppm before releasing into aquatic environments.

1.1.3 Biological pollutants

The effluents of municipal sewage contain enteric bacterial species originating from fecal contaminants, including *E. coli*, *Salmonella spp.*, *Vibrio spp.*, and *Shigella spp.*, that potentially cause fever, cholera and diarrhea symptoms in humans [17]. Further, the health risk for pathogenic microbes (e.g., *Pseudomonas aeruginosa*, *Legionella pneumophila*, *Mycobacterium sp.*, *Aeromonas hydrophila*, *Klebsiella pneumoniae*, *and Campylobacter sp.*) would infect millions of populations, especially in the developing regions without the disinfection technologies for polluted water.

1.2 Water purification and treatment technologies

Water treatment combines multiple steps and technologies to purify polluted water to produce drinking water. Specifically, surface water is sequentially treated by the primary, secondary and tertiary processes, as shown in **Figure 1**. Each process targets different contaminants, and the related technologies are discussed.

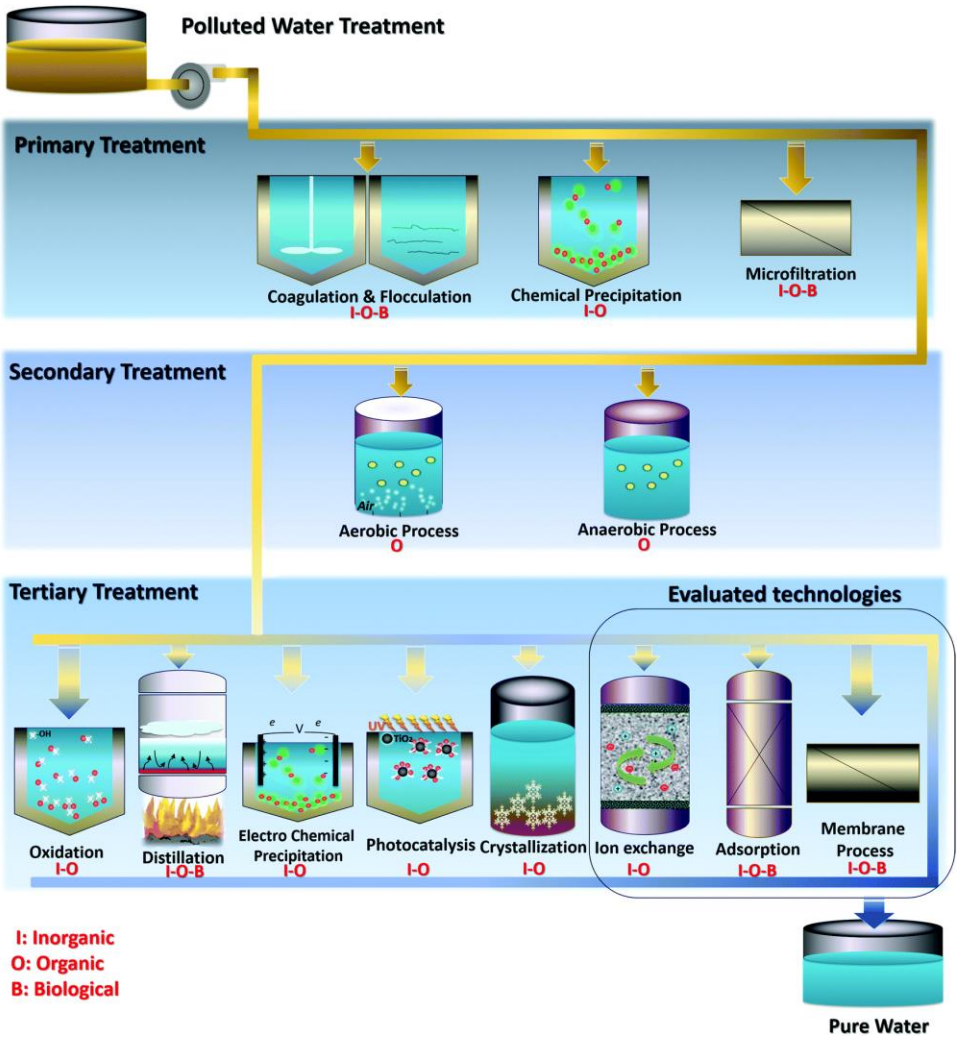

Figure 1. Water treatment technologies in combined primary, secondary and tertiary processes to remove inorganic, organic and biological contaminants. Reprinted from [18].

1.2.1 Technologies in primary treatment

The technologies used in primary treatment involve screening, settling/sedimentation, coagulation/flocculation and chemical precipitation. Such cost-effective techniques can remove sediments and sands on a massive scale.

Coagulation/Flocculation

Coagulation/flocculation of suspended particles occurs by adding coagulants/flocculants (i.e., ferric salts, aluminum salts and polyelectrolytes) into a particle-enriched solution. Then the coagulated solids are separated from the aqueous liquid by gravity. This method is suitable for high-efficient sludge settling and biological contaminants, yet high chemical consumption is an added operational cost for real water treatment.

Chemical precipitation

Chemical precipitation is a simple approach to remove high-concentration heavy metals. In this way, insoluble particles are formed *via* the reactions between heavy metals and chemical agents (i.e., hydroxides, sulfides and lime) and subsequently settled by gravity-induced sedimentation. In real applications, pre-treatment of heavy metals is needed to enrich them so that they reach their precipitation threshold in practical applications.

Settling/Sedimentation

The gravity-induced sedimentation is a relatively slow process, which can be significantly enhanced by adding appropriate coagulants and chemical precipitation agents. For example, suspended solids with a heavier gravity than water would settle to

the bottom of a sedimentation tank. At the same time, the supernatant is pumped out for the next step of treatment.

1.2.2 Technologies in secondary treatment

After solid particles are removed in the preliminary water treatment, organics including organic carbon, nitrogen and phosphorous are reduced in secondary treatment processes in which bacteria are used to consume and metabolize these nutrients. There are two categories of secondary treatment technologies: aerobic treatment and anaerobic treatment.

Aerobic treatment

Aerobic treatment can transform organic pollutants into carbon dioxide and hydrocarbons by a diversity of bacterial communities in the presence of oxygen. Therefore, oxygen/air must be mixed with wastewater by gas sparging or agitation. Membrane bioreactors (MBRs) are widely used for the process, in which microbes consume and degrade organic pollutants in the presence of a submerged membrane system. The bacteria are retained reaction vessel by the membranes while water and bacterial metabolic byproducts are permeated through the membranes. Since microorganisms are susceptible to feed characteristics (e.g., composition, concentration, temperature, pH and oxygen content), *in-situ* monitoring of the physicochemical properties of wastewater and produced water are needed in aerobic treatment.

Anaerobic treatment

Anaerobic digestion of organic pollutants is an alternative process initiated by microorganisms in the absence of oxygen for water decontamination and energy-rich biomasses (e.g., methane and alcohol) production. Anaerobic membrane bioreactors combine anaerobic digestion and low-pressure membrane filtration, addressing the issues of process sensitivity, instability and unsatisfactory removal efficiency [19]. Meanwhile, microbes/biofilms can be regarded as absorbents allowing heavy metal removal.

1.2.3 Technologies in tertiary treatment

Tertiary treatment is necessary when the effluent quality does not reach the standards after secondary biological treatment. This process can remove trace heavy metals, suspended particles and nutrients, as well as stubborn contaminants (e.g., PPCPs and pigments) that are not removed by coagulation/flocculation, sedimentation, and biological digestion. The strategies in tertiary treatment are introduced in the following.

Adsorption

Adsorption is an environmental-friendly and cost-effective approach to removing pollutants (i.e., heavy metals and micropollutants) *via* physical and/or chemical sorption between various adsorbents and pollutants. The surface-to-volume ratio of adsorbents is a determining factor for removal efficiency. Therefore, nanoparticle adsorbents with a high surface area have been developed in water treatment, such as activated carbon (AC), carbon nanotubes (CNTs), graphene, zeolites and nano metal oxides (e.g., α-FeOOH, α-Fe_2O_3, TiO_2, Al_2O_3).

Ion exchange

Ion exchange occurs on the functionalized resins where the targeted ions are trapped and the pre-saturated non-toxic ions are released. A simple application of ion exchange is to reduce the hardness of drinking water using a column packed with porous resins, during which Na^+ from the resins replaces Ca^{2+} and Mg^{2+} in the feed water. Further, regeneration of saturated resins can be easily achieved by acidic solutions.

Distillation

Distillation and evaporation are typical thermal technologies in water treatment. Polluted water is heated to its boiling temperature, in which the pure water is converted to the gas phase and then can be condensed for recovery. Meanwhile, the pollutants possessing a higher boiling point are retained in the retentate. However, this technology is limited because it is energy intensive.

Advanced Oxidation

Advanced oxidation is a well-established technology for wastewater treatment by oxidizing pollutants (organics and some inorganic ions) by the introduction of potent oxidizing agents, such as chlorine (Cl_2), chlorine dioxide (ClO_2), ozone (O_3), permanganate (MnO_4^-) and hydrogen peroxide (H_2O_2).

Electrochemical precipitation/Electrocoagulation

Electrochemical precipitation is an environmental-friendly technology that precipitates metal ions on a cathode in the form of elemental metals. Its removal efficiency relies on the surface properties of the cathode and the overall energy. Electrocoagulation (EC) is

an emerging technology that couples conventional coagulation and electrochemistry. The introduction of electrons destabilizes the suspended pollutants by neutralizing the repulsive forces, followed by forming large particle aggregates. A distinctive advantage of EC is no addition of chemical coagulants; a sacrificial Fe/Al anode is used for EC.

Photocatalysis

Photocatalysis can be used to mineralize pollutants by generating reactive oxygen species (ROS, i.e., hydroxyl radicals) through UV irradiation on a surface embedded by photocatalysts. A representative photocatalyst is TiO_2, with an electron in valence bands and an empty conduction band. After UV irradiation, the electron from valence bands is transferred to the conduction band, generating a hole. The contact of holes with water induces the generation of hydroxyl radicals, one of the most potent oxidizing agents for the degradation of pollutants.

Membrane

Membrane technology has been developed for water purification and water treatment due to its simple modularity, low footprints and ease of operation. This thesis introduces active and reactive ultrafiltration membranes for fouling removal and degradation of refractory pollutants (e.g., nitrophenols and chlorophenols). The following section briefly reviews the membrane-based technologies for pollutants removal in terms of membrane materials, configurations, applications and limitations.

1.3 Membrane technology

1.3.1 Membranes categories

Membranes are categorized based on the membrane pore size, shown in **Figure 2**. Porous membranes involve microfiltration membranes, ultrafiltration membranes and loose nanofiltration membranes. They remove particles by size exclusion that larger particles than the membrane pore size are retained on the feed side. In contrast, dense membranes involve tight nanofiltration membranes and reverse osmosis membranes. Selectivity and separation by dense membranes are determined by solution-diffusion; solubility and diffusivity are vital factors.

Microfiltration (MF) membranes exhibit a pore size ranging from 0.1 um to 1 um for particle-solution separation and bacterial removal under a low-pressure configuration. The high throughput and the cost-effective operation make it attractive for preliminary water treatment. However, its applications are limited by severe fouling and low rejection for viruses and small molecular contaminants. Ultrafiltration (UF) membranes possess a pore size ranging from 10 nm to 100 nm. They are applied to remove biological macromolecules (i.e., proteins, DNA, cell/cell debris, bacteria and viruses) and organic pollutants (i.e., color pigments and organic matters).

In contrast, nanofiltration membrane (NF) and reverse osmosis (RO) membrane for separation are high-pressure-driven processes. NF membranes with less than 10 nm pore can effectively remove dissolved organics. RO membranes are dense membranes that solution-diffusion determines the rejections of ions. Pure water is obtained by RO membranes where fluids pass through a semi-permeable RO membrane by a hydraulic-

pressure against the osmotic pressure. In this case, ions are retained on the feed side. However, high energy consumption, susceptibility to chloride, and significant capital investment are drawbacks of RO membrane technology.

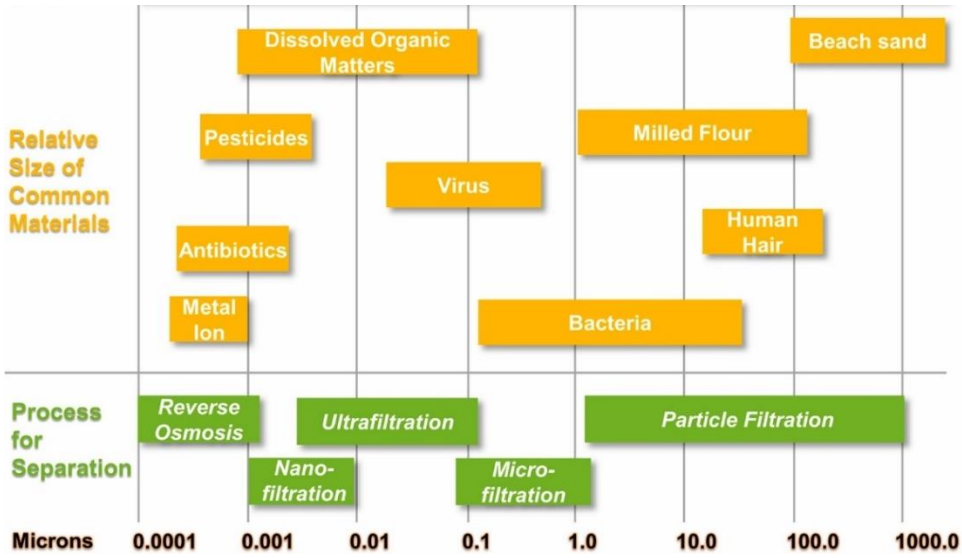

Figure 2. Comparison of membrane pore sizes and pollutant sizes. Reprinted from [20]

1.3.2 Membrane materials

Membrane materials involve organic polymers (i.e., polysulfone, polyethersulfone, cellulose acetate, polyvinylidenefluoride, polyacrylonitrile, polycarbonate, polypropylene, nylon, Teflon) and inorganic materials (i.e., ceramic, glass, stainless steel and derivatized carbon). Additionally, a typical RO membrane - the thin film composite (TFC) polyamide membrane - comprises a selective polyamide layer, a porous polysulfone support layer and a non-woven polyester fabric.

Organic membranes are flexible in various shapes, while inorganic membranes can undergo extreme environments, such as high transmembrane pressures, high temperatures and strong acid/base conditions. Therefore, membrane materials are selected based on the specific applications, considering feed characteristics, operating conditions, surface properties of membrane materials.

1.3.3 Membrane configuration

Membrane elements involve flat sheet membranes, tubular membranes and hollow fiber membranes. The fabrication and applications of bench-scale flat sheet membranes are explored in Chapters 2-6. From the perspective of industrial applications, mounting multiple flat sheet membranes in a spiral wound membrane module allow for the high-throughput separation in a compacted space. Hollow fiber membranes have the advantages of a large membrane surface per unit volume and flexibility in filtration performed in either “inside-out” or “outside-in” configuration. It is worth mentioning that the inside-out design can operate in crossflow mode, and induced shear force enables effective fouling control.

Separation and selectivity of membrane filtration are affected by module characteristics (i.e., packing density, size of the module, material type) and operational characteristics (i.e., submerged or pressurized, crossflow or dead-end filtration, inside-out or outside-in flow) [21]. Pressurized operation is commonly used for separation by applying forces. In contrast, the submerged process can operate continuously in high-solid environments, during which the membrane module is completely submerged by raw water and filtrate exits through the top of the module by a suction pump.

1.3.4. Membrane limitations

Membrane technology has some limitations, such as a selectivity-permeability trade-off and lack of reactivity for contaminant degradation. Additionally, the pressure drop along a membrane module limits the accuracy of pressure as a measurement for the onset and development of foulants across the entire membrane. Therefore, sensitive monitoring of local surface conditions is desired. Chapter 2 and Chapter 3 introduce an electrochemical technique for *in-situ* monitoring membrane fouling development.

1.3.5. Membrane challenges

Membrane fouling is a great challenge for long-term operation, resulting in reduced performance, such as loss of membrane permeability, reduced product quality, increased energy consumption and damage to membrane materials. Various foulants can be accumulated on the membrane surface, involving colloids, organic foulants, biofoulants and scaling.

Colloidal particles, such as latex beads and silica, are rigid foulants on the membrane surface and within the membrane matrix. The increasing amounts of colloidal particles promote the formation of a cake layer, increasing the membrane resistance for filtration.

Organic foulants are soft macromolecules, such as bovine serum albumin (BSA), humic acid (HA), natural organic matters (NOM), sodium alginate (ALG), polyacrylic acid (PAA) and polyethylene glycol (PEG) [22].

Biofouling is regarded as the stickiest foulants throughout membrane filtration. Microorganisms and their excretions - extracellular polymeric substances (EPS) - can

form dense biofilm on the top surface of membranes. Severe scaling occurs when the membranes are used to reduce the hardness of water sources, where charged ions such as Ca^{2+} and Mg^{2+} accumulate on the membrane surface.

Fouling degree on the membrane surface is determined by the surface properties of the membrane (i.e., roughness, wettability and pore sizes), feed conditions (i.e., pH, salt concentration and foulant types) and operating conditions (i.e., transmembrane pressure and cross-flow velocity). Membrane fouling mechanisms include external fouling and internal fouling. External fouling occurs when foulants accumulate on the membrane surface and block the pore entrance. Internal fouling is a process where foulants are trapped in membrane pores. Generally, external fouling is reversible that can be removed by cleaning strategies, whereas internal fouling is an irreversible process in which foulants are firmly deposited on pore walls.

1.3.6. Cleaning strategies for membrane fouling

The performance of membrane filtration can be significantly enhanced by pre-treatment of feed streams by adsorption, coagulation, peroxidation and prefiltration [23, 24], on the basis of the characteristics of feed water. Additionally, advanced cleaning strategies are developed to alleviate membrane fouling, including physical cleaning for reversible fouling and chemical cleaning for irreversible fouling[23, 25].

Physical cleaning

I. Back-Flushing/Cross-Flow Flushing

Periodically mechanical cleaning can prevent membrane surfaces from foulants attachment. For example, back-flushing through the membrane and cross-flow flushing across the membrane are used to recover the membrane permeability. Back-flushing reverses the direction of permeate flow, forcing internal fouling and surface fouling away from the membrane. Alternatively, cross-flow flushing is performed without permeation, and the velocity of the flow determines the cleaning efficiency. Such a shear stress-induced cleaning process allows for surface fouling mitigation. Interestingly, an integrated operation of back-flushing and cross-flow flushing has attracted much attention to optimizing cleaning protocols.

II. Gas sparging/scouring

Gas sparging is generally used in tubular and hollow fiber membrane filtration systems, where bubbles would generate turbulence near the membrane surface. The critical factors affecting cleaning efficiency include air velocity in cross-flow direction, size of air bubbles and movement of provided bubbles.

III. Vibration/ultrasound

Mechanical vibration is a chemical-free and *in-situ* approach for fouling mitigation and minimizing concentration polarization during filtration [26]. The input of mechanical forces can generate cavitation in the liquid phase followed by the collapse of these bubbles. A physical force is induced to detach adhesive particles from the membrane surface.

Chemical cleaning

Membrane fouling can be effectively controlled by adding chemical agents, such as acid solution (i.e., citric acid, hydrochloric acid, formic acid and sulphuric acid, nitric acid) for inorganic fouling control, alkali solution (i.e., sodium hydroxide) for organic fouling, biocides for microorganisms and biofouling, and oxidant (hypochlorite HOCl, hydrogen peroxide) for disinfection [27]. Coupling chemical and physical cleaning is a promising way to address the severe membrane fouling in water purification and treatment.

1.4 Active and reactive membranes

The separation by conventional membranes depends on either size exclusion for porous membranes or diffusion for dense membranes. In comparison, active and reactive membranes combine membrane filtration with other advanced techniques (such as catalysis and electrochemistry) for lab-scale water purification and water treatment, even though they are not commercially available.

Active and reactive membranes extend the role of membranes beyond rejection by combing multiple technologies such as electrochemistry and catalysis. This thesis discusses three types of active and reactive membranes. Electrically conductive membranes (ECMs) are active platforms at which fouling sensing and fouling mitigation can be achieved. The reactive membranes including catalytic membrane microreactors (CMMRs) and electrocatalytic membrane reactors (ECMRs) are integrated platforms for simultaneous separation and reactants/contaminants conversion.

1.4.1 Electrically conductive membranes

1.4.1.1 Conductive materials

Carbon-based nanomaterials, metal/metal oxides, and conductive polymers are widely used as conductive materials loaded on commercial membranes. Carbon-based materials, including carbon nanotubes (CNTs), carbon nanofibers (CNFs), and graphene/graphene oxide (GOs)/reduced graphene oxides (rGOs), have been extensively utilized because of their extraordinary mechanical and conductive properties. Metal/metal oxides are also good candidates for conductive coatings since they have high electrical conductivity with an ultra-thin thickness ranging from 10 to 100 nm. Conductive polymers, in particular, have alternate single and double bond conjugation, conveying the conductive property to polymers. Polyacetylene (PA), polypyrrole (PPy), polythiophene (PT), poly(ethylene dioxythiophene) (PEDOT) and polyaniline (PANI) have been reported as conductive polymers [28]. However, relatively low conductivity and fragile property limit further applications in water reuse.

1.4.1.2 Fabrication methods

Physical casting and surface coating are facile approaches to developing a variety of conductive membranes. Membrane casting is performed by homogenously mixing conductive nanoparticles with casting solutions and preparing the conductive membrane *via* phase inversion. However, the instability of conductive materials in the membrane matrix results in sub-optimal surface conductivity and membrane permeability. Surface modification exhibits high stability of conductive nanoparticles on the membrane through pressure-driven deposition, sputter deposition, spinning deposition, electroless deposition,

electrospinning, electrochemical printing and electrochemical deposition [29, 30]. However, the scale-up fabrication by surface modification needs to be further investigated. The conductive layers modify the selectivity and separation of membrane filtration and provide a new platform for electrochemical reactions.

1.4.1.3 Electroanalytic techniques

The electrical properties of ECMs are of great importance for electro-filtration with high efficiency. Four-point probes can be used to measure the surface conductivity of ECMs, where four probes were assayed in line with equal spacing between each probe. The rounded tips avoided piercing the thin layer compared to sharp needles and provided good electrical contact between thin film samples and probes. The current was applied and collected through the outer two probes and the voltage drop between the inner two probes was measured. Due to the high electrical impedance of the voltmeters, we assumed no current passed through the inner two probes, suggesting only sample resistance contributed to the voltage reduction. The use of four probes eliminated the contact resistances and wire resistances, simplifying the measurement of sheet resistance and electrical conductivity.

Electrical impedance spectroscopy (EIS) is a non-invasive technique for monitoring ECMs fouling conditions. A small-amplitude sinusoidal potential is continuously disturbing the interface with frequency ranges from 0.1 Hz to 1 MHz, and the resulting current will be recorded with changes in phase and amplitude. Such changes in magnitude and phase angle at each frequency are capable of providing information at the membrane-liquid interface where membrane fouling occurs.

An electroanalytic technique, cyclic voltammetry (CV), can probe redox reactions and capacitance behaviors of ECMs. The potential is applied linearly until a final potential is reached and then reversed to its initial potential. As a result, CV curves are obtained in terms of current as a function of applied potentials.

1.4.1.4 Applications of ECMs

The platform of ECMs combing electrical signals and membrane filtration can monitor fouling phenomena, remove surface fouling, and decontaminate pollutants in real-time water treatment.

I. Fouling detection by *in-situ* EIS

Conventional indicators, such as TMP and flux, reflect the membrane fouling rate and degree. However, these global parameters can not demonstrate the local membrane fouling, especially in integrated membrane modules. The fouling is well-established on the inlet side of the membranes, while TMP signals indicate the initial foulant deposition. Hence, *in-situ* fouling detection with high sensitivity is required to determine the cleaning frequency and the dosage of cleaning agents. *In-situ* EIS technique has been reported in non-conductive RO membrane systems, while its ability to monitor the foulants accumulation on the ECMs has not been elucidated. Chapter 2 and Chapter 3 demonstrate the capability of EIS for monitoring fouling and the impact of fouling degree on EIS signals.

II. Fouling control by applying external potentials

Membrane fouling can be alleviated by applying potentials *via* electrostatic repulsion, reactive agent production and bubble generation. For example, scaling caused by Ca^{2+}, SO_4^- and silica in NF membrane filtration can be alleviated by applying potentials, where the overpotential induces water splitting and thus the changes in local pH for mitigating pH-sensitive scaling. The use of cathodic potentials on ECMs allows for the removal of negatively charged organic matters (i.e., humic acid, BSA and biofilms) in either a continuous mode or an intermittent mode, where electrostatic repulsion dominates for the repulsion of organics from the membrane surface. Anodic potentials-empowered fouling removal occurs through electrochemical oxidation, generating ROS such as hydroxyl radicals, H_2O_2 and superoxide reacting with organic foulants. In terms of biofouling, alternating potentials are efficient for simultaneously biofouling inactivation and removal; the anodic potential is to inactivate bacteria by damaging the cell membrane and the cathodic potential is to repel negatively charged bacteria and biofilm [31].

The microbubbles evolution is an alternative mechanism for detaching organic foulants by mechanical force. However, it is not an ideal approach in practical applications due to the sharp drop in permeability and the possible damage to the membrane surface.

III. Decontamination *via* electrochemical reactions

Complete mineralization can be obtained by electrochemical oxidation *via* hydroxyl-mediated degradation, active-chlorine-mediated degradation and

electro-Fenton driven degradation. Electro-filtration by anodic currents can split water to produce hydroxyl radicals, one of the most potent oxidizing agents. Membrane materials and the applied potentials determine the decontamination performance. Active chlorine species (RCS, i.e., chlorine radicals and ClO^-) are induced by oxidizing chloride ions in anodic electro-filtration. Cl^- is initially oxidized to Cl* followed by free chlorine (Cl_2); Cl_2 is decomposed to HClO and ClO^-. Electro-Fenton reaction enables the ·OH generation, where ferrous ions (Fe^{2+}) and the supply of H_2O_2 determine the oxidation rate.

In recent years, electrochemical reduction has been attractive for converting pollutants to less hazardous products without reducing agents. This chemical-free process can be controlled by applied potentials and meanwhile avoid the production of undesirable byproducts. Therefore, electrochemical reduction is promising for degrading organic molecules. Reductive conversion of pollutants occurs on the cathodic ECM electrodes *via* direct electron transfer or indirect conversion by atomic H* radicals.

1.4.2. Catalytic membrane microreactors (CMMRs)

Catalytic membranes combining filtration and catalysis in a single unit is promising for high-efficient water purification. A CMMR takes advantage of the high surface area and interconnected porous network of membranes to increase the availability of reaction sites for catalytic conversion, enabling reaction process intensification, leading to higher conversion, selectivity and yield over conventional reactors [32-34]. The tortuous pore structure of membranes also limits nanocatalyst leaching and can increase catalyst

immobilization [35]. The catalytic performance of CMMRs is affected by catalyst characteristics (i.e., material type, catalyst loading, catalyst particle size, distribution, and density) and operating conditions (i.e., contaminant concentration, liquid flux, and liquid flow conditions).

1.4.2.1 Catalysts

I. Monometallic catalysts (Noble Metals)

The noble metals such as Ag and Pd in the form of nanoparticles have been proven to possess excellent catalytic activity for various chemical reactions, including reduction, oxidation and polymerization reactions. The drawbacks of monometallic catalysts are deactivation of catalytic sites by contaminants attachment and susceptibility of catalytic efficiency to local pH. In addition, individual noble metal catalysts are prone to fouling and attrition of active sites due to the intense competition between reactants and their intermediates. The dispersion of catalysts on the porous membrane can alleviate the undesired catalyst aggregate. Chapter 4 shows Pd catalyst on the membranes by coupling catalysis and filtration to remediate mixed wastewater.

II. Bimetallic Catalysts

Bimetallic catalysts have received increasing attention in recent years. Compared to monometallic catalysts, introducing a secondary metal can increase the available surface area of the noble metal to which it is added [36], reducing the amount of noble metal required and thereby reducing the costs associated with expensive catalyst materials. Additionally, interesting new electronic and catalytic

properties have been discovered from the synergistic effects of bimetals [35, 37-40]. For example, introducing a second metal into the catalyst contributes to reconfiguration in the electronic environment and geometric changes in the catalyst. Bimetallic catalysts possess unique physiochemical properties and are capable of altering the catalysis rate, selectivity of products and deactivation behaviors. Noble metal-based bimetallic catalysts, such as Ag-Cu and Pd-Ni have been reported to possess excellent catalytic activity. CMMR research is an exciting and new direction for membrane technologies, but using non-noble bimetallic catalysts is scarce. Chapter 5 introduces noble metal-free Ni-Cu bimetallic membranes for pollutants transformation.

1.4.2.2 Fabrication

The immobilization of catalysts on the membrane support can be achieved by physical blending, surface coating and impregnation.

I. Physical Blending

The physical blending of catalysts into polymeric structures involves mixing pre-formed catalysts into the casting solution, and then catalytic membranes are prepared *via* phase inversion. However, physical blending faces the challenges of low active site availability, low yield of products, poor stability, and a low active-surface-area-to-mass ratio of the catalysts, which is an inefficient use of the nanocatalyst material.

II. Surface Coating

Surface coating (e.g., spin coating) incorporates catalyst solutions, suspensions, or colloids onto the membrane by physical forces such as through the centrifugal forces achieved in the spin coating. While the catalysts can be stable and can produce uniform coating layers, this process does not coat the internal porous surface area. Thereby catalyst availability is limited. Further, this process is challenging to scale up, rendering it less attractive industrially.

III. Impregnation

Impregnation is a promising method during which membrane supports are immersed into solutions containing metal ions, and then catalysts are formed in the solution and within the membrane pores where they adsorb to the membrane pore walls. Pre-treatment of the membrane surface is necessary to enhance the affinity between metal NPs and polymeric substances. For example, polydopamine modified membranes are used for firmly attaching metallic nanoparticles to the membrane in Chapter 4 and Chapter 5.

1.4.2.3 Applications of CMMRs

Catalytic membrane-based reduction-filtration

Catalytic membrane-based reduction filtration can be used to transform reactants/pollutants into products by adding reducing agents (e.g., sodium borohydride). Catalytic reduction is explored for decontaminating nitro-organic compounds (i.e., nitrophenol, pesticides), -N=N- compounds (i.e., methyl orange), halogenated compounds (i.e., -Cl, -Br), nitrate ions, and heavy metal detoxication. More importantly, molecules with high economic value can be produced by catalytic reduction. For example, toxic 4-

nitrophenol can be converted to 4-aminophenol, an essential intermediate for chemical synthesis and the pharmaceutical industry.

Catalytic membrane-based oxidation-filtration

Catalytic membrane-based oxidation processes (AOPs) have been widely investigated in wastewater treatment. The different integrated catalytic membrane systems with photocatalysis, Fenton oxidation, persulfate oxidation and ozonation are investigated to degrade various organic pollutants. The mechanisms for catalytic membrane-based oxidation-filtration mechanisms are summarized in **Table 1**.

Table 1. Summary of catalytic oxidation/filtration systems. Adjusted from [20]

System	Catalysts	Mechanisms
Photocatalytic oxidation/filtration	TiO_2	Photocatalysts under UV irradiation adsorb photons, electrons in the valence band might be excited to the conduction band, generate holes with strong oxidation ability. ROS, i.e., •OH, $O_2^{\bullet-}$ Orangic pollutants + $\bullet OH / O_2^{\bullet-} \rightarrow$ Degradation products
Fenton oxide/filtration	Iron-based catalysts, e.g., FeS_2, α-FeOOH, α-Fe_2O_3, Fe_3O_4	Fe(II) reacts with H_2O_2 under acidic conditions to produce •OH and Fe(II) is regenerated by the reaction between Fe(III) and H_2O_2. •OH reacts with H_2O_2 to generate $HO_2^{\bullet-}$. Orangic pollutants + $\bullet OH / HO_2^{\bullet-} \rightarrow$ Degradation products
Persulfate oxide/filtration	Metal catalysts, e.g., MnO_2	Persulfate is activated by transition metal oxides catalyst, producing $SO_4^{\bullet-}$. $SO_4^{\bullet-}$ reacts with H_2O to produce •OH, and further persulfate reacts with H_2O to produce H_2O_2, $O_2^{\bullet-}$, $^1O_2$. Orangic pollutants + $SO_4^{\bullet-} / \bullet OH / O_2^{\bullet-} / {}^1O_2 \rightarrow$ Degradation products
Ozonation/filtration	MnO_x/Al_2O_3	Hydroxyl groups (S-OH) on catalysts are protonated under acidic conditions to form $S\text{-}OH_2^+$, which can react with O_3 for a series of chain reactions. Orangic pollutants + $\bullet OH / O_3 \rightarrow$ Degradation products

Despite the satisfactory degradation by catalytic oxidation/filtration, the applications of catalytic membranes are limited on a laboratory scale. Further, the scalability of

fabricating catalytic membranes and complicated impacts of co-existing pollutants on removal efficiency are still challenges in practical water purification. Therefore, an in-depth understanding of catalytic oxidation/filtration systems is desperately required.

1.5 Research objective

This research aimed to develop active and reactive ultrafiltration membranes for next-generation water purification and water treatment technologies in response to water scarcity and water pollution. This research was divided into three phases. Phase 1 explored the use of ECMs for fouling sensing and fouling mitigation in water purification, which involved the fabrication of various ECMs, the establishment of the relation between impedance-based detection signals and fouling degree on the membrane surface, and the evaluation of *in-situ* membrane cleaning strategies. Phase 2 introduces two types of novel catalytic membranes for conversing hazardous pollutants. Phase 3 reports a novel electrocatalytic membrane for detoxifying chlorophenol-contaminated water by electrochemical reductive dechlorination. These studies provided new insights for potable water treatment operators to adopt the appropriate strategies to alleviate regional-related water pollution.

1.6 Research contents

Detailed contents for each project are as follows.

I. Fouling sensing and fouling mitigation on ECMs: (1) Fabrication of CNT membranes by pressure-driven deposition for *ex-situ* detection of latex fouling development, and (2) Fabrication of ultra-thin gold-coated membranes by sputter

coating for *in-situ* biofouling detection by EIS technique and biofouling mitigation by intermittently applied potentials.

II. Development of novel CMMRs for water decontamination: (1) Fabrication of stable Pd-immobilized membranes *via* immersion impregnation for high-efficient purification of mixed wastewater, (2) Fabrication of non-noble metal Ni-Cu bimetallic membranes *via* either sequential impregnation or co-impregnation, and (3) Uncovering the mechanisms of nitrophenol conversion on CMMRs.

III. Fabrication of nickel-phosphorus membranes by electroless deposition for detoxifying chlorophenols *via* electrocatalytic reductive dechlorination.

1.7 Thesis outline

Chapter1

Chapter 1 introduces the technologies in water treatment, the background of membrane technology, the objectives of the research, and a brief overview of research details in each chapter.

Chapter 2

Chapter 2 demonstrates the importance of detecting fouling evolution throughout the membrane filtration process and introduces the use of electrical impedance spectroscopy (EIS) for latex fouling detection on ECMs. Fouling detection enables the adoption of effective cleaning strategies for fouling prevention. However, the conventional fouling indicators, such as transmembrane pressure (TMP) and permeate flux, are lagging for fouling formation. EIS is a non-invasive and real-time monitoring tool that has been

studied to monitor fouling on non-conductive membrane surfaces using four-terminal electrode systems. However, limited studies explored EIS-enabled sensing on conductive membranes using a simplified two-electrode system, and this study filled the gap.

The proof-of-concept study of EIS for fouling detection on CNT membranes was investigated. An electrochemical cell was developed in which a CNT membrane acted as a working electrode and a graphite electrode acted as the counter electrode. Latex beads were chosen as the model foulant due to their non-deformable structure and ease of deposition, allowing fine control of fouling and surface characterization. Membrane fouling was simulated by pressure depositing different amounts of latex beads onto the surface of the membrane, which was monitored by *ex-situ* EIS signals. Possible mechanisms were proposed to interpret the changes in EIS signals, which can help understand how the EIS signals differentiate diverse foulants. EIS has been used to distinguish the level of fouling for the first time.

Chapter 3

The networking structure of the CNT membrane in Chapter 2 encouraged foulants attachment in the initial fouling stage and such rough surfaces negatively impacted the recorded impedance signals. Therefore, the ultra-thin gold film with a flatter surface and higher conductivity was deposited on PES membranes and then was challenged by the sticky biofoulants in the membrane filtration processes.

Chapter 3 investigates the use of electrical impedance spectroscopy (EIS) to monitor biofilm development and the use of electric fields to mitigate biofouling on the surface of

gold-coated membranes. The multi-bacterial communities were developed on gold-coated membranes during which the permeate flux and impedance spectra were recorded to monitor the biofilm growth. The sensitivity of flux-based signals and EIS-based signals was evaluated. Further, either an intermittent cathodic potential or cross-flow flushing was applied to delay the biofilm growth on the ECM. A dual function of ECMs was demonstrated: EIS-enabled detection of biofouling evolution and surface biofouling mitigation.

Chapter 4

In addition to the use of ECMs in water purification, membrane-based technologies are attractive in wastewater treatment. Catalytic membrane microreactor (CMMR), combining membrane filtration and catalytic reactions into a single unit, is an emerging technology for water treatment. Intensified reactive processes occur by flowing reactants/contaminants through CMMRs, leading to high catalytic activity, selectivity and product yield over conventional catalytic processes. More importantly, CMMRs resolve the membrane limitation of size exclusion by coupling ultrafiltration with catalysis, showing a promising perspective for the high-efficient purification of dye- and macromolecules-contaminated water.

Chapter 4 reports a novel Pd-immobilized CMMR for the purification of mixed wastewater by dynamic integration of ultrafiltration and catalysis. The Pd-immobilized membrane was assembled by precipitating well-dispersed Pd precursors on polydopamine-modified PES membrane *via* immersion impregnation. Catalytic

performance of as-prepared Pd-immobilized membranes was evaluated by 4-nitrophenol conversion in the presence of $NaBH_4$ as a reducing agent. Pathways for reducing 4-nitrophenol (4-NP) to 4-aminophenol (4-AP) have been proposed. Further, the mixed wastewater treatment was explored by Pd-immobilized membranes.

Chapter 5

Compared to the noble metal-impregnated CMMRs in Chapter 4, catalysts composed of earth-abundant and inexpensive metals are more attractive for practical applications. In recent years, bimetallic catalysts have received increasing attention because of their desired electronic and geometric properties; however, only limited recent research has been investigated.

Chapter 5 introduces non-noble metal Ni-Cu bimetallic CMMRs *via* either successive impregnation or simultaneous impregnation. Two types of Ni-Cu bimetallic CMMRs were characterized by transmission electron microscopy (TEM), BET physisorption, scanning electron microscopy (SEM), energy-dispersive spectrometers (EDS), Fourier transform – infrared spectroscopy (FTIR) and X-ray photoelectron spectroscopy (XPS). 4-NP conversion was performed under batch and flow-through modes. The influence of residence time and concentration on catalytic performance was further identified. Finaly, the durability of bimetallic CMMRs was demonstrated by their continuous degradation of 4-NP throughout membrane operation.

Chapter 6

The applications of CMMRs in Chapter 4 and Chapter 5 may cause secondary pollution by adding excess reducing agents. Electrocatalytic reductive degradation is a frontier technology for water decontamination by producing atomic H* as the reducing agent.

Chapter 6 reports an inexpensive electrocatalytic membrane for electrochemical reductive dechlorination. The Ni-P nanoparticles were electroless deposited on the ultrafiltration PES membrane. A trade-off between electrical conductivity and membrane permeability for Ni-P membranes was assessed under different operational conditions. Further, Ni-P membranes were characterized by FTIR, XPS, SEM-EDS and BET measurements. Electrochemical dechlorination was performed under different applied cathodic potentials. Additionally, possible mechanisms for dechlorination were elucidated.

Chapter 7

Chapter 7 summarizes the main contributions of this thesis and provides future perspectives to foster next-step research.

1.8 References

[1] L. Joseph, B.M. Jun, J.R.V. Flora, C.M. Park, Y. Yoon, Removal of heavy metals from water sources in the developing world using low-cost materials: A review, Chemosphere 229 (2019) 142-159. https://doi.org/10.1016/j.chemosphere.2019.04.198.
[2] F. Lu, D. Astruc, Nanocatalysts and other nanomaterials for water remediation from organic pollutants, Coordination Chemistry Reviews 408 (2020). https://doi.org/10.1016/j.ccr.2020.213180.
[3] O.M. Rodriguez-Narvaez, J.M. Peralta-Hernandez, A. Goonetilleke, E.R. Bandala, Treatment technologies for emerging contaminants in water: A review, Chemical Engineering Journal 323 (2017) 361-380. https://doi.org/10.1016/j.cej.2017.04.106.
[4] J.L. Liu, M.H. Wong, Pharmaceuticals and personal care products (PPCPs): a review on environmental contamination in China, Environ Int 59 (2013) 208-24. https://doi.org/10.1016/j.envint.2013.06.012.
[5] A.R. Bakr, M.S. Rahaman, Electrochemical efficacy of a carboxylated multiwalled carbon nanotube filter for the removal of ibuprofen from aqueous solutions under acidic conditions, Chemosphere 153 (2016) 508-20. https://doi.org/10.1016/j.chemosphere.2016.03.078.

[6] Z. Liu, M. Zhu, Z. Wang, H. Wang, C. Deng, K. Li, Novel antimony doped tin oxide/carbon aerogel as efficient electrocatalytic filtration membrane, AIP Advances 6(5) (2016). https://doi.org/10.1063/1.4950799.
[7] Z. Liu, M. Zhu, Z. Wang, H. Wang, C. Deng, K. Li, Effective Degradation of Aqueous Tetracycline Using a Nano-TiO(2)/Carbon Electrocatalytic Membrane, Materials (Basel) 9(5) (2016). https://doi.org/10.3390/ma9050364.
[8] P. Gayen, C. Chen, J.T. Abiade, B.P. Chaplin, Electrochemical Oxidation of Atrazine and Clothianidin on Bi-doped SnO2-Ti nO2 n-1 Electrocatalytic Reactive Electrochemical Membranes, Environ. Sci. Technol 52(21) (2018) 12675-12684. https://doi.org/10.1021/acs.est.8b04103.
[9] A.R. Bakr, M.S. Rahaman, Removal of bisphenol A by electrochemical carbon-nanotube filter: Influential factors and degradation pathway, Chemosphere 185 (2017) 879-887. https://doi.org/10.1016/j.chemosphere.2017.07.082.
[10] G. Gao, C.D. Vecitis, Electrocatalysis aqueous phenol with carbon nanotubes networks as anodes: Electrodes passivation and regeneration and prevention, Electrochimica Acta 98 (2013) 131-138. https://doi.org/10.1016/j.electacta.2013.02.127.
[11] A.M. Zaky, B.P. Chaplin, Mechanism of p-substituted phenol oxidation at a Ti4O7 reactive electrochemical membrane, Environ. Sci. Technol 48(10) (2014) 5857-67. https://doi.org/10.1021/es5010472.
[12] H. Liu, A. Vajpayee, C.D. Vecitis, Bismuth-doped tin oxide-coated carbon nanotube network: improved anode stability and efficiency for flow-through organic electrooxidation, ACS Appl Mater Interfaces 5(20) (2013) 10054-66. https://doi.org/10.1021/am402621v.
[13] M. Solís, A. Solís, H.I. Pérez, N. Manjarrez, M. Flores, Microbial decolouration of azo dyes: A review, Process Biochemistry 47(12) (2012) 1723-1748. https://doi.org/10.1016/j.procbio.2012.08.014.
[14] K.T. Chung, Azo dyes and human health: A review, J Environ Sci Health C Environ Carcinog Ecotoxicol Rev 34(4) (2016) 233-261. https://doi.org/10.1080/10590501.2016.1236602.
[15] <Azo Dyes Characterization and Toxicity-A Review.pdf>.
[16] S. Madhav, A. Ahamad, P. Singh, P.K. Mishra, A review of textile industry: Wet processing, environmental impacts, and effluent treatment methods, Environmental Quality Management 27(3) (2018) 31-41. https://doi.org/10.1002/tqem.21538.
[17] B.A. Hemdan, A.M. El Nahrawy, A.M. Mansour, A.B.A. Hammad, Green sol-gel synthesis of novel nanoporous copper aluminosilicate for the eradication of pathogenic microbes in drinking water and wastewater treatment, Environ Sci Pollut Res Int 26(10) (2019) 9508-9523. https://doi.org/10.1007/s11356-019-04431-8.
[18] S. Bolisetty, M. Peydayesh, R. Mezzenga, Sustainable technologies for water purification from heavy metals: review and analysis, Chem Soc Rev 48(2) (2019) 463-487. https://doi.org/10.1039/c8cs00493e.
[19] Y.S. Hu, X.L. Cai, R.D. Du, Y. Yang, C. Rong, Y. Qin, Y.Y. Li, A review on anaerobic membrane bioreactors for enhanced valorization of urban organic wastes: Achievements, limitations, energy balance and future perspectives, Science of the Total Environment 820 (2022). https://doi.org/10.1016/j.scitotenv.2022.153284.
[20] N. Li, X. Lu, M. He, X. Duan, B. Yan, G. Chen, S. Wang, Catalytic membrane-based oxidation-filtration systems for organic wastewater purification: A review, J Hazard Mater 414 (2021) 125478. https://doi.org/10.1016/j.jhazmat.2021.125478.
[21] R. Field, K. Peinemann, S. Nunes, Membrane Technology: Membranes for Water Treatment, Ch, 2010.

[22] S. Wang, S. Liang, P. Liang, X. Zhang, J. Sun, S. Wu, X. Huang, In-situ combined dual-layer CNT/PVDF membrane for electrically-enhanced fouling resistance, J. Membr. Sci 491 (2015) 37-44. https://doi.org/10.1016/j.memsci.2015.05.014.
[23] W. Gao, H. Liang, J. Ma, M. Han, Z.-l. Chen, Z.-s. Han, G.-b. Li, Membrane fouling control in ultrafiltration technology for drinking water production: A review, Desalination 272(1-3) (2011) 1-8. https://doi.org/10.1016/j.desal.2011.01.051.
[24] H. Huang, K. Schwab, J.G. Jacangelo, Pretreatment for low pressure membranes in water treatment: a review, Environmental science & technology 43(9) (2009) 3011-3019.
[25] A. Abdel-Karim, S. Leaper, C. Skuse, G. Zaragoza, M. Gryta, P. Gorgojo, Membrane cleaning and pretreatments in membrane distillation – a review, Chemical Engineering Journal 422 (2021). https://doi.org/10.1016/j.cej.2021.129696.
[26] Z. Wang, J. Ma, C.Y. Tang, K. Kimura, Q. Wang, X. Han, Membrane cleaning in membrane bioreactors: A review, J. Membr. Sci 468 (2014) 276-307. https://doi.org/10.1016/j.memsci.2014.05.060.
[27] N. Porcelli, S. Judd, Chemical cleaning of potable water membranes: A review, Sep. Purif. Technol 71(2) (2010) 137-143. https://doi.org/10.1016/j.seppur.2009.12.007.
[28] F. Ahmed, B.S. Lalia, V. Kochkodan, N. Hilal, R. Hashaikeh, Electrically conductive polymeric membranes for fouling prevention and detection: A review, Desalination 391 (2016) 1-15. https://doi.org/10.1016/j.desal.2016.01.030.
[29] N. Zhang, M.A. Halali, C.-F. de Lannoy, Detection of fouling on electrically conductive membranes by electrical impedance spectroscopy, Sep. Purif. Technol 242 (2020). https://doi.org/10.1016/j.seppur.2020.116823.
[30] N. Zhang, H.-J. Lee, Y. Wu, M.A. Ganzoury, C.-F. de Lannoy, Integrating biofouling sensing with fouling mitigation in a two-electrode electrically conductive membrane filtration system, Sep. Purif. Technol 288 (2022). https://doi.org/10.1016/j.seppur.2022.120679.
[31] C. Thamaraiselvan, A. Ronen, S. Lerman, M. Balaish, Y. Ein-Eli, C.G. Dosoretz, Low voltage electric potential as a driving force to hinder biofouling in self-supporting carbon nanotube membranes, Water Res 129 (2018) 143-153. https://doi.org/10.1016/j.watres.2017.11.004.
[32] M. Liu, X. Zhu, R. Chen, Q. Liao, H. Feng, L. Li, Catalytic membrane microreactor with Pd/γ-Al 2 O 3 coated PDMS film modified by dopamine for hydrogenation of nitrobenzene, Chemical Engineering Journal 301 (2016) 35-41. https://doi.org/10.1016/j.cej.2016.04.116.
[33] V. Hakke, S. Sonawane, S. Anandan, S. Sonawane, M. Ashokkumar, Process Intensification Approach Using Microreactors for Synthesizing Nanomaterials-A Critical Review, Nanomaterials (Basel) 11(1) (2021). https://doi.org/10.3390/nano11010098.
[34] M.I. Domínguez, M.A. Centeno, M. Martínez T, L.F. Bobadilla, Ó.H. Laguna, J.A. Odriozola, Current scenario and prospects in manufacture strategies for glass, quartz, polymers and metallic microreactors: A comprehensive review, Chemical Engineering Research and Design 171 (2021) 13-35. https://doi.org/10.1016/j.cherd.2021.05.001.
[35] Y. Chen, S. Fan, B. Qiu, J. Chen, Z. Mai, Y. Wang, K. Bai, Z. Xiao, Cu-Ag Bimetallic Core-shell Nanoparticles in Pores of a Membrane Microreactor for Enhanced Synergistic Catalysis, ACS Appl Mater Interfaces 13(21) (2021) 24795-24803. https://doi.org/10.1021/acsami.1c04155.
[36] F. Yao, S. Liu, H. Cui, Y. Lv, Y. Zhang, P. Liu, F. Hao, W. Xiong, H.a. Luo, Activated Carbon Supported Non-noble Bimetallic Ni-Based Catalysts for Nitrocyclohexane Hydrogenation to Cyclohexanone Oxime under Mild Conditions, ACS Sustainable Chemistry & Engineering 9(8) (2021) 3300-3315. https://doi.org/10.1021/acssuschemeng.0c09168.
[37] Z. Meng, H. Liu, Y. Liu, J. Zhang, S. Yu, F. Cui, N. Ren, J. Ma, Preparation and characterization of Pd/Fe bimetallic nanoparticles immobilized in PVDF·Al2O3 membrane for

dechlorination of monochloroacetic acid, J. Membr. Sci 372(1-2) (2011) 165-171. https://doi.org/10.1016/j.memsci.2011.01.064.
[38] N. Berahim, W. Basirun, B. Leo, M. Johan, Synthesis of Bimetallic Gold-Silver (Au-Ag) Nanoparticles for the Catalytic Reduction of 4-Nitrophenol to 4-Aminophenol, Catalysts 8(10) (2018). https://doi.org/10.3390/catal8100412.
[39] Y.Y. Li Sip, D.W. Fox, L.R. Shultz, M. Davy, H.-S. Chung, D.-X. Antony, Y. Jung, T. Jurca, L. Zhai, Cu–Ag Alloy Nanoparticles in Hydrogel Nanofibers for the Catalytic Reduction of Organic Compounds, ACS Applied Nano Materials 4(6) (2021) 6045-6056. https://doi.org/10.1021/acsanm.1c00881.
[40] L. Liu, R. Chen, W. Liu, J. Wu, D. Gao, Catalytic reduction of 4-nitrophenol over Ni-Pd nanodimers supported on nitrogen-doped reduced graphene oxide, J Hazard Mater 320 (2016) 96-104. https://doi.org/10.1016/j.jhazmat.2016.08.019.

Chapter 2

Detection of Fouling on Electrically Conductive Membranes by Electrical Impedance Spectroscopy

Reprinted from *N. Zhang, M.A. Halali, C.-F. de Lannoy, Detection of fouling on electrically conductive membranes by electrical impedance spectroscopy, Separation & Purification Technology, 2020.*

2.1 Abstract

Detecting the onset of membrane fouling is critical for effectively removing membrane foulants during microfiltration (MF) separation. This work investigates the use of electrical impedance spectroscopy (EIS) on the surface of electrically conductive membranes (ECMs) to measure the earliest development of membrane surface fouling. An electrochemical cell was developed in which an ECM acted as a working electrode and a graphite electrode acted as the counter electrode. Conductive membranes were fabricated by coating single-walled/double-walled carbon nanotubes (f-SW/DWCNT) on microfiltration polyethersulfone (PES) supporting membranes. Membrane fouling was simulated by pressure depositing different amounts of latex beads onto the surface of the membrane in a dead-end filtration cell. Changes in membrane water permeability were correlated to the degree of membrane fouling. Clean membranes had water permeability of 392 ± 28 LMH/bar. Reduction of membrane water permeability of 13.8 ± 3.3%, 15.8 ± 4.7%, 17.8 ± 0.5% and 27.1 ± 4.6% were observed for membranes covered with 0.028mg/m^2, 0.28 mg/m^2, 1.40 mg/m^2 and 2.80 mg/m^2 on the membranes, respectively. These small differences in fouling degree were statistically resolvable in measured Nyquist plots. It was observed that the diameter of the higher frequency charge transfer region (10^4 ~ 10^6 Hz) of the Nyquist plot semicircles increased with greater fouling. These observations were hypothesized to correspond to decreasing surface conductivities of the membranes by the incorporation of insulating materials (latex beads) within the porous conductive coating. This proposed hypothesis was supported by measured EIS results modeled with a theoretical equivalent circuit. Fouled membrane surface

conductivity, surface hydrophilicity, and pore size were measured by SEM, four-point probe conductivity, contact angle, and MWCO experiments, respectively, to compare conventional characterization techniques with non-destructive EIS measurements.

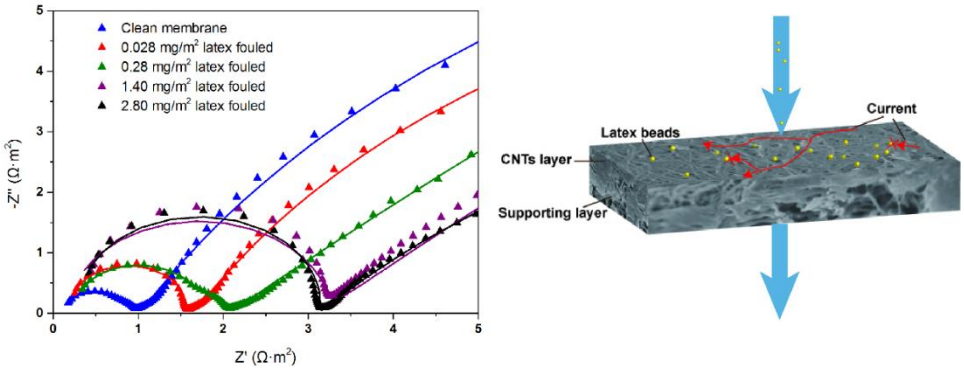

2.2 Introduction

Membranes have been demonstrated to be the most efficient and effective method for water and wastewater treatment, as well as for desalination. The advantages of membranes over conventional chemical and thermal separations are smaller footprints, simpler modularity and lower operational costs. Despite decades of demonstrable operational success, surface fouling is one of membrane technology's greatest challenges [1]. Polymeric membranes, in particular, are susceptible to various forms of fouling, including organic fouling [2, 3], colloidal fouling [4], biofouling [5-7], and mineral scaling [8]. The consequences of fouling involve reduced membrane flux, deteriorated permeate quality, and higher operation costs.

Conventionally, UF and MF membrane fouling is detected by changes in the transmembrane pressure across the membrane and/or changes in measured permeate flux [2, 9-11]. Additionally, RO membrane fouling is also detected by changes in salt

rejection [12]. By the time obvious changes occur within any of these three parameters, fouling has already been established on the membrane surface or within the membrane structure.

The structure of fouling changes as a function of time. As membrane fouling progresses, fouling layers often become thicker, more complex and composed of multiple foulants. In addition, fouling can form within the membrane structure as well as on its surface [13]. Over time these effects can cause irreversible membrane fouling. As such, detecting the onset of membrane fouling is critical to effectively preventing irreversible fouling [14]. During operation, the type of fouling that impacts the membrane is elucidated from feed water composition. In complex feeds, it can be challenging to identify the components responsible for fouling. Oftentimes, fouling type and distribution is only verified in destructive membrane autopsies carried out after a membrane is deemed to have been irreversibly fouled [15, 16]. These *ex-situ* analyses are unable to measure the development of fouling in real-time. There is a dearth of technologies able to provide information about the membrane interfacial behavior changes during the filtration process. A surface sensitive and real-time tool could alert a membrane operator to the onset of fouling enabling early and effective anti-fouling responses. Further, such a sensing tool could provide a comprehensive understanding of the evolution of fouling during membrane operation. Such a tool would enable both effective fouling control, and fundamental insights into complex fouling.

Electrochemical impedance spectroscopy (EIS) has been suggested to be a sensitive and non-destructive technique to detect the onset of membrane fouling, as well as to track

fouling growth *in situ*. Interests in the detection of non-conductive membrane fouling have dramatically increased recently [12, 17-22]. Kavanagh et al. [20] explored *ex-situ* detection of divalent salt fouling on reverse osmosis (RO) membrane surfaces by EIS. The electrical conductivity of the skin layer decreased measurably as small amounts of inorganic foulants precipitated on the membrane surface. Sim et al. [12] used EIS to monitor the *in-situ* fouling process on RO membrane in a flow cell. A noticeable change in the EIS signal was observed in the early stages of fouling compared with a negligible change in transmembrane pressure. Different types of fouling (bovine serum albumin (BSA) and silica) were distinguished based on different forms of impedance spectra. Gao et al. [22] investigated the effect of ionic strength on protein fouling on commercial PVDF membranes during ultrafiltration (UF) by online EIS. They demonstrated significant changes in the membrane-solution interface through the development of BSA fouling on the membrane using EIS.

While interests in the detection of non-conductive membrane fouling have increased, still little attention is being paid to the use of EIS characterization for electrically conductive membranes (ECMs) in the filtration process. Ahmed et al. [9] monitored the colloidal silica fouling on carbon nanostructure (CNS) coated filter paper using EIS in membrane distillation. Their work showed EIS detection provided earlier feedback on fouling onset as compared to the flux decline and decreased salt rejection. In addition, a simple two-electrode system composed of a conductive membrane as an electrode and a counter electrode was employed instead of the typical 4 terminal method used to minimize signal interference from the current in the connecting wires.

In this study, we demonstrate the use of EIS to detect foulants on the surface of electrically conductive microfiltration (MF) membranes. To the best of our knowledge, this is the first time EIS has been used to differentiate the level of fouling that occurs on electrically conductive membranes. Detection at very low fouling concentration was used to demonstrate that EIS can be used to detect the early onset of fouling on ECMs. The novelty of this study is to explore the possibility of using the EIS technique to detect the onset of colloidal fouling on ECMs, where the conductive interface, in this case carbon nanotubes (CNTs) acts as both a filter and the working electrode. As a proof of concept for the use of this technique on ECMs, we performed *ex-situ* EIS measurements on membranes that are fouled by rigid colloidal latex spheres. Latex spheres were selected as a simple model foulant that remain on the membrane surface after filtration and after applied pressure is released. Their non-deformable structure and ease of deposition allows for fine control of fouling and surface characterization. Further latex-induced fouling can be removed from the filtration set-up without substantially deforming the fouling layers. Their rigidity and stable fouling structure enable *ex-situ* measurements to closely mimic what would occur *in-situ*. As such latex fouling enables simple validation of this EIS technique. In this work, electrically conductive MF membranes were fabricated by coating carbon nanotubes (CNTs) onto supporting membranes. Latex fouling was developed in a dead-end filtration cell. Both the permeance (conventionally called pure water permeability) at a fixed transmembrane pressure and EIS impedance signals, were compared as methods to evaluate the sensitivity of the onset of latex fouling detection on ECMs. Additionally, the morphology of fouled membranes, surface

conductivity, surface hydrophilicity, and pore size were measured by SEM, four-point probe conductivity analysis, contact angle measurements, and MWCO experiments, respectively.

2.3 Materials and methods

2.3.1 Materials

Carboxyl functionalized single walled and double walled carbon nanotubes (f-SW/DWCNT, outer diameter: 1 ~ 4 nm, length: 5 ~ 30 μm, purity: >90 wt%, -COOH content: 2.73 wt%, EC > 100 S/cm) were purchased from Cheaptubes (USA). Sodium dodecyl sulfate (SDS) (MW: 288.38 Da) was purchased from Anachemia (USA). Poly (vinyl alcohol) (PVA, MW:31 kDa ~ 50 kDa, 98-99% hydrolyzed), poly (ethylene oxide) (PEO, MW: 0.3 MDa, 0.6 MDa, 1 MDa) and sodium chloride were purchased from Millipore-Sigma-Aldrich (USA). Polyethersulfone membranes (PES, diameter: 47 mm, pore size: 300 nm) were purchased from Sterlitech (USA). Carboxyl latex beads (4% w/v, 100 nm) were purchased from Fisher Scientific (USA). DI water used in this study was from an Arium system (resistivity: 0.048 μS/cm).

2.3.2 Fabrication

Electrically conductive membranes (ECMs) were fabricated by coating CNTs onto supporting membranes, as described in our previous publication [23]. f-SW/DWCNTs were dispersed in DI water by sonication probes for 1 h with 40% intensity at intervals of 2 s on and 2 s off. The surfactant sodium dodecyl sulfate (SDS) was added to increase steric hindrance between f-SW/DWCNTs to prepare a homogeneous mixture under ultrasound treatment for 2 h. Following suspension of f-SW/DWCNTs, dissolved poly

vinyl alcohol (PVA) was added to the mixture and ultrasonicated for an additional 1 h. The mass ratio of f-SW/DWCNTs to SDS to PVA was 1: 1.5: 10. Supporting membranes (polyethersulfone, PES, 47 mm,) were stored in DIW for 2 days before use. A known mass of CNTs (3 mg) in suspension was deposited on a wet pristine PES membrane by vacuum filtration and then cured in an oven at 105 °C for 1 h. After the membranes cooled down to room temperature, they were stored in DI water. The exception was the membranes used for selectivity experiments; these ECMs were fabricated following the steps above but without the addition of PVA, to prevent confounded TOC measurements from possible PVA leaching.

2.3.3 Characterization

2.3.3.1 Surface Morphology

Scanning electron microscopy (SEM, JEOL JSM-7000F) was used to examine the surface area and cross-sectional area of clean membranes and fouled membranes with different masses of latex fouling. Membranes were prepared by drying in an oven at 105 °C for 1 h and then cooling to room temperature. For top surface images, a 10 nm gold layer was coated onto the membrane surface using a sputter coater. For cross-sectional images, membranes were immersed in liquid nitrogen and then cracked without causing defects in the surface morphology. These samples were coated following the same method as mentioned above.

2.3.3.2 Contact angle

Contact angle measurements were used for investigating changes of surface hydrophilicity before and after fouling on the membrane by the sessile drop method using

Drop Shape Analysis. A 4 µL droplet of DI water was dispensed on the dry membrane surface. Steady state contact angle measurements were never observed as droplets that were deposited on the surface spread across the membrane surface quickly. Therefore, contact angles were recorded digitally in order to determine the initial contact angle. At least 10 measurements were conducted on each membrane and the average value was recorded.

2.3.3.3 Resistivity

The resistivity of the membranes was measured by a four-point probe conductivity meter [23]. This instrument measures the resistivity of conductive layers by considering the resistance between two pairs of needle electrodes as a function of the distance from each other. Membranes were dried and cooled at room temperature before measurement and then were cut into a square area of 1 cm^2 to fit in the needles' contact area. When a piece of membrane was placed on the square testing area, sharp needles gently touched the conductive layer of the membrane and were prevented from piercing the CNT skin layer into the PES insulating layer. The resistivity of each membrane was determined by the average value of 5 different measurements on different areas of the membrane.

2.3.3.4 Pure water permeance

Prior to the permeance measurement, the membrane was pressurized with DI water in a dead-end filtration cell (Sterlitech) at room temperature under 6.89 bar (100 psi) for 1 hour in order to compress the membrane. For the permeance test, DI water was filtered through the membrane (effective membrane surface area of 10.75 cm^2) and the volume of the permeate water was recorded every 30 seconds for 3 minutes at a given pressure. The

permeance of pure water through the membrane was calculated by Eq. (1) under applied pressures of 0.5, 1.0, 1.5 and 2.0 bar. Each test was conducted three times at each pressure and the average value was recorded.

$$\text{Permeance} = \frac{\Delta V}{A_{eff} P \Delta t} \quad (1)$$

where ΔV is the volume of the permeate at time intervals Δt ; P is transmembrane pressure and A_{eff} is the effective surface area of the membrane.

2.3.3.5 Selectivity

According to previous work [23], unbound PVA is unstable within the ECM during selectivity experiments. MWCO experiments can lead to PVA leaching through the membrane into the permeate impacting accurate MWCO measurements. Thus, clean and fouled membranes containing CNTs and SDS without PVA (clean membrane) were tested for their selectivity. PVA-free CNT membranes were only made for MWCO experiments, while all other tests were done with CNT-PVA membranes. While, MWCO measurements would be different for membranes made with and without PVA, the purpose of these experiments was to demonstrate the *relative* difference in membrane selectivity as a result of latex fouling. Polyethylene oxide (PEO) is a typical molecule used for membrane selectivity measurements. The selectivity of the porous membrane is associated with the molecular dimensions and the molecular weight of PEO and is expressed as a molecular weight cut-off (MWCO). The rejection of ECMs was tested to determine the MWCO of membranes using polyethylene oxide (PEO) (MW=0.3 MDa,

MW=0.6 MDa and MW=1.0 MDa) at 250 ppm in DI water. The PEO solution was filtered through the membrane under 0.69 bar (10 psi) to ensure that size exclusion was the dominant rejection phenomenon. The rejection is calculated by Eq. (2). The PEO concentrations in feed (C_F) and permeate (C_P) were measured by a total organic content (TOC) analyzer. The MWCO of the membrane was based on the molecular weight of PEO for which at least 90% rejection was achieved.

$$R = (1 - \frac{C_P}{C_F}) \times 100\% \quad (2)$$

2.3.4 Fouling development-EIS testing

Membranes were mounted in a dead-end filtration cell to completely wet the membrane with DIW at 6.89 bar (100 psi) air pressure for at least 1 h. After pretreatment, the conductive membrane was used as a working electrode in an electrochemical cell for EIS testing. Subsequently, membrane latex fouling experiments were conducted, and 0.028 mg/m^2, 0.28 mg/m^2, 1.40 mg/m^2 and 2.80 mg/m^2 of latex was deposited onto the membranes. The impact of different masses of latex that fouled the membrane was monitored by electrical impedance spectroscopy (EIS) (Autolab PGSTAT 302 N) coupled with a frequency response analysis (FRA) module.

Electrical impedance spectroscopy **(**EIS) was used for the detection of membrane fouling both qualitatively and quantitatively. A small amplitude sinusoidal alternating potential was applied to the membrane surface over a large range of frequencies. The changes in the signal response from the applied potential over this frequency range are quantifiable. Specifically, one can measure differences in the phase angle and amplitude of the

resultant impedance at each frequency. The principles of EIS are explained in the following section. We attempted to correlate these differences to the presence and concentration of fouling layers on the membrane. A three-electrode method was set up for EIS characterization (**Figure 1**), namely the conductive membrane was the working electrode, graphite was used as a counter electrode, and silver/silver chloride reference as a reference electrode with 8500 ppm sodium chloride as the electrolyte. A potentiostat with a frequency response analysis module was employed to measure impedance in the range of 10^{-1} to 10^{6} Hz with 5 mV potential perturbation when the electrochemical cell was at open circuit potential (OCP). Each membrane scan was performed for 30 minutes.

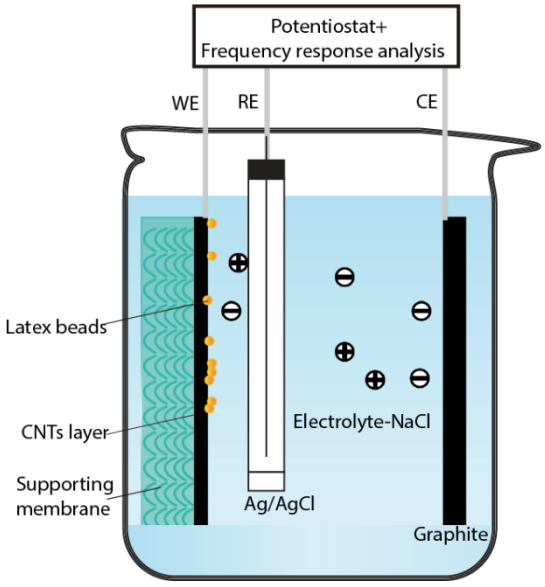

Figure 1. Schematic diagram of EIS testing cell

2.4 Principles of EIS

As EIS is still not a common technique in membrane operation, it is instructive to provide the basic principles. EIS is a non-destructive technique in which a small amplitude sinusoidal potential $E(t) = E_0 \sin(\omega t)$ is applied to a system over a range of frequencies. The resulting sinusoidal current is measured at the same frequencies as potential but shifted in phase angle. The difference in amplitude and phase angle provides electrochemical information of the interfaces between electrodes and the electrolyte.

The current response is expressed as:

$$I(t) = I_0 \sin(\omega t - \theta) \tag{3}$$

where I_0 is current amplitude and θ is the phase-shift.

Impedance is calculated by an expression analogous to Ohm's law.

$$Z = \frac{E(t)}{I(t)} = Z_0(\cos\theta - j\sin\theta) = Z' - jZ'' \tag{4}$$

where *Z'* is real impedance, *Z''* is imaginary impedance, and *j* is the imaginary constant defined by $j^2 = -1$.

The admittance is the reciprocal of the impedance, defined as:

$$Y = \frac{1}{Z} = G(\omega) + j\omega C(\omega) \tag{5}$$

where the conductance *G* is the ability to transfer electrons and the capacitance *C* is the ability to store electric charge.

In general, EIS data is expressed by a Nyquist plot, which maps the real part of impedance as a function of the imaginary part of impedance over a range of different frequencies. The impedance spectrum reflects interfacial properties between the membrane surface and solution. Measured impedance signals are modelled by an equivalent circuit using the software (Nova) and the χ^2 value is used to describe the goodness of the fit under the condition where the maximum number of iterations is 50 and the maximum change in parameter is 0.001.

2.5 Results and discussion

2.5.1 Surface morphology

Electrically conductive membranes (ECMs) were fabricated by depositing carbon nanotubes (CNTs) onto the surface of polyethersulfone (PES) microfiltration (MF) membranes. These conductive surfaces were then fouled with different masses of latex beads. Latex beads were used because of their well-defined geometry (spherical) and diameter (d = 100 nm) as well as their insulating nature similar to that of other typical inorganic foulants [12]. We initially studied the changes to membrane surface morphology as a function of latex bead fouling.

Figure 2 shows SEM images of a pristine ECM surface (**Figure 2A**), ECM surfaces fouled with latex bead coverage ranging from 0.028 mg/m^2 to 2.80 mg/m^2 (**Figure 2B**-**2E**) and a PES supporting membrane surface fouled with 2.80 mg/m^2 of latex beads (**Figure 2F**). The average pore size of the supporting MF membrane was estimated to be 300 nm, which is larger than the average diameter of the latex beads (100 nm). Rejection by size exclusion was not expected on the support membrane, however rejection by adsorption

was possible. Adsorption of some latex beads to the PES surface and within the pores was observed (**Figure 2F**). ECMs had significantly smaller pores sizes due to the dense layer of CNTs formed on the membrane surface, such that size exclusion was expected. ECMs have typically rough surfaces with thicknesses of 0.5 ~ 2 μm composed of randomly distributed CNTs [23] as observed in **Figure 2A** (cross-sectional SEM images shown in **Figure S1-A**). At higher latex concentrations (1.4 mg/m^2 and 2.8 mg/m^2), latex beads can be observed randomly distributed along the surface (**Figure 2D-2E**). At lower concentrations (0.028 mg/m^2 and 0.28 mg/m^2) the presence of the latex beads was challenging to observe. Latex beads were not observed from cross-sectional SEM imaging of the supporting layer with 2.8 mg/m^2 latex fouled (**Figure S1-B**). Nevertheless, it was assumed that some latex beads were embedded into and retained within the porous structure of the conductive surface. Based on SEM analyses, the rough surfaces of ECMs do not seem to be morphologically impacted by the deposited latex beads.

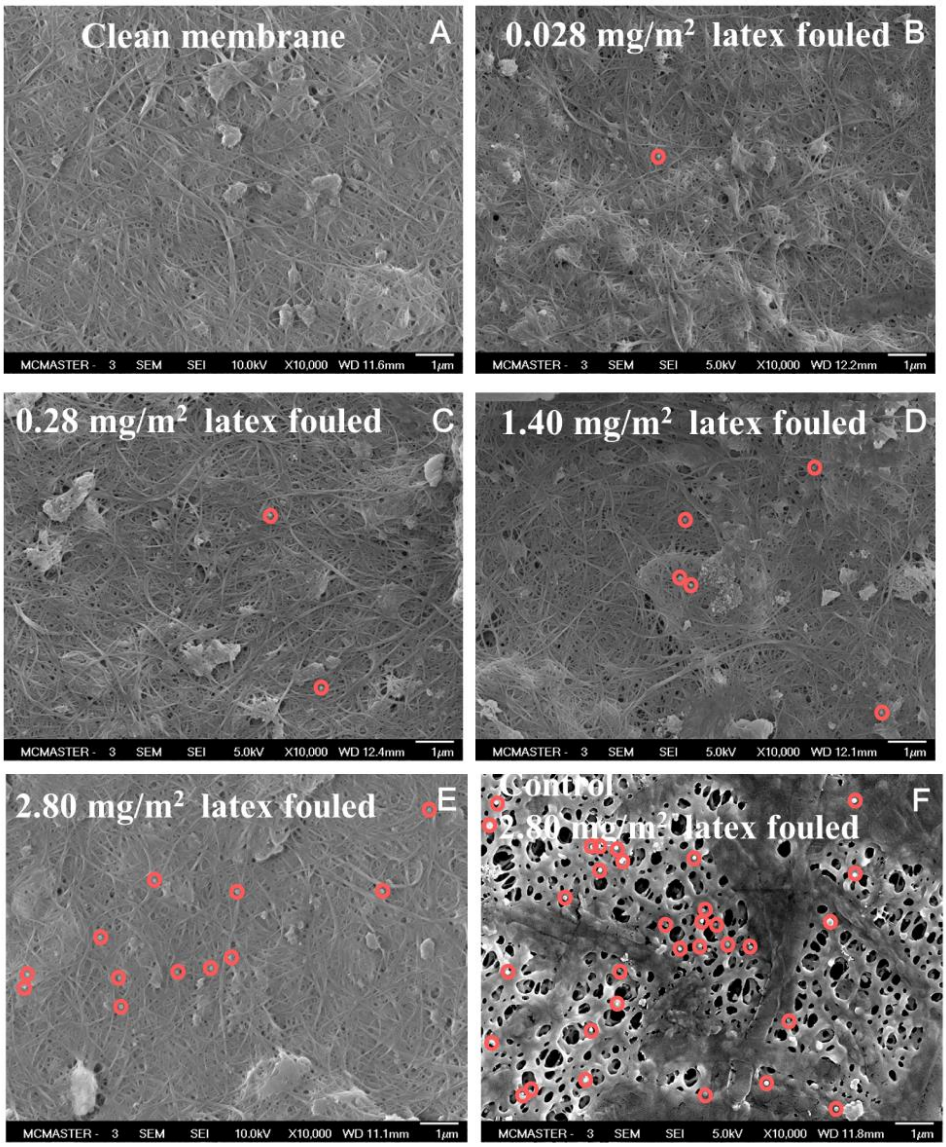

Figure 2. SEM images of different masses of latex beads fouling MF membranes. (A) Clean ECM membrane; (B) 0.028 mg/m^2 latex fouled; (C) 0.28 mg/m^2 latex fouled; (D) 1.40 mg/m^2 latex fouled; (E) 2.80 mg/m^2 latex fouled; (F) Control: 0.028 mg/m^2 latex fouled on PES MF membrane. Red circles highlight deposited latex beads on the surface.

2.5.2 Contact angle

The presence of fouling may increase the hydrophobicity of the ECMs as a result of the hydrophobic properties of natural foulants. The wetting behavior of the membrane is able to reflect the degree of fouling.

ECMs were fouled with latex beads using a dead-end filtration system. To measure contact angles of these surfaces, we needed to remove these membranes from the dead-end filtration cell. As such, during surface analysis, the surface pressure was no longer the same as during the filtration experiments. Nevertheless, all membranes were fouled using the same pressure, latex beads were observed to adsorb to the ECM surface, and all membranes were analyzed in an identical fashion. Therefore, we assumed that we could assess the *relative* difference in surface properties as a function of latex foulant concentration. The validity of this assumption was supported by expected trends in the data that reflect those in the literature [24, 25]. The validity of assessing the relative differences between membranes fouled with different amounts of latex beads is extended to all *ex-situ* measurements including contact angle, surface conductivity, and EIS.

Figure 3 shows the initial contact angles for water droplets deposited on the surfaces of ECM membranes with different masses of latex fouling. It is clearly observed that increasing surface hydrophobicity follows an increase in the mass of latex deposited. Latex fouling on and within the CNT layer increased the hydrophobicity of the conductive layer due to hydrophobic latex deposition. However, in the early and later stages of latex fouling (below 1.40 mg/m^2 latex fouling), the change in measured contact

angle was only slight. The measured values were all statistically significant as measured by their p-values ($p < 0.05$).

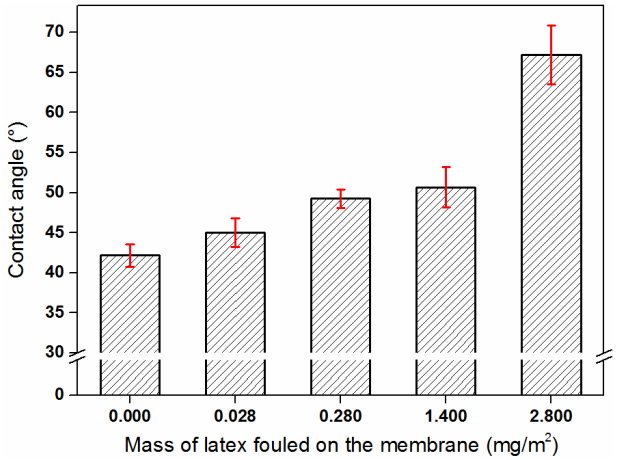

Figure 3. Contact angle of ECMs fouled with different masses of latex beads (Error bars represent the standard deviation; n = 10)

2.5.3 Resistivity

The resistivity of a membrane reflects the charge transfer across the surface and can be correlated to the interfacial properties of the skin layer. The thin layer of CNTs on the membrane allows a current to be generated when small potentials are applied. The factors impacting resistivity include the minimum concentration of CNTs required to achieve electrical percolation (the percolation threshold), the thickness of the electrically conductive skin layer, and the configuration of the CNTs. We deposited 3 mg of CNTs onto the MF membrane surface for comparison with previous work on ECMs [23, 26].

The resistivity of clean and fouled membranes was measured (**Figure 4**). Clean membranes had the lowest resistivity, and membrane resistivity gradually increased with greater latex fouling, as a result of the insulating nature of the latex beads embedded within the CNT layer. At low amounts of fouling, a clear trend exists for increased resistivity as a function of latex fouling. This indicates that electrical resistivity measurements are sensitive to small changes in membrane composition. However, with greater latex fouling (> 0.280 mg/m^2), no trend in resistivity change was statistically resolvable. This lack of trend is likely due to the random nature of the deposition of latex beads throughout the CNT layer.

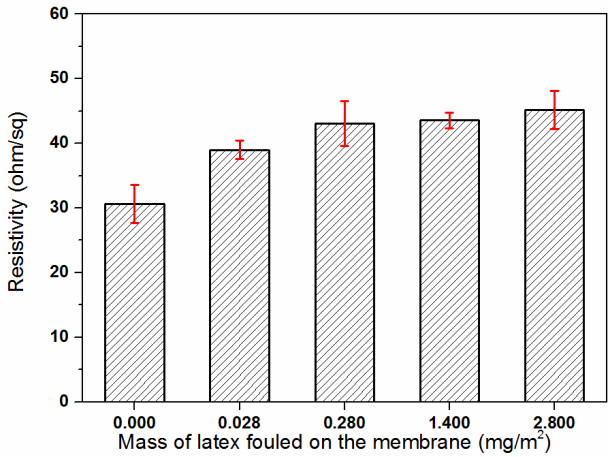

Figure 4. Resistivity of ECM membranes with different masses of latex fouling (Error bars represent the standard deviations; n = 5)

2.5.4 Pure water permeance

Conventionally, change in pure water permeance is a principal parameter that indicates membrane fouling. The fouling layer contributes to the mass transfer resistance of the

membrane, leading to the decrease in permeance during filtration. The permeance of pure water through the membrane under different fouling conditions was calculated in **Figure S2** and normalized permeances of membranes are shown in **Figure 5**, which compares the permeance of clean ECMs (392±28 LMH/bar). Reduction in membrane permeance of 13.8±3.3 %, 15.8±4.7 %, 17.8±0.5 % and 27.1±4.6 % were observed for membranes covered with 0.028mg/m^2, 0.28 mg/m^2, 1.40 mg/m^2 and 2.80 mg/m^2 latex on the membranes, respectively. The rapid decline in flux at low latex fouling mass was likely due to pore blockage during initial latex fouling. The ECMs are composite membranes that contain a porous MF support and a less porous f-SW/DWCNT surface layer. It is well known that foulants of sufficient size block preferential flow paths first, thus it is assumed that latex beads will first block the larger pores within the f-SW/DWCNT surface layer, causing substantial changes in pure water permeance. The surface layer's thickness is on the order of 1 μm, and foulants can be trapped within the surface structure as well as on its surface. As greater amounts of latex beads were accumulated on and in the ECM conductive layer, the membrane continued to foul, causing further flux decline. Accurate detection of latex fouling as measured by flux decline on the MF membrane surface was unreliable due to high errors associated with the measured permeance. This variability is typical for changes in membrane permeance as a function of foulant concentration and motivates the need for early fouling detection.

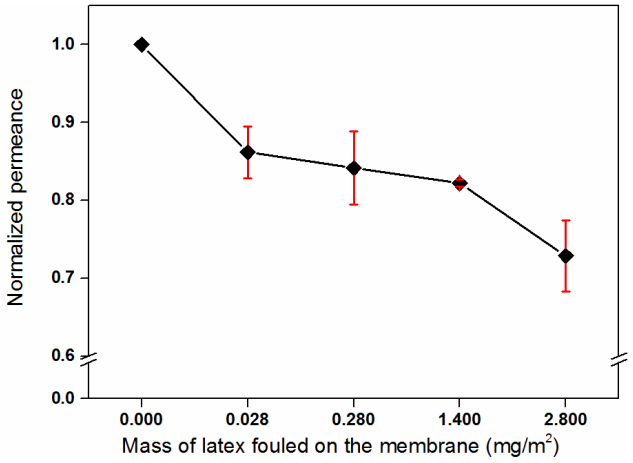

Figure 5. The influence of increased latex fouling on the permeance of ECMs (Error bars represent the standard deviations; n = 3)

2.5.5 Selectivity

Measurements of selectivity were performed on clean and 2.80 mg/m^2 latex-fouled ECMs (without PVA) as well as on pristine PES supporting membrane used as controls. The selectivity of MF membranes for PEO is dominated by size exclusion. The rejection of different molecular weight PEO is shown in **Figure 6**. The 2.80 mg/m^2 latex fouled membrane and clean membrane rejected 1.0 MDa PEO to greater than 90%. The rejection of 0.6 MDa PEO for 2.80 mg/m^2 latex fouled membrane was above 90%, while clean f-SW/DWCNT membranes had substantially lower rejection (60.6 %). The difference in selectivity between latex-fouled and clean membranes suggests that there are fewer pores through which PEO can pass. We hypothesize that latex beads first block larger pores within the f-SW/DWCNT layer and subsequently build up on and within the

CNT layer. The rejection of 0.3 MDa PEO dropped to 56.1 % and 44.3 % for latex-fouled and clean ECMs, respectively.

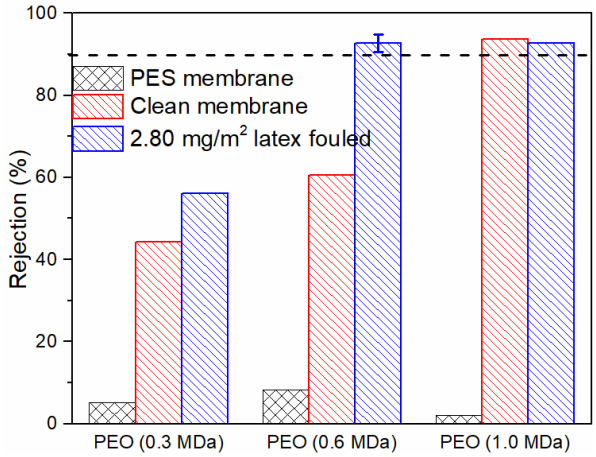

Figure 6. Rejection of clean membrane and latex fouled membrane (Error bars represent the standard deviations; n = 4)

2.5.6 Fouling development-EIS testing

Membranes fouled with different amounts of latex beads were measured by non-faradaic impedance, demonstrating that no redox reactions took place at the electrode interface. Therefore, we concluded that the transient current was achieved by periodic charge storage and charge depletion (membrane charging and discharging) at the electrical double layer (EDL) formed at the surface of the membrane by ions in solution [27]. No current peaks were observed in cyclic voltammetry measurements of ECM working electrodes (**Figure S3**) demonstrating that there were no faradaic reactions occurring at the f-SW/DWCNT membrane surface.

2.5.6.1 Identification of a non-faradaic impedance spectrum

Figure 7 shows a typical Nyquist plot for an unfouled f-SW/DWCNT membrane over a range of frequencies from 1 Hz to 10^6 Hz. We fit the impedance data to the impedance of an equivalent circuit consisting of resistors and capacitors. In this equivalent circuit, R_s refers to the bulk solution resistance, derived from the high-frequency limit of the real part of the impedance. The membrane electrode is modelled by the internal electrode resistor (R_m) in parallel with a non-ideal capacitor indicated by a constant phase element (CPE_m). The CPE is a common distributed circuit element, and is used to represent non-ideal, irregular, and rough electrode surfaces and/or inhomogeneous electrode materials. The irregular geometry of the porous ECM layer likely causes non-uniform current density distribution and potential in the electrolyte adjacent to the conductive surface. These variations and non-idealities are best represented by a CPE. The transient response of the electrode is also better represented by a CPE rather than a perfect double-layer capacitance. A second parallel R_d and CPE_d is introduced into the equivalent circuit to represent the diffusion limitation at low frequencies of ions into the f-SW/DWCNT surface layer. This electrically conductive surface layer is similar to a porous electrode with tortuous and multi-scale porous structures. R_m and R_d can be extracted from the first semicircle and the second pseudo semi-circle, respectively. A χ^2-test value is used to assess the quality of regression in simulation results.

When the potential perturbation is applied onto the working electrode at high frequency (> 10^4 Hz), the semi-circular Nyquist response is attributed to the internal electrode resistance and the imperfect double layer capacitance. In our system, this resistance is

associated with the dielectric and the structural properties of the f-SW/DWCNT layer, including the imperfect double layer capacitance that is established on the f-SW/DWCNT surface. As such, the region of high frequency is of particular interest for an investigation of fouling on and within the ECM. In our experiments, the resistance of the membrane surface increased with the accumulation of latex beads, as shown in **Figure 4**. This change in the electrode internal structure and surface can be more clearly observed by the increasing diameter of the semicircle in the Nyquist plot, shown in **Figure 8**.

At low frequency (< 10 Hz), mass-transfer limitation plays an important role. In our model system, we hypothesize that the diffusion of Na^+ and/or Cl^- from the electrolyte into the ECM structure's micropores lags the variations in applied alternating potential.

At mid frequencies (10 ~ 10^4 Hz), a transition region occurs that bridges the resistance of the electrode double layer capacitance to the resistance associated with the mass transfer of ions from the electrolyte to within the electrode. In our experiment, at mid frequencies, there is a transition from the dominant effect of the ECM's outer structural impact on charge distribution at the membrane/liquid interface (at high frequencies) to the inner microporous structure of the membrane electrode (at low frequencies).

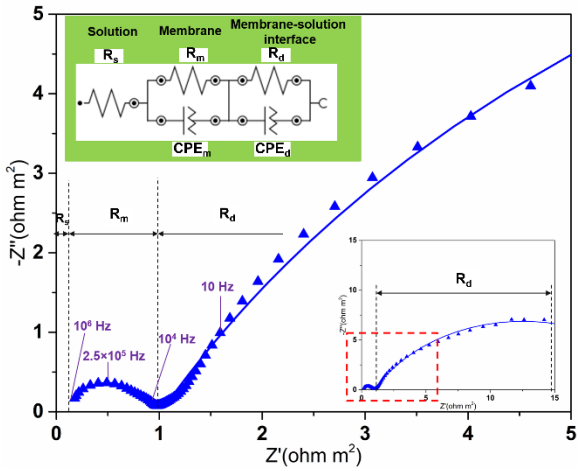

Figure 7. Schematic of a typical Nyquist plot of the MF membrane and the corresponding equivalent circuit

2.5.6.2 The formation of fouling measured by EIS

EIS was used to monitor the changes in the membrane interface as a result of latex fouling. Both Nyquist plots and Bode plots can be used to describe the interfacial properties of the membrane surface, derived from the frequency-dependant impedance. Nyquist plots present the correlation between the real component and the imaginary component of impedance at each frequency. Nyquist plots are used to demonstrate the relationship between the amplitude of impedance and the phase angle. An alternative representation of this data is to use Bode plots, which present the amplitude and the phase angle of impedance as a function of frequency. Bode plots are used to emphasize the impact of frequency on the impedance. To study the impact of fouling, Nyquist plot, Bode-amplitude plot and Bode-phase plot, were measured and are presented in **Figure 8**.

Capacitance-frequency and conductance-frequency graphs were extracted from the experimental impedance data, shown in **Figure 9**.

Latex was deposited onto the surface of the membrane from very low to high concentrations (0.028 mg/m^2 ~ 2.8 mg/m^2). Deposition at low concentrations was likely primarily deposited onto the surface of the CNTs of the ECM layer. The Nyquist plot's distinctive high frequency (> 10^4 Hz) features (semi-circular regions) are directly related to the dominant circuit element within the electrochemical cell and are indicative of changes to the electrode resistance. At this low fouling concentration, the impedance spectra shifted considerably to the right by over 0.5 Ω·m^2 to higher real impedance, as shown in **Figure 8A**. In addition, the diameter of the semicircle increased substantially and a slight flattening of the semicircle was noticeable. As discussed in other papers, the flattening of the semicircle region has also been described as a depressed semi-circle [28], a semi-ellipse shape [22], or a distortion to the semi-circle region [29]. These changes to the size and shape of the semicircle are indicative of increased resistance across the membrane [22]. The impedance of the fouled membrane increased due to the presence of insulating latex beads within the electrically conductive layer. As more latex fouling occurred, the impedance spectra continued to shift to the right to higher real impedance and the semicircle increased in diameter. This trend was observed for all concentrations of latex fouling from 0.028 mg/m^2 to 1.4 mg/m^2.

The electrical property of the active layer depends on the composition of materials. As insulating latex was accumulated onto the membrane surface, there was a delayed response to the bias of potential at high frequencies (10^4 ~ 10^6 Hz), indicated by an

increase in total impedance in **Figure 8B** and a reduction in conductance in **Figure 9B**. At mid frequencies (10 ~ 10^4 Hz), the impedance spectra in the Nyquist plots are supposed to be a vertically line theoretically. The reasons for the large departure from expected are that ionic species have sufficient time to reach the micropores in the CNT layer, possessing relatively large-area interface for EDL charging. The deposition of the insulating foulant significantly blocks the microporous structure within the CNT layer, where the EDL is formed at lower frequencies, resulting in less significant changes in phase angle (**Figure 8C**), a reduction in capacitance (**Figure 9A**) and a reduction in conductance (**Figure 9B**).

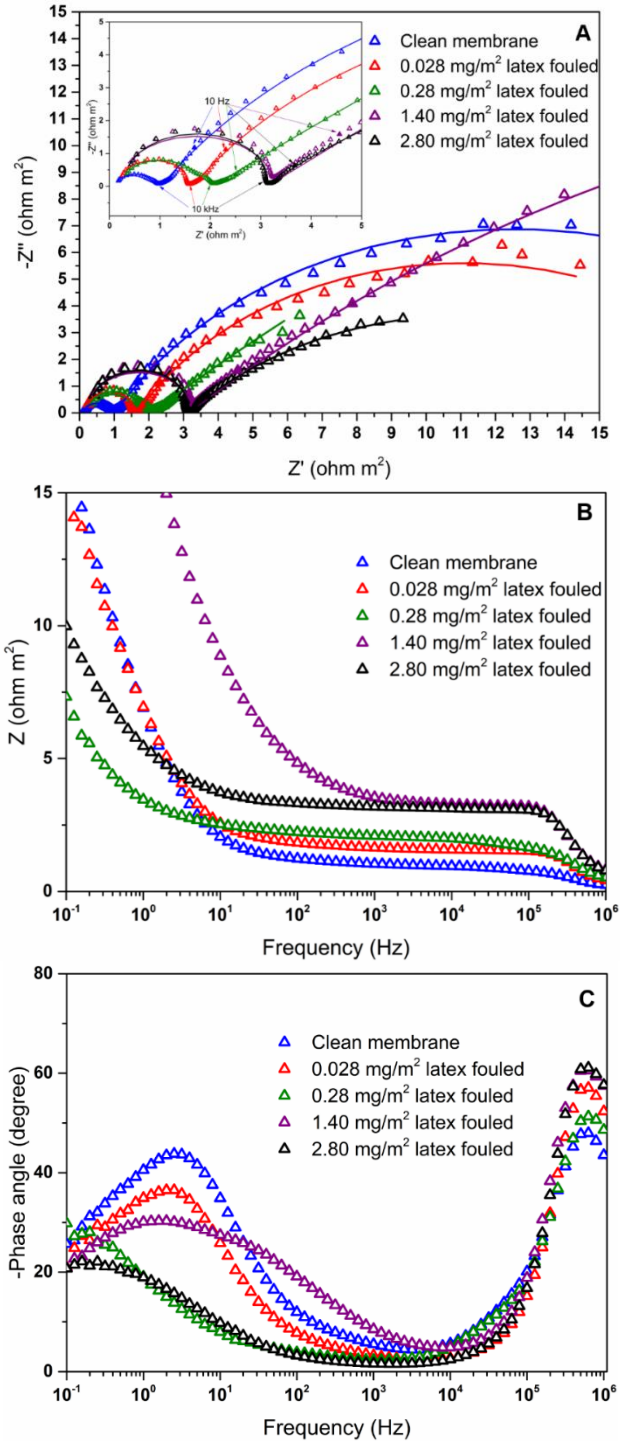

Figure 8. (A) Nyquist plots measured on ECMs fouled with different masses of latex. Nyquist plots were fitted with simulation results. (B) The Bode impedance plot for

different masses of latex fouling. (C) The Bode phase plot for different masses of latex fouling.

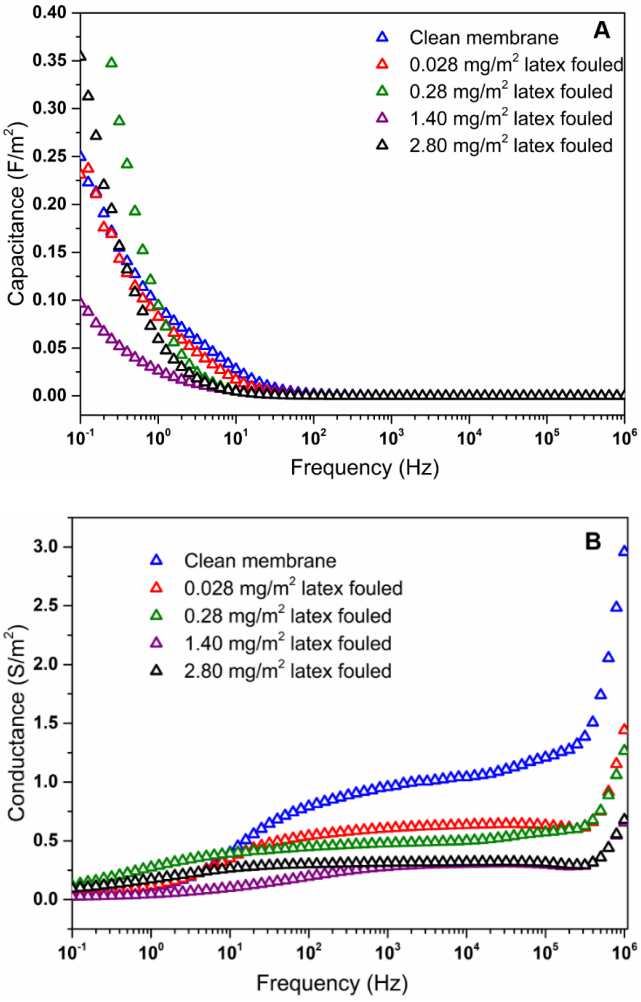

Figure 9. (A) The capacitance-frequency plot for different masses of latex fouling. (B) The conductance-frequency plot for different masses of latex fouling.

The parameter values for the simulations are shown in **Table 1**. The range of N_m (0.8 ~ 1.1) for CPE_m further supports the hypothesis that the membrane electrode interface can be regarded as an imperfect capacitor with non-ideal behavior of capacitance, attributed to surface heterogeneity [27]. Besides, CPE_d with N_d (0.5 ~ 0.6) represented finite

Warburg impedance, indicating ionic species are diffused into the pore channels. The departure from ideality, with slope angle lower than 45°, is due to some of the ions adsorbed onto the carboxylic groups present in CNT micropores [30]. The χ^2 value (< 0.2) showed that the simulation had a good agreement with experimental data.

The combination of solution resistance (R_s) and internal membrane resistance (R_m) can comprehensively represent dielectric property of the medium and the electrical properties of the conductive membrane at the interface. Therefore, it is selected to evaluate the sensitivity of EIS signals as a function of fouling mass (**Figure 10**). The high detection sensitivity of changes in impedance on ECMs is clear from the highly resolvable signals at lower fouling levels. EIS signals are also non-destructive and real-time allowing for *in-situ* fouling sensing. The corresponding SEM images (**Figure 2**) do not show obvious morphological changes in the membrane upper surface as a result of latex deposition. While changes in permeance were measurable between pristine and fouled membranes at fixed pressures (**Figure 5**), the permeance measurements could not resolve the small changes in fouling from 0.028 mg/m^2 ~ 1.40 mg/m^2. Permeance was a good indicator for fouling at higher latex fouling masses. Conversely, we were not able to resolve the difference between high levels of fouling using EIS, as shown in **Figure 8A** and **Figure 10**. At high latex fouling (2.8 mg/m^2) on the membrane surface, the Nyquist plot shifted slightly to the left. The interpretation for this abnormal phenomenon was unclear but may be a result of slight latex detachment for the high latex concentrations when moving the membranes from the flow cell to *ex-situ* EIS measurements, which may also have caused greater bulk resistance through foulant diffusion into bulk solution (electrolyte).

Table 1. Parameters values extracted from the simulated results

Element	Parameter (Unit)	Clean membrane	0.028 mg/m^2 fouled membrane	0.28 mg/m^2 fouled membrane	1.4 mg/m^2 fouled membrane	2.8 mg/m^2 fouled membrane
R_s	R(ohm)	70	202	212	258	316
R_m	R(ohm)	849	1268	1677	2715	2577
CPE_m	Y (mho s^N)	9.73×10^{-9}	1.12×10^{-10}	1.39×10^{-9}	2.45×10^{-10}	5.73×10^{-11}
	N_m	0.84	1.10	0.92	1.00	1.10
R_d	R(ohm)	22276	18648	17000	57430	15538
CPE_d	Y (mho s^N)	4.45×10^{-5}	4.80×10^{-5}	2.20×10^{-4}	2.04×10^{-5}	1.30×10^{-4}
	N_d	0.67	0.66	0.52	0.50	0.53
	χ^2	0.14	0.14	0.15	0.02	0.03

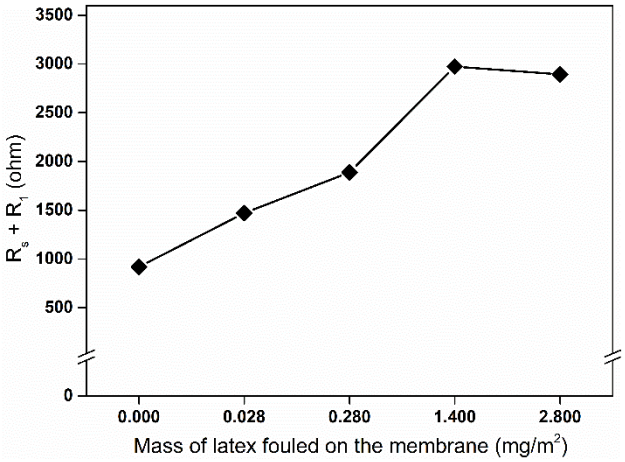

Figure 10. The combination of ohmic solution resistance and membrane resistance with different masses of latex fouling

On the basis of the experimental results above, we hypothesized the mechanism associated with the changes in EIS signal as a function of latex fouling. Latex fouling under small amplitude current (**Figure 11**) occurred randomly on and within the CNT layer. The application of a small potential to the surface caused a small current to flow across the highly electrically conductive CNTs. However, when latex beads accumulated onto/within the CNT layer, the electrical percolation pathway was partially blocked by insulating latex beads, resulting in increasing resistance of the membrane surface. Therefore, the coverage of latex on the membrane could be estimated by measuring the conductive layer resistance.

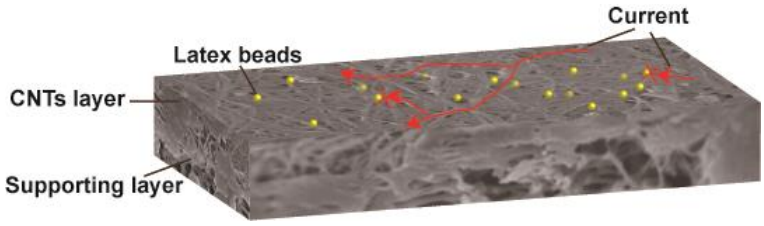

Figure 11. Schematic diagram of the mechanism of increased resistance of the ECM with latex fouling and the impact on EIS measurements.

2.6 Conclusion

This proof-of-concept study demonstrated that low amounts of latex fouling and the difference between fouling degree were sensitively measured through *ex-situ* EIS measurements. As such, EIS could be used to sensitively detect both the onset of fouling and the development of fouling on electrically conductive membranes (ECMs). EIS is

shown to be a particularly sensitive technique as compared to the changes in flux, surface wetting, and conductivity. Latex was used as the model foulant due to its colloidal properties, and different amounts of latex were deposited on ECM surfaces driven at constant pressure. Fouled membranes were analyzed by *ex-situ* EIS as well as *ex-situ* characterization techniques. Nyquist plots significantly shifted to the right with small amounts of fouling. This shift in impedance was correlated to latex surface fouling formation. Furthermore, the Nyquist plot semicircle increased in diameter and irregularity with increasing fouling, representing additional information regarding the onset and progression of fouling layers. The accumulation of latex fouling on and within the ECM skin layer caused increases in the resistance of the membrane and solution. These subtle changes at the onset of surface fouling as well as throughout the progression of fouling were clearly distinguishable in EIS. In contrast, contact angle and permeance measurements were insensitive to the progress of latex fouling.

Electrically conductive membranes (ECMs) can be used as electrodes for an EIS electrochemical system. This system represents a simplification over conventional four-terminal electrode EIS systems in the membrane literature. Using non-conductive membranes, a four-terminal system is used to differentiate between the impedance of the membrane and the impedance of the electrode/liquid interface. In this study, the ECM is used as a working electrode, which enables clearer differentiation between the electrode and the electrode/liquid interface since the impedance of the electrode (i.e. the ECM) is significantly lower than that of the electrode/liquid interface. Although fouled membranes were characterized by *ex-situ* EIS, its impedance data gives an insight into

the mechanism of latex fouling formation, the potential to track fouling development by two-electrode EIS *in situ*, as well as the ability for EIS to distinguish between different types of foulants. This work demonstrates the potential for ECMs to be used in fouling detection in addition to fouling prevention. While most membranes are currently non-conductive, EIS applied to ECMs can be used as canary cells to signal the development of fouling on non-conductive membranes. They could be installed on a side-stream of conventional, non-conductive polymeric membrane modules to detect the development of fouling thereon. Future work aims to develop a miniature EIS sensor, comprising the CNT membrane and EIS technique, to analyze the onset and development of complex, realistic fouling on the real water treatment process. Fouling mitigation strategies would be able to control the irreversible fouling effectively so as to maintain a long-term operation.

2.7 Acknowledgements

The authors thank the support of the Global Water Futures (GWF) research program as well as the China Scholarship Council (CSC). The electron microscopy research described in this paper was performed at the Canadian Centre for Electron Microscopy (CCEM) at McMaster University, which is supported by NSERC and other government agencies. The authors would also like to thank valuable discussions with Prof. Igor Zhitomirsky in the Department of Materials Science and Engineering at McMaster University.

2.8 References

[1] L.N. Sim, T.H. Chong, A.H. Taheri, S.T.V. Sim, L. Lai, W.B. Krantz, A.G. Fane, A review of fouling indices and monitoring techniques for reverse osmosis, Desalination 434 (2018) 169-188. https://doi.org/10.1016/j.desal.2017.12.009.
[2] A.V. Dudchenko, J. Rolf, K. Russell, W. Duan, D. Jassby, Organic fouling inhibition on electrically conducting carbon nanotube–polyvinyl alcohol composite ultrafiltration membranes, J. Membr. Sci 468 (2014) 1-10. https://doi.org/10.1016/j.memsci.2014.05.041.
[3] C.Y. Tang, Y.-N. Kwon, J.O. Leckie, Fouling of reverse osmosis and nanofiltration membranes by humic acid—Effects of solution composition and hydrodynamic conditions, J. Membr. Sci 290(1-2) (2007) 86-94. https://doi.org/10.1016/j.memsci.2006.12.017.
[4] C.Y. Tang, T.H. Chong, A.G. Fane, Colloidal interactions and fouling of NF and RO membranes: a review, Adv Colloid Interface Sci 164(1-2) (2011) 126-43. https://doi.org/10.1016/j.cis.2010.10.007.
[5] A. Ronen, W. Duan, I. Wheeldon, S. Walker, D. Jassby, Microbial Attachment Inhibition through Low-Voltage Electrochemical Reactions on Electrically Conducting Membranes, Environ. Sci. Technol 49(21) (2015) 12741-50. https://doi.org/10.1021/acs.est.5b01281.
[6] S. Shim, S.H. Hong, Y. Tak, J. Yoon, Prevention of Pseudomonas aeruginosa adhesion by electric currents, Biofouling 27(2) (2011) 217-24. https://doi.org/10.1080/08927014.2011.554831.
[7] C.D. Vecitis, M.H. Schnoor, M.S. Rahaman, J.D. Schiffman, M. Elimelech, Electrochemical multiwalled carbon nanotube filter for viral and bacterial removal and inactivation, Environ. Sci. Technol 45(8) (2011) 3672-9. https://doi.org/10.1021/es2000062.
[8] A. Ronen, S.L. Walker, D. Jassby, Electroconductive and electroresponsive membranes for water treatment, Rev. Chem. Eng 32(5) (2016). https://doi.org/10.1515/revce-2015-0060.
[9] F.E. Ahmed, N. Hilal, R. Hashaikeh, Electrically conductive membranes for in situ fouling detection in membrane distillation using impedance spectroscopy, J. Membr. Sci 556 (2018) 66-72. https://doi.org/10.1016/j.memsci.2018.03.069.
[10] A.H. Taheri, L.N. Sim, W.B. Krantz, A.G. Fane, Ultrafiltration with intermittent relaxation using colloidal silica and humic acid as model foulants, Sep. Purif. Technol 212 (2019) 262-272. https://doi.org/10.1016/j.seppur.2018.11.037.
[11] R. de Lara, J. Benavente, Use of hydrodynamic and electrical measurements to determine protein fouling mechanisms for microfiltration membranes with different structures and materials, Separation and Purification Technology 66(3) (2009) 517-524. https://doi.org/10.1016/j.seppur.2009.02.003.
[12] L.N. Sim, Z.J. Wang, J. Gu, H.G.L. Coster, A.G. Fane, Detection of reverse osmosis membrane fouling with silica, bovine serum albumin and their mixture using *in-situ* electrical impedance spectroscopy, J. Membr. Sci 443 (2013) 45-53. https://doi.org/10.1016/j.memsci.2013.04.047.
[13] R. Chan, V. Chen, Characterization of protein fouling on membranes: opportunities and challenges, J. Membr. Sci 242(1-2) (2004) 169-188. https://doi.org/10.1016/j.memsci.2004.01.029.
[14] X.-S. Yuan, Z.-Y. Guo, H.-Z. Geng, D.S. Rhen, L. Wang, X.-T. Yuan, J. Li, Enhanced performance of conductive polysulfone/MWCNT/PANI ultrafiltration membrane in an online fouling monitoring application, J. Membr. Sci 575 (2019) 160-169. https://doi.org/10.1016/j.memsci.2019.01.010.
[15] T. Nguyen, F.A. Roddick, L. Fan, Biofouling of water treatment membranes: a review of the underlying causes, monitoring techniques and control measures, Membranes (Basel) 2(4) (2012) 804-40. https://doi.org/10.3390/membranes2040804.

[16] M.T. Khan, M. Busch, V.G. Molina, A.H. Emwas, C. Aubry, J.P. Croue, How different is the composition of the fouling layer of wastewater reuse and seawater desalination RO membranes?, Water Res 59 (2014) 271-82. https://doi.org/10.1016/j.watres.2014.04.020.
[17] J.S. Ho, J.H. Low, L.N. Sim, R.D. Webster, S.A. Rice, A.G. Fane, H.G.L. Coster, *In-situ* monitoring of biofouling on reverse osmosis membranes: Detection and mechanistic study using electrical impedance spectroscopy, J. Membr. Sci 518 (2016) 229-242. https://doi.org/10.1016/j.memsci.2016.06.043.
[18] J.S. Ho, L.N. Sim, R.D. Webster, B. Viswanath, H.G.L. Coster, A.G. Fane, Monitoring fouling behavior of reverse osmosis membranes using electrical impedance spectroscopy: A field trial study, Desalination 407 (2017) 75-84. https://doi.org/10.1016/j.desal.2016.12.012.
[19] J.S. Ho, L.N. Sim, J. Gu, R.D. Webster, A.G. Fane, H.G.L. Coster, A threshold flux phenomenon for colloidal fouling in reverse osmosis characterized by transmembrane pressure and electrical impedance spectroscopy, J. Membr. Sci 500 (2016) 55-65. https://doi.org/10.1016/j.memsci.2015.11.006.
[20] J.M. Kavanagh, S. Hussain, T.C. Chilcott, H.G.L. Coster, Fouling of reverse osmosis membranes using electrical impedance spectroscopy: Measurements and simulations, Desalination 236(1-3) (2009) 187-193. https://doi.org/10.1016/j.desal.2007.10.066.
[21] Y. Gao, W. Li, W.C.L. Lay, H.G.L. Coster, A.G. Fane, C.Y. Tang, Characterization of forward osmosis membranes by electrochemical impedance spectroscopy, Desalination 312 (2013) 45-51. https://doi.org/10.1016/j.desal.2012.03.006.
[22] F. Gao, J. Wang, H. Zhang, H. Jia, Z. Cui, G. Yang, Role of ionic strength on protein fouling during ultrafiltration by synchronized UV–vis spectroscopy and electrochemical impedance spectroscopy, J. Membr. Sci 563 (2018) 592-601. https://doi.org/10.1016/j.memsci.2018.06.030.
[23] M.A. Halali, C.-F. de Lannoy, The Effect of Cross-Linkers on the Permeability of Electrically Conductive Membranes, Ind. Eng. Chem. Res 58(9) (2019) 3832-3844. https://doi.org/10.1021/acs.iecr.8b05691.
[24] Y. Lee, M.M. Clark, Modeling of flux decline during crossflow ultrafiltration of colloidal suspensions, J. Membr. Sci 149(2) (1998) 181-202. https://doi.org/10.1016/s0376-7388(98)00177-x.
[25] H.M. Ma, L.F. Hakim, C.N. Bowman, R.H. Davis, Factors affecting membrane fouling reduction by surface modification and backpulsing, J. Membr. Sci 189(2) (2001) 255-270. https://doi.org/10.1016/s0376-7388(01)00422-7.
[26] C.F. de Lannoy, D. Jassby, K. Gloe, A.D. Gordon, M.R. Wiesner, Aquatic biofouling prevention by electrically charged nanocomposite polymer thin film membranes, Environ. Sci. Technol 47(6) (2013) 2760-8. https://doi.org/10.1021/es3045168.
[27] L.K. Pan, X.Z. Wang, Y. Gao, Y.P. Zhang, Y.W. Chen, Z. Sun, Electrosorption of anions with carbon nanotube and nanofibre composite film electrodes, Desalination 244(1-3) (2009) 139-143. https://doi.org/10.1016/j.desal.2008.05.019.
[28] C. Fernandez-Sanchez, C.J. McNeil, K. Rawson, Electrochemical impedance spectroscopy studies of polymer degradation: application to biosensor development, Trac-Trends Anal. Chem. 24(1) (2005) 37-48. https://doi.org/10.1016/j.trac.2004.08.010.
[29] A.A. Kulikovsky, A physical model for catalyst layer impedance, J. Electroanal. Chem. 669 (2012) 28-34. https://doi.org/10.1016/j.jelechem.2012.01.018.
[30] J.E. Dykstra, K.J. Keesman, P.M. Biesheuvel, A. van der Wal, Theory of pH changes in water desalination by capacitive deionization, Water Res 119 (2017) 178-186. https://doi.org/10.1016/j.watres.2017.04.039.

Chapter 3

Integrating biofouling sensing with fouling mitigation in a two-electrode electrically conductive membrane filtration system

Reprinted from *N. Zhang, H. Lee, Y. Wu, M..A. Ganzoury, C.-F. de Lannoy, Integrating biofouling sensing with fouling mitigation in a two-electrode electrically conductive membrane filtration system, Separation & Purification Technology, 2022.*

3.1. Abstract

Biofouling detection enables the adoption of effective cleaning strategies for biofouling prevention. This work investigates the use of electrical impedance spectroscopy (EIS) to monitor the biofilm development and the use of electric fields to mitigate biofouling on the surface of gold-coated membranes. The multi-bacterial suspension was injected into a two-electrode crossflow filtration system where the permeate flux and impedance spectra were recorded to monitor the biofilm growth. Permeate flux declined over time while the impedance at low frequency regions (< 10 Hz) rapidly decreased with fouling at the early stages of fouling, and then gradually decreased as biofilm matured. The normalized diffusion-related impedance (R_d), an EIS-derived parameter, was extracted to determine the sensitivity of EIS detection. We observed that impedance-based detection was more sensitive to changes as compared to the decline of permeate flux during the early stage of biofouling. With early detection of fouling, fouling mitigation strategies could be applied more effectively. Further, under the same conditions as fouling detection, either applying an intermittent cathodic potential (-1.5 V) or cross-flow flushing delayed the biofilm growth on the electrically conductive membranes (ECMs). EIS sensitivity was repeatably recovered across four cycles of mechanical fouling removal. Hence ECMs were demonstrated to play a dual function: EIS-enabled detection of biofouling evolution and surface biofouling mitigation.

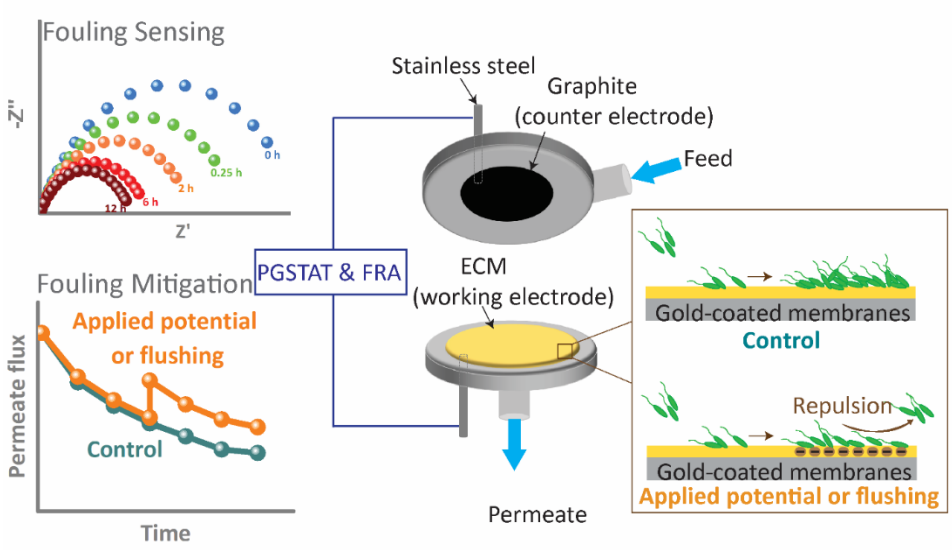

3.2 Introduction

Membranes used in applications, such as wastewater treatment and drinking water purification [15, 31], desalination [32, 33], and bio-products separation [34, 35], are vulnerable to surface and internal biofouling due to microorganisms existing in the feed streams. In general, biofouling is a complicated process that depends on many parameters including the type of bacterial species in the feed, bacterial population density, membrane surface chemistry, membrane surface morphology, local hydrodynamic forces and applied pressure [15, 34]. Biofoulants are regarded as the stickiest foulants in membrane filtration processes and popular strategies to minimize biofouling potential on membrane surfaces include feed water pre-treatment, periodic flow changes such as backwashing, and post-treatment or clean-in-place (CIP) procedures of membrane modules [36-39]. For instance, the pre-treatment of feed streams by introducing cleaning agents (e.g. chlorine and its derivatives) disinfects residual microorganisms and thus prevents bacterial proliferation on the membrane surface [40-43]. Additionally, electrically driven

membrane cleaning has attracted increasing interest as a method to recover the membrane permeability when biofouling is established [26, 44-48].

To determine the optimal dosage of cleaning agents or the frequency of cleaning protocols, real-time monitoring of biofouling evolution would be required. Currently, global parameters, such as transmembrane pressure (TMP) and permeate flux, are monitored in real-time as surrogate indicators for the extent of biofouling [6, 49]. Cleaning protocols are triggered to combat membrane fouling once a pre-set threshold of a surrogate indicator is reached. However, changes in TMP and permeate flux are lagging indicators for fouling formation and they are inaccurate methods of identifying the onset of surface fouling. The pressure drop along a membrane module, and from one module in series to another, limits the accuracy of pressure as a measurement for the onset and development of biofilms across the entire membrane [50]. Inaccuracies in fouling detection may allow a well-established biofilm to form, which may resist cleaning procedures and accelerate membrane decay [50-52].

Electrical impedance spectroscopy (EIS) is a non-invasive and real-time monitoring tool that has been studied to monitor biofouling on membrane surfaces using four-terminal electrode systems. Sim *et al.* [17] monitored *P. aeruginosa* growth on non-conductive RO membranes using the normalized conductance in the diffusion polarization regime. This indicator increased initially due to accumulation of bacteria, respiration products, and salts at the concentration polarization layer. However, as biofouling evolved conductance decreased owing to the production of poorly conductive extracellular polymeric substances (EPS) and the compaction of the biofilm. Four-terminal electrode

EIS systems as monitoring techniques are widely researched at the lab-scale, yet industrial-scale such membrane sensing systems will require further simplification to a two-electrode electrochemical biofouling sensing system. Coupling biofouling sensing with mitigation would make this approach even more appealing.

Here we reported the dual capability of ECMs as EIS platforms to characterize biofilm growth and as antifouling surfaces enabled by applying cathodic potentials in a simple two-electrode membrane system. To this end, highly conductive ultra-thin gold coated UF membranes were fabricated by sputter deposition [53, 54]. The optimal thickness of the gold layer on the PES membrane was determined by the tradeoff between conductivity and water flux. The gold-coated membrane was challenged with a diluted multi-bacterial suspension, during which the permeate flux and impedance signals were compared throughout biofouling as methods to evaluate the capability and sensitivity for biofouling detection. To better understand the biofouling behavior, impedance data were elucidated by fitting an equivalent circuit. Further, combined biofouling sensing by EIS and biofouling mitigation by electric or mechanical forces was explored and the efficacy of this bifunctional platform was evaluated.

3.3 Materials and methods

3.3.1 Fabrication of gold-coated membranes

Polyethersulfone (PES) UF flat sheet membranes (pore size: 0.03 μm, diameter: 47 mm, thickness: 100-150 μm) were directly deposited with a thin film of gold using a sputter coater (Edwards, S150B). This coating procedure was carried out under a sputter current of 30 mA, a sputter voltage of 1.2 kV, a working pressure of 0.3 mbar, and a working

distance of 30 mm in an argon atmosphere. The sputtering duration required to produce a 15 nm gold layer was approximately 1 min and operating time increased linearly with an increase in gold layer thickness. Different thicknesses of the gold layer (30 nm, 45 nm and 60 nm) were deposited on the PES membranes to determine the optimal conductivity and water flux. As-prepared membranes were stored in DI water for subsequent characterization and fouling experiments.

3.3.2 Characterization of gold-coated membranes

3.3.2.1 Electrical conductivity

The conductivity of gold-coated membranes was measured by a four-point probe (Ossila). The working principle was described in the Supporting Information. At least 10 different locations were measured to determine the electrical conductivity for each membrane and the average conductivity was reported.

3.3.2.2 Morphology

The morphology of pristine and biofouled gold-coated membranes was visualized by scanning electron microscopy (SEM, JEOL JSM-7000F) with an acceleration voltage of 10 kV. Pristine gold-coated membranes were imaged without additional coating. The biofouled membranes were gently washed by PBS buffer to remove loosely attached biofilm, and the remaining biofilm was fixed to the membrane surface with 3% (v/v) glutaraldehyde followed by dehydration in an ethanol gradient [26]. After drying overnight at room temperature, fouled membranes were prepared for SEM analysis by coating a 10 nm gold layer through sputter deposition before imaging. The homogeneity and thickness of the gold film on supporting membranes was confirmed by transmission

electron microscopy (TEM, Talos L120C). Surface roughness of these membranes was quantified using AFM (Asylum). Details are described in the Supporting Information.

3.3.2.3 Pure water flux

Pure water flux of as-prepared membranes was measured under different pressures in a dead-end filtration cell (Sterlitech) with an effective surface area of 10.75 cm^2. A detailed protocol was present in the Supporting information. Each measurement was carried out in triplicate and the average was recorded. The pure water permeance, also known as permeability in the membrane literature, was calculated using **eq 1**:

$$\text{Permeate} = \frac{\Delta V}{AP\Delta t} \quad (1)$$

where ΔV is volume of permeate at time intervals Δt; P is transmembrane pressure and A is effective surface area of the membrane.

3.3.2.4 Wettability

Contact angle measurements were conducted for investigating the wettability of as-prepared gold-coated membranes using an optical contact angle device (OCA 35). A 4 µL droplet of water was placed on the dry membrane, which quickly spread across the membrane surface within 15 s. The initial contact angles were recorded using the sessile drop method in the Drop Shape Analysis software [55]. At least 3 measurements were carried out and the mean value was recorded.

3.3.2.5 Electrochemical stability

Cyclic voltammetry (CV) is an emerging electroanalytical technique in separations technology to investigate the redox behaviors and capacitive ability of electrodes and

electrically conductive membranes [56]. In CV, a potential is applied linearly until a final potential is reached, and then reversed to its initial potential. CV curves can be achieved in terms of current as a function of applied potential, from which the charge storage capacity of the tested electrode is calculated by integrating the area of a closed curve. After multiple cycles, changes in an electrode's conductive and capacitive abilities can be observed which are indicators of an electrode's electrochemical stability.

Electrochemical stability of gold-coated membranes was tested by a potentiostat (Autolab PGSTAT 302 N) in a three-electrode setup [57], with a gold-coated membrane acting as a working electrode (WE), Ag/AgCl as a reference electrode (RE) and graphite as a counter electrode (CE) in phosphate-buffered saline (PBS, pH = 7.4) solution. Multiple CV scans were performed at 100 mV/s for 50 cycles with an initial potential of 0 V (vs. Ag/AgCl) and a final potential of -1.5 V (vs. Ag/AgCl), to evaluate the electrochemical stability of the tested membranes.

3.3.2.6 Characterization of biofouled membranes

To investigate the compositions of biofilms, the biofouled membranes were visualized by confocal laser scanning microscopy (CLSM, Leica TCS SP5) under the ×63 objective. The gold-coated membrane was removed from the membrane module after 12 h biofouling. Afterwards, it was gently washed with PBS buffer and the residual biofilm on the gold-coated membranes was stained with the Live/Dead backlight kit (3 µL propidium iodide and 3 µL Syto 9) for 1 h in the dark. The stained cells were observed by CLSM. Images were collected from at least 3 locations. Fourier transform infrared spectroscopy (FTIR) was performed for the pristine and biofouled gold-coated

membranes by a FT-IR spectrometer (Nicolet 6700). Raman spectra were measured using a Laser Raman spectrophotometer (Renishaw InVia) at an excitation wavelength of 785 nm.

3.3.3 Biofouling sensing protocol

Multi-bacterial cell cultures were grown in water by adding 1% yeast extract to tap water and culturing this solution at 37 °C for 24 h. The cells were harvested by centrifugation and then washed three times with PBS buffer (pH = 7.4). The purified cells were resuspended in the PBS solution and diluted to 10^5 colony-forming units (CFU)/mL. The population of bacterial suspension was determined by measuring the optical density at 600 nm (OD_{600}) and counting the number of bacterial colonies on agar plates.

The multi-bacterial suspension (10^5 CFU/mL, OD_{600} = 0.10 ± 0.02, 400 mL) was pumped into the filtration system at room temperature. A constant TMP of 30 psi (2.068 bar) was controlled by the pressure transducer (Omega, PX319-100GV) with a cross-flow velocity of 0.68 cm/s. The collected retentate and permeate were returned to the reservoir, and flow rates were controlled by a control valve and measured by flow meters (Sensirion, SLS-1500 for the permeate stream; Omega, FTB-420 for the retentate stream). The ability of EIS to monitor biofouling development on gold-coated membranes was evaluated in a customized flow cell (**Figure 1**; a picture of membrane filtration system shown in **Figure S2**) with an effective surface area of 3.14 cm^2. The bacterial preparation protocol, detailed description of the system and EIS methodology are present in the Supporting Information. Membrane biofouling was carried out for 12 h during which EIS

spectra were recorded in response to applying 10 mV of an alternating potential over frequencies of 10^{-1} – 10^{6} Hz. All experiments were conducted in triplicate.

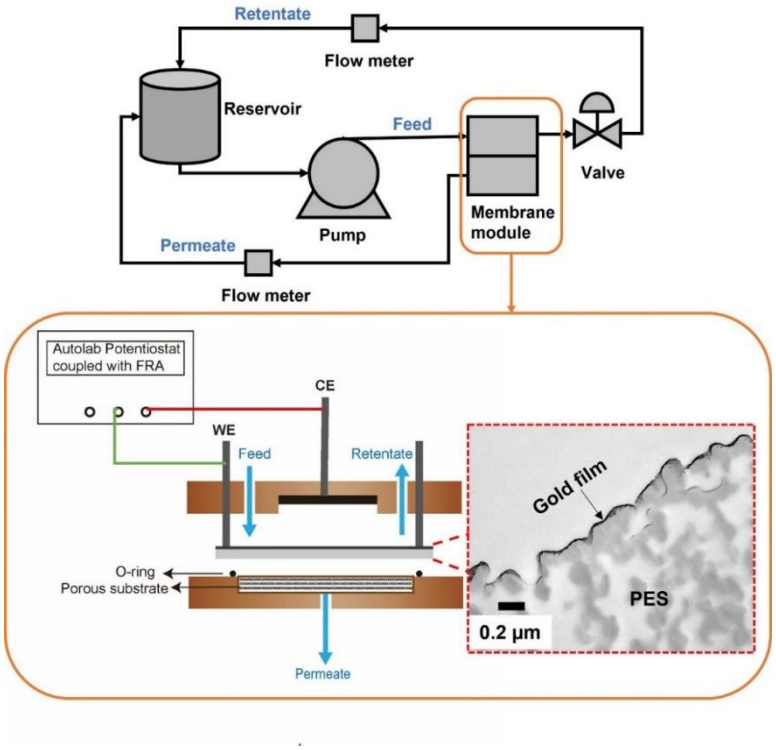

Figure 1. Schematic of a cross-flow membrane system loaded with the 30 nm thick gold coated membrane. A gold-coated membrane and the graphite were used as the working electrode and counter electrode, respectively. Inserted TEM image confirmed the continuous gold film on the PES membrane surface, providing current electrical percolation.

3.3.4 Coupling biofouling sensing and mitigation

In order to evaluate the antifouling performance of gold-coated membranes by applying external potentials, three independent biofouling experiments were conducted for comparing their filtration behaviors with and without electric fields. The operating conditions of the cross-flow filtration cell and the nature of the bacterial suspensions

were the same as what was used in the filtration-EIS setup. To mitigate biofilm formation, a constant cell potential of -1.5 V was applied to the gold-coated membrane over 12 h of biofouling development. As a reference, the identical experiment was performed on PES membranes and gold-coated membranes without the use of electric fields. Membrane permeate flux was measured at a constant TMP of 30 psi (2.068 bar) throughout the filtration process. All the measurements were conducted in duplicate.

To integrate biofouling sensing with mitigation in a two-electrode membrane filtration system, two different cleaning strategies were employed. A) Cross-flow flushing: Biofilms were grown on the gold-coated membrane under 30 psi (2.068 bar) over 12 h, with a cross-flow velocity of 0.68 cm/s. Subsequently the cross-flow flushing under the identical pressure was used for 0.5 h to remove the biofilms. Such processes were repeated for three times in order to evaluate the cleaning efficiency of the cross-flow flushing. B) Intermittent potential: To compare the cleaning efficiency between two different cleaning strategies, the biofouling was developed under the same operating conditions as mentioned above. After biofouling growth for 4 h, a cell potential of -1.5 V was applied on the biofouled membrane and meanwhile the cross-flow velocity was increased to 0.74 cm/s under an applied pressure of 40 psi (2.758 bar) for 5 min, in order to encourage foulant removal. Afterward, these processes were repeated for three times. EIS-based detection and the flux decline were both recorded throughout the processes to monitor biofouling development.

3.4 Results and discussion

3.4.1 Examination of the Conductivity/ Permeance Trade-off

UF membranes with an effective average pore size of 30 nm were coated with gold to produce electrically conductive membranes (ECMs) that were capable of sensitively responding to electrical signals during impedance-based detection and monitoring of biofouling. UF membranes were fabricated with different thicknesses of gold to identify the impact of gold thickness on electrical conductivity and transmembrane flux. Sufficient gold thickness is required to reach the percolation threshold, and additional gold thicknesses lead to higher electrical conductivity. Pure water permeance is negatively impacted by the addition of gold layers, as these can occlude surface pores and increase the mass transfer resistance of the membrane.

Electrical conductivity and permeance of gold-coated membranes were measured, as shown in **Figure 2**. Surface conductivity of modified membranes increased with layer thickness, due to increased coverage of the supporting surface with the highly-conductive gold film. The mean electrical conductivity value for gold-coated membranes was at least 10-fold higher than that of CNT membranes as reported previously [57]. The maximum conductivity achieved was 1.5×10^6 S/m for 60 nm thick ultra-thin gold membranes. Large deviations in conductivity, however, indicated that the gold layer was non-uniformly deposited onto UF asymmetric membranes through sputter coating. This uneven coating may be due to the underlying porosity of the UF membrane, whereby gold nanoparticles are deposited into the membrane structure rather than onto the membrane surface,

resulting in conductivity variations. Using membranes with smaller pores (<30 nm) in the active layer would resolve the issue at the expense of reduced permeance.

The permeance of pristine PES membranes was 3409.6 ± 200.3 LMH/bar, and permeance dropped by 1.7%, 4.3% and 17.5% for gold membranes with a thickness of 30 nm, 45 nm and 60 nm, respectively. The additional resistance contributed by the gold film was calculated in the Supporting information (**eq S3** and **Table S1**). These results confirm that 30 nm thick gold film has a negligible effect on the permeance.

A clear tradeoff was observed between the electrical conductivity and permeance, as has been reported in ECMs [58]. The gold coated membranes with 30 nm of gold were used for all following experiments as they possessed sufficiently high surface conductivity (~5×10^5 S/m) and high-water flux of 3400 ± 88 LMH/bar, nearly that of the unmodified membranes.

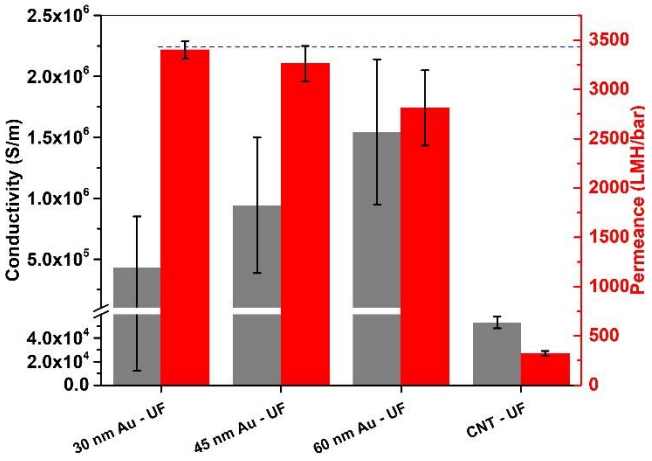

Figure 2. Surface conductivity and permeance of UF membranes with different thicknesses of gold coating. CNT membrane from the reference [57] is used for comparison. The dotted horizontal line is the original permeance value (3409.6 LMH/bar)

of pristine PES membranes. (Error bar represents standard deviation, n = 10 for conductivity and n = 3 for permeance measurements)

3.4.2 Membrane Characterization.

The morphologies, wettability and electrochemical stability of fabricated membranes were based on SEM, AFM, contact angle measurements and cyclic voltammetry, respectively.

3.4.2.1 Surface morphology

The surface morphology and topography of the pristine PES membrane and the gold-coated membranes were observed by SEM and AFM (**Figure 3a-d**). SEM images revealed that the pristine PES exhibited a typical UF membrane structure, and its pore size was reduced as a result of gold deposition. Although the ultra-thin gold film was porous, the electrical conductivity percolation threshold was surpassed, resulting in high surface conductivity as demonstrated above.

The deposited gold layer reduced the surface roughness of the PES membranes, as measured by AFM. From AFM height images, pristine PES membranes had the typical characteristic of peaks and valleys, while gold-coated membranes showed smoother surfaces. AFM images yielded a RMS of 67.4 ± 8.0 nm for the pristine PES membrane and RMS value to 49.7 ± 2.2 nm after gold deposition. Smooth membrane surfaces are less prone to biofouling attachment due to the relatively greater shear rate from fluids across the surface. Rougher surfaces are also more prone to foulant accumulation as particles and microbes preferentially deposit in the valleys of the membrane surface [15,

49]. A recent publication on gold-coated MF membranes demonstrated increased surface roughness with gold layers. The larger pore diameters (50 nm) in that study suggests that pore size has a substantial and non-linear effect on surface roughness [54]. As such, we hypothesize that sputter-deposition may be best-suited for membranes with smaller pore diameters.

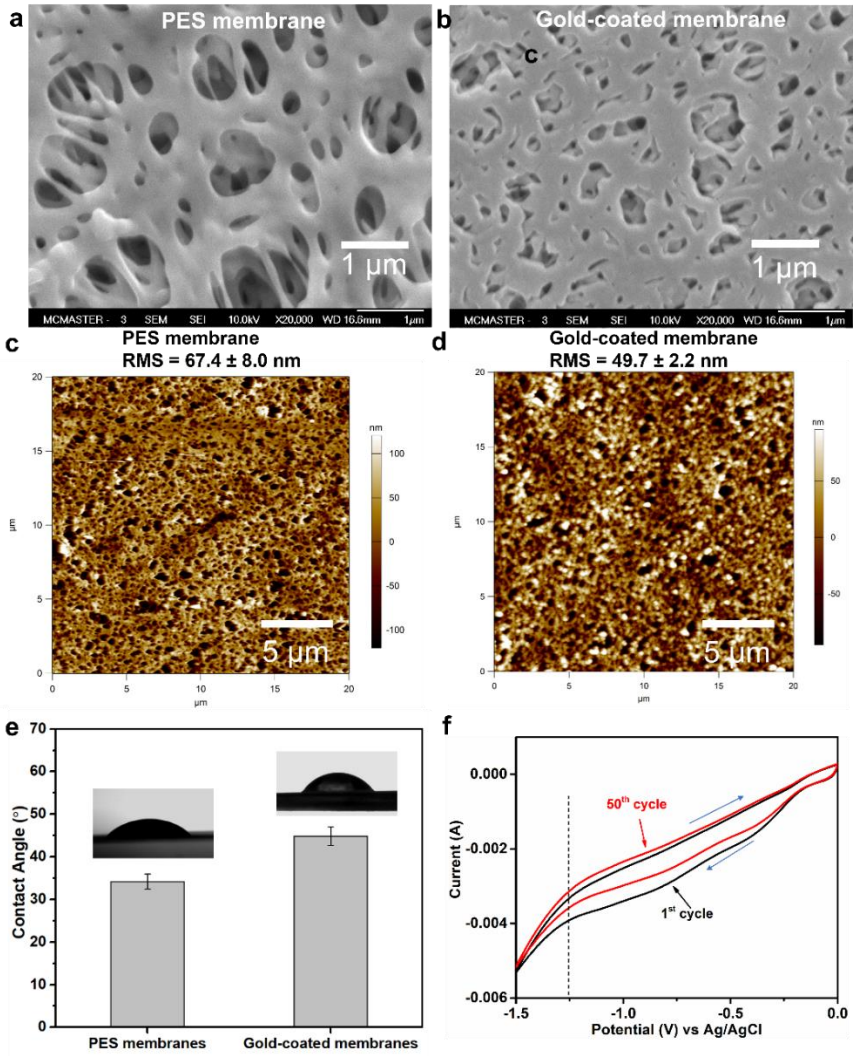

Figure 3. SEM images of (a) the pristine PES membranes and (b) the 30 nm thick gold-coated membrane; AFM images of the (c) pristine PES membrane and (d) the 30 nm thick gold-coated membrane in tapping mode using a scan area of 20 × 20 μm^2. The color

gradient indicates the vertical deviation in the membrane surface, where lighter colours represent elevations and darker colours represent depressions. AFM images were used to calculate the RMS roughness of the membrane, which was defined as the root-mean-square value of distances between the peaks and valleys on the membrane surface. (e) Static contact angle; the initial contact angle of a sessile water drop placed on the PES membrane as control and the 30 nm thick gold coated membrane (Error bar represents the standard deviation, n=3). (f) CV scans for an investigation into electrochemical stability of the 30 nm thick gold-coated membrane. A scan rate of 100 mV/s was used, and potentials were applied between -1.5 V and 0 V (vs. Ag/AgCl). Arrows indicate the direction of CV curves.

3.4.2.2 Wettability

The wetting behavior of both the gold-coated membranes and the pristine PES membranes was characterized by contact angle measurements (**Figure 3e**). The initial contact angle of gold-coated membranes increased to 44.8 ± 2.2º from 34.2 ± 1.8º that of the pristine PES membranes. Despite increased intiail contact angle of the gold-coated membranes due to the deposition of the gold film, their wetability did not change significantly. Membranes modified with gold-coatings remained very hydrophilic, such that the water drops full wetted the membranes within 10 s of initial deposition. Such high water affinity at the interface indicated good electrolyte accessibility to the gold-coated membrane electrode. High wettability implied that low solution resistance was expected for the impedance-based detection.

3.4.2.3 Electrochemical stability

To assess the stability of gold-coated membranes during electro-filtration, multiple CV scans were performed on the pristine gold-coated membrane. The absence of sharp oxidation or reduction peaks (**Figure 3f**) indicated the gold-coated membrane electrode

was a non-faradaic material within the potential window. The generated current was attributed to redistribution of ions at the electrode/electrolyte interface. It was observed that cathodic current continuously increased when the potential was ramped from a starting potential of 0 V to a potential of -1.5 V (vs. Ag/AgCl). Hydrogen evolution took place after a cathodic potential of approximately -1.25 V vs. Ag/AgCl was applied, in accordance with the potential for water electrolysis in a neutral electrolyte [59]. A more negative overpotential would promote bubble generation, which substantially hindered membrane permeability. Thereby the potential of -1.25 V vs. Ag/AgCl (corresponding to a cell potential of -1.5 V) was employed in the two-electrode electrochemical sensing system. After 50 cycles of CV scans, a reduction (< 20 %) in charge storage capacity was observed within the potential window of -1.5 V – 0 V (vs. Ag/AgCl), as well as a slight shift in the CV curve to smaller current at a potential of -1.5 V vs. Ag/AgCl. These indicate that over 50 cycles, gold-coated membranes are electrochemically stable with a slight deterioration in conductance and capacitance.

3.4.3 Biofouling detection

Biofouling experiments were carried out by filtering a feed containing bacterial suspension with a zeta potential of -(3.46 ± 0.66) mV. The weakly negatively charged bacterial cells deposited on the membrane under the applied pressure during membrane filtration and the initial stages of biofilm formation occurred over the course of the experiment [15]. The evolution of biofouling on the membrane throughout the filtration was monitored in two ways: 1) by permeate flux or transmembrane pressure, and 2) simultaneously by impedance-based detection. The impedance approach was used to

track the interfacial properties of the membrane in an attempt to monitor the attachment of bacteria at the early onset of biofilm development. As microorganisms attached to the surface and produced EPS, the physicochemical properties of the membrane-solution interface were altered. We compared these two detection methods to investigate their effectiveness in tracking biofouling throughout the filtration process.

3.4.3.1 Biofouling detection by flux decline

The permeate flux of the modified membrane gradually reduced throughout filtration of the bacteria-contaminated feed, as shown in **Figure 4a**. Bacterial attachment and biofouling occurred once the permeation drag force overcame the electrostatic repulsion of the charged surface. It is well known that the accumulation of bacteria and the production of EPS contributes to further microbial accumulation and biofilm development, which leads to irreversible biofouling and a decline in permeate flux [15, 43].

Biofouling on the gold-coated membrane was visualized by SEM and CLSM, which confirmed successful formation of biofilms. From SEM image in **Figure 4b**, microbial cells and EPS can be clearly observed, which contributed to the deteriorated performance of the gold-coated membrane. The representative CLSM images in **Figure 4c-d** indicated that the microbial cells that adhered to the membrane surface were mostly live cells throughout the filtration.

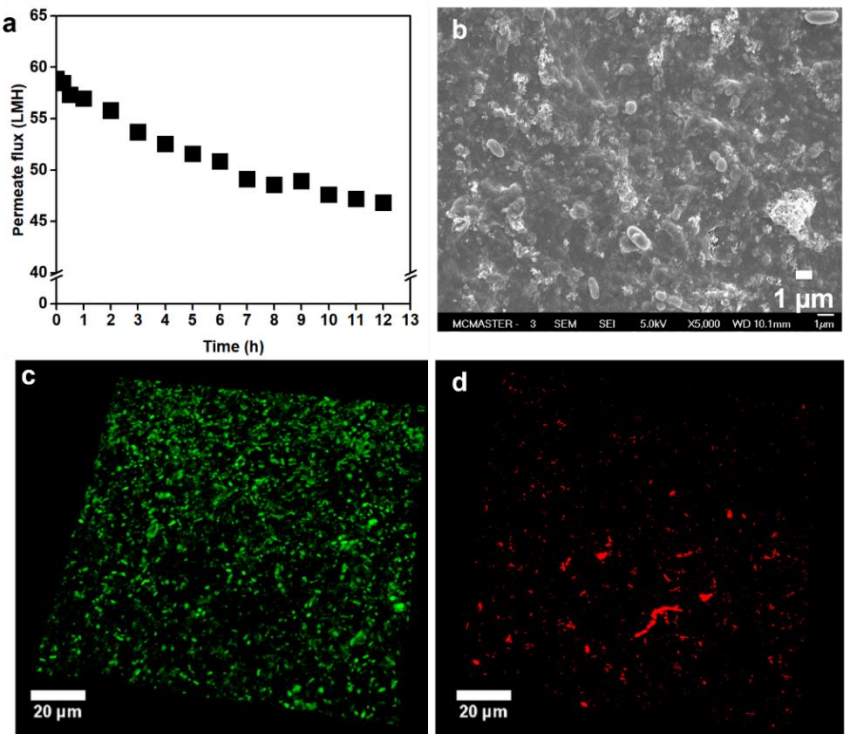

Figure 4. (a) The decline of permeate flux with time. Before membrane biofouling, the gold-coated membrane was compacted at 40 psi (2.758 bar) for 24 h. The time at which the bacterial stock solution was added, was defined as t = 0. (b) Representative SEM image of the biofouled gold-coated membrane after 12 h biofilm growth in a crossflow membrane system; representative bacterial morphologies and the secreted EPS were shown. Representative CLMS images of (c) green-stained cells indicating live cells and (d) red-stained cells indicating dead cells attached on the gold-coated membrane after 12 h growth.

3.4.3.2 Biofouling detection by EIS

Electrical impedance spectroscopy was used to identify the physiochemical properties of the membrane-solution interface where fouling occurs. Among the various impedance spectra collected, the Nyquist plot (**Figure 5a**) provided the relationship between real impedance and imaginary impedance for a wide variety of frequencies while the Bode plot (**Figure 5b**) emphasized changes in impedance and phase-angle as a function of

frequency, respectively. An equivalent circuit was developed to fit the obtained impedance data and to predict the predominant phenomena that were detected at various frequencies.

At low frequencies, charged particles and ions have sufficient time to diffuse towards the solution-electrode interface when a potential bias was applied. Low-frequency elements thus correspond to the diffusion polarization (DP) layer adjacent to the membrane surface, and are capable of revealing the occurrence of biofouling at the membrane surface. As such, the low-frequency regime (0.1 – 10 Hz) is of great interest for fouling detection *in-situ*, as has been reported in monitoring colloidal particles on ECMs in membrane distillation [9].

Using EIS detection on electrically conductive membranes (ECMs) was hypothesized to enable sensitive detection of small changes in membrane surface properties. Impedance data of gold-coated membranes and pristine PES membranes (control) under identical conditions were compared with and without biofouling growth in **Figure S3**, demonstrating the potential for EIS to detect biofouling on ECMs with higher signal sensitivity. Fifteen electrical impedance spectra were collected throughout the progress of biofouling on gold-coated membranes, and their temporal evolution was analyzed. The Nyquist plot in **Figure 5a** showed the distinctive feature of EIS spectra at low frequencies and the Bode-impedance plot in **Figure 5b** showed the decrease in the magnitude of impedance with time over a frequency range of 0.1 – 10 Hz. A sudden decrease in impedance within the first 15 min of biofouling was observed, which was attributed to the introduction of bacteria into the feed stream. During the first stage of

biofouling development (0 – 3 h), the diffusion-dominant impedance decreased rapidly as bacteria attached to the membrane surface and bacterial respiration by-products were produced within the membrane structure. The attachment of microbes on the membrane electrode increased the total surface area of the electrode as well as the total available ions, which may have been associated with the increase in capacitance and the reduction in the total impedance over time.

An equivalent circuit was proposed to fit the measured impedance results to analyze the physical meaning of the impedance measurements (**Figure 5c**). The membrane electrode is modelled by the internal electrode resistor (R_m) parallel with a capacitor (C_1); the diffusion polarization layer behavior is modelled by a parallel diffusion-related resistance (R_d) and a constant phase element (CPE); the bulk solution is represented by the resistance R_s; and the electrical double layer is represented by R_c and C_2 for the counter electrode [9].

The simulation results for the circuit elements are presented in **Table S2**, suggesting a good agreement with the experimental data with a χ^2-test value less than 0.2. To assess the sensitivity of impedance-based signals, we plotted normalized R_d and normalized permeate flux against time in **Figure 5d**. The reduction in R_d was more resolvable than the permeate flux in the initial stage of fouling during which biofouling monitoring would be of great value [12, 57]. After 2 h of filtration, both the permeate flux and diffusion-related impedance demonstrated similar sensitivity changes in fouling development. These results show that impedance-based biofouling detection is more sensitive to changes in solution conditions during the early onset of fouling as compared

with permeate flux-based detection. Hence ECMs used as EIS sensors could be used as canary cells installed on a side-stream of commercial membrane modules for fouling detection in industrial applications. This sensitive detection could help determine the optimal frequency of cleaning protocols.

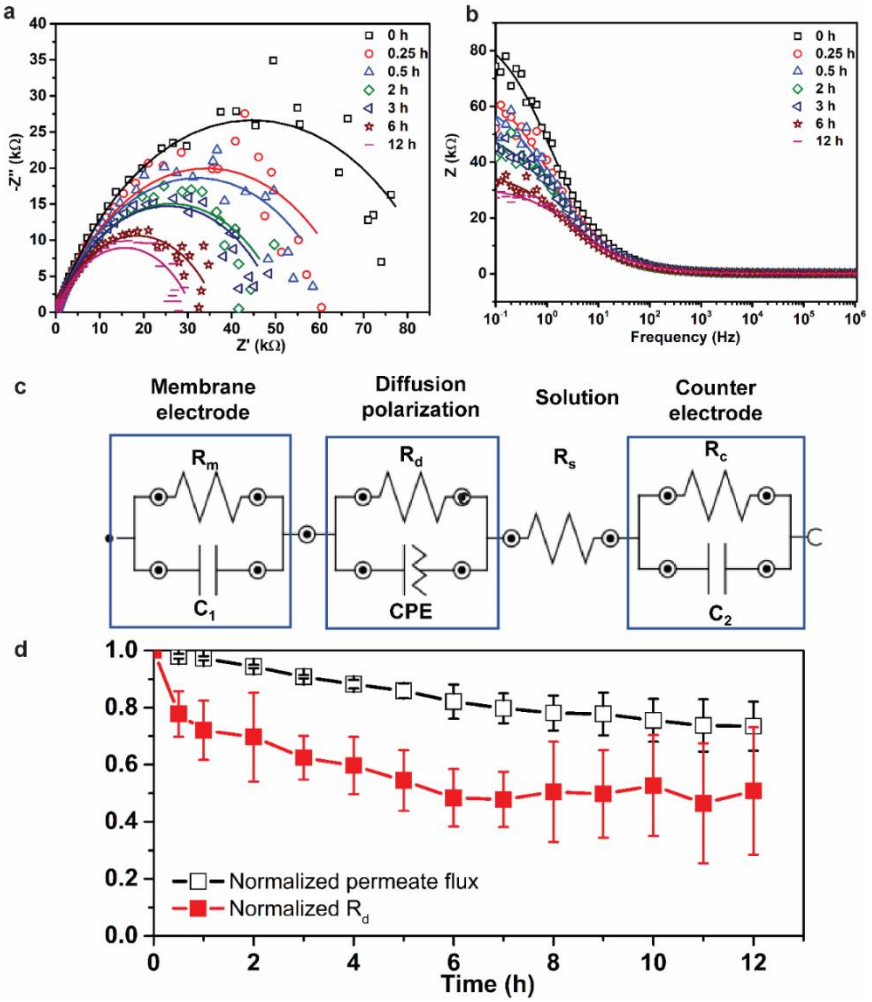

Figure 5. (a) Nyquist plot of the gold-coated membrane and (b) Bode-impedance plot of the gold-coated membrane over 12 h biofouling growth (c) An equivalent circuit fitting impedance. (d) Biofouling detection: Comparison of the normalized diffusion-determined resistance (R_d) and the normalized permeate flux during biofouling; (Error bar represents the standard deviation, n = 2). The lines represent the fitted results obtained from the proposed model.

3.4.4 Coupling EIS biofouling detection with mechanical flushing cleaning

To maintain EIS detection sensitivity over time, mechanical membrane cleaning was used to enhance the removal of biofilms. Gold-coated membranes were filtered with the bacterial suspension for 12 h and subsequently adsorbed foulants were partially removed using cross-flow flushing for 0.5 h. The cleaned membranes were then used to filter a fresh bacterial suspension. This process was repeated for 3 cycles to determine the stability of gold-coated membranes and thus determine the sensitivity of EIS detection over time.

A comparison of the normalized permeate flux and diffusion-related resistance (R_d) demonstrated the stability of the gold-coated membrane as shown in **Figure 6**. By cross-flow flushing with a velocity of 0.68 cm/s, the flux was recovered to 95.6%, 90.3% and 81.5% for Cycle 2, Cycle 3 and Cycle 4, respectively. Over these four cycles, the change in R_d demonstrated high sensitivity for fouling detection. However, the relative change in R_d over a cycle decreased for each subsequent cycle, indicating a decreased sensitivity towards fouling detection over the four cycles. Specifically, in Cycle 1, the reduction rate of R_d was greater than the reduction in the normalized flux, verifying higher sensitivity of EIS biofouling detection than flux decline detection. In Cycle 2, the change in R_d was comparable to the change in flux, while the decline in permeate flux was faster than the change in R_d in both Cycle 3 and Cycle 4. Despite increased R_d after each flushing (indicating a gradual reduction in the sensitivity over time), the decreasing trend of R_d for each cycle was still capable of monitoring biofouling evolution.

This proof-of-concept research verified the capability of *in-situ* biofouling detection by EIS and biofouling removal by flushing on the ultra-thin metal membranes. Further, stability of the gold-coated membranes was satisfactory within 24 h of biofouling development, further confirmed by FTIR spectra (**Figure S4**) and Raman spectra (**Figure S5**) for pristine and fouled membranes ruling out the formation of thiol or thiol derivatives (e.g., gold-sulfur covalent bonds) throughout biofouling development. Cross-flow flushing enabled the effective removal of desorbed foulants, however some remaining biofoulants on the gold-coated membrane contributed to the gradual reduction in sensitivity of EIS detection over time.

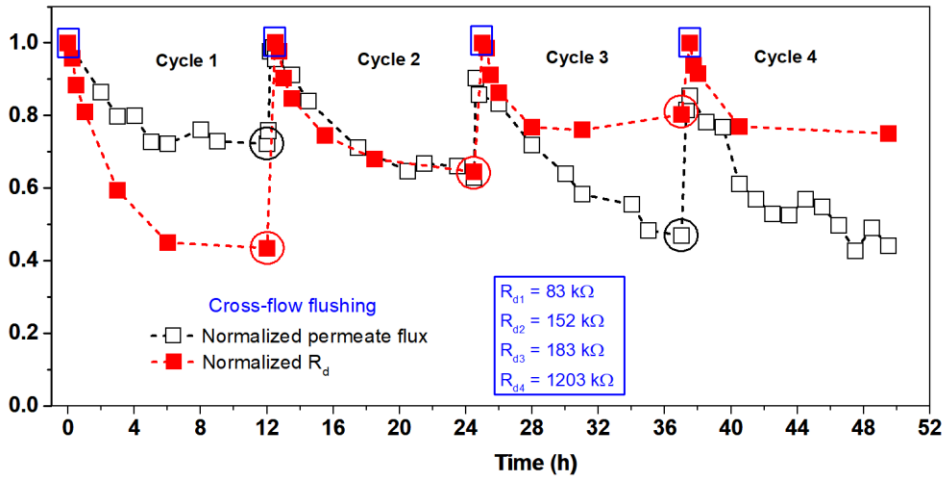

Figure 6. Long term stability of gold-coated membranes during cross-flow flushing of biofouled membranes. Circles represent membrane flushing points. Applied pressure = 30 psi (2.068 bar), cross-flow velocity of 0.68 cm/s, biofouling duration = 12 h and cross-flow flushing duration = 0.5 h for each cycle.

3.4.5 *In-situ* biofouling detection by EIS and self-cleaning by applied potential

ECMs have been extensively researched for their exceptional anti-fouling properties [7, 26, 60-62]. Herein we demonstrate that gold-coated ECMs can be used both as sensitive EIS sensors to detect the onset of biofouling, as well as self-cleaning surfaces to reduce biofouling with the application of an external potential. As demonstrated above, electrochemical stability of gold-coated membranes was confirmed, and water splitting was avoided by operating the membranes under -1.25 V vs. Ag/AgCl (corresponding to a cell potential of -1.5 V). Gold-coated membranes with a cell potential of -1.5 V demonstrated less permeate flux decline as compared to the control gold-coated membranes with no potential applied in **Figure 7a**. Biofouling mitigation was attributed to both the repulsive forces between microbes and the negatively charged membrane electrode, as well as the change in local surface pH [63]. Additionally, both gold-coated membranes with and without applied potential demonstrated less relative permeate flux decline than control uncoated PES membranes. We hypothesize that the smoother surfaces of gold-coated membranes contributed to lower bacterial adhesion and thereby improved antibacterial performance in comparison to PES membranes.

Fouling detection was achieved under an alternating potential of 10 mV throughout membrane filtration, while biofouling mitigation was attempted under an intermittently applied constant potential of -1.5 V. To achieve dual functionality of fouling mitigation and sensing, an intermittent membrane cleaning strategy was employed in **Figure 7b**, where every 4 h a potential of -1.5 V was applied for 5 min with a greater cross-flow velocity of 0.74 cm/s (achieved by a higher TMP) to clear away any desorbed foulants.

EIS-based detection indicated good sensitivity within 4 h whereas negligible change in R_d afterwards indicated reduced sensitivity for continued fouling monitoring. Despite the attempted biofouling removal with intermittent applied potentials, a significant portion of the biofilm likely remained on the membrane surface which reduced the ability to track long-term fouling evolution. This is contrasted with experiments demonstrating EIS signal recovery that were achieved with more effective foulant removal (**Figure 6**). The intermittent applied potential combined with cross-flow flushing is an example of how to combine electrochemical fouling mitigation with sensing; further optimization of intermittent cleaning is required.

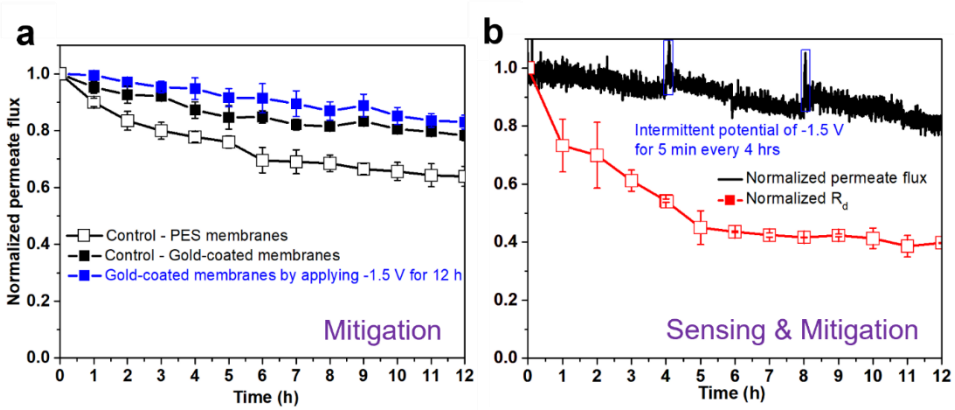

Figure 7. (a) Biofouling mitigation: Comparison of normalized permeate flux over 12 h with and without the applied cathodic potentials.; (b) Dual abilities of ECMs platform for sensing and removing biofouling on gold-coated membranes. Fouled membranes were cleaned by intermittent potential of -1.5 V at 40 psi (2.758 bar) for 5 min every 4 h; vertical rectangles indicated when the membrane cleaning process under electric potentials was applied. (Error bar represents the standard deviation, n = 2)

3.5 Conclusion

In this study, sputter-deposited gold-coated membranes demonstrated 10-fold higher conductivity and 12-fold higher water flux than most reported CNT electrically conductive membranes (ECMs). PES membranes coated with 30 nm gold films were identified as optimal based on the conductivity-flux trade-off identified to exist for ECMs. 30 nm gold films were subsequently used for biofouling experiments. The hydrophilicity and smooth surfaces of these conductive membranes might contribute to the prevention of fouling adhesion, beneficial for maintaining membrane performances in long-term operation. Two real-time fouling monitoring methods were compared to track *in-situ* surface fouling on gold-coated membranes: flux-based and impedance-based detection. Diffusion-related impedance derived from EIS spectra was particularly sensitive to biofouling and thus favorable for monitoring the initial biofouling evolution, while both detection methods had the ability to track long-term fouling development. The sensitivity of EIS analysis to biofouling behavior could be used to determine the optimal frequency of cleaning protocols in industrial applications. This work demonstrates for the first time the idea of combining *in-situ* biofouling detection by EIS coupled to biofouling mitigation using either applied potentials, which could be done without interrupting operation, or using mechanical flushing, which is more effective in recovering EIS signals on ECMs. Further research is warranted to determine how to recover the EIS signal with intermittent applied potentials as well as how to stabilize signal strength during cleaning. This dual platform for biofouling sensing and chemical-free fouling mitigation is promising for practical water treatment.

3.6 Acknowledgements

The authors thank the support of the Global Water Futures (GWF) research program provided through the Canada First Research Excellence Fund (CFREF, Sensors and Sensing Systems for Water Quality Monitoring) as well as the China Scholarship Council (CSC). The electron microscopy research described in this paper was performed at the Canadian Centre for Electron Microscopy (CCEM) at McMaster University, which is supported by the Natural Sciences and Engineering Research Council of Canada (NSERC, Discovery Grant) and other government agencies. We also thank Dr. Turak's lab for the use of their four-point probe.

3.7 References

[1] C. Chiellini, R. Iannelli, L. Modeo, V. Bianchi, G. Petroni, Biofouling of reverse osmosis membranes used in river water purification for drinking purposes: analysis of microbial populations, Biofouling 28(9) (2012) 969-84. https://doi.org/10.1080/08927014.2012.724679.
[2] T. Nguyen, F.A. Roddick, L. Fan, Biofouling of water treatment membranes: a review of the underlying causes, monitoring techniques and control measures, Membranes (Basel) 2(4) (2012) 804-40. https://doi.org/10.3390/membranes2040804.
[3] S. Huang, N. Voutchkov, S.C. Jiang, Investigation of environmental influences on membrane biofouling in a Southern California desalination pilot plant, Desalination 319 (2013) 1-9. https://doi.org/10.1016/j.desal.2013.03.016.
[4] A. Matin, Z. Khan, S.M.J. Zaidi, M.C. Boyce, Biofouling in reverse osmosis membranes for seawater desalination: Phenomena and prevention, Desalination 281 (2011) 1-16. https://doi.org/10.1016/j.desal.2011.06.063.
[5] L. Deng, W. Guo, H.H. Ngo, H. Zhang, J. Wang, J. Li, S. Xia, Y. Wu, Biofouling and control approaches in membrane bioreactors, Bioresour Technol 221 (2016) 656-665. https://doi.org/10.1016/j.biortech.2016.09.105.
[6] A. Ramesh, D.J. Lee, M.L. Wang, J.P. Hsu, R.S. Juang, K.J. Hwang, J.C. Liu, S.J. Tseng, Biofouling in Membrane Bioreactor, Separation Science and Technology 41(7) (2006) 1345-1370. https://doi.org/10.1080/01496390600633782.
[7] S.S. Bucs, N. Farhat, J.C. Kruithof, C. Picioreanu, M.C.M. van Loosdrecht, J.S. Vrouwenvelder, Review on strategies for biofouling mitigation in spiral wound membrane systems, Desalination 434 (2018) 189-197. https://doi.org/10.1016/j.desal.2018.01.023.
[8] J.S. Vrouwenvelder, J.C. Kruithof, M.C. Van Loosdrecht, Integrated approach for biofouling control, Water Sci Technol 62(11) (2010) 2477-90. https://doi.org/10.2166/wst.2010.747.

[9] B.Q. Liao, D.M. Bagley, H.E. Kraemer, G.G. Leppard, S.N. Liss, A review of biofouling and its control in membrane separation bioreactors, Water Environ. Res. 76(5) (2004) 425-436. https://doi.org/10.2175/106143004x151527.
[10] W.A. Hijnen, C. Castillo, A.H. Brouwer-Hanzens, D.J. Harmsen, E.R. Cornelissen, D. van der Kooij, Quantitative assessment of the efficacy of spiral-wound membrane cleaning procedures to remove biofilms, Water Res 46(19) (2012) 6369-81. https://doi.org/10.1016/j.watres.2012.09.013.
[11] H.-J. Lee, M.A. Halali, S. Sarathy, C.-F. de Lannoy, The impact of monochloramines and dichloramines on reverse osmosis membranes in wastewater potable reuse process trains: a pilot-scale study, Environmental Science: Water Research & Technology 6(5) (2020) 1336-1346. https://doi.org/10.1039/d0ew00048e.
[12] A. Lakretz, H. Mamane, E. Asa, T. Harif, M. Herzberg, Biofouling control by UV/H2O2 pretreatment for brackish water reverse osmosis process, Environmental Science: Water Research & Technology 4(9) (2018) 1331-1344. https://doi.org/10.1039/c8ew00183a.
[13] H.-J. Lee, M.A. Halali, T. Baker, S. Sarathy, C.-F. de Lannoy, A comparative study of RO membrane scale inhibitors in wastewater reclamation: Antiscalants versus pH adjustment, Sep. Purif. Technol 240 (2020). https://doi.org/10.1016/j.seppur.2020.116549.
[14] J. Kucera, Biofouling of Polyamide Membranes: Fouling Mechanisms, Current Mitigation and Cleaning Strategies, and Future Prospects, Membranes (Basel) 9(9) (2019). https://doi.org/10.3390/membranes9090111.
[15] L. Cui, P. Chen, B. Zhang, D. Zhang, J. Li, F.L. Martin, K. Zhang, Interrogating chemical variation *via* layer-by-layer SERS during biofouling and cleaning of nanofiltration membranes with further investigations into cleaning efficiency, Water Res 87 (2015) 282-91. https://doi.org/10.1016/j.watres.2015.09.037.
[16] S. West, H. Horn, W.A.M. Hijnen, C. Castillo, M. Wagner, Confocal laser scanning microscopy as a tool to validate the efficiency of membrane cleaning procedures to remove biofilms, Sep. Purif. Technol 122 (2014) 402-411. https://doi.org/10.1016/j.seppur.2013.11.032.
[17] C.F. de Lannoy, D. Jassby, K. Gloe, A.D. Gordon, M.R. Wiesner, Aquatic biofouling prevention by electrically charged nanocomposite polymer thin film membranes, Environ. Sci. Technol 47(6) (2013) 2760-8. https://doi.org/10.1021/es3045168.
[18] B.S. Lalia, F.E. Ahmed, T. Shah, N. Hilal, R. Hashaikeh, Electrically conductive membranes based on carbon nanostructures for self-cleaning of biofouling, Desalination 360 (2015) 8-12. https://doi.org/10.1016/j.desal.2015.01.006.
[19] T.W. Chuo, T.C. Wei, Y. Chang, Y.L. Liu, Electrically driven biofouling release of a poly(tetrafluoroethylene) membrane modified with an electrically induced reversibly cross-linked polymer, ACS Appl Mater Interfaces 5(20) (2013) 9918-25. https://doi.org/10.1021/am4033982.
[20] C. Thamaraiselvan, A. Ronen, S. Lerman, M. Balaish, Y. Ein-Eli, C.G. Dosoretz, Low voltage electric potential as a driving force to hinder biofouling in self-supporting carbon nanotube membranes, Water Res 129 (2018) 143-153. https://doi.org/10.1016/j.watres.2017.11.004.
[21] N. Park, B. Kwon, I.S. Kim, J. Cho, Biofouling potential of various NF membranes with respect to bacteria and their soluble microbial products (SMP): Characterizations, flux decline, and transport parameters, J. Membr. Sci 258(1) (2005) 43-54. https://doi.org/https://doi.org/10.1016/j.memsci.2005.02.025.
[22] S. Shim, S.H. Hong, Y. Tak, J. Yoon, Prevention of Pseudomonas aeruginosa adhesion by electric currents, Biofouling 27(2) (2011) 217-24. https://doi.org/10.1080/08927014.2011.554831.

[23] E.M.V. Hoek, J. Allred, T. Knoell, B.-H. Jeong, Modeling the effects of fouling on full-scale reverse osmosis processes, J. Membr. Sci 314(1-2) (2008) 33-49. https://doi.org/10.1016/j.memsci.2008.01.025.
[24] H. Jia, F. Feng, J. Wang, H.-H. Ngo, W. Guo, H. Zhang, On line monitoring local fouling behavior of membrane filtration process by in situ hydrodynamic and electrical measurements, J. Membr. Sci 589 (2019). https://doi.org/10.1016/j.memsci.2019.117245.
[25] X. Li, Y. Mo, J. Li, W. Guo, H.H. Ngo, *In-situ* monitoring techniques for membrane fouling and local filtration characteristics in hollow fiber membrane processes: A critical review, J. Membr. Sci 528 (2017) 187-200. https://doi.org/10.1016/j.memsci.2017.01.030.
[26] J.S. Ho, J.H. Low, L.N. Sim, R.D. Webster, S.A. Rice, A.G. Fane, H.G.L. Coster, *In-situ* monitoring of biofouling on reverse osmosis membranes: Detection and mechanistic study using electrical impedance spectroscopy, J. Membr. Sci 518 (2016) 229-242. https://doi.org/10.1016/j.memsci.2016.06.043.
[27] T. Mantel, P. Benne, M. Ernst, Electrically conducting duplex-coated gold-PES-UF membrane for capacitive organic fouling mitigation and rejection enhancement, J. Membr. Sci (2020). https://doi.org/10.1016/j.memsci.2020.118831.
[28] M. DuToit, E. Ngaboyamahina, M. Wiesner, Pairing electrochemical impedance spectroscopy with conducting membranes for the in situ characterization of membrane fouling, J. Membr. Sci 618 (2021). https://doi.org/10.1016/j.memsci.2020.118680.
[29] D.Y. Kwok, A.W. Neumann, Contact angle measurement and contact angle interpretation, Advances in colloid and interface science 81(3) (1999) 167-249.
[30] N. Elgrishi, K.J. Rountree, B.D. McCarthy, E.S. Rountree, T.T. Eisenhart, J.L. Dempsey, A Practical Beginner's Guide to Cyclic Voltammetry, Journal of Chemical Education 95(2) (2017) 197-206. https://doi.org/10.1021/acs.jchemed.7b00361.
[31] N. Zhang, M.A. Halali, C.-F. de Lannoy, Detection of fouling on electrically conductive membranes by electrical impedance spectroscopy, Sep. Purif. Technol 242 (2020). https://doi.org/10.1016/j.seppur.2020.116823.
[32] M.J. Larocque, A. Gelb, D.R. Latulippe, C.-F. de Lannoy, Meta-analysis of electrically conductive membranes: A comparative review of their materials, applications, and performance, Sep. Purif. Technol 287 (2022). https://doi.org/10.1016/j.seppur.2022.120482.
[33] W. Li, N. Jiang, B. Hu, X. Liu, F. Song, G. Han, T.J. Jordan, T.B. Hanson, T.L. Liu, Y. Sun, Electrolyzer design for flexible decoupled water splitting and organic upgrading with electron reservoirs, Chem 4(3) (2018) 637-649.
[34] F.E. Ahmed, N. Hilal, R. Hashaikeh, Electrically conductive membranes for in situ fouling detection in membrane distillation using impedance spectroscopy, J. Membr. Sci 556 (2018) 66-72. https://doi.org/10.1016/j.memsci.2018.03.069.
[35] L.N. Sim, Z.J. Wang, J. Gu, H.G.L. Coster, A.G. Fane, Detection of reverse osmosis membrane fouling with silica, bovine serum albumin and their mixture using *in-situ* electrical impedance spectroscopy, J. Membr. Sci 443 (2013) 45-53. https://doi.org/10.1016/j.memsci.2013.04.047.
[36] J. Huang, Z. Wang, J. Zhang, X. Zhang, J. Ma, Z. Wu, A novel composite conductive microfiltration membrane and its anti-fouling performance with an external electric field in membrane bioreactors, Sci Rep 5 (2015) 9268. https://doi.org/10.1038/srep09268.
[37] P. Formoso, E. Pantuso, G. De Filpo, F.P. Nicoletta, Electro-Conductive Membranes for Permeation Enhancement and Fouling Mitigation: A Short Review, Membranes (Basel) 7(3) (2017). https://doi.org/10.3390/membranes7030039.

[38] M.S. Rahaman, C.D. Vecitis, M. Elimelech, Electrochemical carbon-nanotube filter performance toward virus removal and inactivation in the presence of natural organic matter, Environ. Sci. Technol 46(3) (2012) 1556-64. https://doi.org/10.1021/es203607d.
[39] C.D. Vecitis, M.H. Schnoor, M.S. Rahaman, J.D. Schiffman, M. Elimelech, Electrochemical multiwalled carbon nanotube filter for viral and bacterial removal and inactivation, Environ. Sci. Technol 45(8) (2011) 3672-9. https://doi.org/10.1021/es2000062.
[40] M.A. Halali, C.-F. de Lannoy, Quantifying the Impact of Electrically Conductive Membrane-Generated Hydrogen Peroxide and Extreme pH on the Viability of Escherichia coli Biofilms, Ind. Eng. Chem. Res 61(1) (2021) 660-671. https://doi.org/10.1021/acs.iecr.1c02914.

Chapter 4

Ultrafiltration Pd-immobilized catalytic membrane microreactors continuously reduce nitrophenol: A study of catalytic activity and simultaneous separation

4.1 Abstract

Catalytic membrane microreactors (CMMRs) are an exciting new technology that combine catalysis with membranes by seeding the high internal surface area of membranes with catalysts. This enables the continuous purification and production of organic compounds with high catalytic activity, while maintaining nanocatalyst size and stability. This study reports a simple two-step batch reaction approach for synthesizing stable Pd-immobilized catalytic membranes to transform 4-nitrophenol (4-NP) to 4-aminophenol (4-AP) in a flow-through CMMR system. The product (4-AP) is an essential intermediate for the polymer and solvent chemical industry. Pd-immobilized membranes exhibited strong catalytic activity for 4-NP reduction in the presence of $NaBH_4$, with 4-fold higher reduction (79.7%) and 2-fold higher reduction rate (10.1 mol m^{-2} h^{-1}) as compared to control membranes without catalysts. The catalytic mechanisms were elucidated, such that the catalytic reduction processes were conducted *via* a sequential hydrogenation reaction where Pd nanocatalysts facilitated H* transfer from BH_4^- to 4-NP. Ultimately, the 4-AP product was gradually desorbed from the catalytic sites, achieving continuous reduction with high reduction efficiency. Furthermore, by combing ultrafiltration and catalysis, Pd-immobilized membranes showed >99% of 4-NP conversion and >90% of 1 MDa PEO rejection, demonstrating a great potential to be applied in high-efficient wastewater treatment processes.

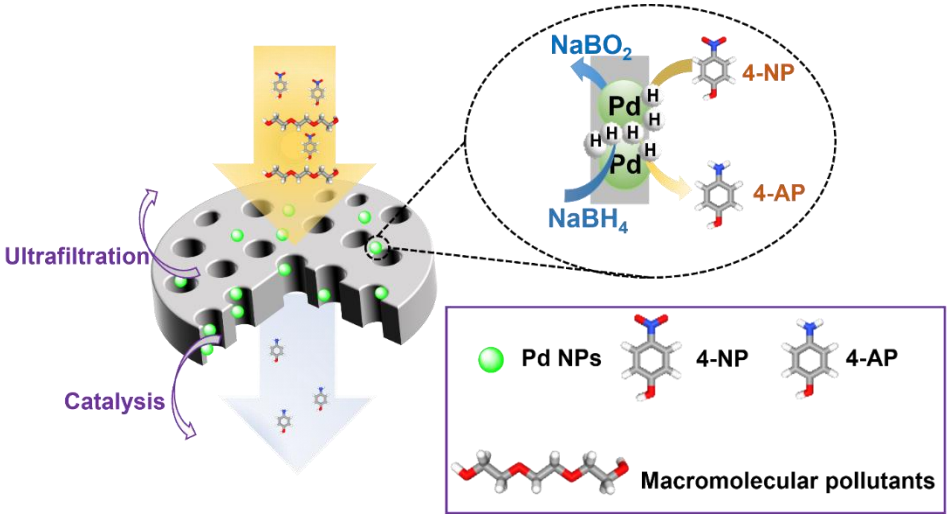

4.2 Introduction

Noble metal, such as Au, Ag, Pd and Pt, in the form of nanoparticles have been extensively used as catalysts as they exhibit high catalytic performance for a variety of reactions including reduction, oxidation and polymerization reactions [1-9]. For example, Ag nanoparticles (NPs) can effectively catalyze the reduction of methyl orange (MO) [4], methylene blue (MB) [9], and 4-nitrophenol (4-NP) [5], the oxidation of alcohols [6] and ethylbenzene [7], and the polymerization of alkylsilanes [8].

The high catalytic activity of metal NPs is dependent on their high surface area, which gradually decreases over time due to nanoparticle aggregation in batch reactors during chemical reactions. Additionally, further NP catalyst aggregation and loss occurs during their separation and regeneration processing, in particular during centrifugation and filtration which are used to separate catalysts from the batch reactor solutions. In addition to loss of catalyst activity, these processing steps add costs to chemical reactions by introducing additional unit operations that require separate expertise, time, and energy.

To address the issues of instability and aggregation, researchers have developed various supports to anchor nanocatalysts, including polymers [2, 10], metal organic frameworks (MOFs) [1, 11], ceramics and silica nanoparticles [6, 7]. For example, Ag NPs and Au NPs were encapsulated within dendrimers to limit NP agglomeration and passivation, while maintaining excellent catalytic performance for 4-NP reduction [2]. Despite their greater stability, these NPs still require separation for regeneration.

Porous polymeric membranes are promising catalyst supports, as they provide stable surfaces onto which catalysts can be anchored and they can be easily regenerated *in-situ* without the need for additional unit operations. By coating the high internal surface area of membranes (~10 – 50 m^2/g) with catalysts, reactants can be flowed through the membrane enhancing mass transfer to catalyst sites and thereby converting batch reactors to high throughput flow reactors [9, 12-14]; an exciting opportunity in catalysis. Such a continuous flow-through system can achieve a highly intensified catalytic process with low energy consumption at mild operating conditions.

Common preparation methods of catalytic membranes include blending, surface coating, and precipitation [15]. The physical blending of catalysts into polymeric structures involves mixing pre-formed catalysts into the casting solution, and then catalytic membranes are prepared *via* phase inversion. This approach leads to catalyst aggregation and delamination, producing sub-optimal catalytic efficiency. Surface coating (e.g., spin coating) incorporates catalyst solutions, suspensions, or colloids onto the membrane by physical forces such as through the centrifugal forces achieved in spin coating. While the catalysts can be stable and can produce uniform coating layers, this process does not coat

the internal porous surface area and thereby has limited catalyst availability, as well as low porosity. Further, this process is difficult to industrially scale rendering it less attractive. In contrast, in the process of immersion precipitation, membrane supports are immersed into solutions containing metal ions, and then catalysts are formed in solution and within the membrane pores where they adsorb to the membrane pore walls. Nonetheless, in each of these processes, low affinity between metal NPs and polymeric substances leads to catalyst physical instability, which needs to be improved to achieve satisfactory long-term catalytic activity. Thus, advanced approaches to anchor catalysts on supports by covalent bonds are warranted.

Polydopamine (PDA) offers strong adhesion on a variety of substances due to the abundance of catechol groups and has been termed a “bio-glue” useful for modification of many surfaces. PDA can be used for metal catalyst NP immobilization through coordination bonds that can form between the catechol groups of PDA and transition metal ions [16-18]. Liu *et al.* reported that incorporating Ag NPs on PDA-modified PVDF membranes inhibited catalyst leaching and thereby enabled long-term catalytic degradation of 4-NP [9]. Additionally, the hydrophilic PDA coating on the membrane surface provided some resistance to the adhesion of organic matter and bacteria, hindering membrane fouling during catalytic degradation [18].

4-aminophenol (4-AP, *p*-AP) is an important chemical intermediate in the manufacturing of pharmaceutical products (i.e., paracetamol, phenacetin and acetanilide), anticorrosive agents, dyes, and lubricants [19, 20]. The production of 4-AP occurs by reducing 4-nitrophenol (4-NP) which can be achieved in the presence of sodium borohydride

($NaBH_4$); this reduction reaction requires the use of catalysts [5]. Thus, the discovery and development of high-efficiency catalysts and catalytic processes are greatly needed.

This study demonstrates a simple two-step batch reaction approach to fabricate a Pd-immobilized catalytic membrane microreactor (CMMR) and its use in continuously catalyzing 4-nitrophenol (4-NP) reduction as it flows through the membrane. The catalytic reactivities of the prepared membranes were evaluated, and the corresponding mechanism behind the 4-NP conversion was elucidated. Further, simultaneous ultrafiltration of large organic molecules (~1 MDa polyethylene oxide (PEO)) and catalysis of small organic molecules (4-NP) was conducted using Pd-immobilized membranes, and the possibility of using such a technique for wastewater treatment was evaluated. The morphology of the prepared membranes was characterized by scanning electron microscopy (SEM) and the distribution of elements on these membranes was mapped by energy dispersive spectroscopy (EDS). The surface area and porosity of the Pd-immobilized membranes were characterized by BET and a gravimetric method, respectively. Molecular weight cutoff of Pd-immobilized membranes was determined by rejecting varying molecular weight of polyethylene oxide (PEO).

4.3 Experimental

4.3.1 Materials

Tris (hydroxymethyl) amonomethane (Tris) HCl, dopamine hydrochloride, sodium hydroxyl (NaOH, 1 M), palladium chloride ($PdCl_2$), sodium borohydride ($NaBH_4$), 4-nitrophenol (4-NP) and polyethylene oxide (PEO, MW: 0.6 MDa, 1.0 MDa, 2.0 MDa) were purchased from Millipore-Sigma-Aldrich (USA). Polyether sulfone membranes

(PES, pore size of 0.03 μm, diameter of 47 mm and thickness of 100-150 μm) were purchased from Sterlitech (USA). All solutions were prepared in distilled (DI) water from an Arium system.

4.3.2 Fabrication of Pd-immobilized membranes

The fabrication process for Pd-immobilized membranes was demonstrated in **Figure 1**. An alkaline dopamine solution (1 mg/mL) was prepared by dissolving dopamine in Tris-HCl solution (pH=8.5). A pristine PES membrane was dipped into 15 mL of aqueous dopamine solution at 60ºC for 24 h to enable the self-polymerization of dopamine. Polydopamine (PDA)-enriched PES membranes were rinsed by DI water to remove excessive dopamine and unattached PDA. Following PDA modification, PDA/PES membranes were immersed in 3 mL of $PdCl_2$ solution (1 g/L) for 30 min, and then soaked in a $NaBH_4$ solution (5.33 g/L, 2 mL) to reduce Pd^{2+} to Pd nanoparticles, henceforth termed Pd nanocatalysts, according to **eq 1**:

$$Pd^{2+} + 2BH_4^- + 6H_2O \rightarrow Pd + 2B(OH)_3 + 7H_2 \quad (1)$$

After reduction, the membrane was rinsed by DI water to wash off reductant, reducing agent, and unstable nanoparticles, and a Pd-immobilized catalytic membrane microreactor (CMMR) was thus produced.

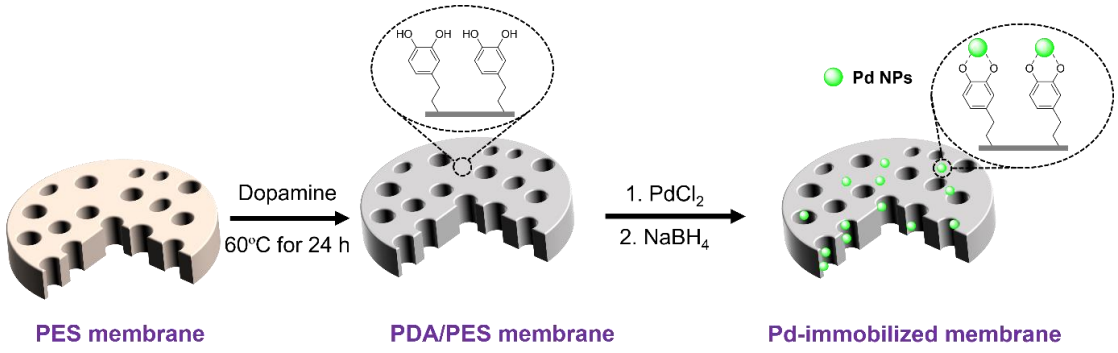

Figure 1. A schematic for the simple two-step batch reaction process used to make a Pd-immobilized catalytic membrane microreactor

4.3.3 Characterization

4.3.3.1 Morphology

The morphology of the top membrane surface and the cross-section for the prepared membranes was characterized by scanning electron microscopy (SEM, JEOL JSM-7000F) with an accelerating voltage of 5 kV. The cross-sectional areas of these membranes were obtained by cracking them in liquid nitrogen. Prior to imaging, PES, PDA/PES and Pd-immobilized membranes were coated with a 10 nm gold layer for surface visualization. Energy dispersive spectroscopy (EDS, X-Maxn) mapping was performed to explore the distribution of Pd nanocatalysts in the Pd-immobilized membrane in which the top surface and the cross-sectional surface were coated with a 10 nm carbon layer. The particle size of Pd nanocatalysts was determined by measuring 20 random particles from SEM images using Image J and the average value was reported.

4.3.3.2 Porosity and surface area

The unsaturated surface area was measured using nitrogen adsorption-desorption isotherms by Brunauer-Emmet-Teller (BET, Autosorb iQ, Quantachrome Instruments). Samples were degassed at 120ºC for 24 h prior to physisorption. Total pore volume (V_{tot}) was estimated based on the density functional theory (DFT) method. The porosity of prepared membranes was determined by a gravimetric method as reported in the literature [21].

4.3.3.3 Selectivity

The selectivity of Pd-immobilized membranes was determined by molecular weight cutoff (MWCO) experiments using polyethylene oxide (PEO) (MW = 0.6 MDa, MW = 1.0 MDa and MW = 2.0 MDa) at 250 ppm in DI water. The Pd-immobilized membrane was compressed by 1 L of DI water under 4.14 bar (60 psi) in a dead-end filtration cell (Sterlitech). Subsequently, the PEO rejection experiments were performed by filtering different molecular weight of PEO solution through control PES membranes and Pd-immobilized membranes at 0.69 bar (10 psi), where size exclusion is the dominant factor for rejection. The PEO concentrations in the feed ($C_{F,PEO}$) and permeate ($C_{P,PEO}$) were measured by a total organic carbon (TOC) analyzer (TOC-L series, Shimadzu). The rejection (R, %) of PEO is defined by **eq 2**. The MWCO of the control and Pd-immobilized membranes was reported based on the molecular weight of PEO that was rejected to at least 90% rejection.

$$R = (1 - \frac{C_{P,PEO}}{C_{F,PEO}}) \times 100\% \quad (2)$$

4.3.4 Catalytic performance of Pd-immobilized membranes

The catalytic degradation of 4-NP was conducted in a dead-end cell (Sterlitech) with an effective surface area of 10.75 cm^2. The degradation occurred in single-pass mode, i.e., the permeate was not recycled back into the feed, thus the feed concentration remained constant throughout the experiments. Different concentrations of 4-NP (0.6 mM or 1.2 mM) were used in the presence of $NaBH_4$ (50 mM) to assess the catalytic effectiveness of the Pd-immobilized membrane. The pristine PES membranes and PDA/PES membranes were employed as controls under identical operating conditions. In the process of catalysis, the dead-end cell was stirred at 200 rpm and the permeate was collected at 10 mL intervals. 200 µL of liquid from each sample was withdrawn to measure the concentration of 4-NP by UV-Vis spectroscopy (Tecan Spark 10 M) at a wavelength of 400 nm.

4.3.5 Combined performance of catalysis and ultrafiltration by Pd-immobilized membranes

A mixed solution of high concentration 4-NP (1.2 mM) and large molecules of PEO (1 MDa, 50 ppm) was used to model a wastewater contaminated with toxic organic contaminants. This experiment was performed to demonstrate that separation and degradation can occur simultaneously, to perform preliminary investigations into the impact of additional organic compounds in solution, and to quantify the impact of surface fouling on catalytic degradation efficiency. The removal efficiency of Pd-immobilized membranes by ultrafiltration was explored by filtering the mixed solution without $NaBH_4$ under 0.69 bar (10 psi). The combined performance of catalysis and ultrafiltration by Pd-

immobilized membranes was conducted by filtering the mixed solution and $NaBH_4$ under the identical operating conditions. During the flow-through process for either ultrafiltration or combined ultrafiltration and catalysis, 4-NP and PEO concentrations in the feed and permeate were determined by UV-Vis spectroscopy and TOC, respectively.

4.3.6 Analytical methods and data analysis

Membrane flux was calculated by **eq 3**. during the catalytic reduction process in the dead-end cell.

$$J = \frac{Q}{A} \tag{3}$$

where J is the flux of the membrane (LMH, L m^{-2} h^{-1}), Q is the volume flow rate (L/h) of the feed solution, A is the effective catalytic area of the membrane (m^2).

Reduction was a critical factor to evaluate the capacity for producing 4-AP, which was defined as:

$$\eta = (1 - \frac{C_P}{C_F}) \times 100\% \tag{4}$$

where C_F and C_P are the 4-NP concentrations (mol/L) of the liquids in the feed and permeate, respectively.

To evaluate the processing capacity of prepared membranes for reducing 4-NP, the reduction rate (mol m^{-2} h^{-1}) was calculated by:

$$\text{Reduction rate} = \frac{\eta}{100} \times C_F \times J \tag{5}$$

4.4. Results and discussion

4.4.1 Characterization of Pd-immobilized membranes

The pristine membrane, PDA/PES membrane and Pd-immobilized membrane were characterized by FTIR as shown in **Figure 2A**. The appearance of the characteristic peak at 1640 cm^{-1} for the PDA/PES membrane and the Pd-immobilized membrane was assigned to C=O stretching due to the oxidation of residual hydroxyl groups in PDA to form quinone structures. This peak was absent for the control PES membrane, as expected, as PES does not contain any C=O bonds. The broad peak at 3420 cm^{-1} was attributed to the O-H stretching in catechol groups in PDA [22]. In addition, these prepared membranes were characterized by Raman spectroscopy in **Figure 2B**. Unlike the pristine PES membrane, the Raman spectrum of the PDA/PES membrane had the characteristic peaks of 1324 cm^{-1} for catechol groups in PDA and 1580 cm^{-1} for the quinone structure owing to the oxidation of PDA [23, 24]. The Raman spectrum for the Pd-immobilized membranes did not show distinctive quinone peaks, although the catechol group may be identified at 1324 cm^{-1}. Pd nanocatalysts immobilization *via* immersion synthesis likely blocked the signal from these characteristic chemical structures. The characteristic peaks associated with Pd nanocatalysts (at 640 cm^{-1}) [25] were not clearly identified in these spectra. Further investigation of Pd nanocatalysts was carried out using SEM and EDS analysis in the following characterizations.

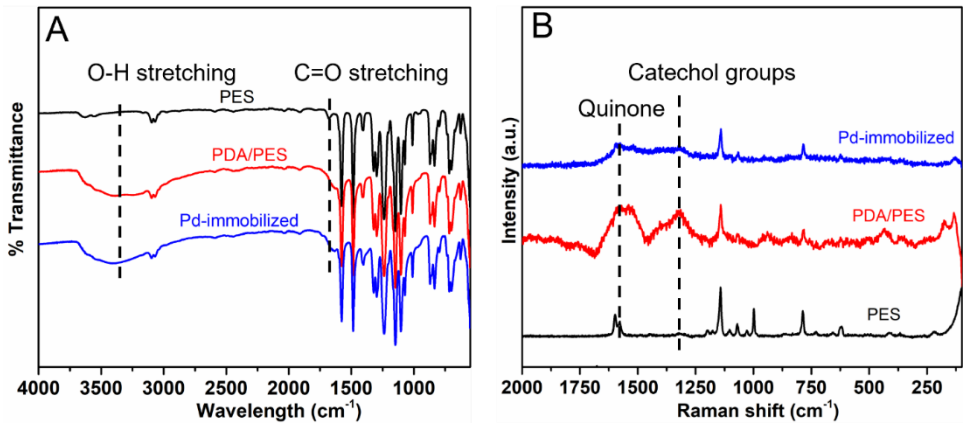

Figure 2. (A) FTIR spectra and (B) Raman spectra for the pristine PES membrane, PDA/PES membrane and Pd-immobilized membrane.

The morphology of the pristine PES membrane, PDA modified PES membrane and Pd-immobilized membranes are shown in **Figure 3**. The pristine PES membrane showed typical porous structures (**Figure 3A**). Coating PES membrane surfaces and internal porous structure with PDA provided an adhesive platform for the immobilization of Pd nanocatalysts. This thin PDA layer had no discernable morphological change on the PDA/PES membranes' active layer surface (**Figure 3B**). When Pd nanocatalysts were immobilized on the PDA-modified PES membrane, the pore sizes decreased and the Pd nanocatalysts were evenly distributed on the membrane surfaces according to EDS elemental mapping shown in **Figure 3C**. The average particle size of Pd nanocatalysts was 52.1 ± 8.6 nm (**Figure 4**). From the top surface of the Pd-immobilized membrane in **Figure 3(C1)**, the presence of C, O and S originated from the supporting PES membranes as well as the inclusion of PDA. The Pd mapping from EDS analysis demonstrated that the anchored Pd nanocatalysts were evenly distributed on the membrane surface.

According to the cross-sectional EDS mapping in **Figure 3(C2)**, the well-dispersed Pd nanocatalysts were also evenly distributed throughout the internal porous structure of the membrane. This demonstrated that by saturating the membrane with the metal precursor, $PdCl_2$, a sufficient amount of Pd diffused to the PDA-adhered inner membrane pores during the immersion process to produce a high density of Pd nanocatalysts within the membrane.

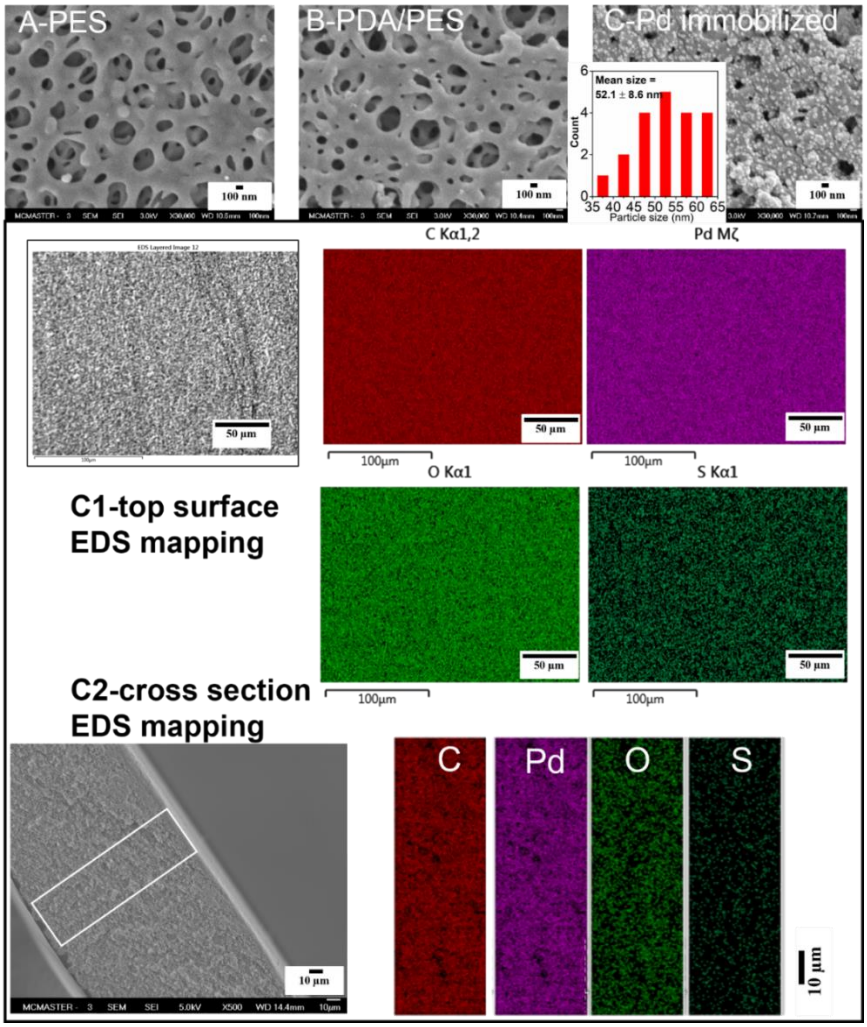

Figure 3. SEM top surface of (A) the PES membrane, (B) the PDA/PES membrane and (C) the Pd-immobilized membrane; the insert shows the particle-size distribution

histogram of Pd nanocatalysts immobilized on PES/PDA membranes with a mean particle size of 52.1 ± 8.6 nm. EDS element mapping of Pd-immobilized membranes: (C1) top surface; (C2) cross section

The successful immobilization of Pd nanocatalysts on the membrane support was further verified by BET measurements indicating higher surface area and greater relative pore volume for catalyst modified membranes. BET surface area, BET pore volume and the gravimetric-determined porosity for the PES membrane, PDA/PES membrane and Pd-immobilized membrane are presented in **Table 1**. The PDA coating on the PES membrane had a negligible influence on the BET surface area and the BET pore volume, while the immobilization of Pd nanocatalysts nearly doubled the surface area to 51.28 m^2/g and more than doubled the pore volume to 0.10 cm^3/g due to the formation of new microporous/mesoporous structures. Accordingly, the Pd-immobilized membrane had higher available surface area for adsorption of reactants, benefiting the catalytic reduction efficiency. In addition, the porosity of modified PES membranes decreased slightly from 0.77 for the control membranes to 0.76 for PDA modified PES membranes and 0.75 for the Pd-immobilized membrane. Such negligible change in membrane porosity suggested that Pd NP agglomeration did not occur to any significant extent during the fabrication process, which is supported by evidence of small Pd nanocatalysts (d = 52.1 nm ± 8.6 nm).

Table 1. Summary of physical properties of Pd-immobilized membranes

	Surface area (m^2/g)	Pore volume (cm^3/g)	Porosity
PES membrane	24.36	0.04	0.77 ± 0.04
PDA/PES membrane	25.90	0.04	0.76 ± 0.01
Pd-immobilized membrane	51.28	0.10	0.75 ± 0.01

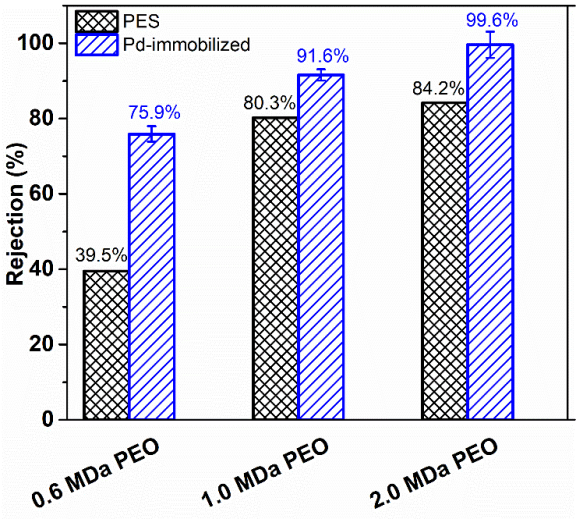

Figure 4. Rejection of PES membranes and Pd-immobilized membranes under varying molecular weights of PEO

The selectivity of PES membranes and Pd-immobilized membranes were explored by rejecting PEO with different molecular sizes, during which PEO rejection is determined by size exclusion. **Figure 4** shows that Pd-immobilized membranes rejected 75.9% of 0.6 MDa PEO, 91.6% of 1.0 MDa PEO, and 99.6% of 2.0 MDa PEO, while PES membrane had much lower rejection under the same conditions. The higher PEO rejection for Pd-

immobilized membranes indicates that there are fewer pores through which PEO can pass, and that the average pore size has slightly decreased as is evident from **Figure 3B-C**, as a result of the introduction of Pd nanocatalysts on the PES membrane. MWCO of Pd-immobilized membranes was 1.0 MDa, at which the rejection degree was greater than 90%.

4.4.2 Catalytic reduction of 4-NP

Catalytic performance of Pd-immobilized membranes was investigated by reducing 4-NP to 4-AP by flowing 4-NP through the membranes in the presence of $NaBH_4$. **Figure 5A** shows the breakthrough curves for 0.6 mM 4-NP, in which complete breakthrough for PES membranes and PDA/PES membranes occurred after 20 mL of feed passed through the membranes. In contrast 4-NP was prevented from breaking through Pd-immobilized membranes during identical experiments. Using Pd-immobilized membranes in the presence of $NaBH_4$, 66.2% of 4-NP reduction was achieved over 100 mL of solution, and a measured reduction rate of 4.0 mol m^{-2} h^{-1} of 4-NP (**Figure 5C**). To demonstrate that catalysis of 4-NP did not occur without the presence of Pd nanocatalysts a series of control experiments were performed. Adsorption of 4-NP to the membrane surface accounted for the small removal achieved by these membranes without catalysts, shown in **Figure 5C**. From 100 mL of filtrate, we measured 11.5% total removal of 4-NP across the pristine PES membrane and 17.3% total removal across the PDA/PES membrane. PDA/PES membranes retained larger amounts of 4-NP than the pristine PES membrane as the PDA has been shown to have a higher affinity for adsorption over PES (a greater stickiness coefficient, α) as well as a slightly higher adsorption capacity than PES

membranes as demonstrated by the abovementioned BET surface areas in Table 1. Additionally, 4-NP removal using Pd-immobilized membranes without $NaBH_4$ was performed as control, showing 21.1% of 4-NP removal and no production of 4-AP (**Figure S1A**). Pd-immobilized membranes were measured to have twice the available surface area (**Table 1**) as PES membranes, attributed to the high number of Pd nanocatalysts decorated throughout the porous structure. As such, 4-NP chemical reduction by catalysis (66.2%) was 3-fold higher than 4-NP removal by adsorption (21.1%) using Pd-immobilized membranes, verifying the high-efficient catalytic process for wastewater treatment. As the filtration progressed, the adsorption sites on all control membranes were rapidly saturated (within 20 mL of filtrate for PES and PDA/PES membranes and within 40 mL of filtrate for Pd-immobilized membranes without $NaBH_4$) and a constant 4-NP concentration was measured in the permeate stream henceforth. As expected, without Pd nanocatalysts, 4-NP was insignificantly reduced even in the presence of $NaBH_4$, and in the presence of Pd nanocatalysts without the presence of $NaBH_4$, 4-NP demonstrated adsorption without chemical reduction (**Figure S1B**). The introduction of Pd nanocatalysts in the presence of $NaBH_4$ into the membranes caused much greater reduction of 4-NP to 4-AP under identical operating conditions. It is worth noting that the flux of the Pd-immobilized membrane was 1160.9 L m^{-2} h^{-1}, 45% less than that of the PES membrane, resulting in longer residence times and therefore a higher catalytic reduction efficiency.

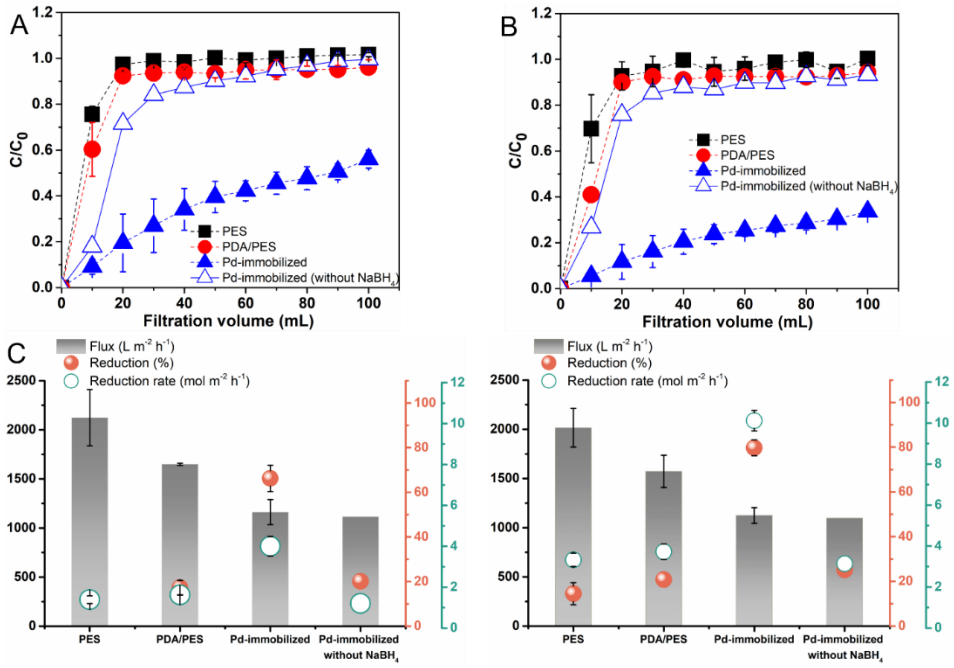

Figure 5. Breakthrough curves of (A) 0.6 mM 4-NP and (B) 1.2 mM 4-NP passing through PES, PDA/PES and Pd-immobilized membranes in the presence of $NaBH_4$ and on Pd-immobilized membranes in the absence of $NaBH_4$; Flux, reduction and reduction rate of PES, PDA/PES and Pd-immobilized membranes were calculated with (C) 0.6 mM 4-NP and (D) 1.2 mM 4-NP filtering through. 4-NP reduction for the non-catalytic membranes and the catalytic membranes were due to adsorption and catalytic conversion, respectively.

Figure 5B shows the breakthrough curves for 1.2 mM 4-NP flowing through the CMMRs. In comparison to **Figure 5A**, when the 4-NP concentration was doubled both the fraction of 4-NP that was reduced, and its reduction rates increased. As expected, the control membranes demonstrated complete breakthrough of 4-NP after only 20 mL of feed was filtered. Further, for a total of 100 mL of solution, the PES and PDA/PES membranes only achieved 14.5% and 20.8% removal of 4-NP respectively, in the presence of $NaBH_4$. In contrast, with the aid of Pd nanocatalysts, complete breakthrough

was not observed over the course of 100 mL of filtrate, and total 4-NP reduction increased to 79.7% when it was made to flow through Pd-immobilized membranes (**Figure 5D**). The greater 4-NP reduction efficiency with higher concentration was attributed to greater 4-NP mass transfer to the catalysts and a greater likelihood of reaction. The maximum 4-NP reduction rate for the Pd-immobilized membranes was 10.1 mol m^{-2} h^{-1}, when the 4-NP concentration was 1.2 mM in the feed and 10 psi (0.689 bar) was applied across the membrane. The fluid flux through the CMMRs was not impacted by the higher 4-NP concentration and was measured to be 1125.0 L m^{-2} h^{-1}, nearly identical to the flux with low 4-NP concentration (1160.9 L m^{-2} h^{-1}). Pd-immobilized membranes are promising candidates to catalyze 4-NP in the presence of excess $NaBH_4$.

4.4.3 Catalytic reduction mechanisms

UV-Vis spectra are presented in **Figure 6A** for the feed and permeate solutions flowing across Pd-immobilized membranes in the presence of $NaBH_4$, which acted as a catalyst and a reducing agent, respectively. These spectra show the catalytic reduction of 4-NP and its conversion to 4-aminophenol (4-AP). The feed solution of 4-NP was neutral (pH = 7.2) and the addition of the fresh $NaBH_4$ solution resulted in the deprotonation of 4-NP into the 4-nitrophenolate ion with an absorption intensity at 400 nm. As demonstrated above, the conversion of 4-NP was insignificant without the Pd NP catalysts as a result of the large activation energy barrier and the mutual electrostatic repulsion between the negatively charged reactants (deprotonated 4-NP and BH_4^-). The Pd nanocatalysts serving as a hydride carrier, assisted electron transfer from the borohydride ions to the nitro groups of 4-NP, which lowered the activation barrier and thus facilitated the 4-NP

reduction reaction [1], as illustrated in **Figure 6B**. The absorption peak at 300 nm assigned to 4-AP (product) in the UV-Vis spectrum (**Figure 6A**) appeared, as the same product was reported for 4-NP conversion using $NaBH_4$ in the literature [26].

The mechanism of 4-NP reduction with $NaBH_4$ and Pd nanocatalysts was proposed in **Scheme 1**. In the heterogeneous catalytic system, 4-NP (**Scheme 1A**) was deprotonated to 4-nitrophenolate (**Scheme 1B**), which adhered to the Pd-immobilized surface. Meanwhile, the electron donor BH_4^- also adsorbed on Pd nanocatalysts and simultaneously Pd-H* bonds were generated by hydrolysis of BH_4^- (Scheme 1C). The reactant (4-nitrophenolate) was reduced on the Pd catalytic sites *via* a sequential hydrogenation reaction along with the occurrence of intermediates (**Scheme 1D-F**), ultimately yielding 4-AP (**Scheme 1G**). More importantly, 4-AP diffused away from the Pd nanocatalyst surfaces freeing the catalytic sites for further reduction of other 4-NP molecules, leading to a continuous catalytic reduction reaction. Overall, the immobilization of Pd nanocatalysts on the membrane support offered extraordinary catalytic activity for the 4-NP reduction.

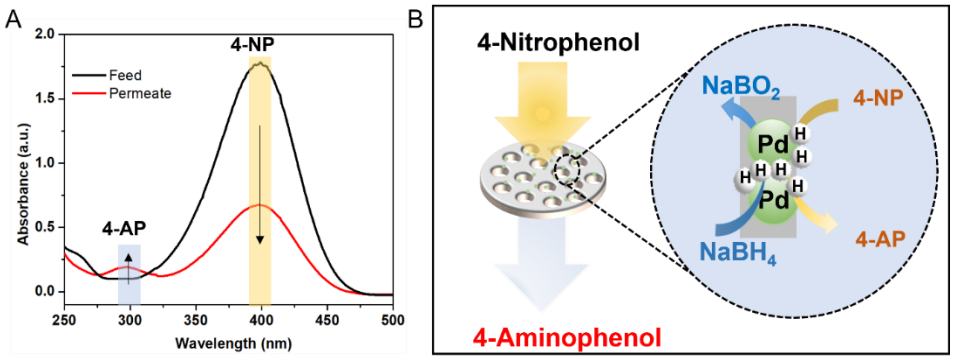

Figure 6. (A) UV absorption spectra of 4-NP in reactant and product solutions. (B) Schematic diagram of 4-nitrophenol degradation in the presence of $NaBH_4$

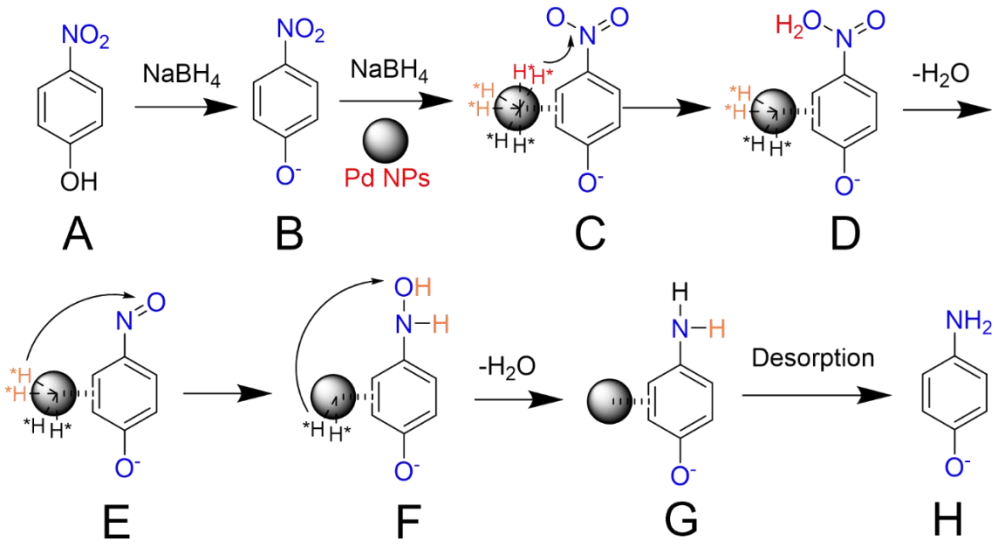

Scheme 1. Reduction pathways of 4-NP catalyzed by the Pd-immobilized membrane with excess $NaBH_4$

4.4.4 Membrane ultrafiltration and catalysis of mixed 4-NP

To investigate the combined effect of ultrafiltration and catalysis for Pd-immobilized membranes, a mixed solution of 4-NP (1.2 mM) and PEO (1 MDa, 50 ppm) was filtered. Pd-immobilized membranes exhibited 91.6% of 1.0 MDa PEO rejection in **Figure 4**, and

therefore we assumed that the presence of 4-NP did not affect the ultrafiltration of PEO by Pd-immobilized membranes. As a mixed solution without $NaBH_4$ was permeated through the Pd-immobilized membrane, size exclusion by ultrafiltration was the dominant separation mechanism. Pd-immobilized membranes rejected PEO but had limited removal of 4-NP, verified by the almost unchanged color of the permeate (**Figure 7A**). **Figure 7B** shows the flux, 4-NP reduction and PEO rejection of Pd-immobilized membranes in the ultrafiltration process. Pd-immobilized membrane showed a flux of 162.6 L m^{-2} h^{-1}, a 4-NP reduction of 30.5% and a PEO rejection of 90.6% in the 10 mL of permeate. Such a significant decline in membrane flux for mixed 4-NP solution was ascribed to the PEO fouling layer formation, compared to membrane flux of 1097.6 L m^{-2} h^{-1} for pure 4-NP solution under the identical conditions (**Figure 5**). The 4-NP removal in the ultrafiltration process was due to 4-NP adsorption on the Pd-immobilized membrane. While the PEO rejection was maintained at greater than 90% throughout the separation experiment, the 4-NP removal was poor at less than 10% (ranging from 8.4% to 2.3%). Membrane flux decreased from 44.8 L m^{-2} h^{-1} to 12.4 L m^{-2} h^{-1}, due to the dense PEO layer that accumulated on the Pd-immobilized membrane surface. Evidently 4-NP removal is not feasible for conventional ultrafiltration membranes even those modified with Pd nanocatalysts.

In the presence of $NaBH_4$, these CMMRs demonstrated strong simultaneous removal of both PEO and 4-NP. Integration of catalysis and ultrafiltration using the Pd-immobilized membrane was performed with the addition of $NaBH_4$ (50 mM). The bright yellow color of the mixed feed solution became a colorless permeate within the first 10 mL of

treatment as shown in **Figure 7C**, due to conversion of 4-NP (bright yellow) to 4-AP (colorless) due to synergistic effect of the Pd nanocatalysts and $NaBH_4$. A membrane flux of 368.0 L m^{-2} h^{-1}, 4-NP conversion of 99.7% and PEO rejection of 90.2% were achieved in the initial 10 mL of permeate (**Figure 7D**). Interestingly, throughout the mixed filtration experiment, both high PEO rejection (>90%) and high 4-NP conversion (>99%) was maintained. While the membrane flux decreased from 69.3 L m^{-2} h^{-1} to 16.3 L m^{-2} h^{-1}, as expected, due to PEO fouling of the surface, fouling did not decrease the reduction rate of 4-NP, rather it encouraged consistently high reduction. Based on these results we hypothesize that as the PEO fouling layer reduces membrane flux it promotes catalytic performance of the Pd-immobilized membranes by increasing the overall residence time of the 4-NP through a lower transmembrane water flux. Overall, by combing ultrafiltration and catalysis, Pd-immobilized membranes are a promising candidate for purification of dye- and macromolecule-contaminated wastewater.

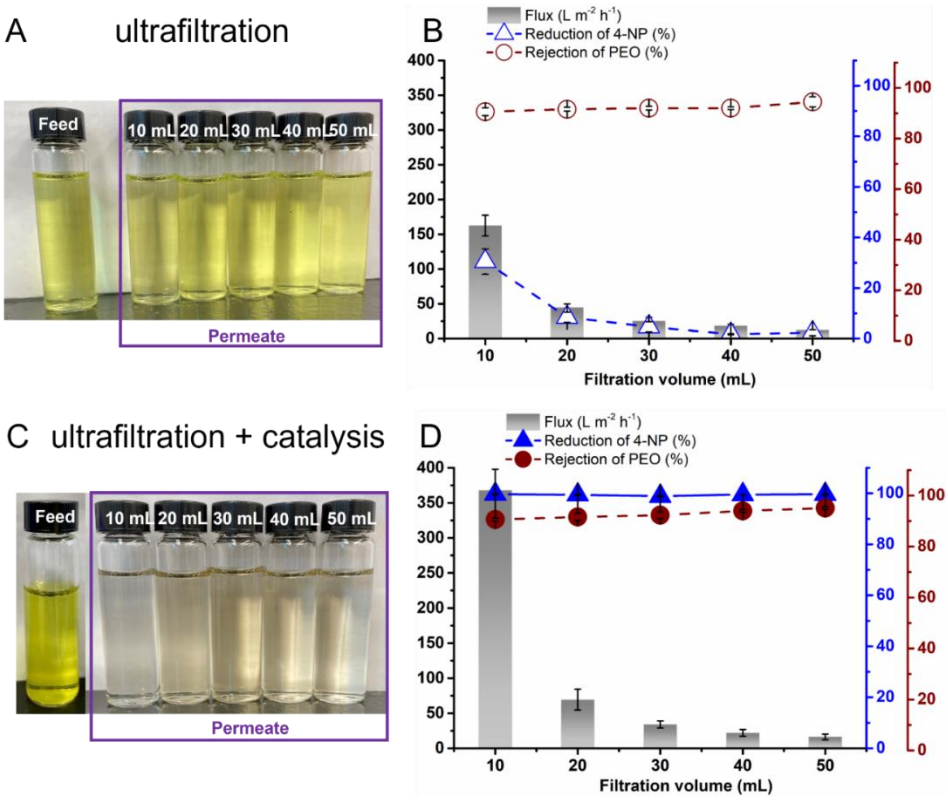

Figure 7. (A) The color change of feed and permeate solutions in the ultrafiltration process; (B) Flux, reduction of 4-NP and rejection of PEO after 50 mL of a mixed solution (1.2 mM 4-NP and 50 ppm of 1 MDa PEO) in the ultrafiltration process; (C) The color change of feed and permeate solutions in the combined filtration and catalysis processes; (D) Flux, conversion of 4-NP and rejection of PEO after 50 mL of a mixed solution (50 mM $NaBH_4$, 1.2 mM 4-NP and 50 ppm of 1 MDa PEO) in the combined filtration and catalysis processes.

4.5 Conclusion

A catalytic membrane was fabricated by assembling Pd nanocatalysts on the PES surface and inner membrane porous structures *via* immersion synthesis. The catalytic activity of the prepared Pd-immobilized membrane was assessed by 4-NP reduction in flow-through mode. The breakthrough time of 4-NP using Pd-immobilized membranes was

significantly larger than the control membranes without catalysts. The maximum reduction degree (79.7 %) and 4-NP reduction rate (10.1 mol m^{-2} h^{-1}) for the Pd-immobilized membranes were obtained with the reactant concentration of 1.2 mM and an applied pressure of 10 psi (0.689 bar). Such improved catalytic performance was mainly due to the stable and well-dispersed Pd nanocatalysts, facilitating H* transfer to the reactants and thus decreasing the activation barrier for 4-NP reduction. We have demonstrated that this catalytic membrane microreactor is an intensified catalytic processes which increases mass transfer to stable, solid-state immobilized catalysts can continuously manufacture 4-AP. Further, Pd-immobilized membranes showed great potential for high efficient treatment of a mixed solution containing 4-NP and PEO by combining ultrafiltration and catalysis, and membrane fouling was shown to improve catalytic reduction by increasing the residence time of contaminants with catalysts. This work demonstrated a new perspective for the treatment of macromolecule- and dye-polluted water by Pd-immobilized membrane in a flow-through CMMR system.

4.6 Acknowledgements

The authors thank the support of the Global Water Futures (GWF) research program provided through the Canada First Research Excellence Fund (CFREF, Sensors and Sensing Systems for Water Quality Monitoring) as well as the China Scholarship Council (CSC). The electron microscopy research described in this paper was performed at the Canadian Centre for Electron Microscopy (CCEM) at McMaster University, which is supported by the Natural Sciences and Engineering Research Council of Canada (NSERC, Discovery Grant) and other government agencies.

4.7 References

[1] N. Berahim, W. Basirun, B. Leo, M. Johan, Synthesis of Bimetallic Gold-Silver (Au-Ag) Nanoparticles for the Catalytic Reduction of 4-Nitrophenol to 4-Aminophenol, Catalysts 8(10) (2018). https://doi.org/10.3390/catal8100412.
[2] M. Nemanashi, R. Meijboom, Synthesis and characterization of Cu, Ag and Au dendrimer-encapsulated nanoparticles and their application in the reduction of 4-nitrophenol to 4-aminophenol, J Colloid Interface Sci 389(1) (2013) 260-7. https://doi.org/10.1016/j.jcis.2012.09.012.
[3] S. De Corte, T. Sabbe, T. Hennebel, L. Vanhaecke, B. De Gusseme, W. Verstraete, N. Boon, Doping of biogenic Pd catalysts with Au enables dechlorination of diclofenac at environmental conditions, Water Res 46(8) (2012) 2718-26. https://doi.org/10.1016/j.watres.2012.02.036.
[4] L.Q. Zheng, X.D. Yu, J.J. Xu, H.Y. Chen, Reversible catalysis for the reaction between methyl orange and NaBH4 by silver nanoparticles, Chem Commun (Camb) 51(6) (2015) 1050-3. https://doi.org/10.1039/c4cc07711c.
[5] M. Mourya, D. Choudhary, A.K. Basak, C.S.P. Tripathi, D. Guin, Ag-Nanoparticles-Embedded Filter Paper: An Efficient Dip Catalyst for Aromatic Nitrophenol Reduction, Intramolecular Cascade Reaction, and Methyl Orange Degradation, ChemistrySelect 3(10) (2018) 2882-2887. https://doi.org/10.1002/slct.201702609.
[6] A. Mohan, J. Peter, L. Rout, A.M. Thomas, S. Nagappan, S. Parambadath, W. Zhang, M. Selvaraj, C.-S. Ha, Facile synthesis of silver nanoparticles stabilized dual responsive silica nanohybrid: A highly active switchable catalyst for oxidation of alcohols in aqueous medium, Colloids and Surfaces A: Physicochemical and Engineering Aspects 611 (2021). https://doi.org/10.1016/j.colsurfa.2020.125846.
[7] V. Raji, M. Chakraborty, P.A. Parikh, Catalytic Performance of Silica-Supported Silver Nanoparticles for Liquid-Phase Oxidation of Ethylbenzene, Ind. Eng. Chem. Res 51(16) (2012) 5691-5698. https://doi.org/10.1021/ie2027603.
[8] Q. Wei, B. Li, C. Li, J. Wang, W. Wang, X. Yang, PVP-capped silver nanoparticles as catalysts for polymerization of alkylsilanes to siloxane composite microspheres, Journal of Materials Chemistry 16(36) (2006). https://doi.org/10.1039/b608643h.
[9] J. Wang, Z. Wu, T. Li, J. Ye, L. Shen, Z. She, F. Liu, Catalytic PVDF membrane for continuous reduction and separation of p-nitrophenol and methylene blue in emulsified oil solution, Chemical Engineering Journal 334 (2018) 579-586. https://doi.org/10.1016/j.cej.2017.10.055.
[10] Y.Y. Li Sip, D.W. Fox, L.R. Shultz, M. Davy, H.-S. Chung, D.-X. Antony, Y. Jung, T. Jurca, L. Zhai, Cu–Ag Alloy Nanoparticles in Hydrogel Nanofibers for the Catalytic Reduction of Organic Compounds, ACS Applied Nano Materials 4(6) (2021) 6045-6056. https://doi.org/10.1021/acsanm.1c00881.
[11] H.N. Abdelhamid, High performance and ultrafast reduction of 4-nitrophenol using metal-organic frameworks, Journal of Environmental Chemical Engineering 9(1) (2021). https://doi.org/10.1016/j.jece.2020.104404.
[12] M.J. Detisch, T.J. Balk, D. Bhattacharyya, Synthesis of Catalytic Nanoporous Metallic Thin Films on Polymer Membranes, Ind Eng Chem Res 57(12) (2018) 4420-4429. https://doi.org/10.1021/acs.iecr.8b00053.
[13] Y. Chen, S. Fan, B. Qiu, J. Chen, Z. Mai, Y. Wang, K. Bai, Z. Xiao, Cu-Ag Bimetallic Core-shell Nanoparticles in Pores of a Membrane Microreactor for Enhanced Synergistic Catalysis, ACS Appl Mater Interfaces 13(21) (2021) 24795-24803. https://doi.org/10.1021/acsami.1c04155.

[14] B. Qiu, S. Fan, Y. Wang, J. Chen, Z. Xiao, Y. Wang, Y. Chen, J. Liu, Y. Qin, S. Jian, Catalytic membrane micro-reactor with nano ZIF-8 immobilized in membrane pores for enhanced Knoevenagel reaction of Benzaldehyde and Ethyl cyanoacetate, Chemical Engineering Journal 400 (2020). https://doi.org/10.1016/j.cej.2020.125910.
[15] N. Li, X. Lu, M. He, X. Duan, B. Yan, G. Chen, S. Wang, Catalytic membrane-based oxidation-filtration systems for organic wastewater purification: A review, J Hazard Mater 414 (2021) 125478. https://doi.org/10.1016/j.jhazmat.2021.125478.
[16] Z. Yan, Y. Zhang, H. Yang, G. Fan, A. Ding, H. Liang, G. Li, N. Ren, B. Van der Bruggen, Mussel-inspired polydopamine modification of polymeric membranes for the application of water and wastewater treatment: A review, Chemical Engineering Research and Design 157 (2020) 195-214. https://doi.org/10.1016/j.cherd.2020.03.011.
[17] H. Li, J. Xi, A.G. Donaghue, J. Keum, Y. Zhao, K. An, E.R. McKenzie, F. Ren, Synthesis and catalytic performance of polydopamine supported metal nanoparticles, Sci Rep 10(1) (2020) 10416. https://doi.org/10.1038/s41598-020-67458-9.
[18] R. Li, Y. Wu, L. Shen, J. Chen, H. Lin, A novel strategy to develop antifouling and antibacterial conductive Cu/polydopamine/polyvinylidene fluoride membranes for water treatment, J Colloid Interface Sci 531 (2018) 493-501. https://doi.org/10.1016/j.jcis.2018.07.090.
[19] Y. Yang, K. Jiang, J. Guo, J. Li, X. Peng, B. Hong, X. Wang, H. Ge, Facile fabrication of Au/Fe3O4 nanocomposites as excellent nanocatalyst for ultrafast recyclable reduction of 4-nitropheol, Chemical Engineering Journal 381 (2020). https://doi.org/10.1016/j.cej.2019.122596.
[20] S. Schultz, M. DeSilva, T.T. Gu, M. Qiang, K. Whang, Effects of the Analgesic Acetaminophen (Paracetamol) and its para-Aminophenol Metabolite on Viability of Mouse-Cultured Cortical Neurons, Basic & Clinical Pharmacology & Toxicology 110(2) (2012) 141-144. https://doi.org/https://doi.org/10.1111/j.1742-7843.2011.00767.x.
[21] J.M. Luque-Alled, A. Abdel-Karim, M. Alberto, S. Leaper, M. Perez-Page, K. Huang, A. Vijayaraghavan, A.S. El-Kalliny, S.M. Holmes, P. Gorgojo, Polyethersulfone membranes: From ultrafiltration to nanofiltration via the incorporation of APTS functionalized-graphene oxide, Sep. Purif. Technol 230 (2020). https://doi.org/10.1016/j.seppur.2019.115836.
[22] Z.J. Sun, Z.W. Jiang, Y.F. Li, Poly(dopamine) assisted in situ fabrication of silver nanoparticles/metal–organic framework hybrids as SERS substrates for folic acid detection, RSC Advances 6(83) (2016) 79805-79810. https://doi.org/10.1039/c6ra16042e.
[23] J. Xing, Q. Wang, T. He, Z. Zhou, D. Chen, X. Yi, Z. Wang, R. Wang, G. Tan, P. Yu, C. Ning, Polydopamine-Assisted Immobilization of Copper Ions onto Hemodialysis Membranes for Antimicrobial, ACS Applied Bio Materials 1(5) (2018) 1236-1243. https://doi.org/10.1021/acsabm.8b00106.
[24] V.K. Thakur, M.-F. Lin, E.J. Tan, P.S. Lee, Green aqueous modification of fluoropolymers for energy storage applications, Journal of Materials Chemistry 22(13) (2012). https://doi.org/10.1039/c2jm15665b.
[25] A. Baylet, P. Marecot, D. Duprez, P. Castellazzi, G. Groppi, P. Forzatti, In situ Raman and in situ XRD analysis of PdO reduction and Pd degrees oxidation supported on gamma-Al2O3 catalyst under different atmospheres, Phys Chem Chem Phys 13(10) (2011) 4607-13. https://doi.org/10.1039/c0cp01331e.
[26] X. Kong, H. Zhu, C. Chen, G. Huang, Q. Chen, Insights into the reduction of 4-nitrophenol to 4-aminophenol on catalysts, Chemical Physics Letters 684 (2017) 148-152. https://doi.org/10.1016/j.cplett.2017.06.049.

Chapter 5

Stable Ni-Cu Bimetallic catalytic membranes for continuous nitrophenol conversion

5.1 Abstract

Inexpensive Ni-Cu bimetallic catalytic membrane microreactors (CMMRs) were synthesized using PES ultrafiltration membranes to catalytically degrade the environmental pollutant, 4-nitrophenol (4-NP), and produce the valuable chemical feedstock, 4-aminophenol (4-AP). Compared to 4-NP conversion in batch mode, flow-through mode demonstrated enhanced mass transfer contributing to 2.5-fold higher conversion (>99 %) and 20-fold higher processing capacity (0.95 $mol \cdot L^{-1} \cdot h^{-1}$). Investigating the influence of operating conditions on catalytic activity indicated that 4-NP conversion followed the Langmuir-Hinshelwood (L-H) mechanism, and that conversion efficiency was highly dependent on flow rate, representing a critical optimization trade-off that must be considered for CMMR applications. The long-term stability of these bimetallic CMMRs was demonstrated and attributed to both the polydopamine-assisted fabrication and the tortuous membrane pore structure. Finally, it was demonstrated that the enhanced activity was attributed to the synergistic electronic effects of the Ni-Cu bimetallic structure, the metal-polydopamine interactions, and the catalysts' unique structure and high surface area.

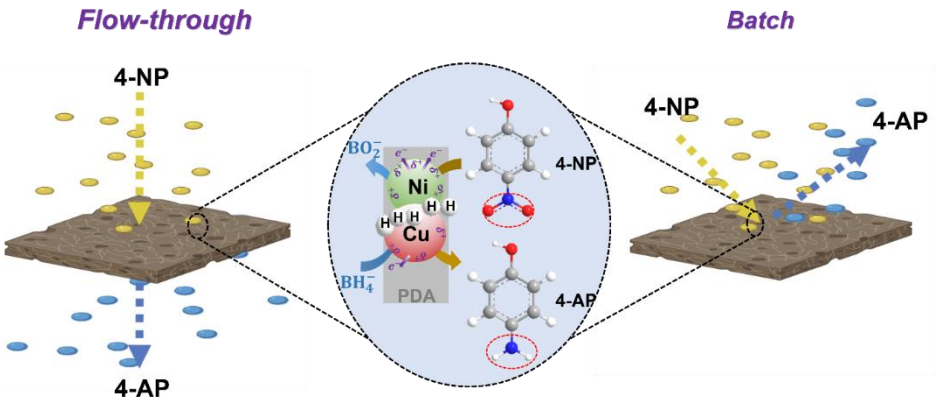

5.2. Introduction

Membrane technology has been extensively applied in wastewater treatment; however, high flux membranes (microfiltration (MF) and ultrafiltration (UF) membranes) used in these treatment trains are unable to separate small organic contaminants from feed stream. Furthermore, conventional membrane technology is a passive treatment approach that does not degrade recalcitrant contaminants in the feed stream. Finally, membrane fouling is a continual operational concern that limits membrane performance [1-3]. These limitations can be simultaneously addressed by an emerging membrane-based water treatment technology - catalytic membrane microreactors (CMMRs) – which combine membrane filtration and catalytic reactions into a single unit. Organic contaminants are filtered through a membrane embedded with catalysts, resulting in simultaneous removal of contaminants from the feed stream and contaminant degradation, which has the beneficial effect of reducing membrane surface fouling by those contaminants[4, 5]. CMMRs can also be used to intensify chemical processes in the fields of chemical synthesis[6], petrochemical processing[7], and biotechnology manufacturing[8]. A CMMR takes advantage of the high surface area and interconnected porous network of membranes to increase the availability of reaction sites for catalytic conversion enabling reaction process intensification, leading to higher conversion, selectivity and yield over conventional reactors[9-11]. The tortuous pore structure of membranes also limits nanocatalyst leaching and can increase catalyst immobilization[12]. The catalytic performance of CMMRs in the conversion of reactants can be controlled both by the catalyst itself (i.e., material type, catalyst loading, catalyst particles size, distribution, and

density) and operating conditions (i.e., contaminant concentration, liquid flux, and liquid flow conditions).

Noble metals have been reported to possess extraordinary catalytic activity for a variety of catalytic reactions [13, 14], however, individual noble metal catalysts are prone to fouling and attrition of active sites due to the strong competition between reactants and their intermediates. In recent years, bimetallic nanocatalysts have received increasing attention because the introduction of a secondary metal can increase the available surface area of the noble metal to which it is added [15], reducing the amount of noble metal required and thereby reducing the costs associated with expensive catalyst materials. Additionally, interesting new electronic and catalytic properties have been discovered from the synergistic effects of bimetals [5, 12, 16-18]. For example, bimetallic Cu-Ag nanoparticles (NPs) demonstrated enhanced site availability and electron transfer between bimetals leading to increased catalytic transformation of nitrophenol as compared to single Cu or Ag catalysts of the same size[12]. In seminal research, Ni-Pd nanodimers supported on nitrogen-doped reduced graphene oxide achieved up to a 4-fold higher reaction constant for 4-nitrophenol reduction compared to their monometallic counterparts[18]. Non-noble bimetallic catalysts composed of earth abundant and inexpensive metals are more attractive for practical applications; only limited recent research has investigated their use in contaminant conversion [19-22]. For example, heterogeneous nanoparticle catalysts of Ni-Cu supported by dendritic ligands were explored for selective oxidation of alcohols and reduction of azo dyes [21]. CMMR research is an exciting and new direction for membrane technologies, but the use of non-noble bimetallic catalysts is scarce.

Several fabrication techniques have been developed for CMMRs including physical blending of metal catalyst nanoparticles into polymer-solvent systems prior to membrane casting, deposition of metal nanocatalysts onto membranes by filtration, and impregnation of metal nanocatalyst precursors into membrane structures followed by chemical reduction to form the nanocatalysts *in-situ* [1, 23]. Physical blending faces the challenges of low active site availability, low yield of products, poor stability, and a low active-surface-area-to-mass ratio of the catalysts, which is an inefficient use of the nanocatalyst material. Deposition by filtration of well-dispersed catalyst nanoparticle solutions tends to favor deposition of nanocatalysts at the membrane surface rather than within the membrane porous structure [24, 25]. This uneven cross-sectional distribution of nanocatalysts within the membrane fails to achieve their full catalytic activity and does not take advantage of the increased mass transfer and stability offered by the internal membrane porous structure. Impregnation of metal precursors can avoid several of these limitations. The impregnation approach filters metal salts through the membrane followed by either thermal or chemical reduction to form the nanocatalysts *in-situ*. Impregnation of membranes with bimetallic catalysts can be achieved by either co-impregnation (CIP) or sequential impregnation (SIP) of metal salts [17, 23]. CIP is a simultaneous process whereby a mixed solution of metal salt precursors permeate through the membrane and deposit on the internal porous structure, and are then chemically reduced together (co-reduced) after deposition. In contrast, SIP is a successive process where one metal salt precursor permeates through the membrane, deposits on the internal pore structure, and is followed by the permeation of the second metal salt precursor. The secondary metal is introduced *via* galvanic replacement reaction in which

the initial active-metal nanoparticles serve as seeds for catalyst growth and electron donors for reduction [12, 26]. In either process, the use of polydopamine (PDA) as a membrane coating can assist in strongly binding impregnated metal nanocatalysts to the membrane pore walls [27-30]. Dopamine can self-polymerize under mild alkaline conditions to produce an adhesive PDA layer, which serve as a versatile platform for nanoparticles immobilization.

In this study, inexpensive and earth abundant bimetallic Ni-Cu CMMRs were synthesized for the catalytic reduction of common organic contaminants in water and wastewater. These CMMRs were produced by impregnating bimetallic metal salts on PDA-modified polyether sulfone (PES) membranes. The metal precursors were permeated through PDA-functionalized membranes, and the coordinated metal-PDA compounds were transformed into well immobilized metal nanocatalysts on and within the membrane structure by co-reduction of the bimetallic salts or by a galvanic replacement reaction, respectively. The catalytic activity of bimetallic CMMRs was investigated by 4-nitrophenol (4-NP) reduction in different reaction modes (batch vs. flow-through mode). The durability of bimetallic Ni-Cu/PES CMMRs was evaluated in the continuous 4-NP reduction process. Further, the mechanism responsible for the enhanced 4-NP catalytic performance by bimetallic Ni-Cu/PES CMMRs was elucidated from material characterizations including scanning electron microscopy – energy dispersive x-ray spectroscopy (SEM - EDX), transmission electron microscopy (TEM), X-ray photoelectron spectroscopy (XPS) and BET measurements.

5.3 Materials and methods

5.3.1 Materials

Polyethersulfone (PES) porous membranes (pore size: 0.03 μm, diameter: 47 mm, thickness: 100-150 μm) were obtained from Sterlitech. Tris (hydroxymethyl) aminomethane hydrochloride (Tris-HCl), dopamine hydrochloride, sodium hydroxyl (NaOH, 1 M), nickel sulfate ($NiSO_4$), copper sulfate ($CuSO_4$), 4-nitrophenol (4-NP, *p*-NP), sodium borohydride ($NaBH_4$), N, N-dimethylformamide (DMF) and nitric acid (HNO_3) were purchased from Sigma-Aldrich. All reagents used in this research were analytical grade, and all solutions were prepared in deionized water (DI water) unless otherwise notified.

5.3.2 Fabrication of CMMRs

The fabrication process of catalytic membrane microreactors (CMMRs) is shown in **Figure 1**. First, an alkaline dopamine solution (0.5 mg/mL) was prepared by dissolving dopamine hydrochloride in Tris-HCl solution (pH=8.5). Second, the PES membrane was put into a commercial dead-end cell (Sterlitech), and then 300 mL of the tris-dopamine mixture was slowly plugged through the PES membrane by nitrogen flow. The adhesive polydopamine was gradually developed on the membrane surface and within the membrane pores due to the self-polymerization of dopamine. Finally, the pristine PDA/PES membrane was achieved after 300 mL of DI water was filtered to remove unfixed polydopamine.

5.3.2.1 Fabrication of the Ni/PES CMMR

To synthesize the Ni/PES CMMR, 50 mL of 0.3 M $NiSO_4$ was permeated through the PDA/PES membrane, and simultaneously the coordinated compound Ni/PDA was

formed. The unfixed Ni ions were washed off by flowing 300 mL of DI water. Afterward, Ni NPs on the membrane support were developed by the permeation of $NaBH_4$ (250 mL, 50 mM) for reduction (eq 1). Finally, the unstable Ni NPs on the membrane surface were removed by DI water.

$$Ni^{2+} + 2BH_4^- + 6H_2O \rightarrow Ni + 2B(OH)_3 + 7H_2 \quad (1)$$

5.3.2.2 Fabrication of the rep-R Ni-Cu/PES CMMR: Replacement reaction

The Ni/PES CMMR was prepared as mentioned above and afterward 250 mL of 1 mM $CuSO_4$ was permeated at room temperature. Consequently, the Cu NPs were precipitated on the membrane by the galvanic replacement reaction as follows:

$$Ni + Cu^{2+} \rightarrow Ni^{2+} + Cu \quad (2)$$

The synthesized *rep-R* Ni-Cu/PES CMMR was washed by 300 mL of DI water and then dried at room temperature overnight for further analysis.

5.3.2.3. Fabrication of the co-R Ni-Cu/PES CMMR: Co-reduction

The *co-R* Ni-Cu/PES CMMR was fabricated *via* the co-reduction of $NiSO_4$ and $CuSO_4$ using $NaBH_4$. The prepared PDA/PES membrane was installed in the dead-end cell and then 50 mL of the mixture (300 mM $NiSO_4$, 5 mM $CuSO_4$) was permeated. The Ni-Cu NPs on the membrane were achieved by filtering 250 mL of 50 mM $NaBH_4$, according to eq 1 and eq 3. Finally, the *co-R* Ni-Cu/PES CMMR was cleaned by 300 mL of DI water and then dried at room temperature overnight for further analysis.

$$Cu^{2+} + 2BH_4^- + 6H_2O \rightarrow Cu + 2B(OH)_3 + 7H_2 \quad (3)$$

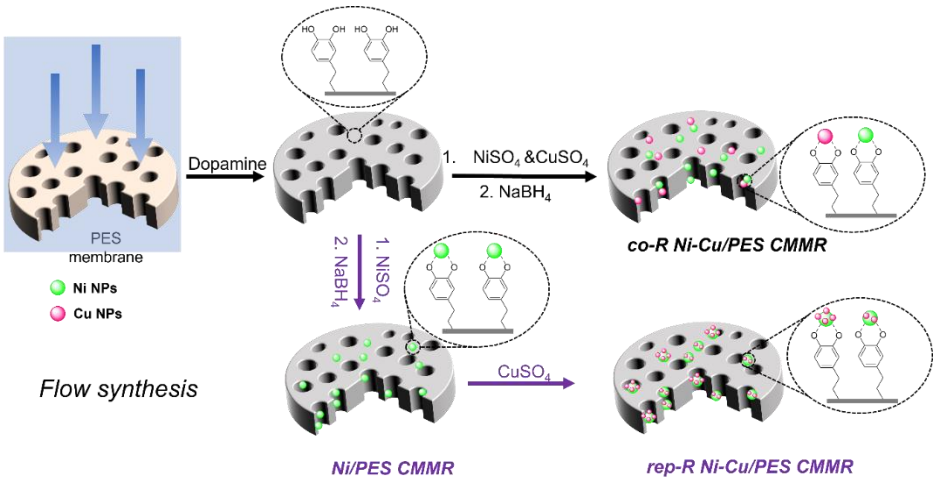

Figure 1. Fabrication of the monometallic and bimetallic CMMRs: monometallic Ni/PES catalytic membrane microreactor (Ni/PES CMMR), replacement reaction bimetallic CMMR (*rep-R* Ni-Cu/PES CMMR) and co-reduced bimetallic CMMR, (*co-R* Ni-Cu/PES CMMR).

5.3.3 Characterization

The morphology of top surfaces and cross-sections for these prepared CMMRs was visualized by scanning electron microscopy (SEM, JEOL JSM-7000F) with an accelerating voltage of 5 kV. To image the cross-sectional area of the CMMRs were immersed in liquid nitrogen and then cracked. Subsequently, the targeted areas were sputter-coated with either a 10 nm gold layer for surface visualization or a 10 nm carbon film for elemental distribution using energy-dispersive spectrometers (EDS, X-Maxn). The particle sizes of bimetallic nanocatalysts were examined by transmission electron microscopy (TEM, Talos 200X). To image the nanocatalysts within the CMMRs, the as-prepared membranes were dissolved in DMF solvent, and the suspended nanocatalysts were drop-casted onto a TEM grid and dried under ambient conditions for TEM characterization.

Fourier-transform infrared spectroscopy (FTIR, Nicolet 6700) was used to identify functional groups of CMMRs, under a specific wavelength range (4000-525 cm^{-1}). Raman spectra were collected using a Laser Raman spectroscopy (Renishaw InVia) with an excitation wavelength of 785 nm. The composition and elemental valence for CMMRs were tested by X-ray photoelectron spectroscopy (XPS, PHI Quantera II). The unsaturated surface area was measured using nitrogen adsorption-desorption isotherms by Brunauer-Emmet-Teller (BET, Autosorb iQ). Samples were degassed at 105 ºC for 24 h before physisorption. Pure water flux of CMMRs was determined by measuring permeate flux at varying pressures in a dead-end filtration cell (Sterlitech) after the membrane compression by DI water for 1 h. The metal contents loaded on the CMMRs were quantified by dissolving CMMRs into 2% HNO_3 for 24 h. The resulting solution was analyzed by inductively coupled plasma-optical emission spectroscopy (ICP-OES, Xseries 2). The measurements were carried out in triplicate, and the average value was reported.

5.3.4 Catalytic performance of CMMRs

5.3.4.1 Batch mode

100 mL of the mixture containing 4-NP solution (0.1 mM) and $NaBH_4$ (2 mM) was added to a 250 mL beaker. The catalytic reduction of 4-NP was initiated by placing the different CMMRs (surface area: 10.75 cm^2) in the beaker under stirred conditions (**Figure S1A**). During the process of 4-NP conversion, 4 mL of the sample was withdrawn in predetermined intervals, and the remaining concentration of 4-NP was determined by UV-Vis spectroscopy (DU 800) at the wavelength of 400 nm^{-1}. All experiments were performed in triplicate.

5.3.4.2 Flow-through mode

The CMMR was mounted into a dead-end cell (Sterlitech) with an effective surface area of 10.75 cm^2 (**Figure S1B**). The 4-NP conversion was conducted by filtering 100 mL aqueous mixture containing 4-NP (0.1 mM) and $NaBH_4$ (2 mM) through the CMMR at 50 psi (3.447 bar) of N_2 flow. The permeate was collected to identify 4-NP concentration by UV-Vis spectroscopy. All experiments were performed in triplicate.

5.3.5 Operating factors affecting catalytic performance of CMMRs

The effect of the 4-NP concentration and the flow rate on the catalytic performance was explored using the *co-R* Ni-Cu/PES CMMR in flow-through mode. 100 mL of 4-NP with different concentrations (0.2 mM, 0.3 mM and 0.4 mM) was permeated through the *co-R* Ni-Cu/PES CMMR at constant pressure. The permeate was collected and the effect of the flow rate on 4-NP reduction was investigated in the dead-end cell under 10 psi (0.689 bar), 15 psi (1.034 bar) and 20 psi (1.379 bar). The permeate was collected for further analysis. All experiments were performed in triplicate.

5.3.6. Durability of CMMRs

The durability of CMMRs was investigated by the continuous 4-NP reduction throughout the membrane operation at 10 psi (0.689 bar) using N_2 flow. The permeate was collected at 100 mL of intervals, and then the remaining 4-NP was determined. Additionally, leached metal nanoparticles in the permeate were treated by 2% HNO_3 for 24 h, and the resulting solution was measured by ICP-OES.

5.3.7 Analysis methods

The conversion of 4-NP to 4-AP in batch mode is defined as:

$$\eta = (1 - \frac{C_t}{C_0}) \times 100\% \quad (4)$$

where η is the conversion degree (%); C_0 is the initial 4-NP concentration (mol/L), and C_t is the 4-NP concentration (mol/L) after time t.

The kinetics of 4-NP conversion is assumed to follow the Pseudo-first-order kinetics, which describes concentration over time exponentially.

$$\frac{dC}{dt} = -kC \quad (5)$$

$$\ln \frac{C_t}{C_0} = -kt \quad (6)$$

where k is the reaction rate constant (min^{-1}) and t is the reaction time (min).

For the 4-NP conversion in flow-through mode, the membrane flux is a critical factor influencing catalytic performance of CMMRs, defined as:

$$J = \frac{Q}{A} \quad (7)$$

where J is the flux of the CMMR (LMH, L m^{-2} h^{-1}), Q is the volumetric flow rate (L/h) of the feed solution, A is the effective catalytic area of the CMMR (m^2).

Similarly, conversion degree in flow-through mode is defined as:

$$\eta = (1 - \frac{C_d}{C_u}) \times 100\% \quad (8)$$

where C_u and C_d are the 4-NP concentrations (mol/L) on the upstream and downstream of the CMMR, respectively.

Given the contact time between reactants and CMMRs, the effective reaction time (residence time, *t*, min) of reactants inside the membrane in flow-through mode is defined [12, 31], using the following equation:

$$t = \frac{l}{Q}\varepsilon A \times 1000 \times 60 = \frac{l\varepsilon}{J} \times 1000 \times 60 \quad (9)$$

where l is the thickness of the CMMR (m); ε is the porosity of the CMMR, determined by a gravimetric method. Briefly, 1 cm^2 of the square PES membrane was immersed in DI water for 24 h and subsequently the water on the membrane surface was removed by tissue paper. Then the wet membrane was weighed by an analytical balance. The water adsorbed in the pores was removed by placing the membrane in the hot plate at 60 ºC for 8 h, and then the dry membrane was weighed [32] . The porosity (ε) was calculated according to **eq 10**.

$$\varepsilon = \frac{\frac{W_w - W_d}{\rho_w}}{\frac{W_w - W_d}{\rho_w} + \frac{W_d}{\rho_p}} \quad (10)$$

where W_w and W_d are the weight of the wet membrane and the dry membrane, respectively. ρ_w is the density of water (0.998 g cm^{-3}) and ρ_p is the density of the PES polymer (1.37 g cm^{-3}). The porosity was reported as the average of three measurements.

The processing capacity (P, mol m^{-2} h^{-1}) of 4-NP conversion is defined as:

$$P = \frac{\eta}{100} \times C_u \times J \quad (11)$$

5.4 Results and discussion

5.4.1 Morphology of CMMRs

Two types of bimetallic catalytic membranes microreactors (CMMRs) were analyzed throughout: Ni-Cu metals formed by a co-reduction reaction on PES membranes (*co-R* Ni-Cu/PES CMMRs) and Ni-Cu metals formed by a replacement reaction on PES membranes (*rep-R* Ni-Cu/PES CMMRs), and these were compared to a monometallic CMMR (Ni/PES CMMR).The surface and cross-sectional areas of these prepared CMMRs were visualized by SEM and the distribution of anchored-metals was displayed by corresponding EDS mapping (**Figure 2**). The pristine PES membrane showed the typical smooth surface with average pore diameter of 30 nm while the porous PES support was deposited with a thick PDA layer after the permeation of dopamine (**Figure S2**). The monometallic Ni/PES CMMR was synthesized *via* the impregnation of the metal precursor during which Ni^{2+} ions were adhered to the PDA-modified surface, followed by $NaBH_4$ induced metallic nanoparticle precipitation which occurred both on the membrane surface and within the membrane pores. The corresponding SEM image (**Figure 2A1**) and EDS mapping (**Figure 2A2-A3**) showed that nano-clustered Ni NPs were uniformly anchored in the membrane structures.

The *rep-R* Ni-Cu/PES CMMR was developed through the galvanic replacement reaction where $CuSO_4$ was permeated through the as-prepared Ni/PES CMMR. SEM-EDX analysis in **Figure 2B1-B3** demonstrates that *rep-R* Ni-Cu/PES CMMR possessed well-distributed Ni-Cu NPs on the top surface as well as throughout the membrane pore structure. Likewise, the *co-R* Ni-Cu/PES CMMR, developed by the co-reduction of the mixture ($NiSO_4$ and $CuSO_4$) wihtin the PDA/PES membrane, demonstrated an even

distribution of the elements of Ni and Cu on the membrane surface and throughout its internal structure (**Figure 2C1-C3**). Such dispersity of bimetallic nanocatalysts for CMMRs is required to achieve high catalytic activity.

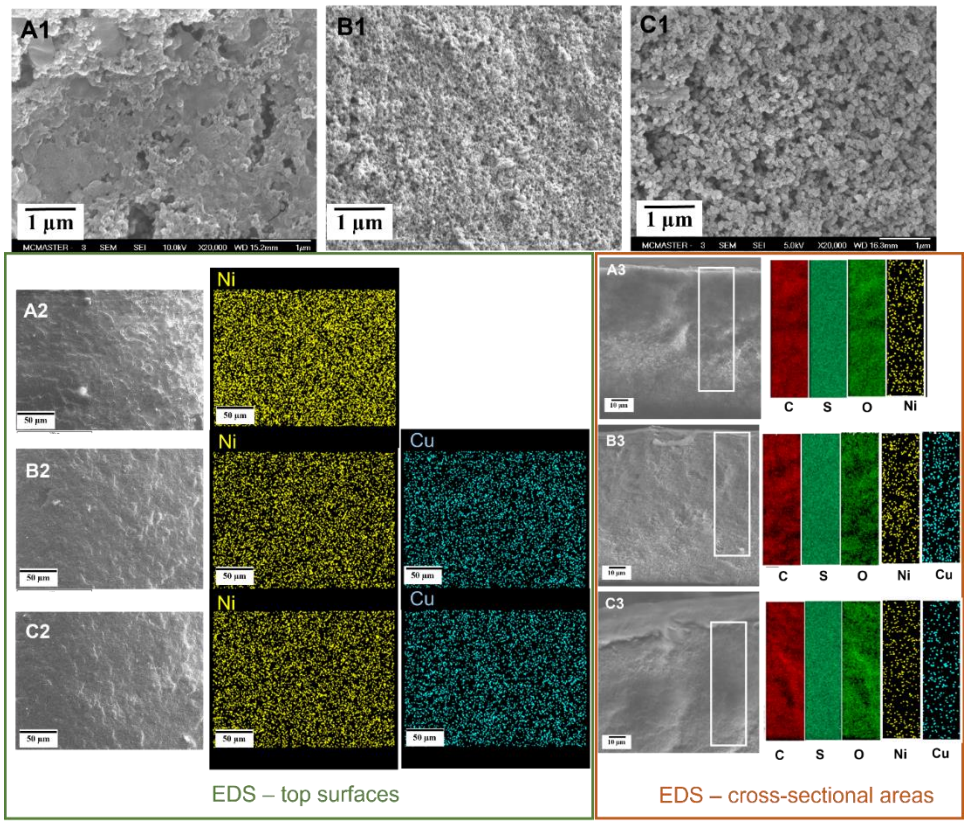

Figure 2. SEM images of top surfaces for (A1) the Ni/PES CMMR, (B1) the replacement reaction bimetallic CMMR (*rep-R* Ni-Cu/PES CMMR) and (C1) the co-reduced bimetallic CMMR (*co-R* Ni-Cu/PES CMMR). EDS mapping of the top surface for (A2) the Ni-PES CMMR, (B2) the *rep-R* Ni-Cu/PES CMMR and (C2) the *co-R* Ni-Cu/PES CMMR. EDS mapping of the cross-section for (A3) the Ni-PES CMMR, (B3) the *rep-R* Ni-Cu/PES CMMR and (C3) the *co-R* Ni-Cu/PES CMMR.

TEM was employed to identify the structure of immobilized nanoparticles. The prepared metal-anchored CMMRs were dissolved in DMF solvent, and then the insoluble NPs were characterized by TEM. **Figure 3** shows the HR-TEM images, the distribution of

particle sizes and the selected area electron diffraction (SAED) pattern of immobilized nanoparticles. The monometallic Ni NPs exhibited granular structures with an average particle diameter of 53.0 ± 12.5 nm (**Figure 3A1-A2**). Interestingly, the HR-TEM images of the *rep-R* Ni-Cu NPs demonstrated a distinct bimodal nanoparticle size distribution in which smaller Cu nanoparticles with an average diameter of 4.0 ± 1.0 nm were attached to larger Ni nanoparticle with an average diameter of 19.0 ± 2.0 nm (**Figure 3B1-B2**). In comparison, the *co-R* Ni-Cu NPs in **Figure 3C1-C2** showed a single composite Ni-Cu nanoparticle with an average diameter of 20.0 ± 5.5 nm. In both the replacement reaction systems (*rep-R* Ni-Cu NPs) and the co-reaction systems (*co-R* Ni-Cu NPs), the smaller size of bimetallic nanoparticles as compared to pure Ni NPs indicates that the introduction of the secondary metal (Cu NPs) inhibited Ni NP growth and aggregation; similar phenomena for other bimetallic systems were reported in the literature [15, 17].

Further, the crystalline properties of the *rep-R* Ni-Cu NPs were confirmed by the SAED pattern of the partial diffraction points in **Figure 3B1** demonstrating distinct diffraction patterns for both Ni and Cu, whereas the Ni NPs in **Figure 3A1** and the *co-R* Ni-Cu NPs in **Figure 3C1** were amorphous in structure demonstrated by amorphous diffraction rings. Specifically, the crystalline *rep-R* Ni-Cu NPs showed a lattice spacing of 0.205 nm in **Figure S3**, assigned to the nanoalloy Ni-Cu (1 1 1) crystal plane [15]. Additionally, the aberration-corrected high-angle annular dark-field scanning transmission electron microscopy (HAADF-STEM) mapping shown in **Figure S4** confirmed the presence of well-alloyed Ni-Cu NPs in both the *rep-R* Ni-Cu CMMR (B, B1, B2) and the *co-R* Ni-Cu CMMR, (C, C1, C2) which aligns well with SEM characterization presented in **Figure 2**.

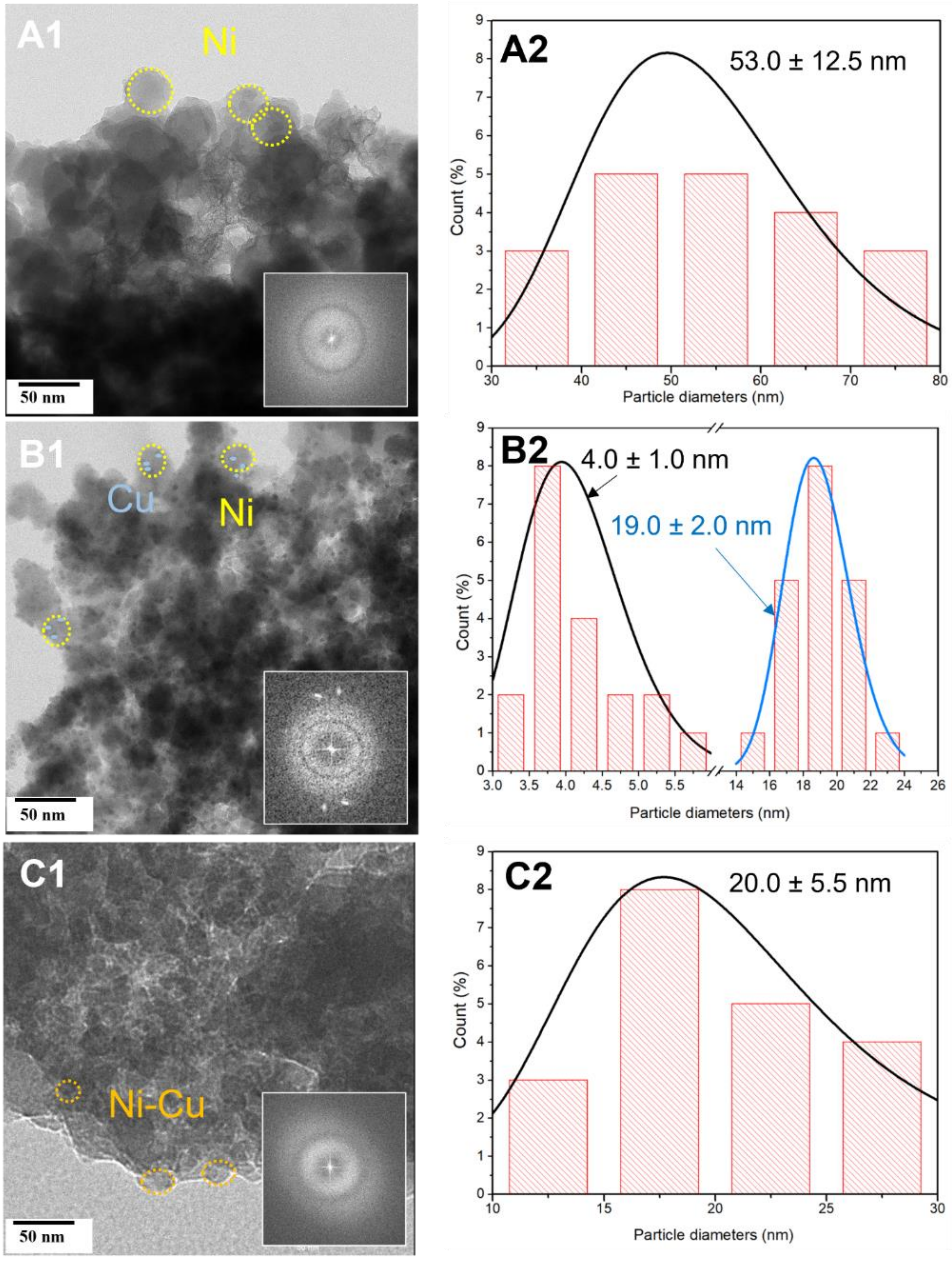

Figure 3. HRTEM images of (A1) the Ni NPs, (B1) Replacement reaction Ni-Cu NPs (*rep-R* Ni-Cu NPs) and (C1) co-reduced Ni-Cu NPs (*co-R* Ni-Cu NPs). The inserted: the selected area electron diffraction (SAED) pattern of (A1) the Ni NPs, (B1) the *rep-R* Ni-Cu NPs and (C1) the *co-R* Ni-Cu NPs. Particle-size distribution histogram of (A2) the Ni NPs, (B2) the *rep-R* Ni-Cu NPs and (C2) the *co-R* Ni-Cu NPs; the particle size was determined by measuring at least 20 random particles using ImageJ and the average value was reported.

5.4.2 Characterization of CMMRs

The prepared monometallic and bimetallic CMMRs were characterized in **Figure 4**. The FTIR spectra in **Figure 4A** shows the characteristic peaks in the range of 1100 – 1700 cm^{-1} for the pristine PES membrane [33]. The appearance of a peak at 3300 cm^{-1} for the PDA/PES membrane is assigned to -OH stretching vibration, due to the catechol groups in PDA [34]. Similarly, the Raman spectra of the PDA/PES membrane in **Figure 4B** shows the appearance of a peak at 1325 cm^{-1} for the catechol groups and a peak at 1574 cm^{-1} for the quinones due to the introduction of PDA. The formation of quinones can be attributed to the oxidation of catechol groups in PDA. As for the monometallic and bimetallic CMMRs, the reduced intensity of these characteristic peaks may be ascribed to the oxidation of hydroxyl groups in PDA during the reduction of metal precursors [35].

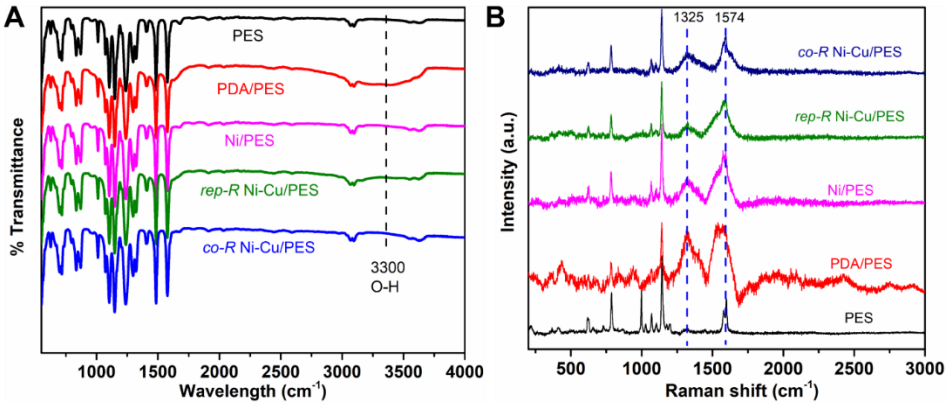

Figure 4. (A) FTIR spectra and (B) Raman spectra of the PES membrane, the PDA/PES membrane, the monometallic Ni/PES CMMR, the replacement reaction bimetallic CMMR (*rep-R* Ni-Cu/PES CMMR) and the co-reduced bimetallic CMMR (*co-R* Ni-Cu/PES CMMR).

XPS was used to identify the oxidation states of the bimetals on the *rep-R* Ni-Cu/PES CMMR and the *co-R* Ni-Cu/PES CMMR (**Figure 5)**.

For the *rep-R* Ni-Cu/PES CMMR (**Figure 5A1**): The high-resolution Ni $2p_{3/2}$ spectrum displays a peak at 856.4 eV for Ni^{2+}/Ni^{3+} , i.e., $Ni(OH)_2$ and NiOOH [15]. Moreover, the broad satellite peak centered at 862.5 eV (Ni $2p_{3/2}$ peak) confirmed the presence of Ni hydroxides. Cu $2p_{3/2}$ XPS spectrum for the *rep-R* Ni-Cu/PES CMMR (**Figure 5A2**) shows the primary peak can be divided into the Cu^0 peak at 932.4 eV and the Cu^{2+}(CuO) peak at 934.4 eV, along with the satellite peak of CuO at 943.2 eV [36]. The presence of both Cu^0 and Cu^{2+} indicates that charge redistribution between Ni and Cu atoms occurred during the fabrication of *rep-R* Ni-Cu/PES CMMRs.

For the *co-R* Ni-Cu/PES CMMR (**Figure 5B1-B2**): Similar peaks were observed for both the Ni $2p_{3/2}$ represented by the peak at 856.2 eV for Ni^{2+}, and for Cu $2p_{3/2}$ represented by the peaks at 932.8 eV for Cu^0/Cu^+ and 934.6 eV for Cu^{2+}(CuO).

Importantly, the *rep-R* Ni-Cu/PES CMMR showed a substantially greater amount of Cu^{2+} as compared to Cu^0, while the *co-R* Ni-Cu/PES CMMR had greater Cu^0 than Cu^{2+}, suggested that more electrons were shared and redistributed in the *rep-R* Ni-Cu bimetallic structures. The assumption of greater electron sharing leading to higher Cu^{2+} content is supported by previous research on a bimetallic Cu-Ag system [17].

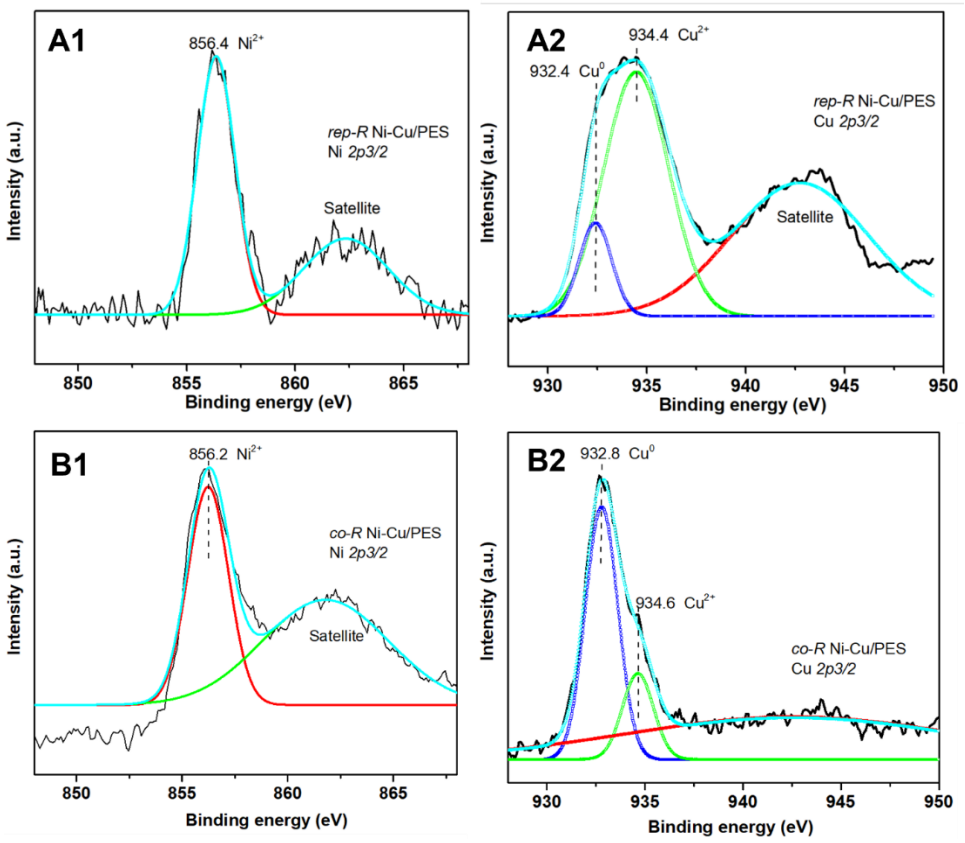

Figure 5. XPS spectra of (A1) Ni $2p_{3/2}$ and (A2) Cu $2p_{3/2}$ for the replacement reaction bimetallic CMMR (*rep-R* Ni-Cu/PES CMMR); XPS spectra of (B1) Ni $2p_{3/2}$ and (B2) Cu $2p_{3/2}$ for the co-reduced bimetallic CMMR (*co-R* Ni-Cu/PES CMMR).

5.4.3 Catalytic activity of CMMRs

The catalytic performance of the monometallic Ni CMMR and the bimetallic Ni-Cu CMMRs was investigated under different operating modes by a model reaction: the reduction of 4-nitrophenol (4-NP) to 4-aminophenol (4-AP) using $NaBH_4$ as a reducing agent (**Figure 6**).

The concentration profiles of 4-NP were measured as a function of time in batch operation (**Figure S5**), and from these trends the reaction rate constant was calculated using pseudo-first order kinetics (**Figure 6A**). As expected, the kinetic rate of conversion

of 4-NP decreased over time. In batch mode, the reaction rate constants within the first 15 min were calculated to be 0.0164 ±0.0053 min^{-1}, 0.0152±0.0047 min^{-1}, 0.0132 ±0.0025 min^{-1} for the *co-R* Ni-Cu/PES CMMR, the *rep-R* Ni-Cu/PES CMMR and the Ni/PES CMMR, respectively, showing that the bimetallic systems (*co*-R Ni-Cu/PES CMMR) achieved up to 24% greater conversion rate compared with the monometallic system. After the initial rapid conversion, the reaction rate was observed to slow substantially. The rate constants for each system decreased to 0.0073 ±0.0008 min^{-1} (45% decrease), 0.0068±0.0035 min^{-1} (45% decrease), 0.0062±0.0013 min^{-1} (47% decrease) for the *co-R* Ni-Cu/PES CMMR, the *rep-R* Ni-Cu/PES CMMR and the Ni/PES CMMR, respectively, over a 60 min timeframe. As such the bimetallic systems achieved up to 18% greater conversion rate than the monometallic systems over longer term operation. The inhibition of the reaction rate over time was probably ascribed to the saturation of the catalyst's surface by the degradation product 4-AP due to its slow desorption [37]. In batch reactions, the catalytic performance of CMMRs was limited by the large diffusion resistance of 4-NP towards the catalytic sites on the membranes. To address this mass transfer limitation, process-intensified reactions can be achieved by flowing reactants through the catalytic membrane micro-reactor. This flow-through configuration increases reactants' access to catalytic sites. **Figure 6B** shows the extraordinary increase in reaction rates in flow-through mode as compared to batch mode, with reaction rates calculated to be 725.03 min^{-1} for the *co-R* Ni-Cu/PES CMMRs, 247.73 min^{-1} for the *rep-R* Ni-Cu/PES CMMRs and 145.79 min^{-1} for the Ni/PES CMMRs. Accordingly, we obtained up to 99.5% of 4-NP conversion for the *co-R* Ni-Cu/PES CMMRs, 84.1 % for the *rep-R* Ni-Cu/PES CMMRs and 68.8 % for the Ni/PES CMMRs in flow-through mode

(**Figure 6C**). The flow-through mode achieves up to five orders of magnitude (10 000x) greater reaction rates and a 2-fold higher conversion degree of 4-NP as compared to batch reactors. The compressed concentration boundary layer thickness in flow-through mode reduced the distance over which mass transfer occurred, greatly increasing the rate at which reactants arrived at immobilized reaction sites enabling faster conversion of 4-NP to 4-AP. Such enhanced mass transfer in confined catalytic membrane microreactors contributed to the improved catalytic performance, similarly reported for noble metal systems in the literature [12, 38]. Therefore, we were able to achieve 30-fold higher contaminant processing capacity in flow-through mode as compared to batch mode (**Figure 6D**).

The bimetallic Ni-Cu CMMRs exhibited higher catalytic performance than the monometallic Ni CMMR in flow-through mode. Synergistic effects of geometric and electronic properties for bimetals contributed to the greater activity of bimetallic Ni-Cu CMMRs [12, 22, 23]. The formation of the specific geometry, such as the bimodal nanoparticle structure (*rep-R* Ni-Cu) and the nanoalloy structure (*co-R* Ni-Cu), promoted the use of both metals in the catalytic conversion of 4-NP. Furthermore, the change in electronic configuration for bimetals adjusted the binding energy of reactants as well as the reaction activation energy. The available surface area and the metal contents in monometallic and bimetallic CMMRs are presented in **Table S1**. The total mass of metal anchored onto the membranes was measured. 0.142 ± 0.001 mg Ni and 0.020 ± 0.004 mg Cu were anchored on the *co-R* Ni-Cu/PES CMMR, and 0.135 ± 0.001 mg Ni and 0.025 ± 0.005 mg Cu were immobilized on the *rep-R* Ni-Cu/PES CMMR, after identical amounts of $NiSO_4$ and $CuSO_4$ solution were flowed through identical PES membrane supports.

The *co-R* Ni-Cu/PES CMMR exhibited a 2.9-fold higher reaction rate constant and a 1.2-fold higher conversion % than the *rep-R* Ni-Cu/PES CMMR in flow-through mode, which cannot simply be attributed to the 5% greater nickel content. Rather, the three-fold higher surface area of the *co-R* Ni-Cu/PES CMMR as compared to the *rep-R* Ni-Cu/PES CMMR likely greatly contributed to its nearly 3-fold greater catalytic activity, since the active area of a catalyst's surface is directly proportional to its catalytic activity.

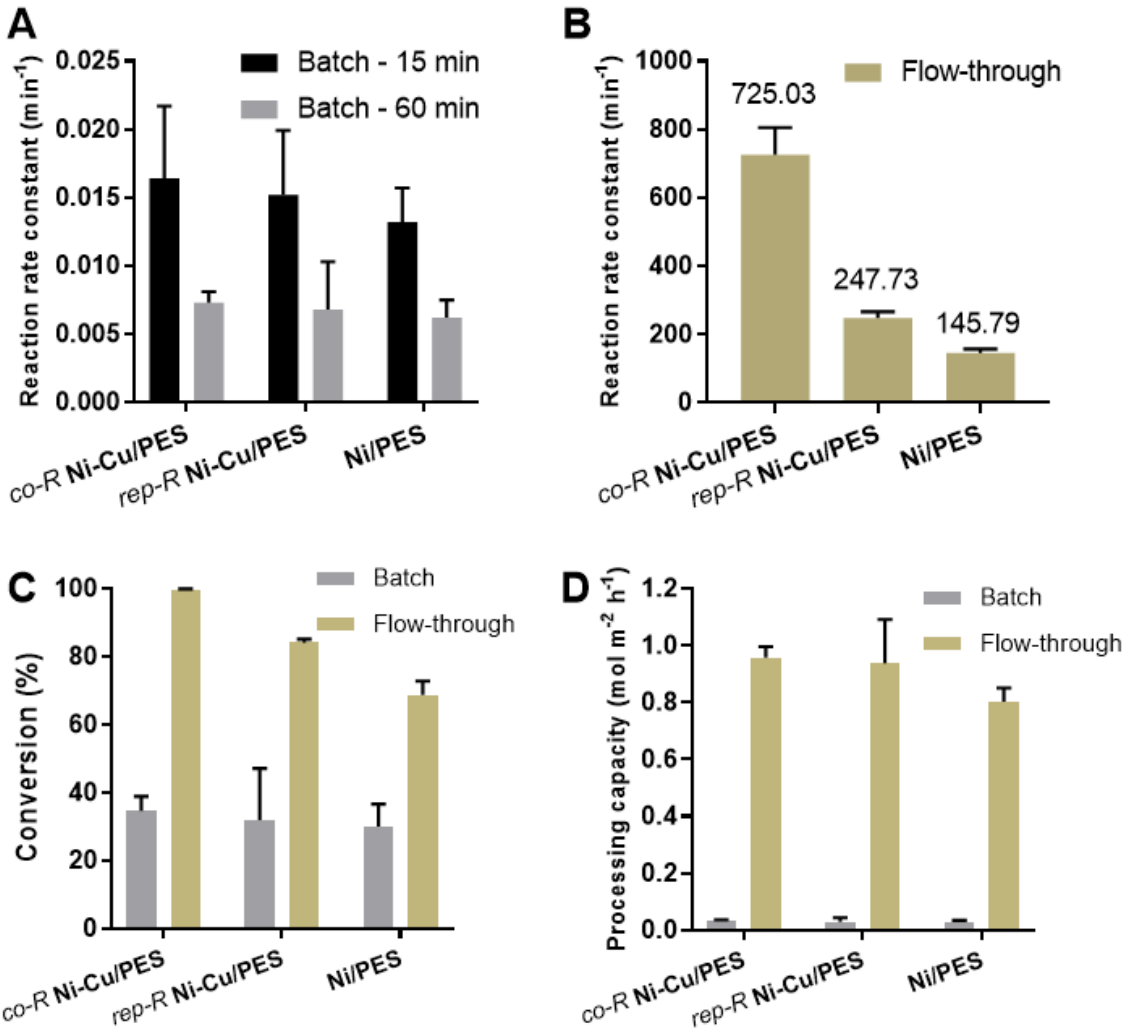

Figure 6. (A) The calculated rate constants in batch mode for different exposure times in the reaction of 4-NP exposed to the co-reduced bimetallic CMMR (*co-R* Ni-Cu/PES CMMR), the replacement reaction bimetallic CMMR (*rep-R* Ni-Cu/PES CMMR) and

monometallic CMMR (Ni/PES CMMR). (B) The calculated rate constants in flow-through mode for continuous reaction of 4-NP flowing through different CMMRs. (C) Comparison of 4-NP conversion degree using different CMMRs under batch and flow-through operation. (D) Comparison of 4-NP processing capacity using different CMMRs under batch and flow-through operation. Conditions: in batch mode the feed concentration was 50 mL 0.1 mM 4-NP and 2 mM $NaBH_4$, magnetic stir bar speed of 100 rpm and total catalytic reaction time of 60 min; in flow-through mode the feed concentration was 50 mL of 0.1 mM 4-NP and 2 mM $NaBH_4$, the applied pressure was 10 psi, and catalytic reaction time was 2 min.

5.4.4 Effect of operating parameters on the catalytic performance for CMMRs

The conversion of 4-NP to 4-AP using the *co-R* Ni-Cu/PES CMMR was further explored under different operating conditions (**Figure 7**). A 100 mL solution with varying 4-NP concentrations (i.e., 0.2 mM, 0.3 mM and 0.4 mM) was permeated through the *co-R* Ni-Cu/PES CMMR at 10 psi (0.689 bar). **Figure 7A** shows that nearly 100% conversion was reached when the 4-NP concentration was $\leq$ 0.3 mM. Using higher 4-NP concentrations of 0.4 mM resulted in an apparent decline in the conversion degree (72 %). The membrane flux linearly decreased for increasing 4-NP concentration from 905.1 $L \cdot m^{-2} \cdot h^{-1}$ at 0.2 mM to 845.7 $L \cdot m^{-2} \cdot h^{-1}$ at 0.4 mM, representing a 6.6 % decrease in flux over a doubling in 4-NP concentration. The corresponding reaction rate constants are presented in **Table S2.** We observed that the rate constant decreased with increasing 4-NP concentration, thus this heterogeneous catalytic reaction followed the Langmuir-Hinshelwood (L-H) mechanism where the reaction of two components occurs after adsorption of both molecules on the catalyst's surface. The L-H model to describe such adsorptive catalytic reaction is further supported in the literature [37, 39]. The optimized molar ratio of 4-NP to $NaBH_4$ was observed to be 0.3:25, which achieved >99 % conversion of 4-NP using the *co-R* Ni-Cu CMMR in flow-through mode. Additionally,

the influence of the flow rate throughout the catalytic process was also investigated (**Figure 7B**). Generally, higher pressures applied across the membrane resulted in the higher permeate flux and shorter contact time between reactants and the active sites. As expected, conversion decreased with greater applied pressure, such that 4-NP conversion decreased from 99.5 % at 10 psi (0.689 bar), to 74.4% at 15 psi (1.034 bar) and down to 67.8% at 20 psi (1.379 bar). Accordingly, the membrane flux increased with higher applied pressures, rising from 888.6 $L \cdot m^{-2} \cdot h^{-1}$ at 10 psi to 1308.1 $L \cdot m^{-2} \cdot h^{-1}$ at 15 psi (1.034 bar) and up to 1800.5 $L \cdot m^{-2} \cdot h^{-1}$ at 20 psi (1.379 bar). Recognizing the trade-offs between transmembrane water flux and catalytic conversion efficiency is critical for optimization in future practical applications of CMMRs.

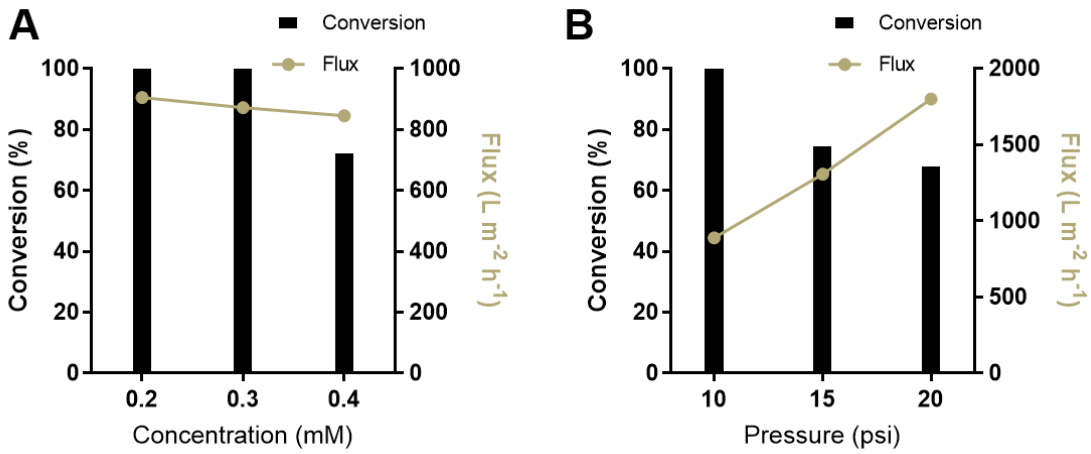

Figure 7. The effect of (A) 4-NP concentration and (B) flow rate on catalytic performance using the co-reduced bimetallic CMMR (*co-R* Ni-Cu CMMR) in flow-through mode. Conditions: (A) 100 mL of varying concentration of 4-NP and 25 mM $NaBH_4$ at the constant pressure of 10 psi; (B) 100 mL of 0.3 mM 4-NP and 25 mM $NaBH_4$ at varying applied pressure.

5.4.5 Durability of CMMRs

To evaluate the long-term stability of our bimtellatic CMMRs, continuous catalytic conversion of 4-NP was performed in flow-through mode. **Figure 8** shows the conversion degree of 99.9%, 86.8% and 81.7% after permeating 100 mL of 0.3 mM 4-NP through the *co-R* Ni-Cu/PES, *rep-R* Ni-Cu/PES and Ni/PES CMMRs, respectively. With further permeation and continuous catalytic conversion of 4-NP, a slight reduction (< 3%) in conversion degree was observed for all CMMRs. Specifically, after 500 mL of 4-NP solution was filtered, the conversion was reduced by 2%, 1.6% and 2.6% for the *co-R* Ni-Cu/PES, *rep-R* Ni-Cu/PES and Ni/PES CMMRs, respectively. Additionally, the leached metal content in the permeate was negligible (<5 % loss of metals) as measured by ICP-OES, suggesting that these non-noble metal CMMRs have promising long-term stability. The strong adhesion of the nanocatalysts on the CMMRs responsible for the minimal metal leaching may be due to the strong adhesion properties of the PDA used to bind the metal nanoparticle precursors to the membranes during CMMR fabrication as well as the tortuous structure of the supporting membrane pores [12]. Nevertheless, the slight loss of catalytic conversion efficiency over 500 mL of filtered solution is a concern and needs to be further investigated in order to continually improve the performance of CMMRs.

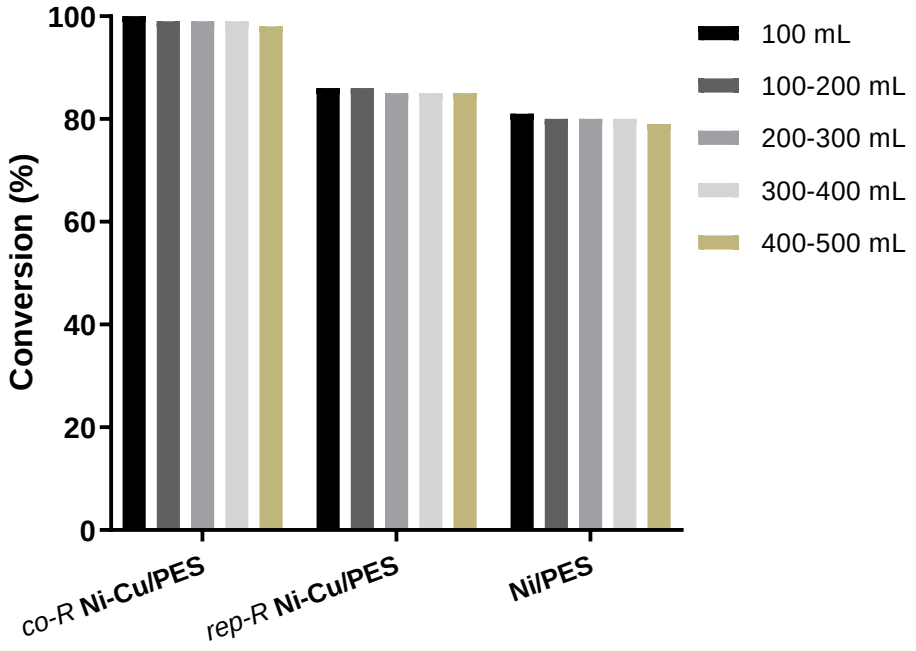

Figure 8. Durability of the co-reduced bimetallic CMMR (*co-R* Ni-Cu/PES CMMR), the replacement reaction bimetallic CMMR (*rep-R* Ni-Cu/PES CMMR) and monometallic CMMR (Ni/PES CMMR) for 4-NP conversion. Conditions: 500 mL of 0.3 mM 4-NP at 10 psi in flow-through mode.

5.4.6 Mechanisms of enhanced catalytic activity

A heterogeneous catalytic process involves adsorption, reaction and desorption of species at the catalyst's surface. In the case of 4-NP reduction on (bi)metal catalysts using $NaBH_4$ in **Figure 9**, both reactants – 4-NP and $NaBH_4$ – must adsorb on the catalyst's surface followed by the generation of H* radicals to reduce 4-NP. Understanding the catalytic process can help tailor the design of advanced CMMRs to achieve high activity. We discuss the mechanisms of bimetallic Ni-Cu CMMRs with respect to our findings during the 4-NP reduction process.

i. Bimetals configuration: The electronic configuration of Ni-Cu bimetals within the CMMRs facilitated reactant adsorption and subsequently enabled favourable redistribution of electron densities between the Ni-Cu bimetals and the adsorbed reactants such that bond cleavage was possible from the generated the intermediate species [40-42]. In addition, the introduction of the secondary metal (Cu) inhibited the growth and agglomeration of the initial metal (Ni), thereby increasing the availability of active sites for the heterogeneous catalytic process [43, 44].

ii. Strong metal-support interaction (SMSI) effect: PDA-supported noble metals have been reported to possess high catalytic activity due to the redistribution of electron density between PDA and the supported metal nanoparticles thereby increasing the magnitude of the reactants' adsorption energy, enabling stronger adsorption [45, 46]. We hypothesize that this PDA-supported noble metal interaction may also be applicable to PDA-supported transition metals, where electron migration from bimetals (Ni-Cu) toward PDA results in electrophilic Ni-Cu catalysts, as shown in this work. Such bimetallic catalysts as electron-acceptors would promote adsorption of negatively-charged reactants, such as BH_4^- and deprotonated 4-NP.

Overall, based on our experimental results we have elucidated the promoting effect of bimetals and PDA on supported non-noble metal catalysts. These non-noble metal catalyst systems offer great potential to design catalysts with controllable functionality and high activity at lower cost.

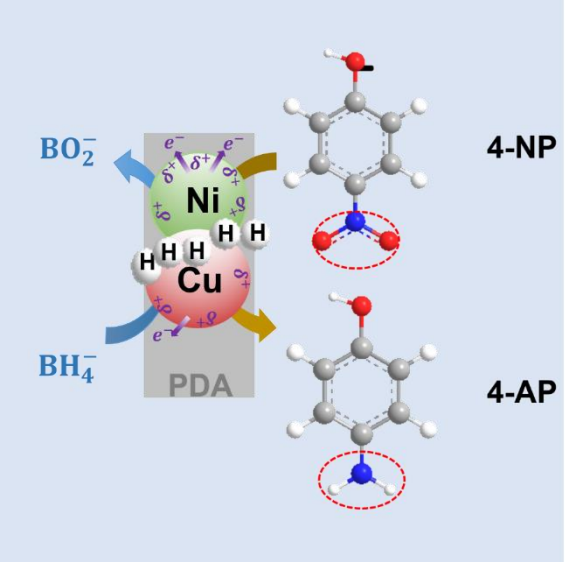

Figure 9. Schematic diagram of the electronic environments in the bimetallic catalytic conversion of 4-NP to 4-AP.

5.5 Conclusion

We have demonstrated the use of inexpensive metals to produce highly active catalytic membrane microreactors (CMMRs) synthesized through either sequential or successive immobilization of metal salts on PDA-modified porous PES ultrafiltration membranes. The interaction of the PDA-modified membrane and the metal salt precursors produced well-dispersed and strongly adhered bimetallic catalysts which provided high surface area for reaction and demonstrated minimal leaching during operation. We demonstrated that flowing contaminants through the porous bimetallic Ni-Cu/PES CMMRs remarkably enhanced mass transfer of contaminants to reaction sites, showing a four-order higher reaction rate constant and a 2-fold higher conversion degree for a model contaminant, 4-nitrophenol (4-NP) than in batch mode. We hypothesized that this unprecedented increase is due to the highly effective seeding of bimetallic nanoparticles throughout the porous

membrane structure, as well as the enhanced catalytic properties of the bimetallic nanoparticles. The bimetallic Ni-Cu/PES CMMRs exhibited higher catalytic activity than monometallic Ni/PES CMMR, as the bimetals formed smaller nanoparticles providing greater catalytic surface area for reaction as well as creating a favorable electrically reducing environment that could enhance organic degradation and 4-NP conversion. Therefore, non-noble, earth abundant Ni-Cu PES CMMRs were demonstrated to have impressive process-intensified abilities to degrade organic contaminants. Such intensive reactors could find many applications from treating recalcitrant contaminants in industrial wastewater to coupling chemical reactions and separations in the chemicals industry.

5.6 Acknowledgements

The authors thank the support of the Global Water Futures (GWF) research program provided through the Canada First Research Excellence Fund (CFREF, Sensors and Sensing Systems for Water Quality Monitoring) as well as the China Scholarship Council (CSC). The electron microscopy research described in this paper was performed at the Canadian Centre for Electron Microscopy (CCEM) at McMaster University, which is supported by the Natural Sciences and Engineering Research Council of Canada (NSERC, Discovery Grant) and other government agencies.

5.7 References

[1] N. Li, X. Lu, M. He, X. Duan, B. Yan, G. Chen, S. Wang, Catalytic membrane-based oxidation-filtration systems for organic wastewater purification: A review, J Hazard Mater 414 (2021) 125478. https://doi.org/10.1016/j.jhazmat.2021.125478.
[2] W. Qing, F. Liu, H. Yao, S. Sun, C. Chen, W. Zhang, Functional catalytic membrane development: A review of catalyst coating techniques, Adv Colloid Interface Sci 282 (2020) 102207. https://doi.org/10.1016/j.cis.2020.102207.
[3] C. Algieri, G. Coppola, D. Mukherjee, M.I. Shammas, V. Calabro, S. Curcio, S. Chakraborty, Catalytic Membrane Reactors: The Industrial Applications Perspective, Catalysts 11(6) (2021). https://doi.org/10.3390/catal11060691.

[4] X. Zhu, Z. Pan, H. Jiang, Y. Du, R. Chen, Hierarchical Pd/UiO-66-NH2-SiO2 nanofibrous catalytic membrane for highly efficient removal of p-nitrophenol, Sep. Purif. Technol 279 (2021). https://doi.org/10.1016/j.seppur.2021.119731.
[5] Z. Meng, H. Liu, Y. Liu, J. Zhang, S. Yu, F. Cui, N. Ren, J. Ma, Preparation and characterization of Pd/Fe bimetallic nanoparticles immobilized in PVDF·Al2O3 membrane for dechlorination of monochloroacetic acid, J. Membr. Sci 372(1-2) (2011) 165-171. https://doi.org/10.1016/j.memsci.2011.01.064.
[6] Z. Yan, J. Tian, K. Wang, K.D.P. Nigam, G. Luo, Microreaction processes for synthesis and utilization of epoxides: A review, Chemical Engineering Science 229 (2021). https://doi.org/10.1016/j.ces.2020.116071.
[7] M. Takht Ravanchi, T. Kaghazchi, A. Kargari, Application of membrane separation processes in petrochemical industry: a review, Desalination 235(1-3) (2009) 199-244. https://doi.org/10.1016/j.desal.2007.10.042.
[8] E. Drioli, L. Giorno, Biocatalytic membrane reactors: applications in biotechnology and the pharmaceutical industry, CRC Press2020.
[9] M. Liu, X. Zhu, R. Chen, Q. Liao, H. Feng, L. Li, Catalytic membrane microreactor with Pd/γ-Al 2 O 3 coated PDMS film modified by dopamine for hydrogenation of nitrobenzene, Chemical Engineering Journal 301 (2016) 35-41. https://doi.org/10.1016/j.cej.2016.04.116.
[10] V. Hakke, S. Sonawane, S. Anandan, S. Sonawane, M. Ashokkumar, Process Intensification Approach Using Microreactors for Synthesizing Nanomaterials-A Critical Review, Nanomaterials (Basel) 11(1) (2021). https://doi.org/10.3390/nano11010098.
[11] M.I. Domínguez, M.A. Centeno, M. Martínez T, L.F. Bobadilla, Ó.H. Laguna, J.A. Odriozola, Current scenario and prospects in manufacture strategies for glass, quartz, polymers and metallic microreactors: A comprehensive review, Chemical Engineering Research and Design 171 (2021) 13-35. https://doi.org/10.1016/j.cherd.2021.05.001.
[12] Y. Chen, S. Fan, B. Qiu, J. Chen, Z. Mai, Y. Wang, K. Bai, Z. Xiao, Cu-Ag Bimetallic Core-shell Nanoparticles in Pores of a Membrane Microreactor for Enhanced Synergistic Catalysis, ACS Appl Mater Interfaces 13(21) (2021) 24795-24803. https://doi.org/10.1021/acsami.1c04155.
[13] M. Nemanashi, R. Meijboom, Synthesis and characterization of Cu, Ag and Au dendrimer-encapsulated nanoparticles and their application in the reduction of 4-nitrophenol to 4-aminophenol, J Colloid Interface Sci 389(1) (2013) 260-7. https://doi.org/10.1016/j.jcis.2012.09.012.
[14] V. Raji, M. Chakraborty, P.A. Parikh, Catalytic Performance of Silica-Supported Silver Nanoparticles for Liquid-Phase Oxidation of Ethylbenzene, Ind. Eng. Chem. Res 51(16) (2012) 5691-5698. https://doi.org/10.1021/ie2027603.
[15] F. Yao, S. Liu, H. Cui, Y. Lv, Y. Zhang, P. Liu, F. Hao, W. Xiong, H.a. Luo, Activated Carbon Supported Non-noble Bimetallic Ni-Based Catalysts for Nitrocyclohexane Hydrogenation to Cyclohexanone Oxime under Mild Conditions, ACS Sustainable Chemistry & Engineering 9(8) (2021) 3300-3315. https://doi.org/10.1021/acssuschemeng.0c09168.
[16] N. Berahim, W. Basirun, B. Leo, M. Johan, Synthesis of Bimetallic Gold-Silver (Au-Ag) Nanoparticles for the Catalytic Reduction of 4-Nitrophenol to 4-Aminophenol, Catalysts 8(10) (2018). https://doi.org/10.3390/catal8100412.
[17] Y.Y. Li Sip, D.W. Fox, L.R. Shultz, M. Davy, H.-S. Chung, D.-X. Antony, Y. Jung, T. Jurca, L. Zhai, Cu–Ag Alloy Nanoparticles in Hydrogel Nanofibers for the Catalytic Reduction of Organic Compounds, ACS Applied Nano Materials 4(6) (2021) 6045-6056. https://doi.org/10.1021/acsanm.1c00881.
[18] L. Liu, R. Chen, W. Liu, J. Wu, D. Gao, Catalytic reduction of 4-nitrophenol over Ni-Pd nanodimers supported on nitrogen-doped reduced graphene oxide, J Hazard Mater 320 (2016) 96-104. https://doi.org/10.1016/j.jhazmat.2016.08.019.

[19] A. Areeb, T. Yousaf, M. Murtaza, M. Zahra, M.I. Zafar, A. Waseem, Green photocatalyst Cu/NiO doped zirconia for the removal of environmental pollutants, Materials Today Communications 28 (2021). https://doi.org/10.1016/j.mtcomm.2021.102678.
[20] J. Bian, M. Xiao, S.J. Wang, Y.X. Lu, Y.Z. Meng, Graphite oxide as a novel host material of catalytically active Cu–Ni bimetallic nanoparticles, Catalysis Communications 10(11) (2009) 1529-1533. https://doi.org/10.1016/j.catcom.2009.04.009.
[21] M.S. Islam, M.W. Khan, A highly effective green catalyst Ni/Cu bimetallic nanoparticles supported by dendritic ligand for chemoselective oxidation and reduction reaction, Chemical Papers 75(6) (2021) 2353-2369. https://doi.org/10.1007/s11696-020-01480-z.
[22] M. Ismail, M.I. Khan, S.B. Khan, M.A. Khan, K. Akhtar, A.M. Asiri, Green synthesis of plant supported Cu Ag and Cu Ni bimetallic nanoparticles in the reduction of nitrophenols and organic dyes for water treatment, Journal of Molecular Liquids 260 (2018) 78-91. https://doi.org/10.1016/j.molliq.2018.03.058.
[23] K.G.N. Quiton, M.C. Lu, Y.H. Huang, Synthesis and catalytic utilization of bimetallic systems for wastewater remediation: A review, Chemosphere 262 (2021) 128371. https://doi.org/10.1016/j.chemosphere.2020.128371.
[24] Y. Liu, Y. Zheng, B. Du, R.R. Nasaruddin, T. Chen, J. Xie, Golden Carbon Nanotube Membrane for Continuous Flow Catalysis, Ind. Eng. Chem. Res 56(11) (2017) 2999-3007. https://doi.org/10.1021/acs.iecr.7b00357.
[25] C. Wang, Y. Wu, J. Lu, J. Zhao, J. Cui, X. Wu, Y. Yan, P. Huo, Bioinspired Synthesis of Photocatalytic Nanocomposite Membranes Based on Synergy of Au-TiO2 and Polydopamine for Degradation of Tetracycline under Visible Light, ACS Appl Mater Interfaces 9(28) (2017) 23687-23697. https://doi.org/10.1021/acsami.7b04902.
[26] N. Eom, M.E. Messing, J. Johansson, K. Deppert, General Trends in Core-Shell Preferences for Bimetallic Nanoparticles, ACS Nano 15(5) (2021) 8883-8895. https://doi.org/10.1021/acsnano.1c01500.
[27] A. Alkhouzaam, H. Qiblawey, Novel polysulfone ultrafiltration membranes incorporating polydopamine functionalized graphene oxide with enhanced flux and fouling resistance, J. Membr. Sci 620 (2021). https://doi.org/10.1016/j.memsci.2020.118900.
[28] R. Li, Y. Wu, L. Shen, J. Chen, H. Lin, A novel strategy to develop antifouling and antibacterial conductive Cu/polydopamine/polyvinylidene fluoride membranes for water treatment, J Colloid Interface Sci 531 (2018) 493-501. https://doi.org/10.1016/j.jcis.2018.07.090.
[29] L. Shao, Z.X. Wang, Y.L. Zhang, Z.X. Jiang, Y.Y. Liu, A facile strategy to enhance PVDF ultrafiltration membrane performance via self-polymerized polydopamine followed by hydrolysis of ammonium fluotitanate, J. Membr. Sci 461 (2014) 10-21. https://doi.org/10.1016/j.memsci.2014.03.006.
[30] Z. Yan, Y. Zhang, H. Yang, G. Fan, A. Ding, H. Liang, G. Li, N. Ren, B. Van der Bruggen, Mussel-inspired polydopamine modification of polymeric membranes for the application of water and wastewater treatment: A review, Chemical Engineering Research and Design 157 (2020) 195-214. https://doi.org/10.1016/j.cherd.2020.03.011.
[31] M. López-Viveros, I. Favier, M. Gómez, J.-F. Lahitte, J.-C. Remigy, Remarkable catalytic activity of polymeric membranes containing gel-trapped palladium nanoparticles for hydrogenation reactions, Catalysis Today 364 (2021) 263-269.
[32] J.M. Luque-Alled, A. Abdel-Karim, M. Alberto, S. Leaper, M. Perez-Page, K. Huang, A. Vijayaraghavan, A.S. El-Kalliny, S.M. Holmes, P. Gorgojo, Polyethersulfone membranes: From ultrafiltration to nanofiltration via the incorporation of APTS functionalized-graphene oxide, Sep. Purif. Technol 230 (2020). https://doi.org/10.1016/j.seppur.2019.115836.
[33] A. Abdel-Karim, S. Leaper, M. Alberto, A. Vijayaraghavan, X. Fan, S.M. Holmes, E.R. Souaya, M.I. Badawy, P. Gorgojo, High flux and fouling resistant flat sheet polyethersulfone membranes incorporated with graphene oxide for ultrafiltration applications, Chemical Engineering Journal 334 (2018) 789-799. https://doi.org/10.1016/j.cej.2017.10.069.

[34] J. Xing, Q. Wang, T. He, Z. Zhou, D. Chen, X. Yi, Z. Wang, R. Wang, G. Tan, P. Yu, C. Ning, Polydopamine-Assisted Immobilization of Copper Ions onto Hemodialysis Membranes for Antimicrobial, ACS Applied Bio Materials 1(5) (2018) 1236-1243. https://doi.org/10.1021/acsabm.8b00106.
[35] F. Mahnaz, M. Mostafa-Al-Momin, M. Rubel, M. Ferdous, M.S. Azam, Mussel-inspired immobilization of Au on bare and graphene-wrapped Ni nanoparticles toward highly efficient and easily recyclable catalysts, RSC Advances 9(52) (2019) 30358-30369. https://doi.org/10.1039/c9ra05736f.
[36] G. Mayakrishnan, V. Elayappan, I.S. Kim, I.M. Chung, Sea-Island-Like Morphology of CuNi Bimetallic Nanoparticles Uniformly Anchored on Single Layer Graphene Oxide as a Highly Efficient and Noble-Metal-Free Catalyst for Cyanation of Aryl Halides, Sci Rep 10(1) (2020) 677. https://doi.org/10.1038/s41598-020-57483-z.
[37] P. Suchomel, L. Kvitek, R. Prucek, A. Panacek, A. Halder, S. Vajda, R. Zboril, Simple size-controlled synthesis of Au nanoparticles and their size-dependent catalytic activity, Sci Rep 8(1) (2018) 4589. https://doi.org/10.1038/s41598-018-22976-5.
[38] Y. Chen, Z. Mai, S. Fan, Y. Wang, B. Qiu, Y. Wang, J. Chen, Z. Xiao, Synergistic enhanced catalysis of micro-reactor with nano MnO2/ZIF-8 immobilized in membrane pores by flowing synthesis, J. Membr. Sci 628 (2021). https://doi.org/10.1016/j.memsci.2021.119233.
[39] R.K. Narayanan, S.J. Devaki, Brawny Silver-Hydrogel Based Nanocatalyst for Reduction of Nitrophenols: Studies on Kinetics and Mechanism, Ind. Eng. Chem. Res 54(4) (2015) 1197-1203. https://doi.org/10.1021/ie5038352.
[40] F.F. Tao, Synthesis, catalysis, surface chemistry and structure of bimetallic nanocatalysts, Chem Soc Rev 41(24) (2012) 7977-9. https://doi.org/10.1039/c2cs90093a.
[41] Y. Han, Y. Wang, T. Ma, W. Li, J. Zhang, M. Zhang, Mechanistic understanding of Cu-based bimetallic catalysts, Frontiers of Chemical Science and Engineering 14(5) (2020) 689-748. https://doi.org/10.1007/s11705-019-1902-4.
[42] <recent Developments in Palladium-Based Bimetallic.pdf>. https://doi.org/10.1002/cctc.v7.14/issuetoc.
[43] A. Alshammari, V. Kalevaru, A. Martin, Bimetallic Catalysts Containing Gold and Palladium for Environmentally Important Reactions, Catalysts 6(7) (2016). https://doi.org/10.3390/catal6070097.
[44] Y.-T. Pan, H. Yang, Design of bimetallic catalysts and electrocatalysts through the control of reactive environments, Nano Today 31 (2020). https://doi.org/10.1016/j.nantod.2019.100832.
[45] M. Zhang, G. Li, X. Sun, Y. Jiang, X. Zhang, General promoting effect of polydopamine on supported noble metal catalysts, J. Mater. Chem. A 5(39) (2017) 20789-20796. https://doi.org/10.1039/c7ta06204d.
[46] Z. Wang, Y. Zou, Y. Li, Y. Cheng, Metal-Containing Polydopamine Nanomaterials: Catalysis, Energy, and Theranostics, Small 16(18) (2020) e1907042. https://doi.org/10.1002/smll.201907042.

Chapter 6

Electrochemical reductive dechlorination of 2-chlorophenol in a Ni-P ultrafiltration membrane reactor

6.1 Abstract

Transition-metal phosphides (TMPs) are emerging electrocatalysts for both hydrogen evolution and the conversion of reactants/contaminants by various electrochemical reactions. TMPs are promising catalysts because they are earth abundant, have high electrical conductivity, and high chemical stability. In this seminal work, a noble metal-free nickel phosphorous (Ni-P) ultrafiltration membrane was fabricated and used for electrochemical reductive dechlorination of chlorophenols. Amorphous Ni-P nanoparticles were grown on an ultrafiltration polyethersulfone (PES) membrane *via* electroless deposition. The prepared Ni-P membrane was used as a cathode for electrochemical reductive dechlorination of 2-chlorophenol (2-CP) in flow-through mode. It was observed that a dechlorination efficiency of 42.7%, a reaction rate constant of 1.621 min^{-1} and a Faradaic efficiency of 24.5% were achieved at an optimized cathodic potential of -2.50 V. The high dechlorination was primarily attributed to the partial positively charged $Ni^{\delta+}$ on the Ni-P membrane surface which facilitated atomic H* evolution by forming reactive Ni-H* bonds for dechlorination. Additionally, doping P atoms in Ni retarded the deactivation of electrocatalytic Ni sites. This work demonstrates that the cost-effective Ni-P membrane electrocatalyst is a promising technology to degrade chlorinated compounds with applications to industrial wastewaters and landfill leachates.

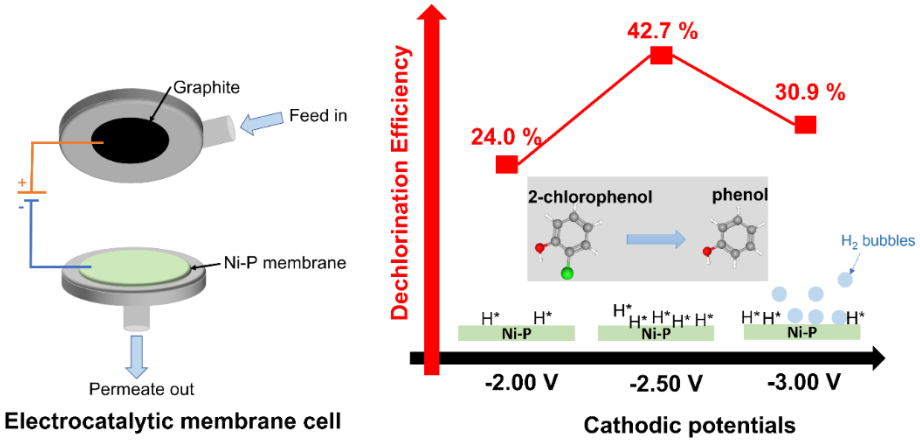

6.2. Introduction

Chlorophenols (CPs) are extensively used in the paper and textile industry [1], and predominantly include organochlorides of phenols, such as mono-chlorophenols (i.e., 2-chlorophenol, 3-chlorophenol and 4-chlorophenol) and poly-chlorophenols (i.e., 2,4-dichlorophenol and 2,3,4-trichlorophenol). CPs have been classified as priority pollutants by the United States Environmental Protection Agency [2], due to their hazard to human nervous and respiratory systems, their mutagenic and carcinogenic characteristics even at trace levels, and their persistence in eco-systems [3, 4]. The toxicity of CPs mainly originates from the chlorine moieties [5]; therefore, dechlorination of CPs during wastewater treatment is a high priority.

Various methods have been explored for dechlorination of CPs. Biological degradation is limited due to the strong resistance of chlorine bonds to biodegradation. Advanced oxidation processes (AOP) such as photo-oxidation and chemical oxidation have been investigated as high-efficiency processes for the dechlorination of CPs [6-8], however, during these oxidation reactions CPs can be uncontrollably converted to more toxic

intermediates/byproducts. Reductive hydro-dechlorination [9-12], especially electrochemical reductive dechlorination, is a promising approach to treating chlorophenol-contaminated waters due to the controllable product formation through electrical potential selection, the absence of chemical reagents used, and the comparative ease of operation.

Noble metals (i.e., Pd and Pt) are ideal electrocatalysts, with high activity for water splitting and generation of atomic H* [13-15]. Unfortunately, the low abundance of noble metals, and thus their high costs, limits their practical use in wastewater treatment. Therefore, the development of noble metal-free electrocatalysts for electrochemical reductive dechlorination is needed.

Transition-metal phosphides (TMPs) are emerging electrocatalysts for electrochemical reduction, with the advantages of high electrical conductivity, high chemical stability and natural abundance[16-19]. To date, six types of TMPs, Ni-, Co-, Fe-, Mo, W-, and Cu-based phosphides, have demonstrated high activity for hydrogen atom evolution, attributed to proton-acceptor phosphorous sites and hydride-acceptor metal sites on TMPs [17]. For example, amorphous Ni_2P nanoparticles supported on nickel foam as a non-noble metal cathode was prepared for dechlorination of trichloroacetic acid (0.5 ppm, 150 mL) in an electrochemical cathode cell, showing a removal efficiency of 94.3% and a pseudo-first-order kinetic reaction rate of 0.0283 min^{-1} at a cathodic potential of -1.2 V vs. saturated calomel electrode (SCE) [20]. Similarly, Liu *et al*. reported a cobalt-phosphorous/oxide (Co-P/O) composite cathode for reductive dechlorination of florfenicol (20 ppm, 30 mL) in a dual-chamber reactor, with a dechlorination efficiency

of 91% at -1.2 V vs. SCE [21]. Specifically, the chlorinated compound (florfenicol) was quickly trapped by electrocatalytic sites due to the formation of Co-Cl bonds between the Co-P/O composite electrode and florfenicol, resulting in the weakened strength of the C-Cl bond in florfenicol. As such, the statistical likelihood of the C-Cl bond cleavage in the presence of atomic H* increased, enabling highly efficient reductive dechlorination. Despite a few investigations on electrochemical reductive dechlorination of chlorine substitutes on aliphatic chains, (i.e., trichloroacetic acid and florfenicol), the dechlorination performance of TMPs on chlorophenols (chlorine substitutes on aromatic rings) has not been studied.

The use of dense electrodes for dechlorination has been widely performed in electrocatalytic reactors (ECRs), however, the mass transfer by diffusion towards active sites in the batch configuration causes low reactors' processing capacity and limits the ability for scale-up wastewater treatment [22]. Additional operations such as continuous agitation are required in ECRs to address this issue, which in turn increases the overall operational costs. Alternatively, a porous membrane electrode can be used to improve the mass transfer in electrocatalytic membrane reactors (ECMRs) through filtering reactants/contaminants through electrocatalytic membranes [23, 24]. The membrane anode/cathode possesses the dual functions of being both filters towards microscopic contaminants and electrodes for *in-situ* flow-through electrolysis [22, 24-27]. By coupling electrochemical degradations with membrane filtration, ECMRs enable process intensification in wastewater treatment while degrading difficult to treat priority

pollutants; however, there is little research regarding the use of TMPs-modified membranes for electrochemical reductive dechlorination.

In this study, an inexpensive Ni-P membrane was developed *via* electroless deposition and then used for electrochemical reductive dechlorination of 2-chlorophenol (2-CP). Inspired by the adhesive nature of dopamine, instability of metal nanoparticles on polymeric membranes was addressed by using a polydopamine (PDA)-modified membrane surface, which provided a versatile platform for metal immobilization *via* coordination bonds [28]. Electrocatalytic Ni-P membranes were prepared by immobilizing Pd seeds on PDA-modified polyether sulfone (PES) ultrafiltration (UF) membranes, and then growing Ni-P nanoparticles under different durations. We optimized the measured surface conductivity with membrane permeance of the prepared Ni-P membranes by controlling Ni-P nanoparticle growth time in the electroless deposition process. The capability of electrochemical reductive dechlorination of 2-CP using Ni-P membranes was explored by cyclic voltammetry (CV). Further, the effect of varying cathodic potentials on the performance of electrochemical reductive dechlorination was investigated, and some possible mechanisms of degradation were proposed. Additionally, morphology, wettability, crystalline structure and electronic environments of the Ni-P membrane surface were characterized by SEM, contact angle measurements, XRD and XPS, respectively.

6.3. Experimental and materials

6.3.1 Materials

Tris (hydroxymethyl) aminomethane hydrochloride ($NH_2C(CH_2OH)_3 \cdot HCl$) (i.e., Tris HCl), dopamine hydrochloride, sodium hydroxide (NaOH, 1 M), palladium chloride ($PdCl_2$), nickel sulfate ($NiSO_4$), trisodium citrate (CH_2Na_3), ammonium chloride (NH_3Cl), sodium hypophosphite (NaH_2PO_2), ammonia ($NH_3 \cdot H_2O$), 2-chlorophenol (2-CP), and sodium sulfate (Na_2SO_4) were purchased from Sigma-Aldrich (USA). Polyethersulfone (PES) porous membranes (pore size: 0.03 µm, diameter: 47 mm, thickness: 100-150 µm) were obtained from Sterlitech (USA). All solutions were prepared in distilled (DI) water.

6.3.2 Membrane fabrication

Electrocatalytic Ni-P membranes were developed *via* electroless deposition, shown in **Figure 1**. Tris-HCl solution (1.575 mg/mL) was prepared and its pH was adjusted to 8.5 using NaOH. Then 200 mg of dopamine was dissolved in Tris-HCl solution (100 mL) to obtain alkaline dopamine solution (2 mg/mL). A pristine PES membrane was dipped into the prepared dopamine solution at 60ºC for 24 h, during which polydopamine (PDA) was gradually formed on the membrane surface by the self-polymerization of dopamine. Subsequently, the PDA-modified membrane was rinsed with water to remove excess dopamine and unattached PDA. Subsequently, a Pd-precursor was introduced by immersing the PDA-modified membrane into a $PdCl_2$ solution (1 g/L, 2 mL) for 30 min, followed by Pd seed formation in the presence of $NaBH_4$ (5.33 g/L, 2 mL). The coordination bonds between Pd seeds and catechol groups in PDA accounted for the firm adhesion of Pd seeds. As-prepared Pd-immobilized membranes were dipped into an

electroless plating nickel bath (32 g/L $NiSO_4$, 20 g/L $C_6H_5Na_3O_7 \cdot 2H_2O$, 25 g/L NH_3Cl, 28 g/L NaH_2PO_2, pH was adjusted to 9 by $NH_3 \cdot H_2O$, temperature = 45 ºC) [29, 30]. Pd seeds initiated the deposition of Ni-P nanoparticles and then Ni-P nanoparticles continued to grow on the membrane surface (**eq. 1**). Ni-P membranes coated for 1 min, 2 min, 3 min and 4 min were prepared, and they were stored in DI water for further analysis.

$$Ni^{2+} + 2H_2PO_2^- + 2OH^- \rightarrow Ni + 2H_2PO_3^- + H_2 \quad (1)$$

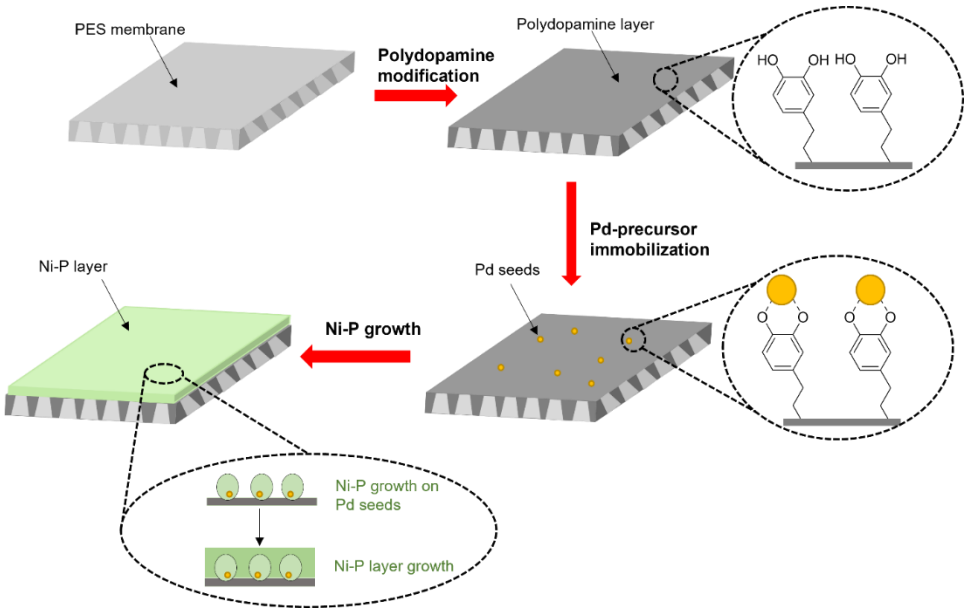

Figure 1. Schematic diagram of Ni-P membranes preparation.

6.3.3 Characterization

Electrical conductivity of Ni-P membranes was tested by a four-point probe (Ossila). Pure water flux of Ni-P membranes was determined by measuring permeate flux at varying pressures in a dead-end filtration cell (Sterlitech) after membrane compression.

The morphology of Ni-P membranes was characterized by scanning electron microscopy (SEM, JEOL JSM-7000F) with an accelerating voltage of 5 kV. The cross-sectional area of Ni-P membranes was obtained by cracking them in liquid nitrogen. Before imaging, the targeted area of Ni-P membranes was coated with a 10 nm gold layer for SEM analysis and coated with a 10 nm carbon layer for elemental distribution by energy-dispersive spectrometers (EDS, X-Maxn). The Ni-P nanoparticles on the membrane was also characterized by transmission electron microscopy (TEM, Talos 200X). The surface of the Ni-P membranes was scraped followed by sonication in ethanol, and the suspension was drop-casted onto a TEM grid and dried under ambient conditions for TEM characterization. The wettability of PES membranes and Ni-P membranes was measured by contact angle measurements using an optical contact angle device (OCA 35). X-ray diffraction (XRD) patterns of PES membranes and Ni-P membranes were demonstrated by an X-ray diffractometer (Davinci.Design) with Cu radiation in the 2θ range of 35º - 80º. The electronic environment of Ni-P membranes was determined by X-ray photoelectron spectroscopy (XPS, PHI Quantera II).

Cyclic voltammetry (CV) was carried out in a two-electrode filtration system (**Figure S1**) using a potentiostat (Autolab PGSTAT 302 N), with the Ni-P membrane as the working electrode (WE) and graphite as the counter electrode (CE) in an electrolyte of 50 mM Na_2SO_4 and 10 ppm 2-CP. CV scans were performed at 50 mV/s with a starting cell potential of 0 V and a final cell potential of -3 V. Additionally, the relation between cell potentials and potentials vs. Ag/AgCl was established by CV scans in a typical three-

electrode electrochemical cell with using a Ag/AgCl electrode as the reference electrode (RE).

6.3.4 Experimental procedures

Electrochemical reductive dechlorination was performed in a customized two-electrode flow-through cell (**Figure S1**) with an effective area of 3.14 cm^2. A feed of 10 ppm 2-CP and 50 mM Na_2SO_4 was filtered through the Ni-P membrane by nitrogen gas flow. Simultaneously, varying cathodic potentials (i.e., 0 V, -2.00 V, -2.25 V, -2.50 V, -2.75 V and -3.00 V) were applied to the Ni-P membrane for 90 min by chronoamperometry using a potentiostat. All the experiments were repeated in duplicate. The permeate was collected at a predetermined duration, and then determined by gas chromatography/mass spectrometry (GC/MS, Agilent 5973).

6.3.5 Analytical methods and data analysis

The electrochemical reductive dechlorination efficiency of Ni-P membranes is defined as:

$$\eta = (1 - \frac{C_P}{C_F}) \times 100\% \quad (2)$$

where η is the removal (%); C_F is the initial 2-CP concentration (ppm) in the feed, and C_P is the 2-CP concentration (ppm) in the permeate.

The electrochemical reductive dechlorination process is fitted by Pseudo-first-order kinetics [31], where concentration decreases over time exponentially (**eq 3**).

$$\ln \frac{C_P}{C_F} = -kt \quad (3)$$

where k is the reaction rate constant (min^{-1}), and t is the effective reaction time (min).

The Faradaic efficiency (FE, %) is defined as the ratio of electrons for dechlorination of 2-CP to total electrons transferred in the external circuit [32-34], calculated by **eq 4**.

$$FE = \frac{(C_F - C_P)}{1000 \times M \times \int_0^t Idt} nVF \times 100\% \quad (4)$$

where n is the number of electron transfer for dechlorination, n = 2; V (L) is effective electrolyte volume; F is Faradic constant, F = 96485 C/mol; I (A) is the current; t (s) is the reaction time; M (= 128.56 mol/g) is the relative molecular weight of 2-CP.

6.4. Results and discussion

6.4.1 Resistivity and permeance

Ni-P membranes were developed by electrolessly-coating Ni-P nanoparticles on ultrafiltration PES membranes. Surface resistivity and transmembrane flux (and permeance) of electrically conductive membranes (ECMs) are a function of coating layer thickness [35, 36]. Since the duration of electroless coating is directly proportional to the Ni-P layer thickness, resistivity and permeance of Ni-P membranes were demonstrated under varying periods of electroless coating.

Figure 2 shows a decreasing resistivity for greater electroless coating duration, specifically resistivities of 50.2 ± 1.96 ohm/sq, 18.5 ± 2.1 ohm/sq, 4.5 ± 0.7 ohm/sq, and 2.5 ± 0.6 ohm/sq for 1, 2, 3, and 4 min of Ni-P coating, respectively. The lower surface resistivity with longer coating time was attributed to the higher coverage of conductive Ni-P nanoparticles. Conversely, membrane permeance decreased with greater electroless

coating duration of Ni-P coating, exhibiting 920 ± 40 LMH/bar, 381.4 ± 58.6 LMH/bar, 134.7 ± 22.9 LMH/bar, and 101.2 ± 12.3 LMH/bar for 1, 2, 3, and 4 min coating respectively. The relation between surface resistivity, permeance and coating time was observed, as reported for different types of ECMs [36].

Lower resistivity leads to greater electrochemical reactivity and higher energy efficiency, while lower permeability increases the residence time and thereby increases the removal degree of contaminants at the expense of lower processing capacity. Taking the removal degree-processing capacity tradeoff into account, electrocatalytic membranes benefit from lower resistivity while maximizing higher permeance. Therefore, the PES membrane with 2 min of Ni-P coating was used for electrochemical reductive dechlorination in all subsequent experiments.

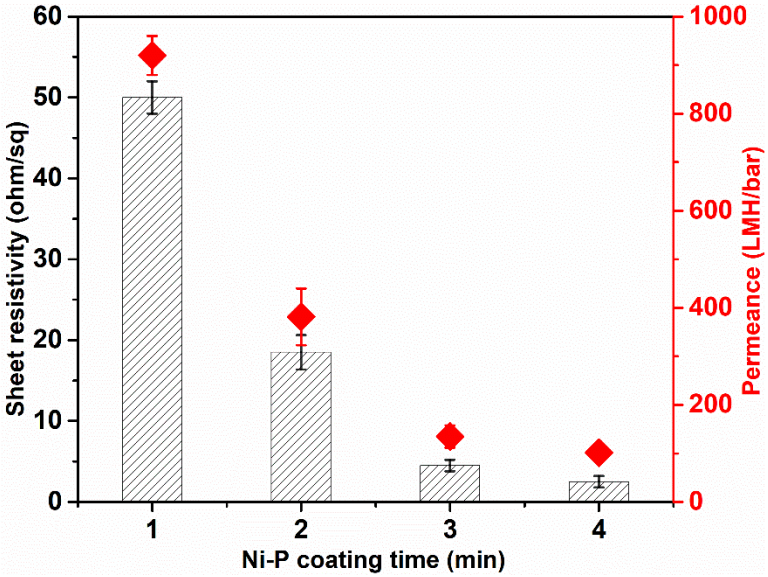

Figure 2. Electrical conductivity and permeance of Ni-P membranes under varying duration of electroless coating. (Error bar represents standard deviation, n = 10 for resistivity and n = 3 for permeance measurements).

6.4.2 Membrane characterization

The morphology, elemental distribution, wettability, the crystalline structure, and chemical states of Ni-P membranes were characterized by SEM, EDS, contact angle, XRD and XPS, respectively.

6.4.2.1 Surface Morphology

The morphology, elemental distribution, wettability, the crystalline structure, and chemical states of Ni-P membranes were characterized by SEM, EDS, contact angle, XRD and XPS, respectively.

The morphology of Ni-P membranes was visualized by SEM (**Figure 3**). PES membranes showed a typical porous structure (**Figure S2**), while the pore sizes were reduced after Ni-P nanoparticles were deposited on the PES membranes (**Figure 3A-D**). We observed that the as-prepared Ni-P membranes possessed an increasing coverage of Ni-P nanoparticles with a longer coating time. The elemental distribution of Ni-P membranes with 2 min of coating was further analyzed by EDS mappings. As shown in the top surface in **Figure 3B-1**, the elements of Ni and P were observed to be uniformly distributed indicating an evenly formed Ni-P layer, while the presence of O, C and S was ascribed to the polyethersulfone (PES) substrate. According to a qualitative EDS spectrum in **Figure S3,** the top surface of Ni-P membranes possessed a weight percent of 81.0% for Ni and a weight percent of 10.3% for P, in accordance with previously reported phosphorous content, which have been measured to be less than 15% using electroless deposition [37, 38]. **Figure 3B-2** shows that conductive Ni-P nanoparticles mainly existed on the membrane surface, with a thickness of 2.5 μm after 2 min of Ni-P

coating on the PES membranes (**Figure S4**). Additionally, a small proportion of the Ni-P nanoparticles penetrated a few microns into the membrane matrix, likely due to the strong adhesion between the conductive Ni-P layer and the polydopamine-modified PES surfaces; a similar phenomenon was reported by Wessling *et al* [30]. This hypothesis was supported by SEM images before and after electrochemical treatment; the conductive Ni-P layer on the PES membrane did not show any delamination or detachment after electrochemical reductive dechlorination at -3 V for 1.5 h (**Figure S5**).

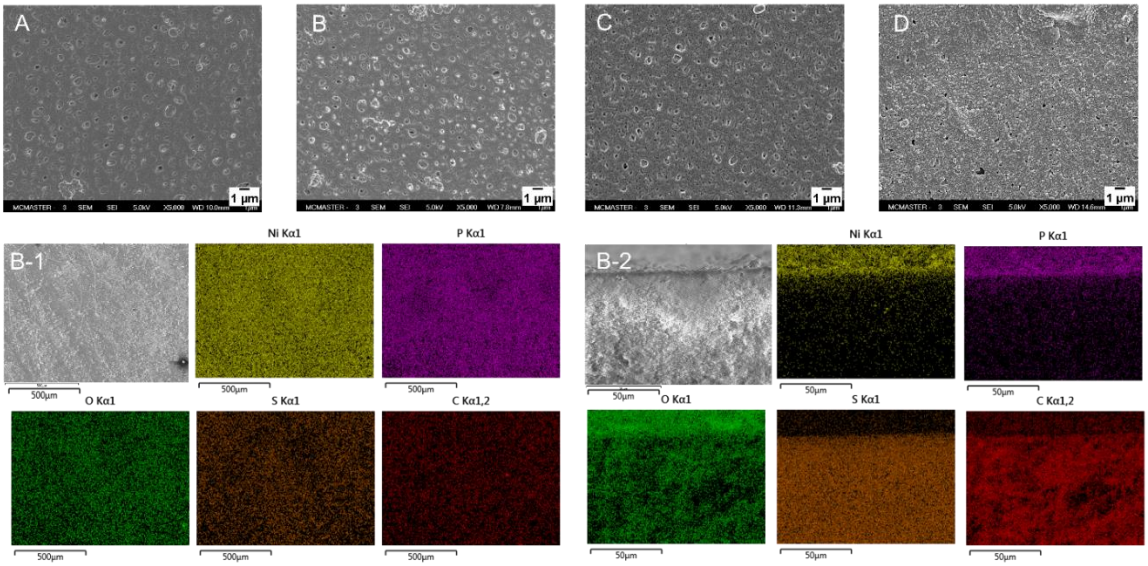

Figure 3. SEM images of Ni-P membranes under varying duration of electroless coating: (A) Ni-P coating for 1 min, (B) Ni-P coating for 2 min, (C) Ni-P coating for 3 min and (D) Ni-P coating for 4 min. EDS mappings of Ni-P membranes with 2 min of Ni-P coating: (B-1) surface and (B-2) cross sectional surface.

The surface structure of Ni-P membranes was characterized by TEM. The high resolution (HR)-TEM images, particle-size distribution and aberration-corrected high-angle annular

dark-field scanning transmission electron microscopy (HAADF-STEM) mappings were shown in **Figure 4. Figure 4A-C** shows granular nanoparticles with an average particle diameter of 50.9 ± 10.6 nm, which were Ni-P nanoparticles with Pd seeds attached on the polymeric aggregates according to the elemental maps in **Figure 4D**.

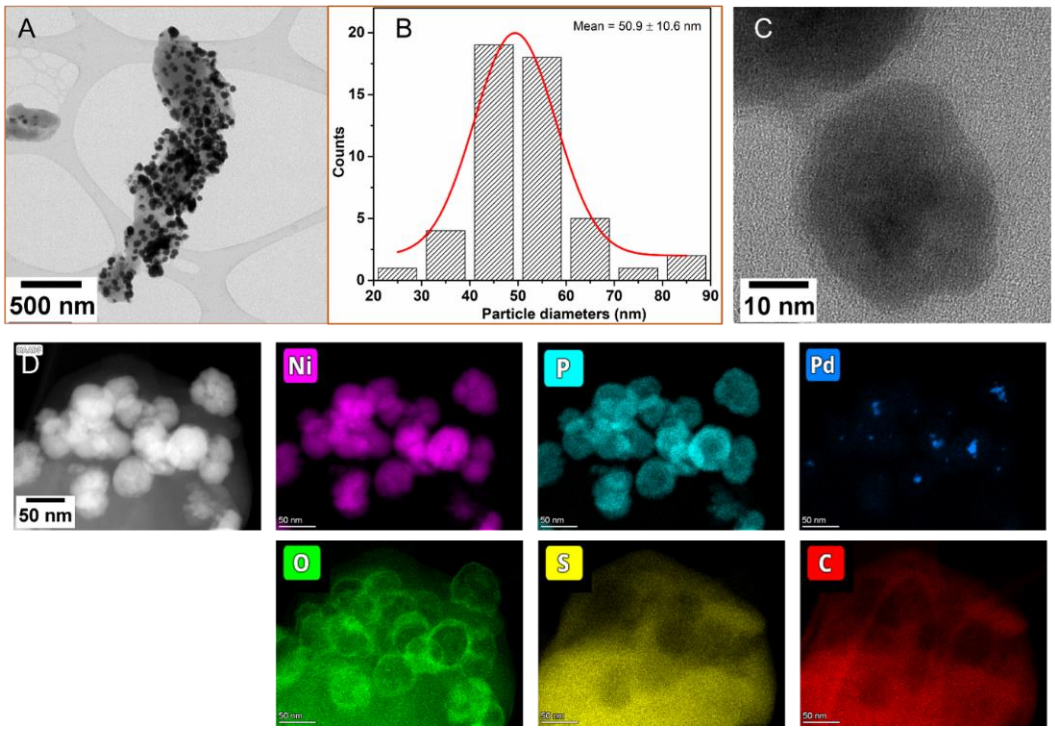

Figure 4. HR-TEM image of (A) Ni-P membranes and (B) Particle-size distribution histogram. The particle size was determined by measuring at least 50 random particles from (A) using ImageJ and the average value was reported. (C) HR-TEM image of Ni-P membranes with higher magnification. (D) Aberration-corrected high-angle annular dark-field scanning transmission electron microscopy (HAADF-STEM) mappings of Ni-P membranes.

6.4.2.2 Wettability

The wettability of unmodified PES membranes and Ni-P membranes with 2 min coating are demonstrated in **Figure 5A**. The initial contact angle for the pristine PES membranes was 34.2 ± 1.8º, indicating the hydrophilicity of PES substrates. After Ni-P nanoparticles were coated on the PES membranes for 2 min, super hydrophilic Ni-P membranes were developed with a contact angle of 16.9 ± 3.1º. Such improved water affinity is beneficial for enhancing electrolyte-electrocatalyst contact during electrochemical reductive dechlorination. Greater surface hydrophilicity is also generally beneficial for reducing the resistance to water permeance across the membrane and in reducing organic fouling by forming a strong surface hydration layer [39, 40].

6.4.2.3 Structure

The structure of the Ni-P coating on PES membranes was characterized by XRD and XPS. **Figure 5B** shows XRD diffraction peaks for pristine PES membranes and Ni-P membranes. A sharp peak of PES membranes at $2\theta = 19^{o}$ was assigned to the crystalline polyether sulfone polymer [41]. The absence of new diffraction peaks on Ni-P membranes implied that the Ni-P nanoparticles were amorphous, which was further supported by the high phosphorus content (10.3 %, **Figure S3**) preventing the nucleation of crystalline nickel [42, 43]. Amorphous Ni-P membranes exhibit more structural defects than crystalline nickel phase or nickel-phosphide phase [44]; therefore, more active sites are provided for electrocatalytic dechlorination.

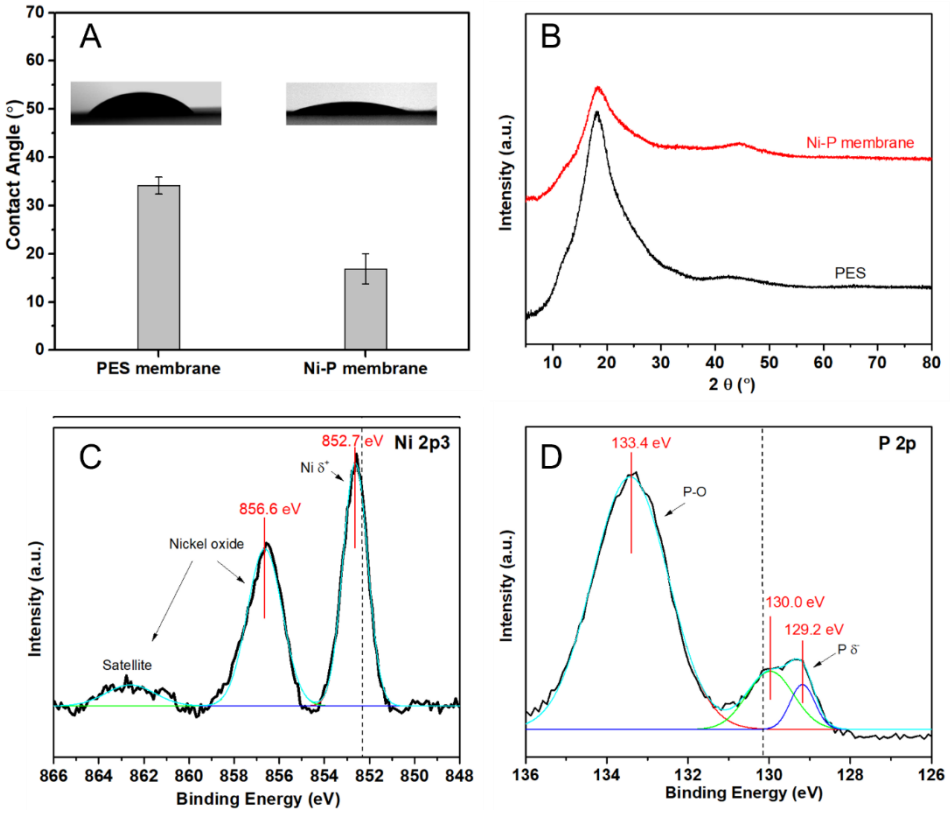

Figure 5. (A) Contact angle and (B) XRD patterns of the pristine PES membrane and Ni-P membrane with 2 min coating. (C) High resolution XPS Ni 2p3 spectrum for Ni-P membranes with 2 min coating; the dot line indicates the reported binding energy of 852.2 eV for pure metallic Ni^0. (D) High resolution XPS P 2p spectrum for Ni-P membranes with 2 min coating; the dot line indicates the reported binding energy of 130.1 eV for pure P^0. (Error bar represents standard deviation, n = 5)

XPS spectra of Ni-P membranes are presented in **Figure 5C-D**. The Ni 2p3 spectrum in **Figure 5C** was deconvoluted to a strong peak at 852.7 eV for metallic Ni^0, and a peak at 856.6 eV coupled with a satellite peak at 862.5 eV for nickel oxides [37]. The metallic Ni^0 peak was slightly positively shifted by around 0.5 eV compared to the reported binding energy of 852.2 eV for pure Ni^0, which was attributed to Ni being partially

positively charged ($Ni^{\delta+}$) when formed as nickel phosphide [20]. Accordingly, peaks at 129.2 eV and 130.0 eV in the P 2p spectrum (**Figure 5D**) were assigned to the negatively charged phosphorus ($P^{\delta-}$) in nickel phosphide, which was slightly negatively shifted by 0.1 - 0.9 eV from the reported position of metallic P at 130.1 eV [20]. In addition, a significant peak at 133.4 eV in the P 2p spectrum implied oxidized phosphate species originating from the oxidation of sodium hypophosphite (the reducing agent used for electroless deposition). These results suggested that doping P atoms in Ni crystal structures contributed to electron transfer from Ni to P, such that $Ni^{\delta+}P^{\delta-}$ dominated in the Ni-P membranes. This electronic configuration of $Ni^{\delta+}P^{\delta-}$ was hypothesized to be capable of stabilizing atomic H* formation by forming Ni-H* bonds.

6.4.3 Electrocatalytic performance

The feasibility of Ni-P membranes for electrochemical reductive dechlorination of 2-CP was explored by CV scans over a cell potential from -3.00 V to 0 V. **Figure 6** shows a reductive peak at a cell potential ranging from -2.00 V to -2.50 V (from -0.80 V vs. Ag/AgCl to -1.20 V vs. Ag/AgCl, **Figure S6**), implying the generation of atomic H* for 2-CP conversion (**eq 5-8**) [13]. Further, a cathodic potential more negative in cell potential than -2.50 V (corresponding to -1.20 V vs Ag/AgCl) was expected to induce the production of hydrogen gas (byproduct) over the generation of atomic H*, shown in **eq 9**. We hypothesized based on previous experience and reports in the literature that hydrogen bubbles would both physically block electrocatalytic sites as well as scavenge atomic H* and thereby decrease the overall dechlorination efficiency of the electrocatalytic membrane reactor towards the conversion of 2-CP. With this hypothesis in mind, we

explored the effect of applied cathodic potentials on electrocatalytic activity of Ni-P membranes.

$$2H_2O + 2e^- + Ni - P \rightarrow 2H^*_{ads}(Ni - P) + 2OH^- \quad (5)$$

$$R - Cl + Ni - P \rightarrow (R - Cl)_{ads}(Ni - P) \quad (6)$$

$$(R - Cl)_{ads}(Ni - P) + 2H^*_{ads}(Ni - P) \rightarrow (R - H)_{ads}(Ni - P) + (H - Cl)_{ads}(Ni - P) \quad (7)$$

$$(R - H)_{ads}(Ni - P) \rightarrow R - H + Ni - P \quad (8)$$

$$2H_2O + 2e^- \rightarrow H_2 + 2OH^- \quad (9)$$

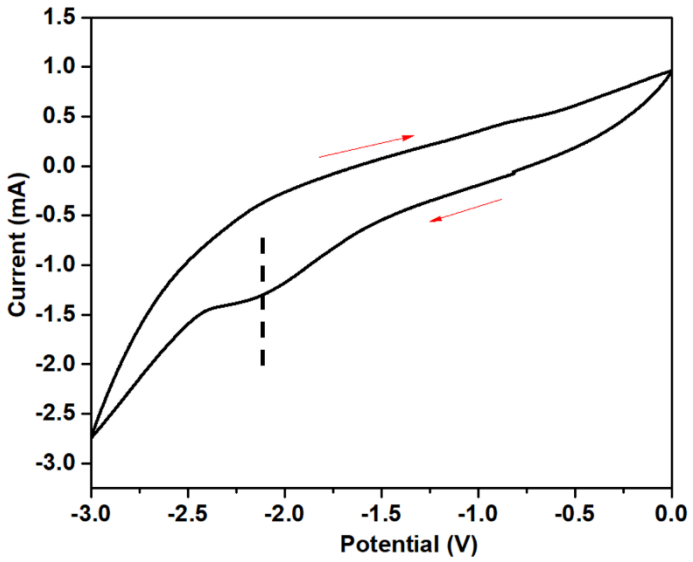

Figure 6. (A) CV curve of Ni-P membranes with 2 min coating in a two-electrode electrochemical cell. Conditions: [2-CP] = 10 ppm, [Na_2SO_4] = 50 mM. A scan rate of 50 mV/s was used, and potentials were applied between -3.00 V and 0 V. Arrows indicate the direction of CV curve and the dotted line shows the reductive peak.

The activity of Ni-P membranes for electrochemical reductive dechlorination was explored under different cathodic potentials in a flow-through electrochemical cell. A feed containing 50 mM Na_2SO_4 and 10 ppm (0.08 mM) 2-CP was filtered through the Ni-P membrane under a constant flow rate of 0.35 mL/min. Electrochemical reductive dechlorination of 2-CP was carried out under predetermined cathodic potentials (from -2.00 V to -3.00 V), while 2-CP removal under identical conditions without the application of potentials was performed as control (**Figure 7A-D**). **Figure 7A** shows that 2-CP concentration in the permeate achieved either a steady-state degradation rate or an increased degradation rate after 30 min of filtration through the ECMR. It was observed that 2-CP removal was greater when applying cathodic potentials than that without applied potentials. Applying various negative potentials to Ni-P membranes achieved 24.0% - 42.7% dechlorination of 2-CP. The removal trend demonstrates a constant or decreasing concentration of 2-CP in the permeate during flow-through separation indicating continual 2-CP degradation rather than a saturation-breakthrough curve. In contrast, a typical saturated adsorption-site breakthrough curve is observed for the control with no applied potential (**Figure 7A**). Furthermore, the increasing degradation rate of 2-CP over the course of electrochemical flow-through degradation indicates an absence of reactive site saturation or catalyst attrition. Given that Cl^- is a byproduct of the electrochemical degradation of 2-CP, and Cl^- ions poison pure Ni catalysts, the lack of catalyst deactivation suggests phosphorous' role in protecting Ni-P membranes from deactivation.

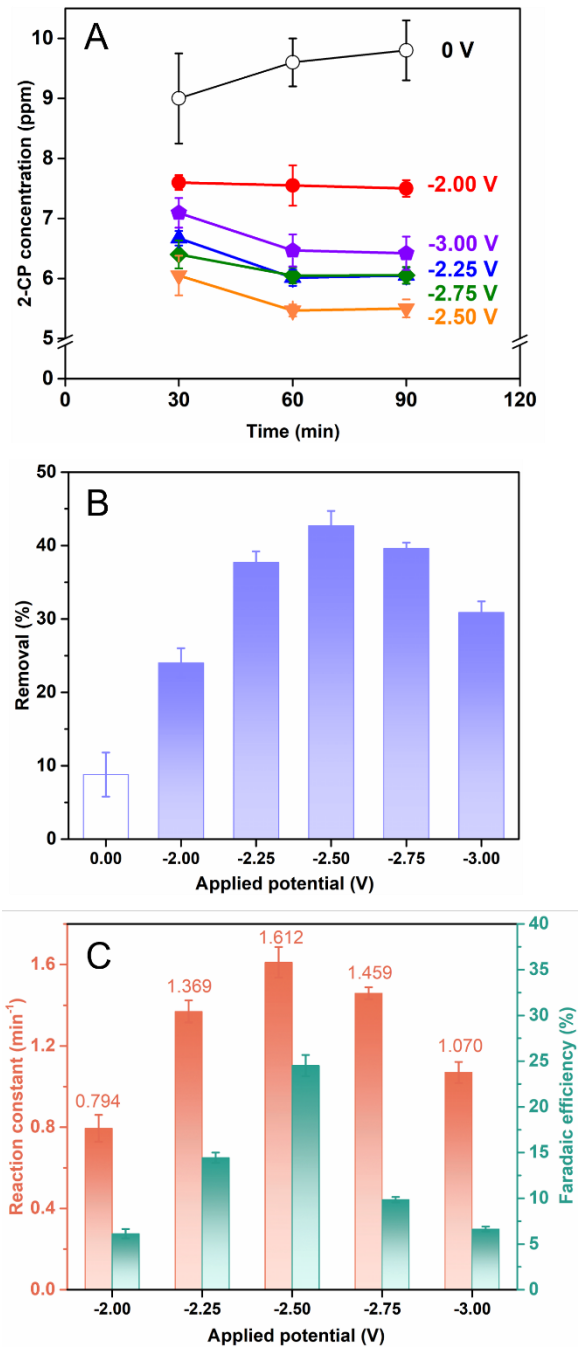

Figure 7. (A) 2-CP concentration profiles in permeate stream using a flow-through electrocatalytic cell under varying applied potentials. Conditions: [2-CP] = 10 ppm, [Na_2SO_4] = 50 mM and flow rate of 0.35 mL/min. (B) The removal under varying cathodic potentials from -2.00 V to -3.00 V. (C) Reaction rate constant and faradaic

efficiency in electrochemical reductive dechlorination under varying applied potentials. (Error bar represents standard deviation, n = 2)

Figure 7B-C show the impact of applied cathodic potentials on the dechlorination performance of the Ni-P membranes. The application of a negative potential of -2.00 V (-0.80 V vs Ag/AgCl) on Ni-P membranes contributed to 20.0% dechlorination (20% 2-CP degradation) (**Figure 7B**) and a reaction constant of 0.794 min^{-1} (**Figure 7C**). When the applied cell potential was increased to -2.50 V (-1.2 V vs. Ag/AgCl), the resulting overpotential enhanced water splitting and the evolution of atomic H* radicals. The maximum dechlorination achieved was 42.7% was obtained with a reaction constant of 1.612 min^{-1}, under a cathodic potential of -2.50 V. Electrochemical reductive dechlorination of 2-CP likely proceeded *via* atomic H* attack, which could be scavenged by H_2 gas evolution at higher applied potentials. When the applied cathodic potential was more negative than -2.50 V, the ECMR promoted the recombination of atomic H* to hydrogen (H_2), and this H_2 evolution outperformed the dechlorination reaction of radical H* with 2-CP. This scavenging reaction was further supported by the observation of gas production at a cathodic potential more negative than -2.50 V during CV measurements (**Figure 6**). The produced H_2 bubbles would inhibit the electrocatalytic sites and reduce the mass transfer of 2-CP towards Ni-P membranes, which resulted in an evident decline in dechlorination efficiency (30.9 %) and reaction constant (1.070 min^{-1}) at a cathodic potential of -3.00 V. Faradaic efficiency (FE) represents the current consumed for electrochemical reductive dechlorination to the current transferred in the electrical circuit.

Electrocatalytic Ni-P membranes showed a FE of 6.12% at -2.00 V, a FE of 14.4% at -2.25 V, a FE of 24.5% at -2.50 V, a FE of 9.9% at -2.75 V and a FE of 6.6% at -3.00 V (**Figure 7C**), additionally supporting the hypothesis that increasing electrical energy was spent in H_2 gas evolution at negative potentials greater than -2.50 V. The highest energy utilization efficiency was achieved under a cathodic potential of -2.50 V, with the maximum FE of 24.5%, comparable to noble metal-free electrocatalysts' FE ranging from 13% to 28% in electrochemical reductive dechlorination processes [45-47].

A noble metal-free Ni-P electrocatalytic membrane is a promising technology to eliminate trace chlorinated compounds from industrial wastewaters and landfill leachates, in comparison to the Pd-based electrocatalysts which are orders of magnitude more expensive while in the best cases only a factor higher dechlorination activity (**Table S1**).

6.4.4 Mechanisms

The electrocatalytic activity of Ni-P membranes for dechlorination may be attributed to the following mechanisms, illustrated in **Figure 8**.

- Partial positive charged $Ni^{\delta+}$ in Ni-P membranes promote 2-CP adsorption *via* Ni-Cl bonds.
- Under the influence of an external applied negative potential, $Ni^{\delta+}$ in Ni-P membranes enable atomic H* formation by water splitting.
- H* are stabilized on the electrocatalytic sites *via* Ni-H* bonds. Similar mechanisms have been proposed for a cobalt-phosphorous/oxide (Co-P/O) composite coated Ti electrode [21].

- Locally stabilized atomic H* attack Ni-Cl bonds to form Cl^-, leaving dechlorinated phenol.

The isolation of Ni sites by P atoms decreases the possibility of chloride adsorption on nickel sites [48], which would poison the Ni surface by forming $NiCl_2$. [18]. Additionally, excess hydrogen species (H*) may enhance the removal of chloride ions from the surface of electrocatalytic sites in the form of HCl.

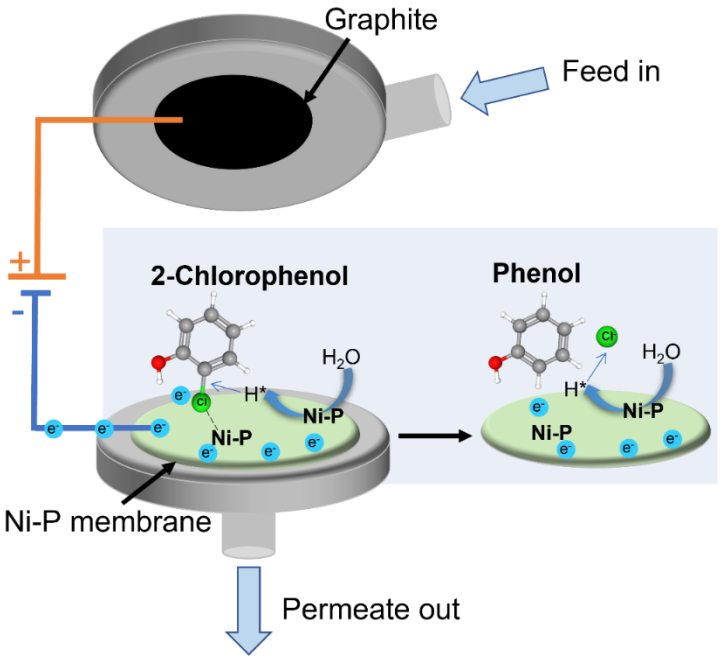

Figure 8. Schematic illustration of the electrochemical reductive dechlorination of 2-CP using Ni-P membranes

6.5 Conclusion

This work reported a facile electroless-depositing approach to fabricate a non-noble metal-based electrocatalytic membrane for electrochemical reductive dechlorination. The

amorphous Ni-P nanoparticles were uniformly grown on the surface of ultrafiltration PES membranes, imbuing the membrane with super hydrophilicity, high electrical conductivity, catalytic and atomic H* acceptor properties. These Ni-P membranes facilitated the dechlorination of 2-chlorophenol under an applied cathodic potential. It was hypothesized that this was achieved by the catalytic production of atomic H* by water splitting, the stabilization of atomic H* *via* Ni-H* bonds and the adsorption of chlorinated compounds *via* Ni-Cl bonds. The 2-CP dechlorination efficiency of 42.7%, reaction rate constant of 1.612 min^{-1} and Faradaic efficiency of 24.5% were achieved when an optimized cathodic potential of -2.50 V was applied to the Ni-P membrane. Doping of P atoms in Ni sites increased resistance of Ni-P membranes to deactivation, which was demonstrated by an increasing electrochemical activity over 1.5 h during electrochemical reductive dechlorination. Inexpensive Ni-P electrocatalytic membrane reactors show great potential in detoxification of chlorinated compounds, which are an increasing emissions concern from industrial wastewater and landfill leachates.

6.6 Acknowledgements

The authors thank the support of the Global Water Futures (GWF) research program provided through the Canada First Research Excellence Fund (CFREF, Sensors and Sensing Systems for Water Quality Monitoring) as well as the China Scholarship Council (CSC). The electron microscopy research described in this paper was performed at the Canadian Centre for Electron Microscopy (CCEM) at McMaster University, which is supported by the Natural Sciences and Engineering Research Council of Canada (NSERC, Discovery Grant) and other government agencies.

6.7 References

[1] Z.N. Garba, W. Zhou, I. Lawan, W. Xiao, M. Zhang, L. Wang, L. Chen, Z. Yuan, An overview of chlorophenols as contaminants and their removal from wastewater by adsorption: A review, J Environ Manage 241 (2019) 59-75. https://doi.org/10.1016/j.jenvman.2019.04.004.
[2] J. Earls, The US Environmental Protection Agency National Pollutant Discharge Elimination System (NPDES), Proc. of the Ann. Conf. of NASA Clinic Directors, Environ. Health Offic., and Med. Program Advisors, 1975.
[3] Y. Liu, F. Yang, P.L. Yue, G. Chen, Catalytic dechlorination of chlorophenols in water by palladium/iron, Water Research 35(8) (2001) 1887-1890.
[4] E.O. Igbinosa, E.E. Odjadjare, V.N. Chigor, I.H. Igbinosa, A.O. Emoghene, F.O. Ekhaise, N.O. Igiehon, O.G. Idemudia, Toxicological profile of chlorophenols and their derivatives in the environment: the public health perspective, The Scientific World Journal 2013 (2013).
[5] M. Czaplicka, Sources and transformations of chlorophenols in the natural environment, Sci Total Environ 322(1-3) (2004) 21-39. https://doi.org/10.1016/j.scitotenv.2003.09.015.
[6] M. Pera-Titus, V. García-Molina, M.A. Baños, J. Giménez, S. Esplugas, Degradation of chlorophenols by means of advanced oxidation processes: a general review, Applied Catalysis B: Environmental 47(4) (2004) 219-256.
[7] A. Karci, Degradation of chlorophenols and alkylphenol ethoxylates, two representative textile chemicals, in water by advanced oxidation processes: the state of the art on transformation products and toxicity, Chemosphere 99 (2014) 1-18. https://doi.org/10.1016/j.chemosphere.2013.10.034.
[8] M. Czaplicka, Photo-degradation of chlorophenols in the aqueous solution, Journal of hazardous materials 134(1-3) (2006) 45-59.
[9] N. Li, X. Song, L. Wang, X. Geng, H. Wang, H. Tang, Z. Bian, Single-Atom Cobalt Catalysts for Electrocatalytic Hydrodechlorination and Oxygen Reduction Reaction for the Degradation of Chlorinated Organic Compounds, ACS Appl Mater Interfaces 12(21) (2020) 24019-24029. https://doi.org/10.1021/acsami.0c05159.
[10] G. Jiang, M. Lan, Z. Zhang, X. Lv, Z. Lou, X. Xu, F. Dong, S. Zhang, Identification of Active Hydrogen Species on Palladium Nanoparticles for an Enhanced Electrocatalytic Hydrodechlorination of 2,4-Dichlorophenol in Water, Environ. Sci. Technol 51(13) (2017) 7599-7605. https://doi.org/10.1021/acs.est.7b01128.
[11] N. Li, H.-d. Chen, Y.-z. Lu, M.-c. Zhu, Z.-x. Hu, S.-w. Chen, R.J. Zeng, Nanoscale zero-valent iron-modified PVDF membrane prepared by a simple filter-press coating method can robustly remove 2-chlorophenol from wastewater, Chemical Engineering Journal (2020). https://doi.org/10.1016/j.cej.2020.127701.
[12] S.S. Raut, R. Shetty, N.M. Raju, S.P. Kamble, P.S. Kulkarni, Screening of zero valent mono/bimetallic catalysts and recommendation of Raney Ni (without reducing agent) for dechlorination of 4-chlorophenol, Chemosphere 250 (2020) 126298. https://doi.org/10.1016/j.chemosphere.2020.126298.
[13] M.A. Arellano-Gonzalez, I. Gonzalez, A.C. Texier, Mineralization of 2-chlorophenol by sequential electrochemical reductive dechlorination and biological processes, J Hazard Mater 314 (2016) 181-187. https://doi.org/10.1016/j.jhazmat.2016.04.048.
[14] K. Miyoshi, Y. Kamegaya, M. Matsumura, Electrochemical reduction of organohalogen compound by noble metal sintered electrode, Chemosphere 56(2) (2004) 187-93. https://doi.org/10.1016/j.chemosphere.2004.02.013.
[15] Q. Wang, L. Zhou, Q. Chen, M. Mao, W. Jiang, Y. Long, G. Fan, Oxygenated functional group-driven spontaneous fabrication of Pd nanoparticles decorated porous carbon nanosheets for

electrocatalytic hydrodechlorination of 4-chlorophenol, J Hazard Mater 408 (2021) 124456. https://doi.org/10.1016/j.jhazmat.2020.124456.
[16] Z. Pu, T. Liu, I.S. Amiinu, R. Cheng, P. Wang, C. Zhang, P. Ji, W. Hu, J. Liu, S. Mu, Transition-Metal Phosphides: Activity Origin, Energy-Related Electrocatalysis Applications, and Synthetic Strategies, Advanced Functional Materials 30(45) (2020). https://doi.org/10.1002/adfm.202004009.
[17] Y. Wang, B. Kong, D. Zhao, H. Wang, C. Selomulya, Strategies for developing transition metal phosphides as heterogeneous electrocatalysts for water splitting, Nano Today 15 (2017) 26-55. https://doi.org/10.1016/j.nantod.2017.06.006.
[18] J. Cecilia, A. Infantes-Molina, E. Rodríguez-Castellón, Hydrodechlorination of polychlorinated molecules using transition metal phosphide catalysts, Journal of hazardous materials 296 (2015) 112-119.
[19] C. Li, H. Gao, W. Wan, T. Mueller, Mechanisms for hydrogen evolution on transition metal phosphide catalysts and a comparison to Pt(111), Phys Chem Chem Phys 21(44) (2019) 24489-24498. https://doi.org/10.1039/c9cp05094a.
[20] Q. Yao, X. Zhou, S. Xiao, J. Chen, I.A. Abdelhafeez, Z. Yu, H. Chu, Y. Zhang, Amorphous nickel phosphide as a noble metal-free cathode for electrochemical dechlorination, Water Res 165 (2019) 114930. https://doi.org/10.1016/j.watres.2019.114930.
[21] T. Liu, J. Luo, X. Meng, L. Yang, B. Liang, M. Liu, C. Liu, A. Wang, X. Liu, Y. Pei, J. Yuan, J. Crittenden, Electrocatalytic dechlorination of halogenated antibiotics via synergistic effect of chlorine-cobalt bond and atomic H, J Hazard Mater 358 (2018) 294-301. https://doi.org/10.1016/j.jhazmat.2018.06.064.
[22] H. Wang, Q. Guan, J. Li, T. Wang, Phenolic wastewater treatment by an electrocatalytic membrane reactor, Catalysis Today 236 (2014) 121-126. https://doi.org/10.1016/j.cattod.2014.05.003.
[23] P. Kumari, N. Bahadur, M. Cretin, L. Kong, L.A. O'Dell, A. Merenda, L.F. Dumée, Electro-catalytic membrane reactors for the degradation of organic pollutants – a review, Reaction Chemistry & Engineering 6(9) (2021) 1508-1526. https://doi.org/10.1039/d1re00091h.
[24] Y. Yang, J. Li, H. Wang, X. Song, T. Wang, B. He, X. Liang, H.H. Ngo, An electrocatalytic membrane reactor with self-cleaning function for industrial wastewater treatment, Angew Chem Int Ed Engl 50(9) (2011) 2148-50. https://doi.org/10.1002/anie.201005941.
[25] P. Gayen, C. Chen, J.T. Abiade, B.P. Chaplin, Electrochemical Oxidation of Atrazine and Clothianidin on Bi-doped SnO2-Ti nO2 n-1 Electrocatalytic Reactive Electrochemical Membranes, Environ. Sci. Technol 52(21) (2018) 12675-12684. https://doi.org/10.1021/acs.est.8b04103.
[26] A.J. Sutherland, M.-X. Ruiz-Caldas, C.-F. de Lannoy, Electro-catalytic microfiltration membranes electrochemically degrade azo dyes in solution, J. Membr. Sci 611 (2020). https://doi.org/10.1016/j.memsci.2020.118335.
[27] H.-J. Lee, N. Zhang, M.A. Ganzoury, Y. Wu, C.-F. de Lannoy, Simultaneous Dechlorination and Advanced Oxidation Using Electrically Conductive Carbon Nanotube Membranes, ACS Applied Materials & Interfaces 13(29) (2021) 34084-34092.
[28] Z. Yan, Y. Zhang, H. Yang, G. Fan, A. Ding, H. Liang, G. Li, N. Ren, B. Van der Bruggen, Mussel-inspired polydopamine modification of polymeric membranes for the application of water and wastewater treatment: A review, Chemical Engineering Research and Design 157 (2020) 195-214. https://doi.org/10.1016/j.cherd.2020.03.011.
[29] R. Bernasconi, G. Natale, M. Levi, L. Magagnin, Electroless Plating of NiP and Cu on Polylactic Acid and Polyethylene Terephthalate Glycol-Modified for 3D Printed Flexible

Substrates, Journal of The Electrochemical Society 163(9) (2016) D526-D531. https://doi.org/10.1149/2.1201609jes.
[30] D. Bell, R. Sengpiel, M. Wessling, Metallized hollow fiber membranes for electrochemical fouling control, J. Membr. Sci 594 (2020). https://doi.org/10.1016/j.memsci.2019.117397.
[31] Z. He, K. Lin, J. Sun, L. Wen, C. Gao, J. Chen, S. Song, Y. Qian, W. Liu, Kinetics of electrochemical dechlorination of 2-chlorobiphenyl on a palladium-modified nickel foam cathode in a basic medium: From batch to continuous reactor operation, Electrochimica Acta 109 (2013) 502-511. https://doi.org/10.1016/j.electacta.2013.07.207.
[32] D. Liu, L. Lei, B. Yang, Q. Yu, Z. Li, Direct electron transfer from electrode to electrochemically active bacteria in a bioelectrochemical dechlorination system, Bioresour Technol 148 (2013) 9-14. https://doi.org/10.1016/j.biortech.2013.08.108.
[33] Z. Gu, Z. Zhang, N. Ni, C. Hu, J. Qu, Simultaneous Phenol Removal and Resource Recovery from Phenolic Wastewater by Electrocatalytic Hydrogenation, Environ. Sci. Technol 56(7) (2022) 4356-4366. https://doi.org/10.1021/acs.est.1c07457.
[34] J. Li, Y. Chen, R. Bai, C. Chen, W. Wang, Y. Pan, Y. Liu, Construction of Pd/Ni2P-Ni foam nanosheet array electrode by in-situ phosphatization-electrodeposition strategy for synergistic electrocatalytic hydrodechlorination, Chemical Engineering Journal 435 (2022). https://doi.org/10.1016/j.cej.2022.134932.
[35] M.J. Larocque, A. Gelb, D.R. Latulippe, C.-F. de Lannoy, Meta-analysis of electrically conductive membranes: A comparative review of their materials, applications, and performance, Sep. Purif. Technol 287 (2022). https://doi.org/10.1016/j.seppur.2022.120482.
[36] N. Zhang, H.-J. Lee, Y. Wu, M.A. Ganzoury, C.-F. de Lannoy, Integrating biofouling sensing with fouling mitigation in a two-electrode electrically conductive membrane filtration system, Sep. Purif. Technol 288 (2022). https://doi.org/10.1016/j.seppur.2022.120679.
[37] H. Wu, A. Susanto, K. Lian, Thin and flexible Ni-P based current collectors developed by electroless deposition for energy storage devices, Applied Surface Science 394 (2017) 63-69. https://doi.org/10.1016/j.apsusc.2016.10.067.
[38] L. Li, J. Wang, J. Xiao, J. Yan, H. Fan, L. Sun, L. Xue, Z. Tang, Time-dependent corrosion behavior of electroless Ni–P coating in H2S/Cl− environment, International Journal of Hydrogen Energy 46(21) (2021) 11849-11864. https://doi.org/10.1016/j.ijhydene.2021.01.053.
[39] Z. Xiong, J. Liu, Y. Yang, Q. Lai, X. Wu, J. Yang, Q. Zeng, G. Zhang, S. Zhao, Reinforcing hydration layer on membrane surface via nano-capturing and hydrothermal crosslinking for fouling reduction, J. Membr. Sci 644 (2022). https://doi.org/10.1016/j.memsci.2021.120076.
[40] K. Wang, L. Xu, K. Li, L. Liu, Y. Zhang, J. Wang, Development of polyaniline conductive membrane for electrically enhanced membrane fouling mitigation, J. Membr. Sci 570-571 (2019) 371-379. https://doi.org/10.1016/j.memsci.2018.10.050.
[41] L.M. Munirathnamma, H.B. Ravikumar, Microstructural characterization of short glass fibre reinforced polyethersulfone composites, Journal of Applied Polymer Science 133(32) (2016). https://doi.org/10.1002/app.43647.
[42] J. Balaraju, K. Rajam, Electroless deposition and characterization of high phosphorus Ni–P–Si3N4 composite coatings, Int. J. Electrochem. Sci 2 (2007) 747-761.
[43] Y. Tan, D. Sun, H. Yu, B. Yang, Y. Gong, S. Yan, Z. Chen, Q. Cai, Z. Wu, Crystallization mechanism analysis of noncrystalline Ni–P nanoparticles through XRD, HRTEM and XAFS, CrystEngComm 16(41) (2014) 9657-9668. https://doi.org/10.1039/c4ce01130a.
[44] P. Li, H. Ni, S. Jiang, H. Wang, Sol–gel preparation of crystalline Ni12P5/N-doped carbon and amorphous Ni–P–C catalysts and their high catalytic performances toward hydrogenation reduction reaction of 4-nitrophenol, New Journal of Chemistry 45(35) (2021) 15801-15807. https://doi.org/10.1039/d1nj01616d.

[45] M. Dauda, C. Basheer, M.H. Al-Malack, M.N. Siddiqui, Efficient Co-MoS2 electrocatalyst for cathodic degradation of halogenated disinfection by-products in water sample, Sep. Purif. Technol 259 (2021). https://doi.org/10.1016/j.seppur.2020.118085.
[46] G. Gan, X. Li, L. Wang, S. Fan, J. Li, F. Liang, A. Chen, Identification of Catalytic Active Sites in Nitrogen-Doped Carbon for Electrocatalytic Dechlorination of 1,2-Dichloroethane, ACS Catalysis 9(12) (2019) 10931-10939. https://doi.org/10.1021/acscatal.9b02853.
[47] G. Gan, S. Fan, X. Li, L. Wang, Z. Yin, J. Wang, G. Chen, Effects of oxygen functional groups on electrochemical performance of carbon materials for dechlorination of 1,2-dichloroethane to ethylene, Chemical Engineering Journal 434 (2022). https://doi.org/10.1016/j.cej.2022.134547.
[48] X. Liu, J. Chen, J. Zhang, Hydrodechlorination of chlorobenzene over silica-supported nickel phosphide catalysts, Ind. Eng. Chem. Res 47(15) (2008) 5362-5368.

Chapter 7

Contributions and future perspectives

7.1 Contributions

This thesis introduces active and reactive ultrafiltration membrane-based technologies for water treatment. Specifically, (1) membrane-based water purification effectively alleviates the shortage of potable water, during which a great challenge of surface fouling was investigated on the platform of ECMs *via* electrically impedance spectroscopy (EIS)-enabled fouling monitoring. The early sensing of surface fouling enlightens water treatment operators to adopt appropriate membrane cleaning strategies. Additionally, integrating fouling sensing and fouling removal was achieved in a two-electrode membrane system. (2) Novel catalytic membrane microreactors (CMMRs) were prepared for pollutants degradation *via* catalysis-membrane filtration. Dye- and macromolecular-contaminated wastewater was treated by CMMRs *via* catalytic conversion and membrane separation with the assistance of reducing agents. (3) A novel electrocatalytic membrane reactor (ECMR) was prepared for reductive detoxification of chlorophenols in the processes of industrial wastewater treatment.

Chapter 2 investigates electrical impedance spectroscopy (EIS) on the surface of electrically conductive membranes (ECMs) to measure the earliest development of membrane surface fouling. The surface fouling degree on conductive CNT membranes was correlated to the change in *ex-situ* impedance spectra, implying that the impedance in the high-frequency regime (10^4 ~ 10^6 Hz) increased with greater amounts of latex fouling deposited. We hypothesized that increased membrane impedance was attributed to the incorporation of insulating materials (latex beads) within the porous conductive coating, which was supported by a theoretical circuit showing increased membrane resistance.

Despite the quantitative correlation of *ex-situ* EIS signals and fouling degree in Chapter 2, *in-situ* monitoring of surface fouling on ECMs is critical for practical applications.

Chapter 3 reports the fouling sensing by *in-situ* EIS on ultra-thin gold-coated membranes and further explores the integration of fouling sensing and fouling control on the platform of ECMs. We observed that the diffusion-related impedance at low-frequency regions (< 10 Hz) was a sensitive indicator for monitoring biofouling development, especially in the early stage of biofouling. With early detection of fouling, fouling mitigation strategies could be applied more effectively. Further, the combination of EIS-enabled fouling monitoring and intermittently cathodic potential-induced fouling mitigation was achieved on ECMs in the cross-flow membrane system.

Chapter 4 introduces catalytic membrane microreactors (CMMRs) for water decontamination by combining catalysis and membrane separation. CMMRs enable the continuous purification and production of organic compounds with high catalytic activity while maintaining nanocatalyst size and stability. Stable Pd-immobilized catalytic membranes were developed for catalytic degradation of an environmental pollutant, 4-nitrophenol (4-NP), and simultaneous production of a valuable chemical feedstock, 4-aminophenol (4-AP). Well-dispersed Pd nanoparticles attached to the porous membranes contributed to high catalytic activity in the presence of in the presence of $NaBH_4$, with 4-fold higher reduction (79.7%) and 2-fold higher reduction rate (10.1 mol m^{-2} h^{-1}) as compared to control membranes without catalysts. Furthermore, by combing ultrafiltration and catalysis, Pd-immobilized membranes showed >99% of 4-NP

conversion and >90% of 1 MDa PEO rejection, demonstrating a great potential to be applied in highly efficient wastewater treatment processes.

The usage of noble metals in CMMRs limits scale-up industrial processes. Therefore, Chapter 5 reports inexpensive Ni-Cu bimetallic catalytic membrane microreactors (CMMRs) for catalytic transformation. We observed 2.5-fold higher conversion (>99%) and 20-fold higher processing capacity (0.95 $mol \cdot L^{-1} \cdot h^{-1}$) in flow-through mode, compared to 4-NP conversion in batch mode. Enhanced catalytic activity in a flow-through manner was attributed to synergistic electronic effects of the Ni-Cu bimetallic structure, the metal-polydopamine interactions, and the catalysts' unique structure and high surface area. Investigating the influence of operating conditions on catalytic activity indicated that 4-NP conversion followed the Langmuir-Hinshelwood (L-H) mechanism, and a critical optimization trade-off between separation and permeability. The stability of bimetallic CMMRs was due to both the polydopamine-assisted fabrication and the tortuous membrane pore structure. Non-noble metal bimetallic membranes offer great potential to design catalysts with controllable functionality and high activity at a lower cost.

Chapter 6 introduces an inexpensive nickel phosphorous (Ni-P) ultrafiltration membrane for electrochemical reductive dechlorination. Amorphous Ni-P nanoparticles were developed on an ultrafiltration polyethersulfone (PES) membrane *via* electroless deposition. The prepared Ni-P membrane was used as a cathode for electrochemical reductive dechlorination of 2-chlorophenol (2-CP) in flow-through mode. Removal of 42.7%, a reaction rate constant of 1.621 min^{-1} and a Faradaic efficiency of 24.5% were

achieved at an optimized cathodic potential of -2.50 V, primarily attributed to the partial positive-charged $Ni^{\delta+}$ on the Ni-P membrane surface facilitating the atomic H* evolution for dechlorination *via* Ni-H* bonds, as well as enhancing the affinity between 2-CP and the Ni-P membranes *via* Ni-Cl bonds. Additionally, doping of P atoms in Ni sites in Ni-P membranes retarded the deactivation of electrocatalytic sites.

7.2 Future perspectives

Future perspectives of these projects in the thesis are discussed in the following aspects.

I. EIS technique

The power of EIS as a technique for fouling detection can be broadened to fouling differentiation compared with only monitoring the degree of surface fouling on ECMs as demonstrated in this thesis. EIS monitoring might enable distinguishing the stages of biofouling and thus identifying optimized cleaning frequency. Biofouling is a complicated process where microbial cells in a planktonic stage attach to the membrane surface followed by the growth of biofilms and the formation of dense biofilms with the secretion of extracellular polymeric substances (EPS). As such, different stages of biofouling exhibit different surface chemistry of the fouled surface, and we hypothesize that the stages of biofouling can be identified by interpreting EIS signals. This is both scientifically interesting and practically important. Critically, a young biofilm caused by microbial attachment is susceptible to potential-induced electronic repulsion and biocidal-based chemical cleaning. On the contrary, a well-established (mature) biofilm increases the resistance to foulant detachment, because the microbe- and EPS-enriched

biofilm hinders the diffusion of cleaning agents to microbial cells, thereby protecting them from chemical attack. The existence of a mature film thus reduces cleaning efficiency. Therefore, future research can explore the feasibility of EIS-enabled ECMs for differentiating biofouling stages and determine a proper cleaning frequency at which mature biofilms have not yet been developed and high cleaning efficiency can be obtained.

Alternatively, the EIS technique has been used for *ex-situ* latex fouling and *in-situ* biofouling monitoring on the surface of ECMs, implying the ability to distinguish different types of foulants according to the impacts of foulants' natures on EIS signals. Thus, future research should explore the capability of EIS to distinguish between different types of foulants deposited on the surface of ECMs and to identify contaminants in real-time as opposed to conventional approaches, which require an *ex-situ* autopsy of the fouled membrane. Accordingly, optimized cleaning methods and the cleaning frequency can be determined.

Additionally, future work may explore EIS sensing on conductive hollow fiber membranes which possess high packing density and are appropriate for industrial applications. In one possible design, one single hollow fiber membrane within the bundle of hollow fibers can be modified by depositing porous conductive materials on the lumen side. High-solids content wastewater can be treated by these hollow fiber membranes in an outside-in fluid flow configuration, while the one conductive membrane can act as the sensing electrode. Similar to a typical three-electrode system for monitoring fouling on a flat sheet membrane, the fouling sensing system for hollow fiber membranes can be

established where the conductive lumen side of the hollow fiber membrane acts as the working electrode, and auxiliary electrodes (a counter electrode and a reference electrode) are submerged into the wastewater.

II. Cleaning strategies

Fouling prevention and fouling removal have attracted attention to maintain membrane performance. Fouling prevention can be achieved by adding biocides to a feed stream and operating the membranes at or below the critical flux, above which irreversible fouling is developed. Various biocidal agents for fouling prevention have been widely explored whereas the investigation and optimization of critical flux operation for membranes are scarce. Future work should explore the filtration performance of low-pressure membranes at the critical flux to establish the relationship between fouling concentrations, applied pressures, and transmembrane fluxes. Identifying the critical flux for each membrane-foulant system is important to continue the investigation of advanced cleaning strategies.

Fouling removal by cross-flow flushing and cathodic potential-induced cleaning has been investigated in the thesis. To date, anodic potentials show a stronger effect on biofouling control. Anodic potentials can generate local low pH conditions, produce oxygen bubbles and hydroxyl radicals, and cause direct oxidative inactivation of biofilms and destruction of cell integrity. Cathodic potentials on the other hand, generate local high pH conditions, repel bacteria and negatively charged solutes *via* electrostatic repulsion, and produce hydrogen gas bubbles as well as peroxide. However, the exploration of fouling removal by combined anodic and cathodic potentials (alternating potentials) is scarce. Future

research can investigate the effects of potential types (i.e., direct potential, alternating potential, variable potential and pulsating potential), potential waveforms (i.e., sinusoidal wave, square wave, rectangular wave and triangular wave) and the duty cycle of the applied alternating potential on fouling removal, especially biofouling removal. The cleaning effectiveness by applying alternating potentials should be evaluated, and the underlying mechanisms should be well demonstrated.

III. CMMRs for scale-up applications

CMMRs possessing high catalytic activity have attracted researchers' interest in process-intensified water treatment. It is necessary to explore the durability and scalability of CMMRs for future work. These two factors are critical to achieving scale-up applications. The durability of CMMRs can be determined by catalytic activity in continuous operation and monitoring the leaching of catalysts in the permeate. The loss of activity may be attributed to instability, dissolution and/or passivation of catalysts, and therefore the identification of the primary reasons for decreased activity is helpful to optimize material recipes for CMMR fabrication. In addition, scalable fabrication of CMMRs can be explored *via* solution-based approaches such as phase inversion and batch impregnation.

Additionally, future research can extend the applications to produce various high-value chemical and biological feedstocks. For example, the synthesis of chemicals (i.e., ammonia, hydrogen peroxide and polydimethylsiloxane) can be explored by metal-impregnated CMMRs. Similarly, pharmaceuticals (i.e., penicillin, amoxicillin and L-aspartic acid) could be produced by enzyme-immobilized CMMRs.

VI. Dechlorination by ECMRs in real wastewater treatment

Electrochemical reductive dechlorination is a controllable process for detoxifying chlorophenols. The dechlorination performance has been evaluated on a simplified wastewater system where sodium sulfate and 2-chlorophenol exist in an aqueous solution. However, the interacting species in the real wastewater might affect the dechlorination performance. For example, the presence of sodium chloride would promote the passivation of Ni-P electrocatalysts by forming $NiCl_2$, reducing the dechlorination process. Therefore, future research should investigate the impact of co-existing ions on dechlorination performance in order to mimic the dechlorination process in real wastewater.

Additionally, dechlorinated products (i.e., phenols and their derivatives) still pose environmental threats to ecosystems. Therefore, future research should consider the complete mineralization of chlorophenols *via* multiple treatment processes. For example, sequential reductive dechlorination-oxidative degradation is promising for the complete degradation of chlorophenols from industrial wastewaters and landfill leachates. Alternatively, the produced phenols can be enriched as essential intermediates to manufacture plastics, producing value from waste, which will contribute to critically needed innovation for a circular/green manufacturing economy.

Appendix A. Supplementary Material

Chapter 2 Supplementary Information

Calculation of the mass of latex beads

The diameter of membrane active area $d_M = 0.037$ m, the diameter of a latex bead $d_L = 1\times10^{-7}$ m and density of latex $\rho = 1.055\times10^{3}$ kg/m^3.

Take 2nd adding latex on the membrane for example:

Diameter of membrane active area is $d_M = 0.037$ m

Mass of latex beads:

$$7.5\times10^{-6}\times4/100 = 3\times10^{-4}\,\text{mg}$$

Mass of latex beads per area:

$$\frac{3\times10^{-4}}{\pi(\frac{d_M}{2})^2} = 0.28\,\text{mg/m}^2$$

Table S1. Calculation of the mass of latex beads on the membrane

Number of adding latex fouling on the membrane	Amount of carboxyl latex beads solution (4% w/v) (mL)	Mass of latex beads per surface area (mg/m^2)
1st	7.5×10^{-7}	0.028
2nd	7.5×10^{-6}	0.28
3rd	3.75×10^{-5}	1.4
4nd	7.5×10^{-5}	2.8

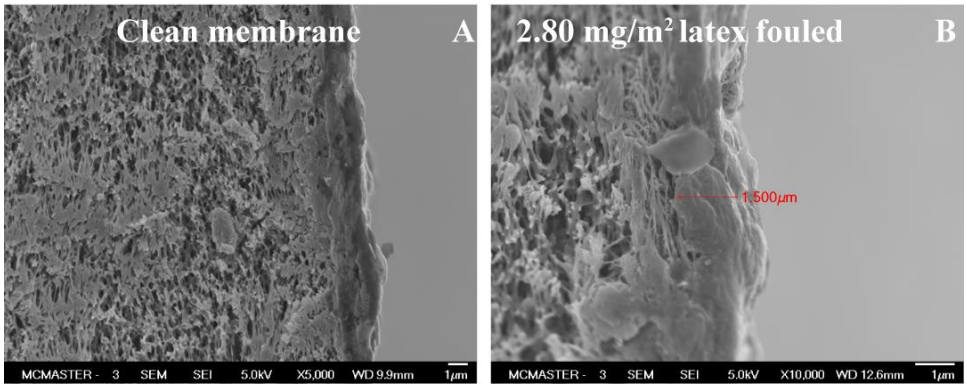

Figure S1. Cross-sectional area of clean membrane (A) and 2.80 mg/m^2 latex fouled membrane (B)

Calculation of pure water permeance

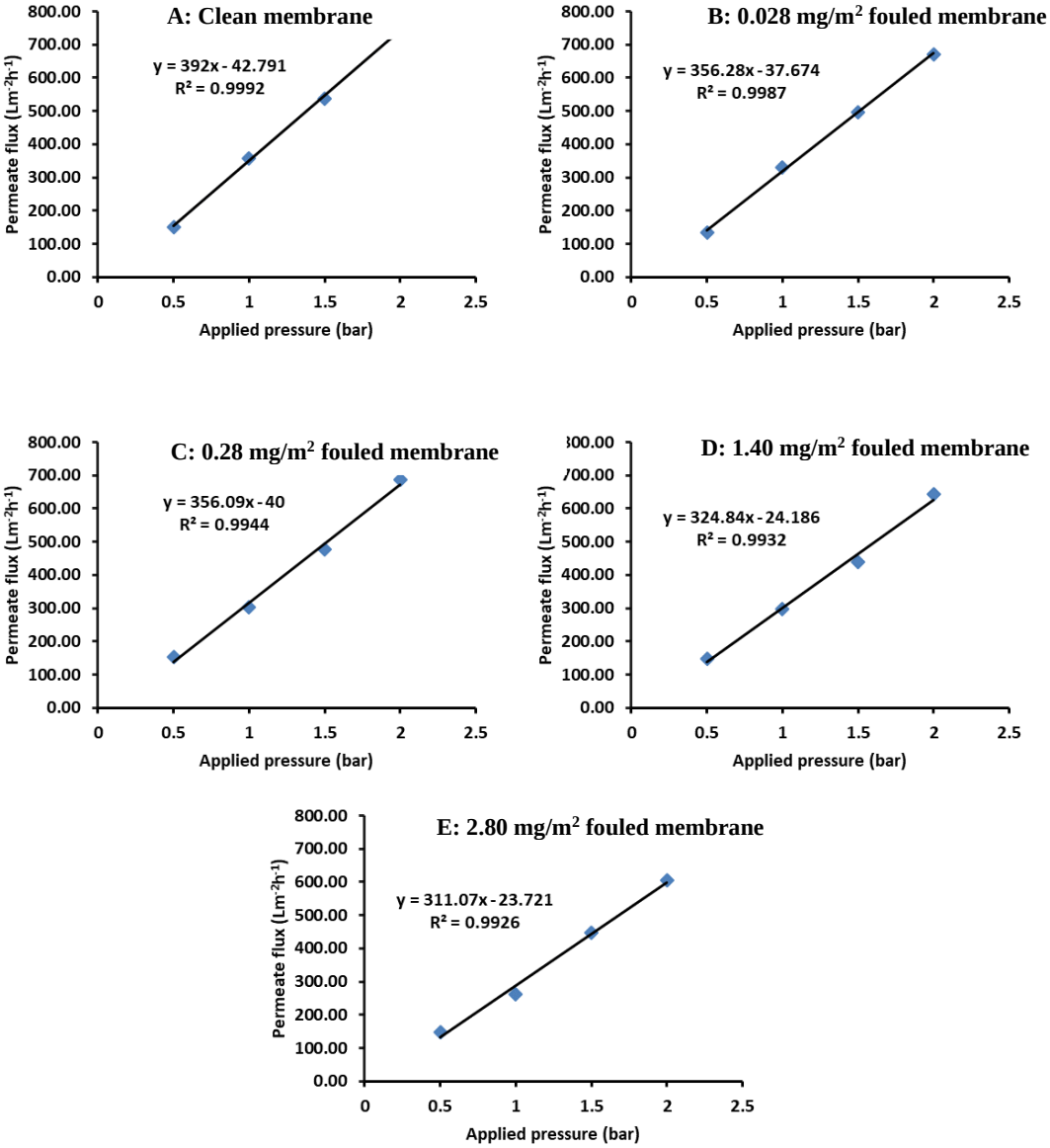

Figure S2. Pure water flux as a function of applied pressure for clean (A) and fouled membranes (B ~ E)

Electrochemical characteristics

CV measurement was conducted in a three-electrode setup to determine whether the redox reactions were occurring on the surface of the CNTs membrane electrode (without foulant). **Figure S3** shows the voltammogram of the clean CNTs membrane in 8500 ppm supporting salt solution. No oxidation and reduction peaks were observed, indicating the CNTs membrane is non-faradaic. The current is generated by the electrical double layer (EDL) capacitor due to coulombic interactions rather than electrochemical reactions [1].

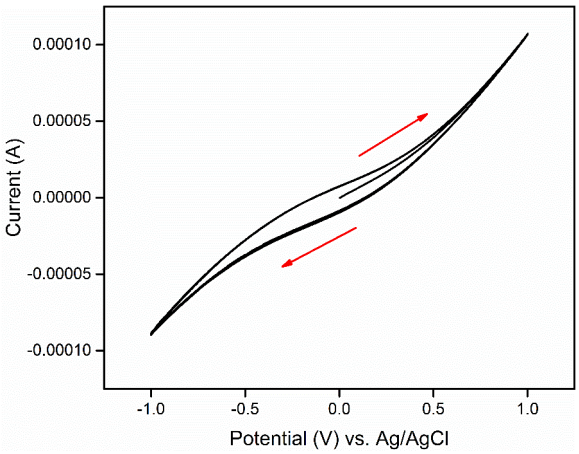

Figure S3. Cyclic Voltammogram of the CNTs membrane electrode (without foulant) in 8500 ppm NaCl at 5 mV/s sweep rate

References

[1] L.K. Pan, X.Z. Wang, Y. Gao, Y.P. Zhang, Y.W. Chen, Z. Sun, Electrosorption of anions with carbon nanotube and nanofibre composite film electrodes, Desalination 244(1-3) (2009) 139-143. https://doi.org/10.1016/j.desal.2008.05.019.

Chapter 3 Supplementary Information

Materials

Polyethersulfone membranes (PES, diameter: 47 mm, pore size: 30 nm) were purchased from Sterlitech (USA). Yeast extract used in microbial growth medium was purchased from Sigma-Aldrich. 50% Glutaraldehyde and 95% alcohol, phosphate-buffered saline (PBS) tablets obtained from Fisher Scientific were dissolved in water (100 mL/tablet) yielding buffer containing 0.01 M phosphate, 0.0027 M KCl and 0.137 M NaCl with pH of 7.4. Live/Dead backlight bacterial viability kit (L7012, Invitrogen-molecular probe, Syto 9 and propidium iodide) for cells microscopy and quantitative assays was obtained from Thermo Fisher Scientific. Deionized water (DI water) used in the following experiments was from an Arium system with the resistivity of 0.048 μS/cm.

Electrical conductivity.

The conductivity of gold-coated membranes was measured by a four-point probe (Ossila, UK), where four probes were assayed in line with equal spacing between each probe. The rounded tips avoided piercing the thin layer compared to sharp needles, and therefore provided good electrical contact between thin film samples and probes. Current was applied and collected through the outer two probes and the voltage drop between the inner two probes was measured. Due to the high electrical impedance of the voltmeters, we assumed no current passed through the inner two probes, suggesting only sample resistance contributed to the voltage reduction. The use of four probes eliminated the

contact resistances and wire resistances, simplifying the measurement of sheet resistance and electrical conductivity.

Morphology.

Surface roughness of pristine membranes was measured by atomic force microscopy (AFM, Asylum) where a silicon cantilever was used for scanning membrane surface in tapping mode over a surface area of 20 μm × 20 μm. The visualized profiles were achieved and correspondingly a parameter of RMS (root mean square average of the height deviation) was obtained using NanoScope Analysis.

Pure water flux.

As-prepared membranes were rinsed in DI water for 24 h prior to flux measurements in a dead-end filtration cell (Sterlitech). Then DI water was used to compress the membrane with an effective surface area of 10.75 cm^2 at 100 psi (6.89 bar) for 1 h. Subsequently, pure water flux was measured under the pressures of 20 psi (138 kPa), 40 psi (276 kPa), 60 psi (414 kPa) and 80 psi (552 kPa), and the volume of permeate was recorded every 10 seconds for 1 min at each pressure.

Calculation of pure water permeance.

Figure S1 shows the permeance derived from the slope of water flux plotted against applied pressure. The linear regression shows a strong linear relationship and 2041.5 LMH/bar of permeance for the gold-coated membrane is achieved.

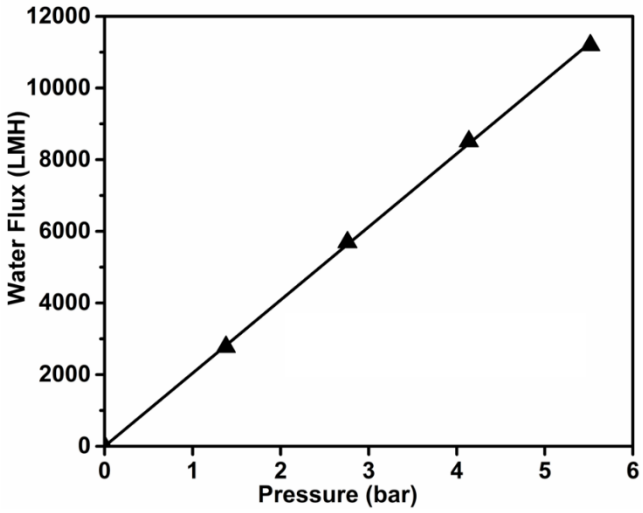

Figure S1. Pure water flux as a function of applied pressure for the membrane coated with 30 nm gold film. The regression line is expressed by $Y = 2041.5\ x$ with $R^2 = 0.9998$.

Calculation of the membrane coating resistance.

The membrane resistance is determined by measuring the water flux as a function of transmembrane pressure and calculated using eq S1:

$$J = \frac{\Delta P}{\mu(R_{PES} + R_{gold})} \quad \text{(S1)}$$

Where J is permeate flux (LMH), ΔP is transmembrane pressure (bar), μ is dynamic water viscosity (Pa·s), and R_{PES} and R_{gold} are membrane substrate resistance and gold film resistance (m^{-1}), respectively. μ is the dynamic viscosity of water, which is a constant of 8.9×10^{-4} Pa·s at room temperature.

Table S1. The resistance of the PES substrate and different thicknesses of the gold coating

	R_{PES} (m^{-1})	R_{gold} (m^{-1})
Pristine PES membrane	1.19×10^{11}	0
30 nm thick gold coated membrane	1.19×10^{11}	3.37×10^{8}
45 nm thick gold coated membrane	1.19×10^{11}	5.36×10^{9}
60 nm thick gold coated membrane	1.19×10^{11}	2.52×10^{10}

Description of the two-electrode crossflow membrane system

A two-electrode system consisting of the working electrode (ECM) and the counter electrode (graphite) was included in the filtration system. The simplified system with two electrodes provided insufficient space for a reference electrode within the lab-scale membrane module, but more closely resembled an industrial membrane system. The two electrodes were independently connected by stainless steel wires to the potentiostat (Autolab PGSTAT 302 N coupled with the FRA module) for obtaining impedance signals. EIS spectra were recorded in response to applying 10 mV of an alternating potential over frequencies of 10^{-1}-10^{6} Hz as membrane biofouling was developed over the course of 12 h. Each individual impedance measurement took approximately 5 min. All experiments were conducted in triplicate.

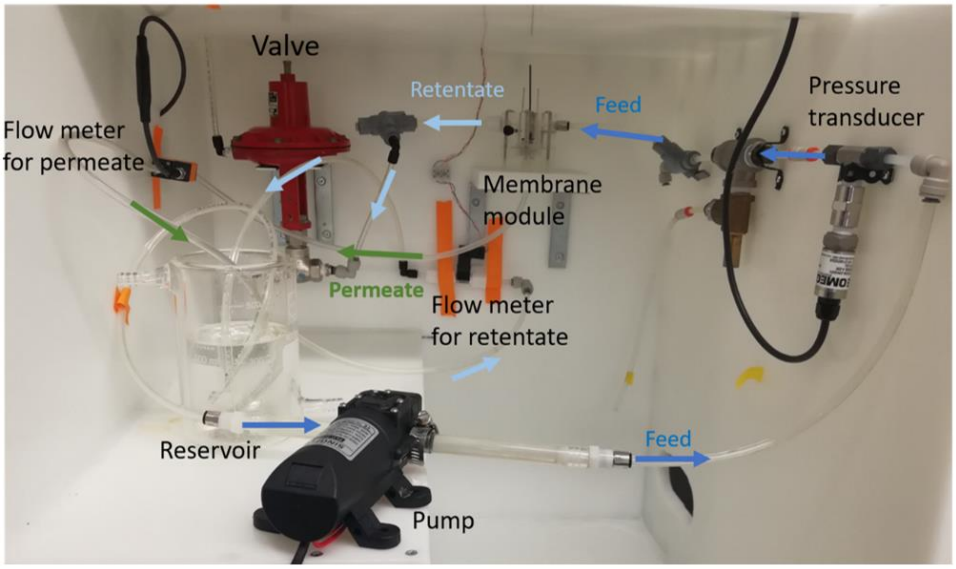

Figure S2. The picture of membrane filtration system

EIS methodology

A detailed description of the principle and experimental protocols for using EIS to detect the membrane fouling has been reported in our previous work [1]. Briefly, a small alternating current $I = i_0 \sin(\omega t)$ with a known amplitude, i_0, and angular frequency, ω, was applied to the ECM surface and the resultant potential across the electrodes at each frequency were measured and expressed as:

$$V = V_0 \sin(\omega t - \theta) \quad \text{(S2)}$$

where V_0 is the magnitude of the potential and θ is the phase angle.

Changes in the amplitude of the measured voltage, $|V|$, and phase angle, θ, could indicate changes at the membrane interface where biofouling occurs. The obtained impedance

data are represented by the correlation between real impedance (Z') and imaginary impedance (Z''), corresponding to Nyquist plots.

$$Z = \frac{V}{I} = Z_0(\cos\theta - j\sin\theta) = Z' - jZ \quad \text{(S3)}$$

where Z_0 is the magnitude of impedance; j is the imaginary constant, defined by $j^2 = -1$.

Alternatively, magnitude of the impedance ($|Z|$) and phase angle for each frequency can be illustrated by the Bode-impedance plot and the Bode-phase plot, respectively.

Biofouling detection by EIS

The non-conductive PES membranes demonstrate large impedance, as expected. Moreover, after biofouling occurred on the PES surfaces, the impedance spectra showed little change from that on the pristine PES membranes, indicating that adhered microorganisms had no resolvable influence on EIS responses due to the lack of electrical sensitivity in a two-electrode system. On the contrary, impedance spectra for gold-coated membranes significantly shifted as a result of biofilm growth, as shown in **Figure S3**, demonstrating the potential for EIS to detect biofouling on ECMs with high signal sensitivity.

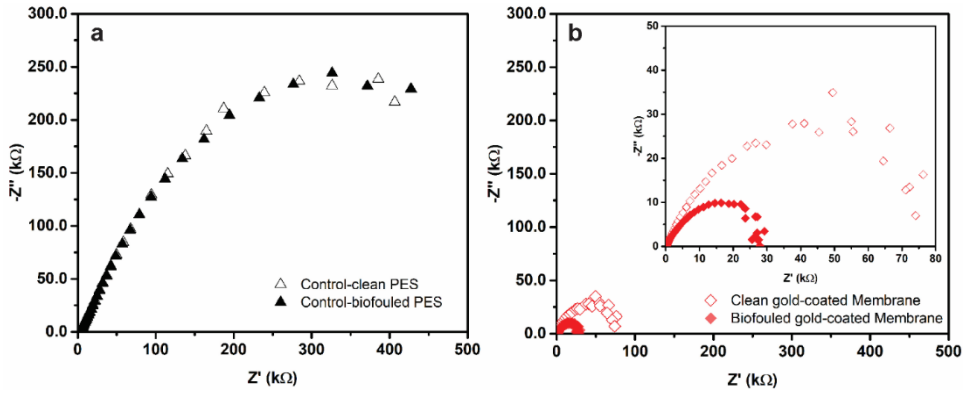

Figure S3. Nyquist plot comparing the real (Z') and imaginary ($-Z''$) impedance for PES membranes (a) and gold-coated membranes (b). The inset in panel (b) is the corresponding impedance spectrum with high magnification. The impedance of biofouled PES and gold-coated membranes were tested after developing biofilms for 12 h.

Elements in the equivalent circuit

Table S2. Simulation results of the proposed circuit

Time (h)	R_S (Ω)	R_m (Ω)	C_1 (F)	**R_d** (Ω)	CPE-Y_0 (s^N/Ω)	CPE-N	R_c (Ω)	C_2 (F)	χ^2
0	163.42	32.98	6.22E-07	87259	3.57E-06	0.70	42.92	5.16E-09	0.09
0.25	123.74	27.45	9.00E-09	67326	4.58E-06	0.68	25.79	1.03E-06	0.19
0.5	117.18	25.44	9.05E-09	63123	4.89E-06	0.68	21.91	7.57E-07	0.16
1	109.51	22.99	1.16E-08	56421	5.20E-06	0.68	29.40	9.87E-07	0.17
2	98.66	18.91	1.74E-08	51438	5.15E-06	0.68	23.74	1.34E-06	0.13
3	91.91	18.07	1.68E-08	50093	4.64E-06	0.68	16.47	7.22E-07	0.08
4	88.00	16.56	7.18E-07	46177	4.73E-06	0.68	18.96	1.25E-08	0.08
5	81.69	15.53	1.95E-08	41141	4.93E-06	0.68	16.91	7.41E-07	0.16
6	78.00	6.43	7.71E-07	36513	5.58E-06	0.67	13.63	1.79E-08	0.09
7	80.89	14.06	1.78E-08	36181	5.69E-06	0.66	7.44	1.34E-06	0.10
8	86.62	19.13	8.90E-07	33447	4.85E-06	0.68	17.74	1.65E-08	0.12
9	96.18	20.54	1.58E-08	34353	4.74E-06	0.67	10.00	1.11E-06	0.14
10	93.15	19.16	1.13E-08	35405	4.93E-06	0.66	11.55	7.91E-07	0.08
11	81.53	14.25	2.16E-08	27863	5.85E-06	0.67	11.93	1.58E-06	0.06
12	93.13	19.09	1.67E-08	30731	4.69E-06	0.67	22.32	9.08E-07	0.14

Simulation results for fitting equivalent circuits to the Nyquist plots are presented in **Table S2**. The EIS signals were recorded in triplicate and the similar trend of impedance against time was obtained.

Characterization of biofouled membranes

According to the FTIR spectra in **Figure S4**, biofilm was developed on the membrane surface due to the presence of lipid and fatty acid region (3000 – 2800 cm^{-1}) and protein or amide region (1700 – 1600 cm^{-1}). [2, 3] These spectra ruled out the formation of covalent gold-sulfur bond (500 – 750 cm^{-1}) and alkyl thiol chains (2900 - 2950 cm^{-1}).

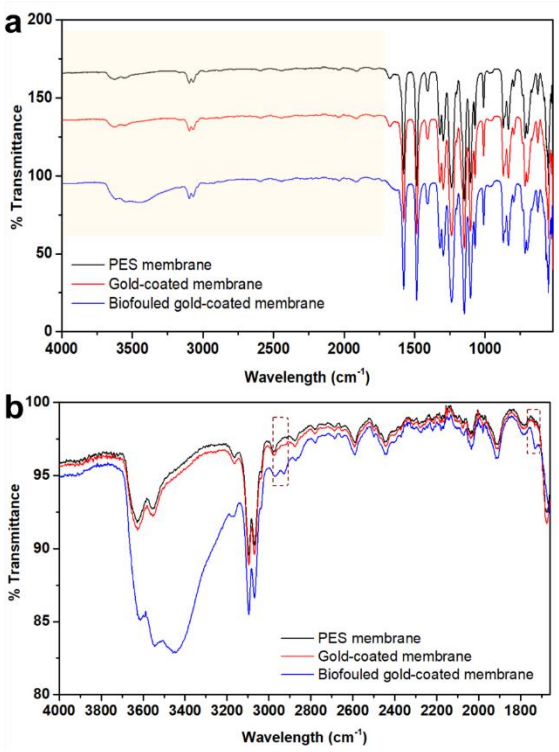

Figure S4. (a) Full FTIR spectra and (b) magnified FTIR spectra of pristine PES, gold-coated membranes and biofouled gold-coated membranes. Rectangular regions are verified the biofilm formation: -OH (3000-2800 cm^{-1}); lipid and fatty acid region (3000-

2800 cm^{-1}, CH_2 and CH_3 asymmetric stretches); amide region (1700-1600 cm^{-1}, C=O stretching and C-N bending; 3500-3400 cm^{-1}, N-H)

Further, the absence of thiol groups was confirmed by Raman Spectra in **Figure S5**, without characteristic peaks (400-200 cm^{-1}) [4, 5].

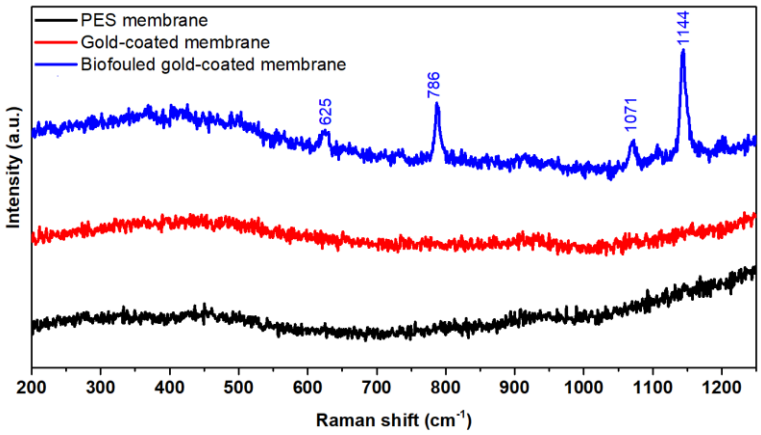

Figure S5. Raman spectra of pristine PES, gold-coated membranes and biofouled gold-coated membranes

Table S3. Raman peak assignment to biofilm [6, 7]

Raman shift (cm^{-1})	**Peak assignments**
625	polysaccharides
786	Polysaccharides, C-C stretching, C-O-C glucosidic link, C-OH
1071	C-O and C-N stretching of proteins
1144	C-O and C-N stretching of carbohydrates

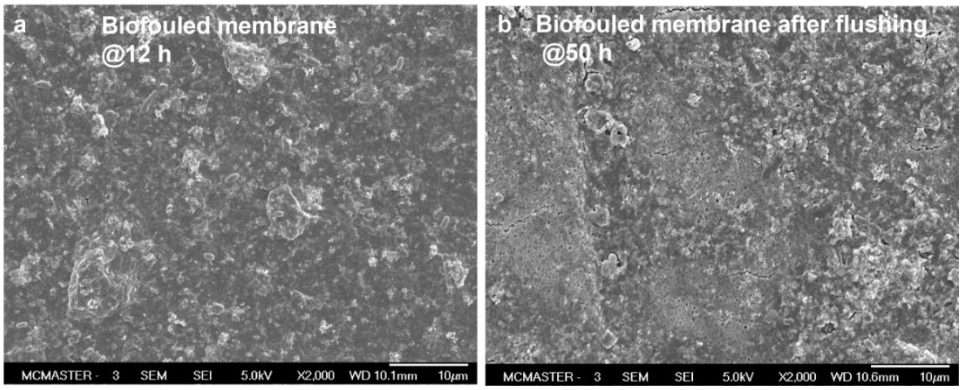

Figure S6. SEM images of biofouled membranes before and after cross-flow flushing

References

[1] N. Zhang, M.A. Halali, C.-F. de Lannoy, Detection of fouling on electrically conductive membranes by electrical impedance spectroscopy, Sep. Purif. Technol 242 (2020). https://doi.org/10.1016/j.seppur.2020.116823.
[2] M. Hassan, E. Gonzalez, V. Hitchins, I. Ilev, Detecting bacteria contamination on medical device surfaces using an integrated fiber-optic mid-infrared spectroscopy sensing method, Sensors and Actuators B: Chemical 231 (2016) 646-654. https://doi.org/10.1016/j.snb.2016.03.044.
[3] F. Villa, F. Secundo, F. Forlani, C. Cattò, F. Cappitelli, Biochemical and molecular changes of the zosteric acid-treated Escherichia coli biofilm on a mineral surface, Annals of Microbiology 71(1) (2021). https://doi.org/10.1186/s13213-020-01617-1.
[4] T. Burgi, Properties of the gold-sulphur interface: from self-assembled monolayers to clusters, Nanoscale 7(38) (2015) 15553-67. https://doi.org/10.1039/c5nr03497c.
[5] C.K.A. Nyamekye, S.C. Weibel, E.A. Smith, Directional Raman scattering spectra of metal–sulfur bonds at smooth gold and silver substrates, Journal of Raman Spectroscopy 52(7) (2021) 1246-1255. https://doi.org/10.1002/jrs.6124.
[6] R. Manisekaran, E. Jiménez-Cervantes Amieva, C.M. Valdemar-Aguilar, L.M. López-Marín, Novel synthesis of polycationic gold nanoparticles and their potential for microbial optical sensing, Gold Bulletin 53(3-4) (2020) 135-140. https://doi.org/10.1007/s13404-020-00283-0.
[7] N.P. Ivleva, M. Wagner, H. Horn, R. Niessner, C. Haisch, Towards a nondestructive chemical characterization of biofilm matrix by Raman microscopy, Anal Bioanal Chem 393(1) (2009) 197-206. https://doi.org/10.1007/s00216-008-2470-5.

Chapter 4 Supplementary Information

Figure S1 shows that 4-NP was insignificantly reduced by adsorption, in the presence of Pd naocatalysts without the presence of $NaBH_4$ and without Pd nanocatalysts, even in the presence of $NaBH_4$.

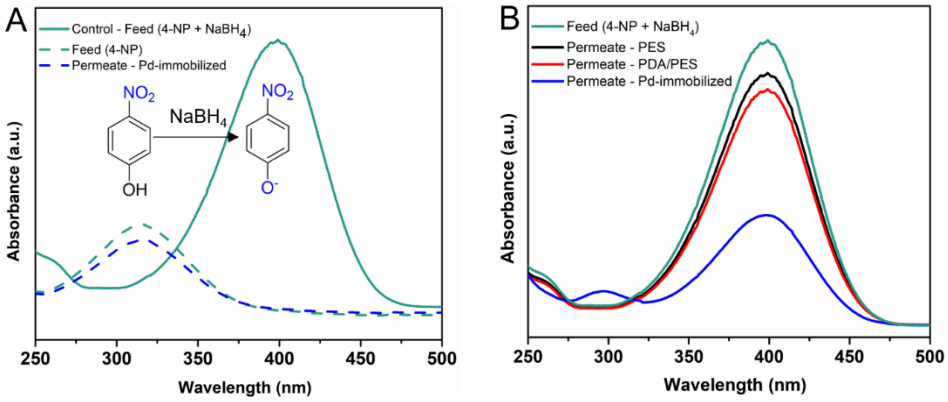

Figure S1. (A) 4-NP reduction by Pd-immobilized membranes in the absence of $NaBH_4$; the peak at 317 nm is 4-nitrophenol and the peak at 400 nm is 4-nitrophenolate ions. (B) 4-NP reduction by PES membranes, PDA/PES membranes and Pd-immobilized membranes in the presence of $NaBH_4$; the peak at 300 nm is 4-aminophenol.

Chapter 5 Supplementary Information

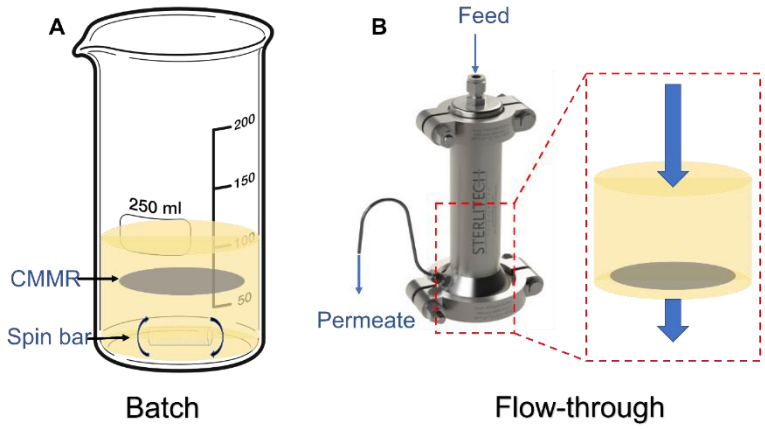

Figure S1. Schematic diagram of (A) batch and (B) flow-through configuration.

Table S1. Summary of physical properties of CMMRs

	Surface area (m^2/g)	Porosity	Ni loading (mg)	Cu loading (mg)
Ni/PES	24.70	0.752±0.012	0.146±0.042	-
rep-R* Ni-Cu/PES	34.06	0.748±0.004	0.135±0.001	0.025±0.005
co-R* Ni-Cu/PES*	93.83	0.747±0.004	0.142±0.001	0.020±0.004

* *rep-R* Ni-Cu/PES CMMR: the replacement reaction bimetallic CMMR

** *co-R* Ni-Cu/PES CMMR: the co-reduced bimetallic CMMR

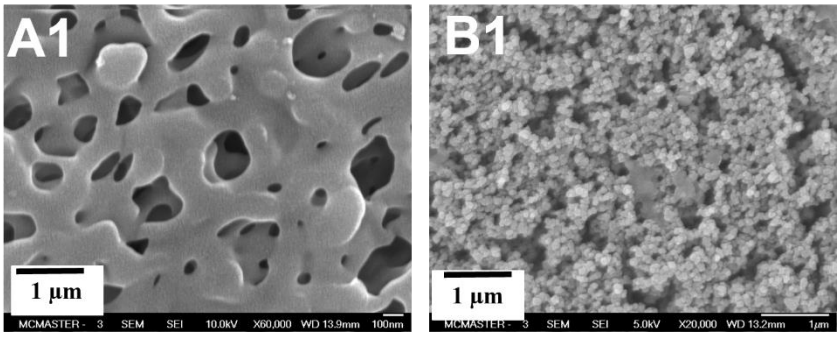

Figure S2. SEM images of (A1) the pristine PES membrane and (B1) the PDA/PES membrane

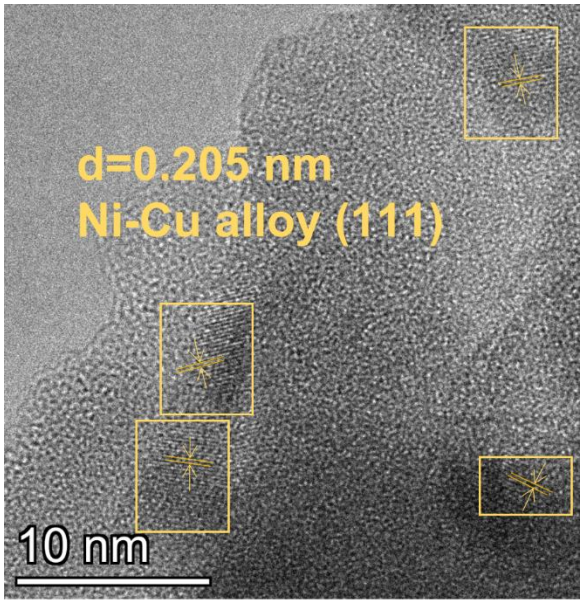

Figure S3. The lattice space of the *rep-R* Ni-Cu NPs and the fast Fourier transform (FFT) pattern in ImageJ was used for analysis.

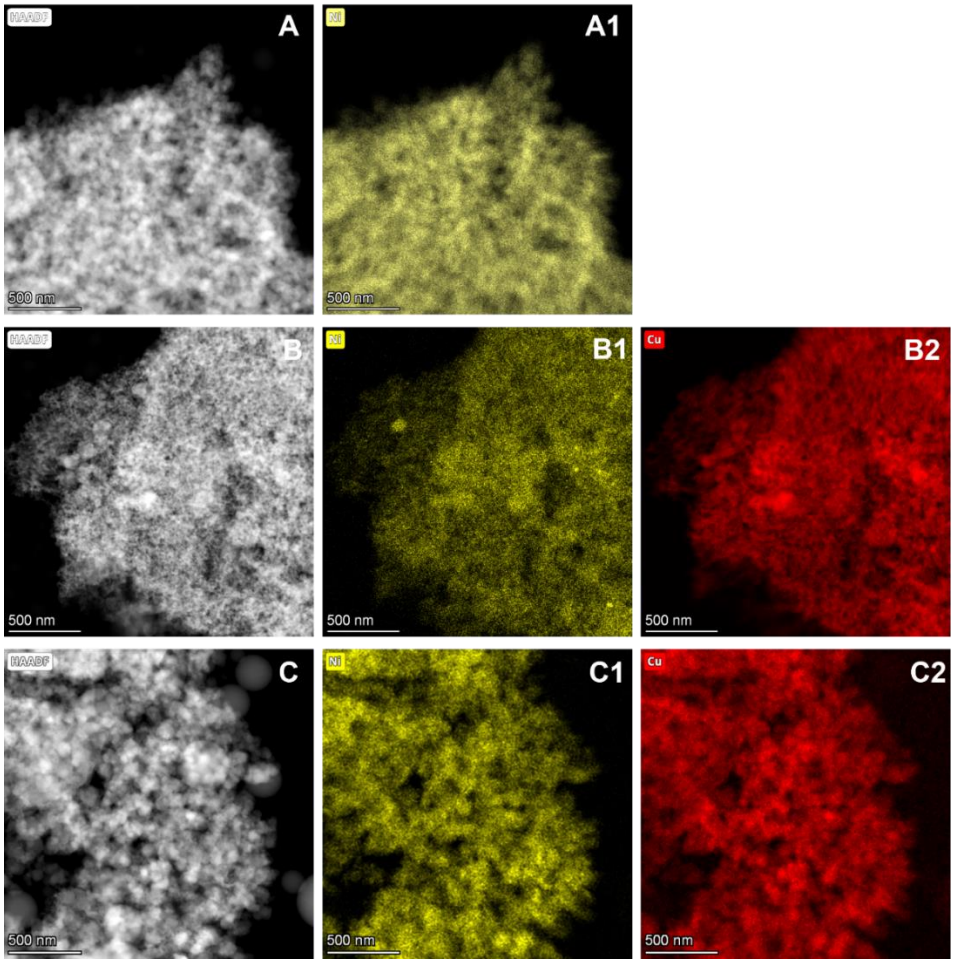

Figure S4. HAADF-STEM mappings of (A) the Ni NPs, (A1) Ni elemental mapping; (B) the *rep-R* Ni-Cu NPs, (B1) Ni elemental mapping, (B2) Cu elemental mapping; (C) the *co-R* Ni-Cu NPs, (C1) Ni elemental mapping, (C2) Cu elemental mapping

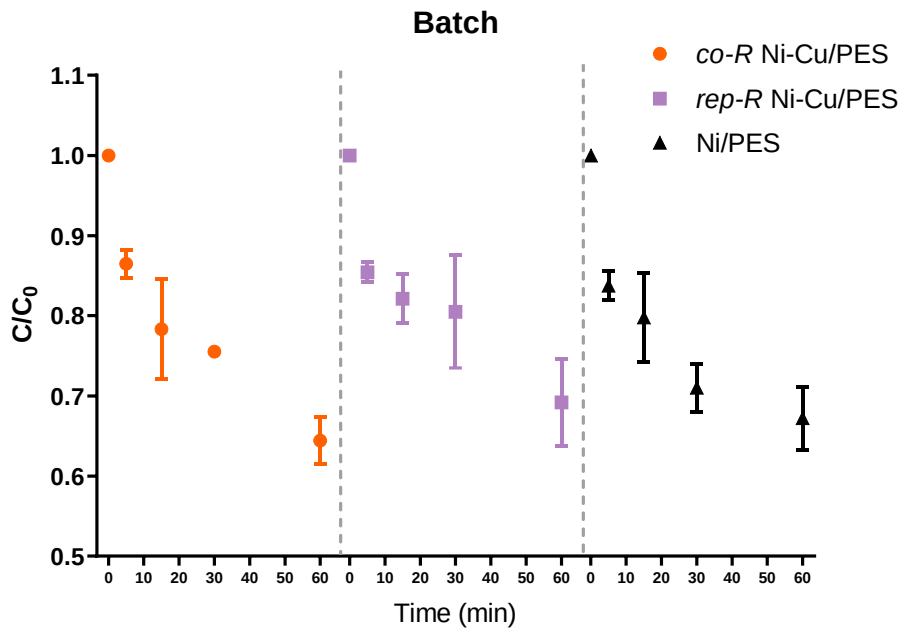

Figure S5. 4-NP conversion using different CMMRs in batch mode

Table S2. Reaction rate constant for *co*-R Ni-Cu/PES membranes under varying conditions

Variables		Rate constant (min^{-1})
4-NP concentration (mM)	0.2	619.98
	0.3	597.37
	0.4	579.27
Applied pressure (psi)	10	608.67
	15	251.90
	20	303.48

Chapter 6 Supplementary Information

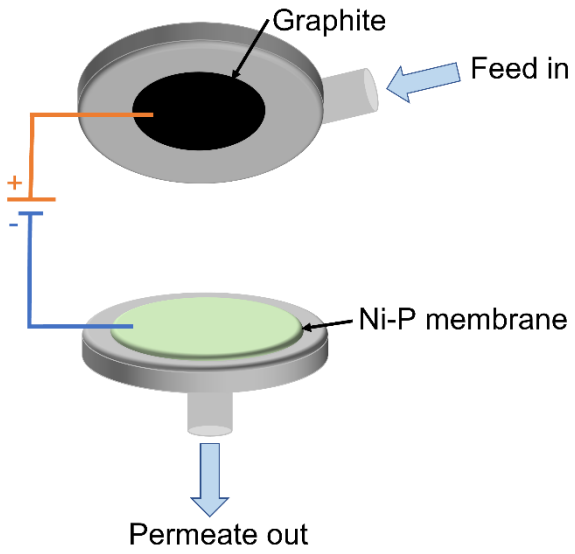

Figure S1. Schematic of a two-electrode membrane cell where the Ni-P membrane acts as the working electrode, and a graphite acts as the counter electrode. Cathodic potentials were applied on the Ni-P membrane.

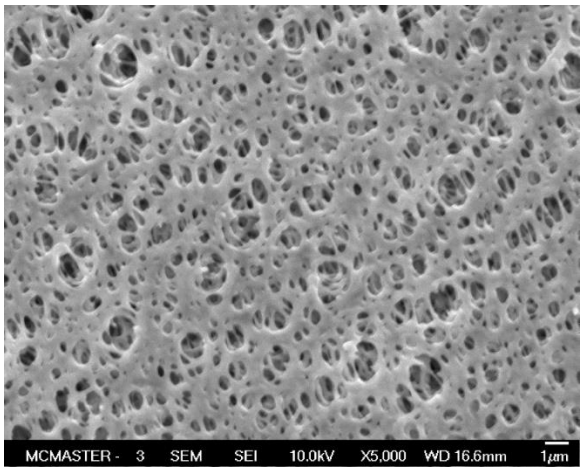

Figure S2. SEM image of the uncoated PES membrane, showing a typical porous structure.

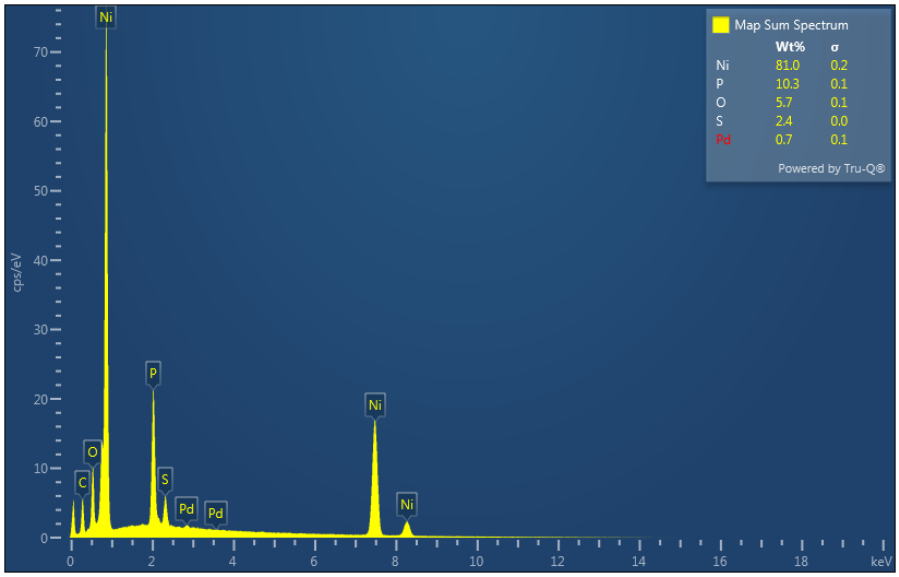

Figure S3. EDS spectrum of Ni-P membranes with 2 min coating

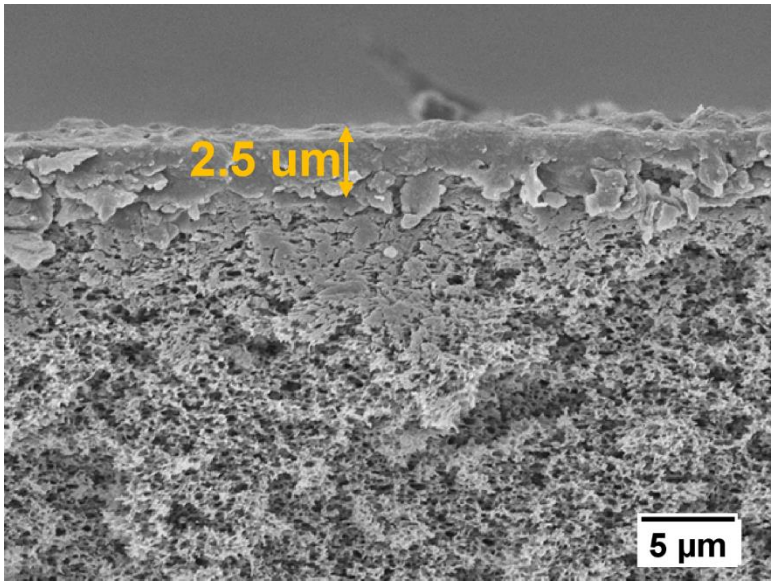

Figure S4. High magnification of the cross-sectional area for Ni-P membranes with 2 min coating

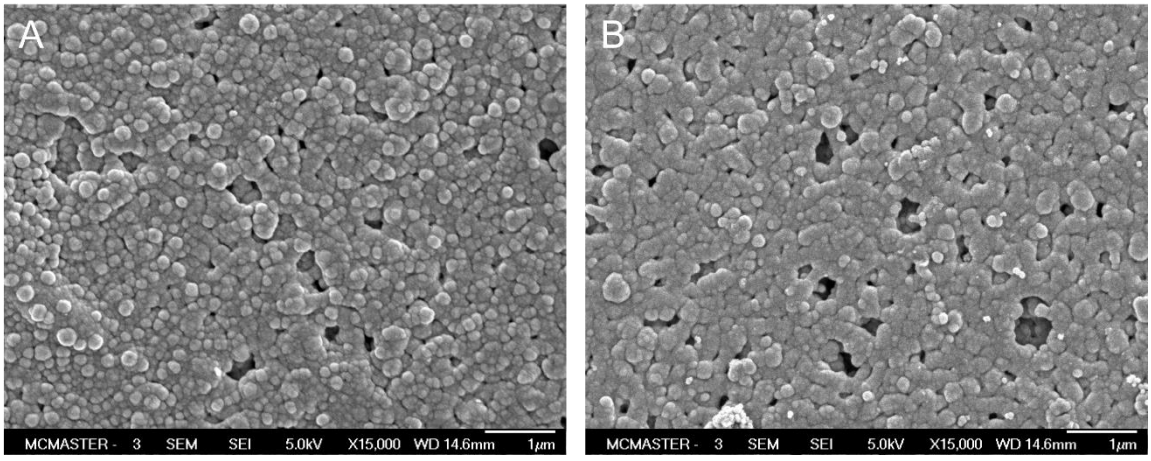

Figure S5. SEM images of Ni-P membranes (A) before and (B) after electrocatalytic dichlorination -at 3 V for 1.5 h.

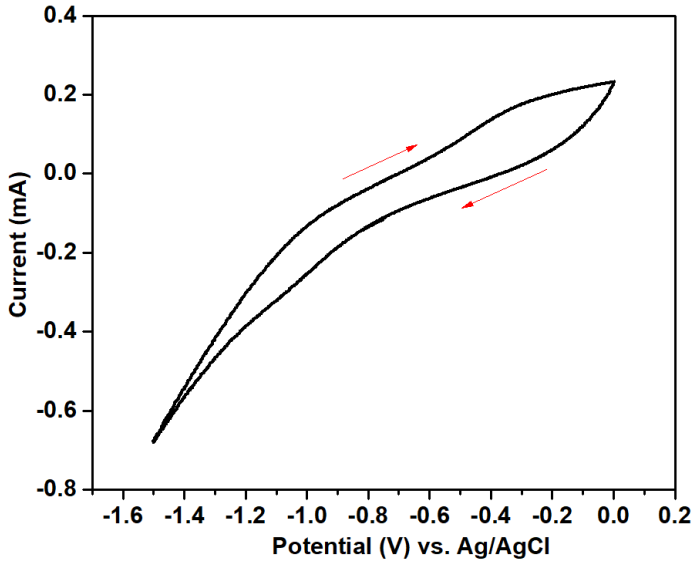

Figure S6. CV curve of Ni-P membranes with 2 min coating in a typical three-electrode electrochemical cell, with Ag/AgCl as a reference electrode. Conditions: 10 ppm 2-CP and 50 mM Na_2SO_4 were used as electrolyte. A scan rate of 50 mV/s was used, and potentials were applied between -1.5 V vs. Ag/AgCl and 0 V. Arrows indicate the direction of CV curve.

Table S1. Comparison of Pd-based cathodes and the noble metal-free membrane cathode on the removal efficiency of 2-CP *via* electrochemical reductive dechlorination

Cathode materials	**Conditions**	**Removal efficiency**	**Reference**
Nanoporous Pd/Ti	$[2\text{-CP}]_0$ = 0.78 mM; [acetate buffer] = 50 mM, initial pH=4, current density =2.5 mA/cm^2; a single compartment electrochemical cell in batch mode	30% (3h)	[1]
Pd-Ni alloy/Ti	$[2\text{-CP}]_0$ = 50 ppm (0.388 mM), $[H_2SO_4]$ = 0.1 M, $[Na_2SO_4]$ = 50 mM at a potential of −0.40 V vs Ag/AgCl(s)/KCl(sat); two half-cells with a salt bridge in batch mode	100% (3 h)	[2]
Pd/Graphite plate	$[2\text{-CP}]_0$ = 50 ppm, $[Na_2SO_4]$ = 50 mM, electrode gap of 8 cm, a cathode cell of 250 mL, current density of 20 mA cm^{-2}; a two-compartment cell in batch mode	95% (2 h)	[3]
Noble metal-free Ni-P ultrafiltration membrane	$[2\text{-CP}]_0$ = 10 ppm (0.08 mM), $[Na_2SO_4]$ = 50 mM, a flow rate of 0.35 mL/min at a cell potential of -2.50 V; a two-electrode membrane reactor in flow-through mode	42.7% (1.5 h)	This work

References

[1] E. Escobedo, J. Kim, D. Oh, K. Cho, Y.-S. Chang, Electrocatalytic dehalogenation of aqueous pollutants by dealloyed nanoporous Pd/Ti cathode, Catalysis Today 361 (2021) 63-68. https://doi.org/10.1016/j.cattod.2020.01.010.

[2] M.A. Arellano-González, A.C. Texier, L. Lartundo-Rojas, I. González, Electrochemical Dechlorination of 2-Chlorophenol on Pd/Ti, Ni/Ti and Pd-Ni Alloy/Ti Electrodes, Journal of The Electrochemical Society 162(10) (2015) E223-E230. https://doi.org/10.1149/2.0021510jes.

[3] S.A. Popli, P. Patel, M. Date, J. Ruparelia, U.D. Patel, Rapid electro-catalytic reduction of azo dyes and phenolic compounds in the presence of metallic palladium, Sep. Purif. Technol 254 (2021). https://doi.org/10.1016/j.seppur.2020.117658.